# Failure Modes Analysis and Life Prediction Modeling of Phosphor Converted White Lighting Emitting Diode under Harsh Environment

by

Hao Zhang

A dissertation submitted to the Graduate Faculty of
Auburn University
in partial fulfillment of the
requirements for the degree of
Doctor of Philosophy

Auburn, Alabama
August 5, 2017

Keywords: Lighting Emitting Diode, HTSL, WHTOL, Color Shift, Lumen Maintenance, Life Time Modeling, Reliability Test



Approved by

Pradeep Lall, Chair, John and Anne MacFarlane Professor of Mechanical Engineering and Director, NSF Center for Advanced Vehicle Electronics
Jeffrey C. Suhling, Quina Distinguished Professor and Chair of Mechanical Engineering
David Beale, Professor of Mechanical Engineering
John Hung, Professor of Electrical Engineering
Lynn Davis, Research Triangle Institute Fellow

## ABSTRACT

The development of light-emitting diode (LED) technology has resulted in widespread solid state lighting use in both consumer and industrial applications due to their high-energy efficiency, long expected life, and less toxic than compact fluorescent lighting.

Previous research shows that there are at least two predominate degradation mechanisms. One mechanism is the degradation of the LED chip due to the increase of non-radiative recombination which reduces the total number of emitted photons. The other predominate mechanism is the degradation of the accumulated optical parts from temperature or electric stresses. Both failure mechanisms could cause the reduction of luminous flux output. Also, degraded optics work as a light spectrum filter and will rescale the intensity of light at each wavelength, which will cause the color coordinates to shift. Besides, increase of non-radiative recombination of electron and holes will create more heat in the die region that will worsen the degradation of optical parts of the LED package. Both failure mechanisms could cause the reduction of luminous flux output and color shift of LED packages.

Currently, TM 80 is the established test method for LED packages to access the quality, reliability and durability before being introduced into to the customers. However, TM80 test only concerns the temperature stress form the operation environment. In LED-based luminaire applications, some are operated in the harsh environment. During the operation, the LED package not only experiences the high bias current and ambient temperature, but also the humidity around the package, especially for the road lighting and automobile lighting. There is literature gap for the accelerated test methods for high power LED packages that includes both the thermal and

humidity effects from the ambient environment. Currently, TM21 long term lumen maintenance projecting method are used to extend the test data to the desired time to predict the lumen maintenance time. One principal issue of TM21 is that it is derived based on the Arrhenius equation and is lack of additional stresses to characterize the non-temperature dependent failure mechanism, such as humidity. Therefore, there exists a need of physics based method to estimate the life time of LED packages under certain operation condition which includes both ambient temperature and humidity.

The disadvantage and deficiencies in TM80 and LM21 validates the needs to develop new acceleration test method and estimation techniques to quantify the reliability of high power LED package under a variety of operation conditions. In this paper, experiments are set up to explore the different effects of the humidity and the thermal stress on various LED packages. Commercial available warm white (3000K) and cool white high power LED packages are used to study the degradations caused by temperature and humidity. The test results in this work increases the understating the reliability of LED packages through the investigation of failure mechanism under various acceleration test conditions. Besides, the prognostic health management method developed in this work increases the accuracy of estimation of remaining useful life of high power LED package. These methods will greatly reduce the time and effort needed to estimate the lumen maintenance time of LED package during the application.

## ACKNOWLEDGMENTS

My sincerest thanks to my professor and mentor, Dr. Pradeep Lall, for his support and guidance during my study at Mechanical Engineering Department of Auburn University for my Ph.D degree. A special thanks to Dr. Lynn Davis for his sponsorship and help during the difficult time of my research and for agreeing to be one of my committee members. I would also like to thank Dr. Jeff Suhling, Dr. John Hung, Dr. David Beale, and Dr. Michael Bozack for supporting me in the completion of my Ph.D study and this dissertation. Special thanks to my lab mates and friends for their help in some form or another to the success of my research, such as Peter Sakalaukus, Di Zhang, Shantanu Shashikant Deshpand, Ryan Lowe and Kalyan Dornala. I would also like to thank the staff of the Mechanical Engineering Department for offering assistance when needed, especially our technician Mr.John Marcell. A very special thanks to my beautiful wife, Lei, for being there when my stress level was at the max and for taking on extra duties at home. I love you and would not have succeed without you. I would give my deepest gratitude to my parents Shiwei Zhang, Suzhen and my aunt Xiaoli Zhang, for their endless love, and spiritual support throughout my life.

## TABLE OF CONTENTS

## LIST OF FIGURES

## LIST OF TABLES

# 1. INTRODUCTION

LEDs packages are called solid state lighting devices, because they utilize semiconductor material instead of a filament or neon gas. An LED package consists of a tiny semiconductor chip encapsulated in a silicone enclosure, which makes LEDs far sturdier than traditional incandescent light bulbs or fluorescent tubes. Since the package of LED don't have fragile components such as glass and filaments, LED packages are able to withstand shock, vibration and relative high temperature (DOE EERE, 2013c) (DOE: EERE, 2013b) (DOE: EERE, 2014a) (DOE: EERE, 2013a) (DOE: EERE, 2012) (DOE: EERE, 2013d).

An LED light will last over 7 years (constant use) before needing replacement. On average, LED bulbs can last 10 times as long as compact fluorescent bulbs, and 133 times longer than typical incandescent bulbs. Long lifespan of LEDs will dramatically reduce maintenance costs and lower long term operating costs compared with traditional incandescent and fluorescent tubes (EERE, 2006).

LEDs are extremely energy efficient and consume up to 90% less power than incandescent bulbs. LEDs are the most efficient way of providing illumination and lighting, with an estimated energy efficiency of 80%-90% when compared to traditional lighting. With traditional incandescent light bulbs who operate at 20% energy efficiency and 80% of the electricity is lost as heat. Since LEDs use only a fraction of the energy of an incandescent light bulb there is a dramatic decrease in power costs. Also, money and energy is saved in maintenance and replacement costs due to the long LED lifespan (Miller N. K., 2014a) (Miller N. M., 2013).

Most compact fluorescent lamp contains a variety of toxic material such as mercury that are dangerous to our environment. LED packages contains not toxic material and 100% of the material can recycled. Also, the long operational lifetime could also save lots of material to build light bulbs.

The illumination from LED packages don't contain infrared light and ultra violet (UV) emission. By adjusting the material used in the device, the spectrum can be controlled according to the requirement. Because of this, LED lighting is highly suitable for illumination of UV sensitive objective, materials and buildings, such as museums, art galleries, archeological sites etc. When powered on, LED lights can brighten up immediately, which has great advantages for infrastructure project, such as traffic and signal lights. Also, LED lights can be switched off and on at a high frequency, without affecting the LED's reliability and light output. In contrast, traditional lighting may take several minutes to reach full brightness, and high frequency switching will drastically decrease the expected life time. LED package is a point light source. Therefore, several packages can be arranged in any shape to achieve the illumination design requirement. By controlling the driver, individual LEDs can be dimmed, resulting in a dynamic control of light, color and distribution. Well-designed LED illumination systems can achieve fantastic lighting effects, not only for the eye but also for the mood and the mind: LED mood illumination is already being used in airplanes, classrooms and many other locations and we can expect to see a lot more LED mood illumination in our daily lives within the next few years.

## 1.1. SOLID-STATE LIGHTING

The LED package typically consists of optical semiconductor devices, optical parts and electronic connections. The core part of the package is the two-lead semiconductor light source. It is a p-n junction diode which can emit light when forward biased. When a suitable voltage is

applied to the leads, electrons can recombine with electron holes within the device, releasing energy in the form of photons. This effect is called electroluminescence and the color the LED is determined by the energy band gap of the material used in the p-n junction (Zukauskas, 2002).

Initially LED colors were very restricted. For the first years, only red LEDs were available. However, as semiconductor processes were improved and new research was undertaken to investigate new materials for LEDs, different colors became available. The two main types of LEDs presently used for lighting systems are aluminum gallium indium phosphide (AlGaInP, sometimes rearranged as AlInGaP) alloys for red, orange and yellow LEDs; and indium gallium nitride (InGaN) alloys for green, blue and violet LEDs. Slight changes in the composition of these alloys changes the color of the emitted light. There are various combinations, each of which releases varying amounts of energy per the semiconductor material's bandgap. When charge carriers are recombined, photons are emitted according to specific discrete energy levels. This specifies the light color. Each LED light color is limited to a very narrow range of wavelength which accordingly only represents a specific light color. Invisible light spectrum can also be produced by LED such as infrared and ultraviolet color. The only spectra that cannot be produced directly from the chip are broad band emission, such as the white light spectrum, since white light represents a mixture of all light colors.

## 1.2. P-N JUNCTION

The LED is a p-n junction device with two type of semiconductor materials, p-type and n-type. The two different semiconductor materials are created by doping, for example by diffusion, ion plantation, and sputter. For LED device, it is usually creased by epitaxy, growing a layer of crystal doped with one type of dopant on top of another layer of crystal doped with another type of dopant. With different crystal of the p-n junction, the LED will emit different color spectrum.

P-N junction servers as the elementary building blocks of most semiconductor electronic devices such as diodes, bipolar junction transistor, solar cells and LEDs. A LED is essentially a P-N junction diode typically made from a direct bandgap semiconductor, for example GaAs, in which the electron-hold pair recombination results in the emission of a photon. The emitted photons' energy is approximately equal to the bandgap energy (Schubert, 2006) (Colinge, 2005) (Pierret R. F., 1996) (Pierret R. F., 2003).

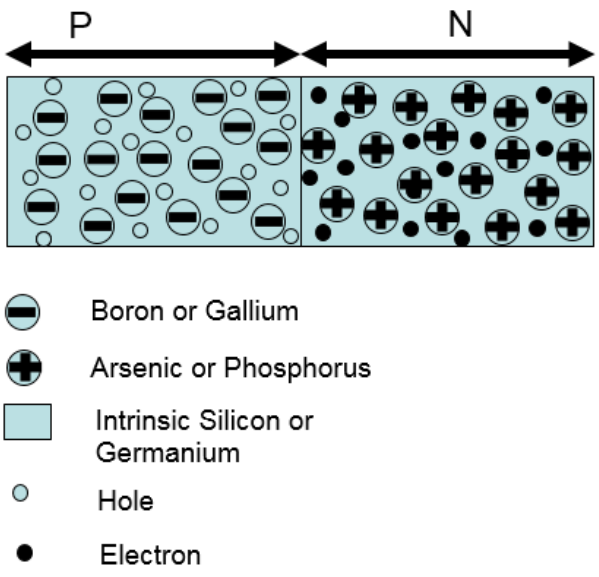


Figure 1: P-N Diodes with dopants.

Figure 1 shows a p-n diodes structure (Kasap, 2001). The positive donor is As and the negative acceptor is B. In the N region, there is immobilized ionized donors and the free electrons. In the P region, there is fixed ionized acceptors and holes.

The concentration of donor in the N region is Nd and the concentration of the acceptor in the P region is Na. Due to the hole concentration gradient from the p-side where $p=p_{p0}$ to the N-side where the $p=p_{no}$, holes will diffuse towards the right and enter the N-side. As a result, holes

will recombine with the electrons in the N-sides. The N-side near the junction becomes depleted of holes which is the majority carrier. Therefore, the N-sided will have a small area where positive donor ions (As+) are exposed and at the concentration of Nd. Similarly, the electrons concentration is higher in N-region than the electrons concentration in p-region. The concentration gradient will drive the electron to diffuse toward the P-region. As a result, electrons will recombine with the holes in the P-region which will expose the acceptor ions (B-).

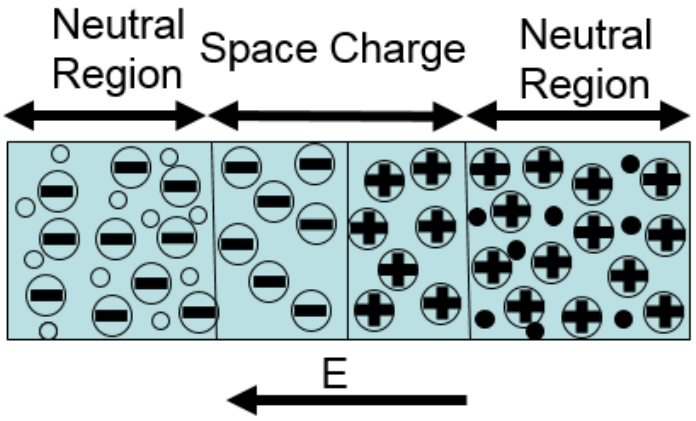


Figure 2: Space charge region and neutral region in P-N junction at equilibrium.

The junction region on both P-region and N-region are consequently depleted of free carriers such as holes and electrons. Therefore, there is a space charge layer (SCL) around the junction. However, most of the area in both P-region and N-region are still neutral. Figure 2 illustrates the neutral region and the depletions region aground the junction region.

There exists an electrical field point from n-region to the p-region, due to the space charge region. With the Gauss's law, also known as Gauss's flux theorem, the generated electrical filed can be related with the distribution of electric charge in the space charge region. Gauss’s saw may be expressed as:

$$\Phi_E = \frac{Q}{\varepsilon_0} \tag{1}$$

Where the $\Phi_E$ is the electric flux through a closed surface S enclosing any volume V, Q is the total charge enclosed within S, and $\varepsilon_0$ is the electric constant. The electric flux $\Phi_E$ is defined as a surface integral of the electric field:

$$\Phi_E = \oiint_S E \bullet dA \tag{2}$$

Where E is the electric field, dA is a vector representing an infinitesimal element of area of the surface and · represents the dot product of two vectors.

If the electric filed distribution is known, it is quite easy to find the distribution of electrical charges according to the Gauss's law. The charge in any given area could be calculated by integrating the electrical field. However, in a p-n diode, the reverse problem should be solved. In the SCR, the charge distribution is known. It is the electrical field should be calculated.

By the divergence theorem, Gauss's law can alternatively be written in the differential form:

$$\nabla \bullet E = \frac{\rho}{\varepsilon_0} \tag{3}$$

Where the divergence of electrical field can be found based on the total electrical charge density and electrical constant $\varepsilon_0$ of the crystal. In the p-n diode case, the divergence could be simplified into the derivation of electrical field in one dimension.

$$\frac{dE}{dx} = \frac{\rho(x)}{\varepsilon} \tag{4}$$

Where $\varepsilon$ equals $\varepsilon_r * \varepsilon_0$. $\varepsilon_r$ and $\varepsilon_0$ are the absolute and relative permittivity of the semiconductor material. $\rho(x)$ is the electrical charge distribution in the SCR.

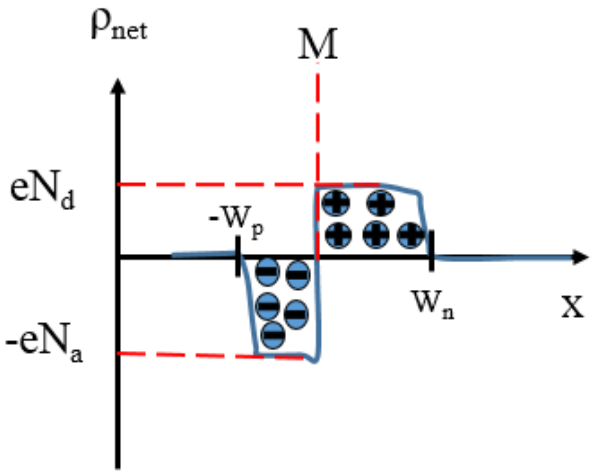


Figure 3: Electrical chareg density of p-n diodes at equliburium. (Kasap, 2001)

The electrical field distribution could be calculated out easily according to the above equation, since the electrical charge density is the same in the depletion region. The distribution of electrical charge density is given in the Figure 3 (Kasap, 2001):The electric field distribution could be calculated by integrating the ρ(x) across the diodes. When the electrical charge density is constant in depletion region, the electrical filed should charges linearly according to the Gauss's law. There is an internal electrical filed E from positive ions to the negative ions. Therefore, the electrical is from n-region from p-region. All those are concluded at the equilibrium condition which means there is no applied bias, or photoexcitation. $p*n=ni^2$ everywhere. The electrical field is given in Figure 4 (Schubert, 2006):

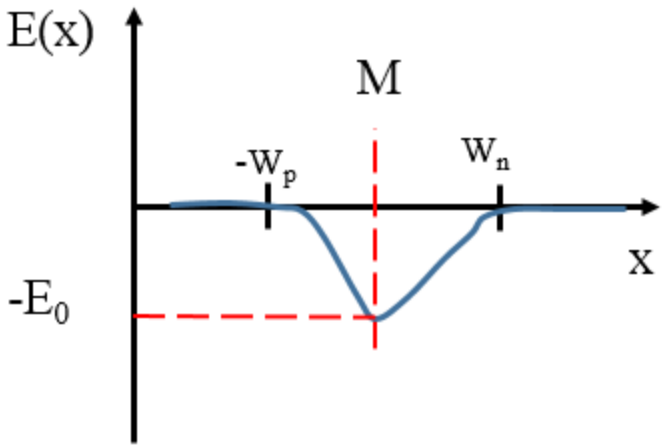


Figure 4: Electrical Distribution in the p-n diodes at equilibrium. (Schubert, 2006)

The internal electrical field points from n-region to p-region which tries to stop the holes diffusing from p-region to n-region. As the same time, it also prevents the electrons to diffusion from n-region to p-region. Figure 5 shows the carrier density distribution in the diode.

The build in electrical field imposes a drift force on holes in the –x direction, whereas the hold diffusion flux in in the +x direction. A similar situation can be observed for electrons in the n-region. The electrons try to diffusion –x direction against the drift force applied by the electrical field. It is obvious that as more and more diffuse towards the right, and electrons diffuse to the left, the electrical field will increase. There will be a threshold where an equilibrium is reached. The rate of holes diffusing towards the n-region is balanced by the holes drifted back by the electrical field. At the same time, the electron diffusion will also be balanced by the drift.

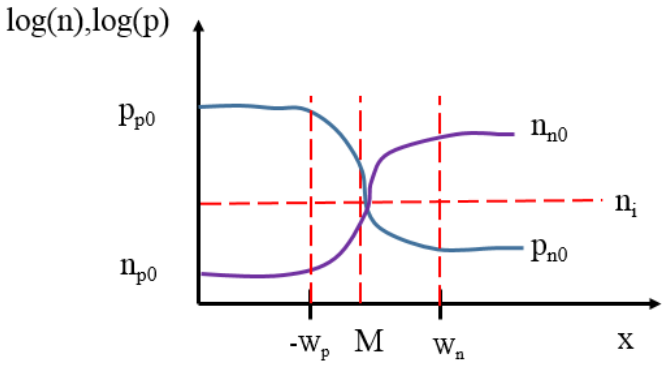


Figure 5: Carrier density in the p-n diodes at equilibrium. (Schubert, 2006)

For uniformly doped p and n regions, the net space charge density ρ in the p-region is constant and equals -eNa. In the n-region space charge density equals +eNd. The total charge on the left side of the depletion region should equal the charge on the right side. Therefore, the following condition should be satisfied:

$$N_a * W_p = N_d * W_n \tag{5}$$

Where the $W_p$ is the depletion length in the p-region and $W_n$ is the depletion length in the n-region. If the $N_a > N_d$, the depletion region penetrates the n-side, lightly doped slides, more than the p-sides, heavily doped side. If $N_a >> N_d$, then the depletion region is almost entirely in the n-region. By the calculation, the electrical filed research the maximum value at the interface of the depletion area.

The potential V of the depletion area can be calculated out by the integration of the electrical field.

$$E = \frac{dV}{dx} \tag{6}$$

Potential increases in the depletion region from p side to the n side. It reaches its maximum value at the interface between SCR and depletion region in the n region. If use the potential in the far left as reference voltage, the maximum value in the n region is called the built-in potential. Given the doping profile, the maximum electrical field $E_{max}$ and build in potential $V_{bi}$ could be calculated with equations (7) and (8):

$$E_{\max} = -\frac{e * N_a * W_n}{\varepsilon} = -\frac{e * N_a * W_p}{\varepsilon} \tag{7}$$

$$V_{bi} = -\frac{e * N_a * N_d * (W_n + W_p)^2}{2 * \varepsilon * (N_a + N_d)} \tag{8}$$

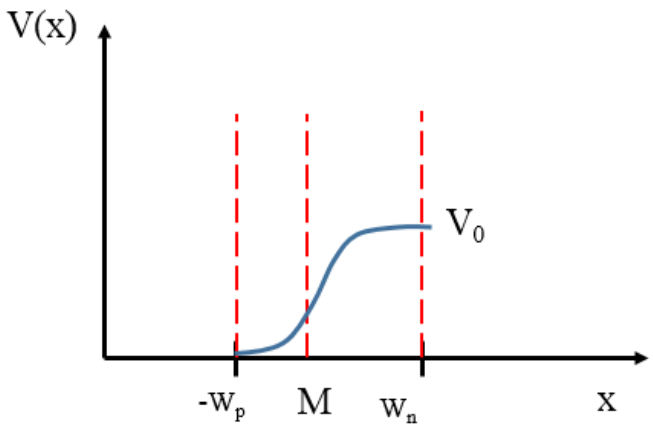


Figure 6: Potential distribution of p-n diode at equilibrium. (Schubert, 2006)

The distribution of potential V(x) is illustrated in Figure 6.When the p-n diode is forward biased with a voltage of V so that the positive terminal of the battery is attached to the p-region and negative terminal to the n-side. The power supply will change the equilibrium of the junction by reducing the build in potential by V. Most of the potential change will happen in the depletion

region as there are full of immobile ions, in comparison with the bulk region in which there are plenty of majority carriers.

As a result, the potential barrier against diffusion is reduced to ($V_{bi}$-V). This will have dramatic effects on the equilibrium of drift and diffusion. The probability that a hole in the p-region will go cross the potential barrier and diffuse to the n-region will changes from 0 to exp (-e*(Vbi-V)/$K_B$T). In other words, the applied forward voltage reduced the build-in potential which act against the diffusion. Consequently, many holes can diffuse into the n-region now. This effect is called minority carrier injection. Holes can diffuse and inject into n-region, becoming injected minority carriers. Similarly, electrons can diffuse and inject into the p-region through the same process. When holes are injected into the neutral n-side, they draw some electrons form the battery. As a result, there is a small increase in the electrons concentration in n-region. This small amount of increase in the majority carrier is necessary to the charge balance and maintain neutrality in the n-region. The electrostatic analysis of a p-n diode is of interest since it provides knowledge about the charge density and the electric field in the depletion region. It is also required to obtain the capacitance-voltage characteristics of the diode. The analysis is very similar to that of a metal-semiconductor junction. A key difference is that a p-n diode contains two depletion regions of opposite type. The width of depletion on the p side is $W_p$ and the depletion region width in the n side is $W_n$. The full-depletion approximation assumes that the depletion region around the metallurgical junction has well-defined edges. It also assumes that the transition between the depleted and the quasi-neutral region is abrupt. We define the quasi-neutral region as the region adjacent to the depletion region where the electric field is small and the free carrier density is close to the net doping density. The full-depletion approximation is justified by the fact that the carrier densities change exponentially with the position of the Fermi energy relative to the band edges.

The total depletion layer width can be calculated with the following equation:

$$W_p + W_n = \sqrt{\frac{2*\varepsilon}{e} * (\frac{1}{N_a} + \frac{1}{N_d}) * (V_{bi} - V)} \quad (9)$$

From which the solutions for the individual depletion layer widths, $W_p$ and $W_n$ are obtained:

$$W_n = \sqrt{\frac{2*\varepsilon}{e} * \frac{N_a}{N_d} * (\frac{1}{N_a + N_d}) * (V_{bi} - V)} \quad (10)$$

$$W_p = \sqrt{\frac{2*\varepsilon}{e} * \frac{N_d}{N_d} * (\frac{1}{N_a + N_d}) * (V_{bi} - V)} \quad (11)$$

The hole concentration $p_n(0)$, on the interface of depletion region and charge neutrality region becomes larger as a result of minority carrier injection. This concentration is determined by the applied voltage and the minority concentration in the n –region. It is also called law of the junction which is described in the following equation:

$$p_n(0) = p_{n0} * \exp(\frac{e*V}{K_B * T}) \quad (12)$$

Where $p_{n0}$ equals ni^2/$N_d$, $K_B$ is the Boltzmann constant and equals: $8.6173324(78)\times10^{-5}$ eV/K. T is the ambient temperature in Kelvin. The above equation depicts the effects of the applied voltage on the injected minority carrier concentration just outside the depletion region. If the applied voltage is 0 volt, $p_n(0)$ equals $p_{n0}$ which is exactly what is expected.

Injected holes in the n-region will recombine with the electrons in this region. The recombined electrons will be replenished by the negative terminals of the battery connected to the diode. The current due to the holes diffusion can be stable, because more holes can be supplied by the p-region.

Electrons have the similar behavior and will inject from n-region to the p-region of the diodes if forward voltage is applied. The electron concentration $n_p(0)$ just outside the depletion region in the p-side can be calculated in the same manner:

$$n_p(0) = n_{p0} * \exp(\frac{e*V}{K_B*T}) \quad (13)$$

In the p-region, the injected electrons diffused toward the positive terminal and they will recombine with the many holes in this region. The recombined holes will be resupplied by the positive terminal of the battery connected to the diode. The current due to the diffusion of electrons in the p-region can be sustained by the supply of electrons from n-side.

It is obvious that an electric current can be maintained through a pn junction if the diode is forward biased. The current flow is caused by the diffusion of minority carriers. If the lengths of the p and n-region is longer than the minority carrier diffusion lengths, then it can be assumed as the long base boundary condition. It is expected that the hole's concentration $p_n(x)$ on the n-side will fall exponentially towards the thermal equilibrium value $p_{n0}$. The diffusion holes' concentration in the n-region can be calculated as:

$$p_n(x) = p_{n0} + p_{n0}(\exp(\frac{e*V}{K_B*T}) - 1) * \exp(\frac{-x}{L_h}) \quad (14)$$

Where $p_{n0}$ is the hole's concentration at thermal equilibrium, $L_h$ is the hole diffusion length defined by:

$$L_h = \sqrt{D_h * \tau_h} \quad (15)$$

In which $D_h$ is the diffusion coefficient of holes and $\tau_h$ is the mean hold recombination lifetime (minority carrier lifetime) in n-region. The diffusion length is the average distance diffused by a minority carrier before it disappears by recombination. The rate of recombination of injected holes at any given x in the neutral region is proportional to the excess hole concentration at that point x. In the steady state, this recombination rate at x just balanced by the rate of holes brought to x by diffusion.

The diffusion current density $J_{D,hole}$ is the hold diffusion flux multiplied by the hole charge. The diffusion current of holes in the n-region can be calculated by:

$$J_{D,hole} = \frac{e * D_h * ni^2}{L_h * Nd} * (\exp(\frac{e * V}{K_B * T}) - 1) * (\exp(\frac{-x}{L_h})) \quad (16)$$

Although the above equation shows that the hold diffusion current depends on the location, the total current at any given location is fixed. The total current is the sum of holes current and electron current which is independent of location. The decrease of hole current will be made up by the increase in the current due to the drift of majority carriers in n-region.

There is a similar expression for the electron diffusion current density $J_{D,elec}$ in the p-region. The electron diffusion current density can be expressed as:

$$J_{D,elec} = \frac{e * D_e * ni^2}{L_e * Na} * (\exp(\frac{e * V}{K_B * T}) - 1) * (\exp(\frac{-x}{L_e})) \quad (17)$$

The total current density in the diode under forward bias can be expressed as:

$$J_{D,elec} = e(\frac{D_h * ni^2}{L_h * Nd} + \frac{D_e * ni^2}{L_e * Na}) * (\exp(\frac{e * V}{K_B * T}) - 1) \quad (18)$$

This is the expanded diode equation and it is also called the Shockley equation. It represents the diffusion of minority carriers in the neutral regions. The constant part of the above equation is also called the reverse saturation current density. If a reverse bias V=-Vr which is greater than the thermal voltage $K_BT/e$ (25mV), the current density will become $-J_s$. $J_s$ depends on the doping concentration $N_a$, $N_d$, and the material property such as $D_h$, $D_e$, $L_h$, $L_e$.

$$J_s = e * (\frac{D_h * ni^2}{L_h * N_d} + \frac{D_e * ni^2}{L_e * N_a}) \quad (19)$$

For now, it is assumed that the injected minority carriers diffuse and recombine in the neutral region only under forward bias. However, some of the minority carriers will recombine in the depletion region. The external current must therefore also supply the carriers lost in the recombination process in the space charge region.

The net expression for the net steady-state recombination rate can be drastically simplified under certain condition. The simplified expression for the net recombination inside an R-G

depletion region is a special case result that is encountered quite often in device analysis. An R-G depletion region is formally defined to be a semiconductor volume where n<<n1 and p<<p1. Since np<<n1p1=$ni^2$, a deficit of carriers always exists insides the envisioned depletion region.

At the metallurgical junction at the center of the depletion region, the hold and electron concentration are $p_m$ and $n_m$. They are equal. The recombination current can be found by considering electros recombining in the p-region with the length of $W_p$ and holes recombining in the n-side with the length of $W_n$. $W_n$ plus $W_p$ equals the total depletion length in the diode. Suppose that the mean hole recombination time in $W_n$ is $\tau_h$ and mean electron recombination time in $W_p$ is $\tau_e$. The total electrons number is the integration of the electron concentration from the center of the depletion region to the interface of the depletion region and neutral area. Dividing the total electron by the mean electron recombination time gives the recombination rate. Thus, the recombination current density is:

$$J_{recom} = \frac{e * W_p * n_M}{2 * \tau_e} + \frac{e * W_n * p_M}{2 * \tau_e} \tag{20}$$

Under steady state and equilibrium conditions, the electron concentration at the middle of depletion region can be calculated by the Boltzmann statistics.

$$\frac{p_M}{p_{po}} = \exp(-\frac{e*(V_{bi} - V)}{2K_B * T}) \tag{21}$$

The $p_{p0}$ equals the doping concentration Na. The above equation can be further simplified to:

$$p_M = n_i \exp(-\frac{e*(V)}{2K_B * T}) \tag{22}$$

This means that the recombination current equals:

$$J_{recom} = \frac{e * n_i}{2 * \tau_e} * (\frac{W_p}{\tau_e} + \frac{W_n}{\tau_e}) * \exp(\frac{e*(V)}{2K_B * T}) \tag{23}$$

For a better quantitative analysis, the expression for the recombination current can be shown to be:

$$J_{recom} = J_0 * (\exp(\frac{e*(V)}{2K_B*T}) - 1) \quad (24)$$

Where $J_0$ is pre-exponential constant. The above equation shows the current that supplies the recombined carriers in the depletion region. The total current inside the diodes includes the carriers for the minority diffusion in the neutral region and the recombination carrier in the space charge layer. So the total current is given in the following equation:

$$J_{total} = J_0 * (\exp(\frac{e*(V)}{2K_B*T}) - 1) + J_s * (\exp(\frac{e*V}{K_B*T}) - 1) \quad (25)$$

Where $J_0$ is the constant for the recombination current in the depletion region, $J_s$ is constant for the diffusion current in the neutral region. Generally, the diode current can be written as:

$$I = I_0 * (\exp(\frac{e*(V)}{\eta*K_B*T}) - 1) \quad (26)$$

Where $I_0$ is a constant and $\eta$ is called the diode ideality factor. $\eta$ is 1 for diffusion current controlled diode. $\eta$ is 2 for space charge layer recombination controlled characteristics. Figure 7 shows the forward and the reverse I-V characteristics of typical p-n diode (Pierret R. F., 1996).

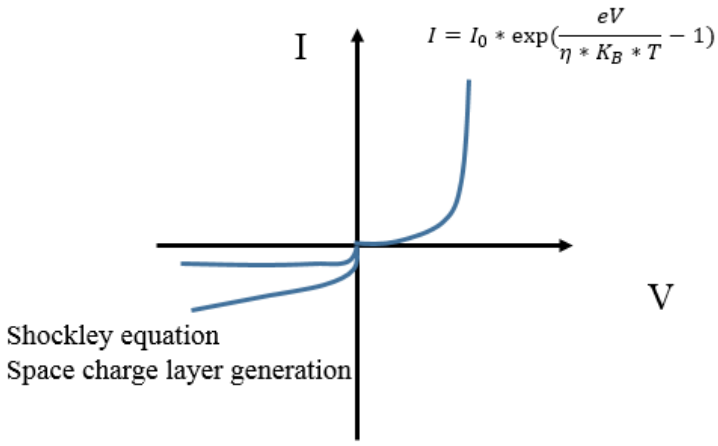


Figure 7: Diode I-V curve. (Pierret R. F., 1996)

### 1.3. RECOMBINATION

Electrons sitting inside the conduction band is not a stable state and will eventually stabilize to a lower energy state in the valence band. When this happens, the electron will move into an empty state which is a hole. This process is called recombination. Electrons and holes in semiconductors recombines either radiative, i.e. accompanied by the emission of a photon, or non-radiative. There are three types of recombination in the bulk of semiconductor. The first is called radiative recombination. The second is called Shockley-Read -Hall recombination which is a non-radiative recombination. Phonons will be emitted from the process rather than the photons. The last recombination is called Auger recombination. Auger Recombination involves three carriers. An electron and a hole recombine, but rather than emitting the energy as heat or as a photon, the energy is given to a third carrier, an electron in the conduction band. This electron then thermalizes back down to the conduction band edge. In LED, the radiative is obvious the preferred process. However, non-radiative recombination can, under practical conditions, never be reduced to zero.

Thus, there is a completion between radiative and no-radiative recombination. Maximum the radiative process and minimization of the non-radiative process can be controlled in several methods.

Any semiconductor has two types of carrier, electrons and holes. Under thermal equilibrium condition, without external stimulation such as light or minority injection, the product of electron and holes concentration is a constant (Colinge, 2005) (Schubert, 2006) (Pierret R. F., 1996):

$$n_0 * p_0 = ni^2 \tag{27}$$

Where n and p are electron and holes concentration, ni is the intrinsic carrier concentration.

Excess carriers in semiconductors can be generated by external stimulation either by absorption of light or by an injection current. The total carrier concentration becomes:

$$n = n_0 + \Delta n \tag{28}$$

$$p = p_0 + \Delta p \tag{29}$$

Where Δn and Δp are the excess electron and hole concentration respectively. The number of recombination events will be proportional to the concentration of elects and holes. Thus, the recombination rate is proportional to the product of electrons and holes concentration. Using a proportionality constant, the recombination rate per unit time per unit volume can be written as:

$$R = B * n * p \tag{30}$$

This equation is the bimolecular rate equation and the proportionality constant B is called the bimolecular recombination coefficient. It has typical value of $10^{-11}$ to $10^{-19}$cm$^3$/ for direct band gap III-V semiconductor. Consider a semiconductor subjected to photoexcitation. The recombination dynamics can be analyzed as a function a time. Since the electrons and holes are generated in pairs, the excess concentration of electrons and holes are the same:

$$\Delta n = \Delta p \tag{31}$$

With the bimolecular rate equation, the recombination rate is given by:

$$R = B*[n_0 + \Delta n(t)]*[p_0 + \Delta p(t)] \tag{32}$$

For the low-level excitation, the photo generated carrier concentration is much small than the majority carrier concentration. Therefore $\Delta n << (n_0+p_0)$, using $\Delta n(t)= \Delta p(t)$, the above equation can be simplified to:

$$R = B*ni^2 + B*[n_0 + p_0]*\Delta n(t) = R_0 + R_{excess} \tag{33}$$

The time dependent carrier concentration can be calculated from the continuity equation:

$$\frac{dn(t)}{dt} = -R = -(R_0 + R_{excess}) \tag{34}$$

At time =0, the illumination is switched off. The recombination rate can then be calculated by:

$$\frac{d\Delta n(t)}{dt} = -B*[n_0 + p_0]*\Delta n(t) \tag{35}$$

The solution of the above differential equation can be obtained by the separation of variables.

$$\Delta n(t) = \Delta n_0 * \exp(-B*(n_0 + p_0)*t) \tag{36}$$

The carrier lifetime $\tau$ can be identified as:

$$\tau = \frac{1}{B*(n_0 + p_0)} \tag{37}$$

For semiconductor with specific doping, the carrier life time can be rewritten as:

$$\tau_n = \frac{1}{B*(N_a)} \tag{38}$$

For p-type semiconductor and

$$\tau_p = \frac{1}{B*(N_d)} \tag{39}$$

For n-type semiconductor. Once the photon excitation is terminated, the minority carrier concentration decays exponentially with a characteristic time constant denoted as the minority carrier lifetime. It is the mean time between generation and recombination of a minority carrier. For the case of high level excitation, the photon generated carrier concentration is larger than the equilibrium carrier concentration. The bimolecular rate equation is then given by:

$$\frac{d\Delta n(t)}{dt} = -B * \Delta n^2 \tag{40}$$

Solving the differential equation above yields the solution:

$$\Delta n(t) = \frac{1}{B * t + \Delta n_0^{-1}} \tag{41}$$

There are several reasons that can cause the non-radiative recombination, such as defects in the crystal structure. In the radiative recombination process, photon will be released and its energy equals the bandgap energy of the semiconductor. During the non-radiative recombination, the electron energy is released in the form of phonons, which is the vibration energy of lattice atoms. As a result, the electron energy is converted to the heat in the semiconductor. Figure 8 (Pierret R. F., 1996) shows the recombination process.

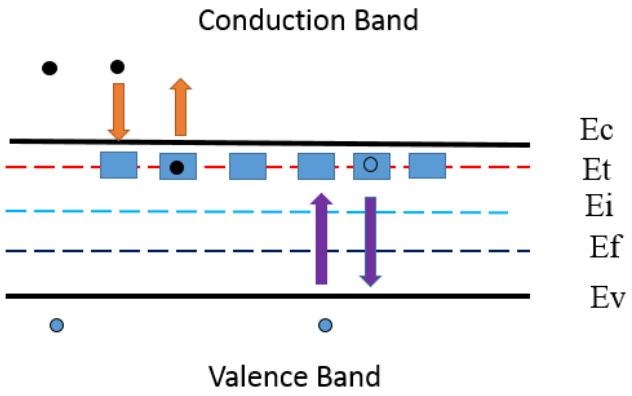


Figure 8: Generation and Recombinationin Steady State. (Pierret R. F., 1996)

The lattice defects can include crystal defects, dislocation and lattice dislocation. Those defects can introduce extra energy levels that different from the energy level of the original semiconductor. It is very often that those defects introduce several energy levels that between the forbidden gap of the semiconductor. Those energy levels are efficient recombination center, especially if the energy level is close to the middle value of the forbidden gap. The recombination of carriers in those energy level will be non-radiative recombination and transfer electron energy to heat.

Shockley, Read and Hall analyzed the process of recombination via traps in details. The non-radiative recombination rate through a trap of energy $E_T$ and concentration of $N_T$ is given by:

$$R = \frac{p_0 * \Delta n + n_0 * \Delta p + \Delta n * \Delta p}{\frac{n_0 + n_1 + \Delta n}{N_T * v_p * \sigma_p} + \frac{p_0 + p_1 + \Delta p}{N_T * v_n * \sigma n}} \quad (42)$$

Where $\Delta p$ equals $\Delta n$, and $v_n$ and $v_p$ are the electron and hole thermal velocities, $\sigma_n$, $\sigma_p$ are the capture cross sections of the traps. $N_1$ and $p_1$ are the electron and hole concentration whose Fermi energy is the same with $E_T$.

$$n_1 = n_i * \exp(\frac{E_i - E_T}{K_B * T}) \quad (43)$$

$$p_1 = n_i * \exp(\frac{E_{Ti} - Ei}{K_B * T}) \quad (44)$$

The time dependent carrier concentration can be calculated from the continuity equation:

$$\frac{dn(t)}{dt} = -R \quad (45)$$

Then the non-radiative lifetime of excess carriers can be calculated by:

$$\frac{1}{\tau} = \frac{p_0 + n_0 + \Delta n}{\frac{n_0 + n_1 + \Delta n}{N_T * v_p * \sigma_p} + \frac{p_0 + p_1 + \Delta p}{N_T * v_n * \sigma n}} \quad (46)$$

Lots of non-radiative carrier's recombination can happen at the surface of semiconductor devices where abundant perturbation of periodicity of a crystal exists. The perturbation of

periodicity of crystal lattice will introduce additional energy levels to the forbidden band gap. As a result, addition electrons states in the forbidden gap of the semiconductor appears. Atoms at the surface don't have the same bonding structure as the bulk atoms due to lack of neighboring atoms. It is possible that the surface electrons will rearrange themselves and form bonds between nearest neighbors. This reconstruction will lead to a new atomic structure with different energy state compared with bulk electrons. Their energy state is very difficult to predict. Surface recombination will lead to non-radiative recombination and increase the heat of the surface. Both effects are unwanted in the LED devices.

There are several mechanisms that can caused non-radiative carrier recombination in the LED device. Shockley Read Hall recombination, Auger recombination and surface recombination are the dominated non-radiative carrier recombination. It is possible to reduce the non-radiative recombination; however, it is impossible to get rid of it completely. Any semiconductor crystal will have some native defects. The concentration of these crystal lattice can be low, it is never zero. Also, semiconductor may have chemical impurity. It is very difficult to fabricate materials with high impurity levels. The luminous efficiency has improved a lot since the first III-V LED are demonstrated. Most of the process are made by improving the crystal quality and reducing the defects inside the crystal lattices.

If the radiative lifetime is denoted as $\tau_r$ and the non-radiative lifetime is denoted as $\tau_{nr}$, the total recombination happened can be calculated as the sum of radiative and non-radiative carriers:

$$\frac{1}{\tau} = \frac{1}{\tau_r} + \frac{1}{\tau_{nr}} \tag{47}$$

The probability of radiative recombination over the total recombination is called the internal quantum efficiency and is given by:

$$\eta_{\text{int}} = \frac{\frac{1}{\tau_r}}{\frac{1}{\tau_r} + \frac{1}{\tau_{nr}}} \tag{48}$$

The internal quantum efficiency calculates the ratio of emitted photons to the number of recombined carriers inside the semiconductors. However, not all emitted photons can escape from the semiconductor device. Some of them may be reflected back by the interface of package and semiconductor device or even absorbed by the semiconductor material.

The light extraction efficiency of a LED is defined as the ratio of the number of photons that comes out of the LED per second in the correct direction to the number of photons emitted from the active region of the LED per second. The external quantum efficiency is the product of extraction efficiency with internal quantum efficiency. It is defined as the ratio between the number of photons that come of the LED per second in the correct direction and the number of charges flowing into the device per second. The external quantum efficiency gives the ratio of the number of useful photons to the number of the injected carriers. A simple designed LED device usually doesn't work efficiently. Most of the photons which are emitted from the active region will be either reflected back or absorbed. It requires efforts to design the devices and package to increase the external efficiency. From the electrical power perspective, the power efficiency is calculated as:

$$\eta_{power} = \frac{P}{IV} \tag{49}$$

Where P is the total emitted power and IV is the electrical power provided to the LED active region. It is also called wallplug efficiency.

LED emits light through spontaneous recombination of electron-hole pairs, rather than stimulated emission process. Spontaneous recombination will determine several optical characteristics of LED, such as wavelength, light spectrum distribution. The common spontaneous

life time of carriers in the active region is range from 1-100ns, which means the maximum frequency of LED can achieve GHz easily. These properties make it a very good candidate for communication. During the recombination, the emitted photons' energy can be calculated as:

$$E = \hbar * \omega = h * \nu \tag{50}$$

Where h is the Planck's constant, ħ is Planck's constant divide by 2π, ω is angular velocity and v is the frequency of photons. The available electrons energy band diagram has parabolic relation with wave vector. Energy and moment conservation requires that the released photon energy and moment should be the same with the recombined electrons and holes. The electrons moment is larger than the photon momentum. To keep moment conservation, the electrons' moment can't change significantly during the recombination process. Therefore, for radiative recombination, the electrons will recombine with the hole that has nearly identical momentum. Since momentum equals h bar multiple k, electrons will recombine with holes that have the same k. The momentum of photons can be calculated according to the following equation:

$$P = m * V = \frac{h}{2 * \pi} * k = \frac{h}{2 * \pi} * \frac{2 * \pi}{\lambda} = \frac{h * \nu}{c} \tag{51}$$

According to the conservation of momentum, the electron and holes will have the same momentum, then the photon's energy can be written:

$$h * \nu = Ec + \frac{\hbar^2 * k^2}{2 * m^*_e} - Ec - \frac{\hbar^2 * k^2}{2 * m^*_h} = Eg + \frac{\hbar^2 * k^2}{2 * m^*_r} \tag{52}$$

Where $m^*_r$ is the reduced mass and equals:

$$m^*_r = \frac{1}{\frac{1}{m^*_e} + \frac{1}{m^*_h}} \tag{53}$$

The probability of electrons and holes distribute in certain energy state obeys the Fermi function at thermal equilibrium. At each energy level the probability to have filled states is different. The Fermi probability function is also changed according to the ambient temperature.

The solution of Fermi probability function at different temperature is given by the Fermi-Dirac distribution function:

$$f(E) = \frac{1}{1 + \exp(\frac{E - E_f}{K_B * T})} \tag{54}$$

Where $E_f$ is the Fermi energy of electrons in the solids. It is defined as the energy of the topmost filled level in the ground state of the N electron system. In one dimension, $E_f$ can be calculated as:

$$E_f = \frac{\hbar^2}{2 * m} * (\frac{N * \pi}{2 * L})^2 \tag{55}$$

Where L equals N*a and a is the lattice constant. According to the above equations, the energy of an emitted photon from an LED is not simply equal to the band gap energy of the semiconductor.

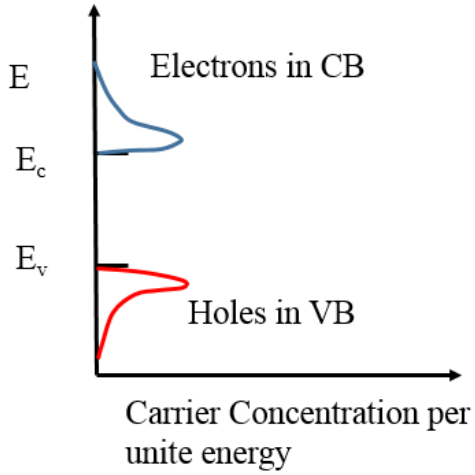


Figure 9: Electron and Holes Distribution.

The electrons and holes concentration is a parabolic distribution along the energy. An energy band is actually a collection of discrete energy states from quantum mechanics. Each state

is basically a solution to the Schrodinger's equation and has a k and E. The number of states per energy interval per volume, called density of states under periodic boundary condition which gets rid of any surface and boundary issues. The electron concentration is a function of energy in the conduction band and can be calculated as g(E)*f(E), where g(E) is density of states and f(E) is the Fermi-Dirac function which depicts the probability of finding an electron in a state at energy E. Density of states is proportional to $(E-Ec)^{1.5}$. The holes distribution is also follows production of density of state and the probability function. Figure 9 shows the energy distribution of the electrons and holes:

The spectrum distribution of the LED depends on the electrons and holes distribution in the energy band. There is a peak intensity in the spectrum. The spectrum width when the intensity drops to the half is called the line width. The emitted power can be calculated by:

$$P_{sp} = D_0 * (h\nu - E_g)^{1/2} * \exp(\frac{-(h\nu - E_g)}{K_B T}) \quad (56)$$

Where D0 is the density of state at specific energy E=hv. The rate of spontaneous emission the rate at which photons are emitted. Therefore, the intensity is determined spontaneous emission spectrum. The emission spectrum intensity of LED is the production of density states with the carrier's distribution probability function as shown above. The maximum intensity of the emission spectrum happens at the $Eg+0.5*K_B*T$. It corresponds to the energy of recombination where electrons and holes have the maximum concentration. The spectrum start at the frequency whose energy equals the band gap energy. The spectrum distribution corresponds with the electron hole concentration along the energy diagram. The linewidth $\Delta v$ is approximately $2.5K_BT$. Both the linewidth and the peak frequency is sensitive to the temperature. At high temperature, the intensity of the spectrum will decrease due to high non-radiative recombination rate. At the same time, the spectrum will shift, because the band gap is very sensitive to the ambient temperature. Also, the

linewidth of the spectrum will also increase which will make the spectrum flatter. Intensity of the spectrum can be also plotted against the wavelength, since the wavelength and frequency can be related by speed. Figure 10 shows the relative intensity of the emitted light spectrum:

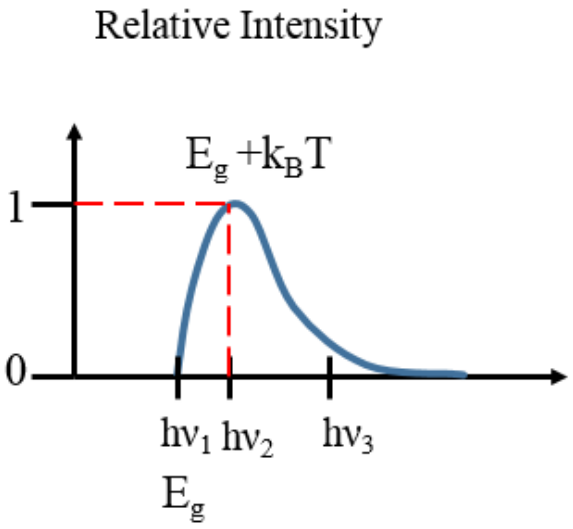


Figure 10: Emitted Light Spectrum of LED.

However, commercial LEDs has less asymmetrical spectrum output than the calculated spectrum out. The shape cut off frequency is covered by some lower frequency. In the band diagram, there should no states between the conduction band and the valence band. However, in doped semiconductor, there are always some states inside the forbidden gap. Those band tail states allowed the density of state has a variation. As a result, the spectrum is not sharp any more. There are several reasons that can cause band narrowing. The randomly distributed dopants and crystal defects are the dominant reasons. In the presence of dopants and lattice defects, the assumed period potentials didn't work anymore.

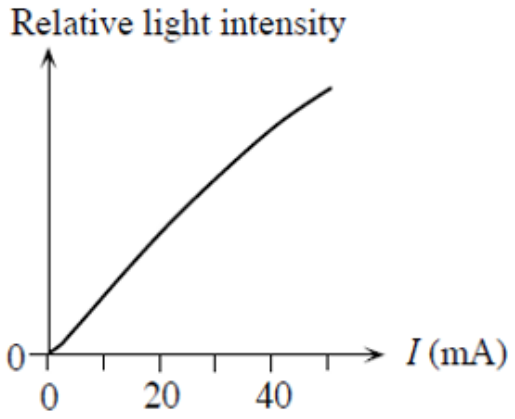


Figure 11: Light intensity vs Current. (Schubert, 2006)

The intensity is the number of photons rather than the energy of photons. The energy of photons only depends on the frequency. As the current increase, the concentration of injected carriers will increase also. Thus, the recombination and light intensity will increase. The intensity of the light spectrum will increase corresponding to the increase of current. The relationship between the output spectrum power and the current can be given based on the frequency and wavelength which is shown below:

$$P_{out} = \sum \eta_{external} * \frac{i}{e} * h\nu \quad (57)$$

$$P_{out} = \sum \eta_{external} * \frac{i}{\lambda} * 1.24 \quad (58)$$

According to the equation, the output spectrum power should always increase with the increase of current. However, the increase in the output spectrum power is not linear with the LED current in real situations. The typical output power will saturate with the increase of current as shown in the Figure 11 (Schubert, 2006).

There are several reasons caused the saturation of light output. The first reason is the Joule heating. The second reason is the carrier leakage loss. The last reason is the stimulated emission during the recombination. The Joule heating is calculated by the Ohm's law:

$$P = I^2 * R \tag{59}$$

When the input current increase, there will be more and more heat generated. Heating of the devices will increase the availability of much more photons in the material. As a result, the non-radiative recombination start to dominate the recombination process. The external efficiency of LED will reduce significantly. If a p-n junction is forward biased, the band diagram of n sided will be lifted. The barrier for the electrons will be reduced. In the p side, there are plenty of vacant states. Therefore, the electrons in the n side will simply rush to the p side and get collected. During these process, there is no generation of photons. This is called carrier leakage current. Some amount of carrier leak without leading to recombination. Stimulated emission is different from the previous phenomenon. It actually increases the light emitting. However, during the high current, the previous two process still dominate the recombination process. Therefore, the output spectrum power will saturate at high current, even the stimulated emission happens.

The output spectrum of LED depends not only on the semiconductor material but also on the structure of the p-n junction. For a heavily doped n-type semiconductor, there are some many donors that the electron wave functions at those donors overlap to generate a narrow impurity band centered at $E_d$, but extending into the conduction band. Thus, the donor impurity band overlaps the conduction band. At high current levels, strong of minority current leads to the recombination time depending on the injection carrier concentration and hence on the current itself.

The spectrum width of LED is very narrow which have several important effects on the light characteristics of LED. The emission spectrum of LED is narrower than the spectral width of

a single color that human will perceive as a single color. Therefore, human will perceive that LED light is single color.

## 1.4. HETEROJUNCTION STRUCTURE

There are two methods can be applied, in order to increase the internal quantum efficiency. The first method is to increase the radiative recombination probability and the second method is to decrease the non-radiative recombination probability. According to the biomolecular recombination rate equation, the radiative recombination rate will increase if the free-carrier concentration increase. Therefore, it is important to increase the injected carrier concentration in the active region. Double heterojunction is an excellent method to increase the carrier concentration in the active region.

In a normal p-n junction diodes, the junctions are formed on the same material on both n-region and p-region. Therefore, it is called homo junction. The building potential inside the junction is caused by the difference in the material doping. The govern equation is shown below:

$$\Phi_{bi} = \Phi_t * \ln(\frac{N_a * N_d}{ni^2}) \tag{60}$$

In the homojunction, it is very hard to achieve high electrons and holes in the active region due to long diffusion length. During the injection process, the injected carriers are distributed along the device junction length which means the recombination process will happens long the device length. After recombination of the carriers, there is high possibility that the emitted photos are reabsorbed by the semiconductor since the emitted photons must travel a long distance before escape. Figure 12 shows the carriers distribution in a forward biased homo junction LED (Kasap, 2001).

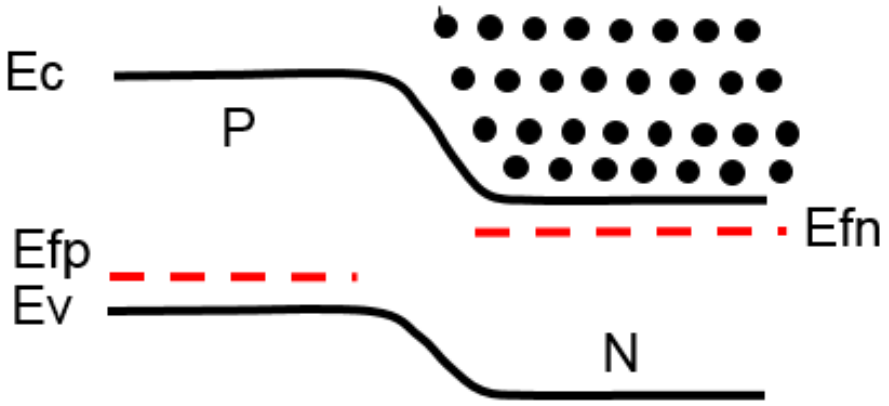


Figure 12: Carriers Distribution of forward biased homojunction. (Kasap, 2001)

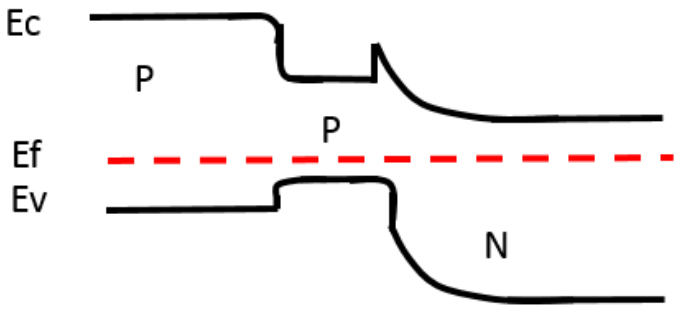


Figure 13: Heterojunction of LED. (Kasap, 2001)

Extreme high doping is needed for the homo junction LED, in order to achieve high injection levels. However, the high doping will worsen the material quality and reduces efficiency; it also further increases the absorption. For the homo junction LED, the p-region must be very narrow to avoid the reabsorption of the emitted photons. When the p-region is very narrow, some of the injected electrons will diffuse to the end of p-region. As a result, it will recombine with the electrons at the surface the junction. As mentioned earlier, the surface will have lots of crystal

defects. The non-radiative recombination rate with increase significantly which will decrease the light out and increase the junction temperature. Besides, if the recombination process happens along the long diffusion length. The chance of reabsorption will become higher, since the amount of reabsorption increases with material volume.

The long diffusion path and corresponding lower carrier concentration can be avoided by the employment of a double hetero structure. Today most LED device use multiple hetero structure. In the hetero structure, the potential barriers for electrons and for holes are different. The potential barriers for electrons and holes are determined by both the composition and the doping difference. By adopting different material, the potential barriers can be changed. A double heterojunction consists of an active region and two confinement layers. The active region is sandwiched between the two confinement layers. The material of confinement layers has larger bandgap than the material of active region. Figure 13 shows the heterojunction structure in LED (Kasap, 2001).

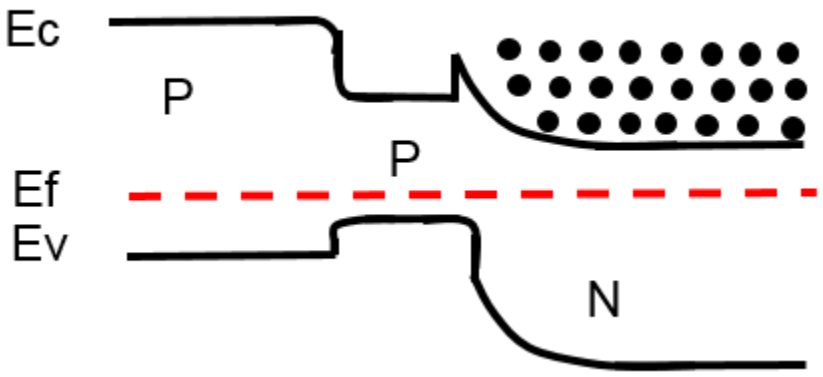


Figure 14: Band diagram of a hetero junction LED. (Kasap, 2001)

A double hetero structure diode has two junctions which are between two different band gap semiconductors (AlGaAs and GaAs). The band gap energy of AlGaAs is 2eV and band gap energy of GaAs is 1.4eV. Figure 14 shows the band diagram of a double hetero junction LED (Kasap, 2001) (Schubert, 2006).

The active region of the heterojunction is also called quantum well. The quantum well provides a confinement of minority carrier injection which greatly increase the internal quantum efficiency. When a forward bias is applied to the junction, most of the voltage drops at the p-n junction. The bias reduced the build in potential that formed by the carrier diffusion. This allow the electrons in the conduction band to be injected into p region. However, this injected electron is confined in the active region since this is a barrier between the p-GaAs and p-AlGaAs. The wide AlGaAs junction forms a confining layer that restrict the injected electrons inside the quantum well. The radiative recombination happens in the quantum well results the spontaneous photon emission. Figure 15 shows the carrier distribution of a heterojunction under forward bias (Kasap, 2001).

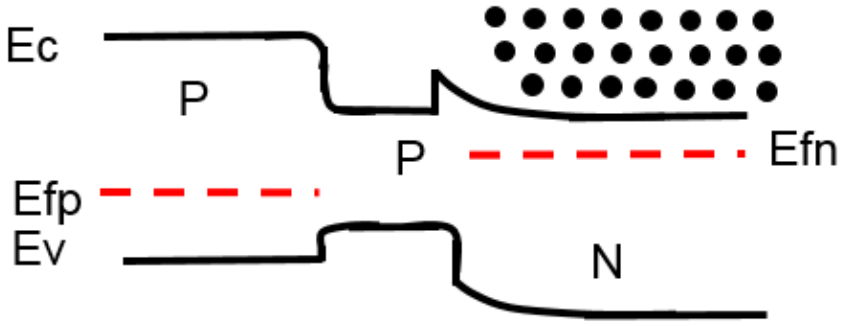


Figure 15: Forward biased heterojunction. (Kasap, 2001)

Compared with the homo junction, the injected minority carriers are confined into the thickness of active layer which will greatly increase the internal quantum efficiency. The emitted photons can be reflected to the active region and increase the light output, since the emitted photons can't be reabsorbed by the wide gap semiconductor material. Another advantage of heterojunction is that, there is very few lattice mismatch between the two p-type semiconductors. Therefore, the strain induced interfacial defects such as dislocation is very insignificant compared with the defects at the semiconductor surface in the homo junction LED.

### 1.5. EMISSION PATTERN

The light generated inside a semiconductor can't escape from the semiconductor if it is totally internally reflected at the semiconductor-air interface. If the emitted light ray is vertical to the emitted surface, light can escape from the semiconductor totally. However, if the light rays hit the emitted surface in an angle, reflection and refraction can happen which will reduce the emitted light intensity. Even worse if total internal reflection happens, the external quantum efficiency will degrade significantly. Total internal reflection happens a lot in LED, for LED package which consists of high-refractive index material. Performance of light-emitting diodes is defined to the great extent by two figures of merit, the internal quantum efficiency of the active region and the light extraction efficiency. Internal quantum efficiency reflects the quality of the semiconductor and the hetero junction quality. The internal quantum efficiency can be as high as 90%. The extraction efficiency depends on the design of the optical package and can be as low as 2%. Improvement of the luminous efficiency performance requires extensive studying of optical transmission processes in the device. Moreover, the optimal design of the device can vary depending on the optical properties of the material that is used in the LED, since extraction of light is related to the optical properties of material.

Assume that the angle of emitted light rays at the semiconductor-air interface is given by $\theta_c$. Then the refracted ray of the incidence light has another angle $\theta$ with the normal direction at the semiconductor-air interface. Then the angle of incidence ray and the refracted ray can be related by the Snell's law

$$\frac{n_{air}}{n_s} = \frac{\sin(\theta_c)}{\sin(\theta)} \tag{61}$$

Where $n_s$ and $n_{air}$ are the refractive index of the semiconductor and the air respectively. The critical angle for the total internal reflection is obtained when $\theta$=90°. With the Snell's law, the critical angle is:

$$\theta_c = \arcsin(\frac{n_{air}}{n_s}) \tag{62}$$

The refractive index for semiconductor is quite high compared with air. For example, the refractive index of GaAs is 3.4. According to the above equation, the critical angle of total internal reflection is: 17° which is quite small. Most of the emitted lights are reflected to the semiconductor area. As a result, the extraction efficiency is quite low.

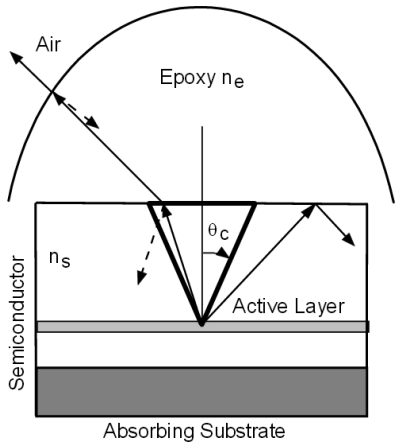


Figure 16: Light Escape cone. (Schubert, 2006)

If the critical angle was rotated 360°, this emitted ray will form a cone which is defined as the light escape cone. Light emitted into this cone can escape from the semiconductor. The left lights are subjected to total internal reflection. The light escape cone is illustrated in Figure 16 (Schubert, 2006):

If a light source is emitting out energy $P_{source}$ from a point-like source in a semiconductor active region. Then the power can only emit out from the light escape cone. The surface area of the cone with radius r can be calculated by:

$$A = \int dA = \int_{\theta=0}^{\theta=\theta c} 2*\pi*\sin\theta**r*d\theta = 2*\pi*r^2*(1-\cos\theta_c) \tag{63}$$

Then the power that can escape from the semiconductor can be calculated by:

$$P_{escape} = P_{source} * \frac{2*\pi*r^2*(1-\cos\theta_c)}{4*\pi*r^2} = \frac{(1-\cos\theta_c)}{2} \tag{64}$$

The result indicates that only a fraction of the emitted photons can escape from the semiconductor. The fraction of escaped light is in cosine relation with the critical angle of total internal reflection. The critical angle of the total internal reflection is very small for high-index materials such as GaAs. The escape problem is a significant problem for high efficiency LED. In most semiconductors, the refractive index is quite large. As a result, the extraction efficiency is very small. For GaAs, the critical angle is 17.9° and the extraction efficiency is (1-cos(17.9°))/2, which yields the fraction of light that can escape is 2.21%. This is a quite small. The escape problem is less significant in semiconductor with small refractive index, such as polymer whose refractive index is 1.5.

The light extraction efficiency can be greatly increased if a dome-shaped encapsulation was used. The encapsulation has a higher refractive index compared with air. As a result, the critical angle for the total internal reflection will be increase by:

$$\theta_C = \arcsin(\frac{n_{epoxy}}{n_{semi}}) \tag{65}$$

The ratio of extraction efficiency with and without epoxy encapsulation can be calculated by:

$$\frac{\eta_{epoxy}}{\eta_{air}} = \frac{1-\cos(\theta_{c,epoxy})}{1-\cos(\theta_{c,air})} \tag{66}$$

Where $\theta_{c,epoxy}$ and $\theta_{c,air}$ are the critical angles for air and epoxy. Since epoxy has higher refractive index than air, the critical angle of total internal reflection of epoxy is higher than air. Thus, total internal reflection losses in epoxy is smaller. The refractive index of encapsulation epoxy can range from 1.4-1.8 and it will increase the extraction efficiency by 200%-400%.

The refractive index differences of the semiconductor and the surrounding encapsulation lead LED to emit light different emission pattern. The spontaneous recombination emits photos isotopically in different angle. By tuning the geometrical parameters of the encapsulated lens, LEDs can come in many varieties and with a wide range of radiation patterns. Figure 17 (Davidson, n.d.)shows various emission pattern of LED.

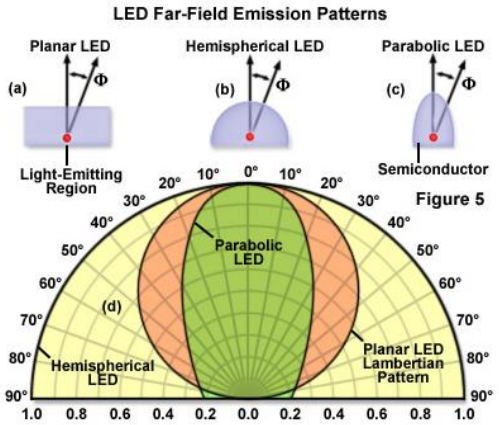


Figure 17: LED emission pattern (Davidson, n.d.)

The emission beam angle of LED can range from narrow to wide and is determined by the geometry of the lens. Most planar emitters exhibit a Lambertian emission pattern where the intensity profile is proportional to the cosine of the emission angle, which is measured from the axis perpendicular to the die surface. Assume a point source in the active region which is below the semiconductor air interface. The emitted light ray is refracted at the semiconductor-air interface. The refracted ray has an angle of Φ and the incidence ray has an angle of θ with respect to the surface normal. These two angles are related by Snell's law. Light emitted into the angle of dθ in the semiconductor is emitted into the angle of dΦ in the air as shown in Figure 18:

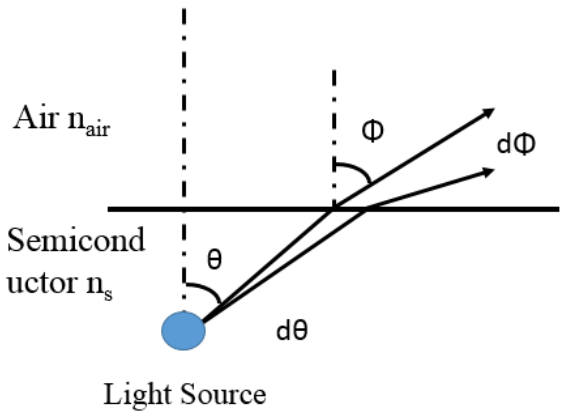


Figure 18: Gemoetrical Used to Calculate the light pattern.

Light emitted into the angle dθ will be refracted into dΦ. The relationship between dθ and dΦ can be related together by Snell's law.

$$d\Phi = \frac{n_s}{n_{air}} * \frac{d\theta}{\cos(\theta)} \tag{67}$$

The area element of dθ and dΦ in the air and the semiconductor can be calculated as:

$$dA_{air} = 2 * \pi * r * \sin\Phi * d\Phi \tag{68}$$

$$dA_{semi} = 2*\pi*r*\sin\theta*d\theta \tag{69}$$

This surface element can be related by the energy conservation. The power of the light emitted into the angle dθ equals the light power in dΦ. Also, dθ and dΦ and can be related together also. The conclusion can be expressed as:

$$I_s*2*\pi*r*\sin\theta*r*d\theta = I_{air}\,2*\pi*r^2*\frac{n_s{}^2}{n_{air}{}^2}*\frac{\theta*d\theta}{\cos(\theta)} \tag{70}$$

Where $I_s$ and $I_{air}$ are the light intensities ($W/m^2$) in the semiconductor and air. Is should equal $P_{source}$ divided by $4*\pi*r^2$. Then $I_{air}$ can be calculated as:

$$I_{air} = \frac{P_{source}*n_{air^2}}{4*\pi*r^2*n_{s^2}}*\cos\theta*\frac{\sin\theta}{\theta} \tag{71}$$

Since θ is small, the light intensity in the air can be treated as a function of cosine and depends on θ. This cosine light intensity pattern is called Lambertian emission pattern. At the angle of 60°, the light intensity will decrease to half of the maximum value.

One of the most critical issues in the high efficiency LED is the occurrence of the total internal reflection. The critical angle for high refractive index semiconductor is so small that most of the emitted rays are reflected. Thus, most of the light emitted by the active region is trapped inside the semiconductor. The trapped light has high possibility to be reabsorbed by the substrate. LED with hemisphere dome-like lens have been demonstrated to improve extract efficiency, since the silicone lens will have higher refractive index compared with air.

Epitaxial growth is the most important process during the semiconductor device fabrication. Thus, most of the LED is in vertical structure. The extraction efficiency would be very high if LED can be built into a sphere shape with a point light active region inside. Then, the internal total reflection would not happen. Another design can also increase the extraction efficiency which already has been fabricated. In this structure, the semiconductor-air surface was etched to forms a cone structure. The light rays that hit the cone-air boundary are either transmit

through the interface or guided by the cone. The guided light undergoes several reflections and ultimately escape from the cone. Therefore, the total internal reflection is avoided. An LED with cylinder shape also increase the extraction efficiency. On the top of the LED, there will be total internal reflection. However, on the edge of the cylinder, the total internal reflection will disappear. The round source will form an escape ring and improve the extraction efficiency significantly. Etched surface and cylinder LED can both increase the extraction efficiency. However, they will also increase processing steps compared with cubic LED.

## 1.6. HIGH POWER PACKAGE

III-V Material system is currently the only practical solution for short wavelength semiconductor emitter. Several technical improvements in the 90s enables the fast process in the fabrication of blue LED. There are two fundamental reasons to choose the III-nitride for blue light sources. The foremost reason is that AlN, GaN and InN have direct band gap energies of 6.2, 3.4 and 0.7 eV, respectively, at room temperature, so they cover the spectra from ultraviolet (UV) to the entire visible spectrum. The other main advantage of III-N over other wide-band semiconductors is the stronger chemical bond, which makes the nitride very stable and resistant to degradation under strong electric current and high temperature. In semiconductor materials atoms are organized in a three-dimensional lattice, where the same periodic structure is repeated over the space of the crystal. The future especially for general lighting application is promising, since white light can be produced by exciting wide band phosphors by blue or UV-LEDs (Xie, 2007). The driving force behind the fast development of III-N semiconductors has been the demand for short wavelength emitters. To date there exists only a few semiconductor material systems suitable for such applications. The first nitride-based LED with external quantum efficiency of 2.7 % was commercialized in 1993. The first LEDs employing InGaN/GaN quantum wells were fabricated

in 1995. Currently the III-nitrides are considered as the best material system for efficient solid-state lighting.

Generally, the structure of an LED is a combination of several semiconductor epitaxial films which grows on a suitable substrate. There are two most used techniques that have been very popular in the production process. The first is called molecular beam epitaxy (MBE) and the second method is called metal organic chemical vapor deposition (MOCVD). MOCVD is a technique for depositing thin layers of atoms onto a semiconductor wafer. Many layers can be built up to create a material which has specific optical and electrical properties. A feature of MOCVD technology is that it can create a thin uniform film in nanometer units. This is a really dominant feature for growing the GaN layers on a sapphire substrate. During the growth process, the vapor transport of the precursors and subsequent reactions of group-III alkyls and group-V hydrides happens in a heated zone. In the MOCVD machine, epitaxial layers were grown on (0001) orientated sapphire substrate. During the growth, the chamber pressure was controlled at 100-300 Torr. Trimethylaluminum (TMAl), trimethylgallium (TMGa), trimethylindium (TMIn) and ammonia (NH3) were used as aluminum, gallium, indium and nitrogen sources, respectively. Critical dimension is the thickness of the epitaxial p –layer. The thickness should be larger than the diffusion length of electrons. In other words, the electrons should recombine radiative in the epitaxial grown p layer before reaching the surface. The p -layer should be of sufficiently high quality to meet the condition for efficient recombination. In addition, the side surfaces may have to be etched to remove damage. Damage and other defects where the p - n junction intercepts the chip surface can lead to a substantial leakage current that reduces efficiency, especially at low drive levels. During the doping process, Biscyclopentadienyl magnesium (CP2Mg) and disilane (Si2H6) were used as the p-type and n-type doping source, respectively.

Prior to the epitaxial growth, the whole substrates were cleaned by $H_2SO_4$: $H_2O_2$ (3:1) solution for 10 minutes. Then the substrate was etched in 2% HF solution and rinsed in deionized water, followed by $N_2$ blow-drying. After loading, an in situ thermal cleaning procedure was applied to the sapphire substrates for 10 min at 1080°C under H2 ambient to remove native oxide from the substrate surfaces. After the thermal cleaning process, a GaN buffer layer of 30nm was deposited at 525°C. After that, the temperature was elevated to 1020 °C to grow a 1μm thick GaN layer and then a 1μm thick Si-doped, n-type GaN layer. The substrate temperature was subsequently ramped down to grow the InGaN well layer at 715 C and grow the GaN barrier layer at 840°C. The InGaN/GaNMQW active region consists of three pairs of 3 nm thick In0.4Ga0.6N-well layers and 10 nm thick GaN-barrier layers. After the growth of the active region, a 30 nm GaN cap layer was grown on the multi-quantum wells and the substrate temperature was elevated to 727°C to grow a 250-nm thick Mg-doped p-type GaN layer. Figure 19 shows the epitaxial layers on the substrate (Nguyen, 2010) (Neudeck, 2002).

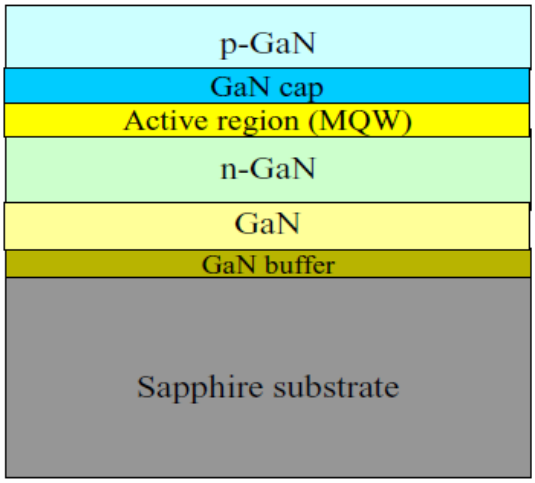


Figure 19: Vertical Structure of LED. (Nguyen, 2010)

After the annealing, the surface of the samples is etched until the n-type GaN layer was exposed for the ohmic contact. The conductivity of p-type GaN is not good enough for current spread. A Ni/Au contacts were evaporated on the p-type GaN to serve as the semi-transparent metal ohmic contact to improve the holes current spread. Then a 200 nm Au contact was deposited on top of the semi-transparent layer to serve as the p electrode. On the other hand, Ti/Al/Ni/Au (10 nm/200 nm/30 nm/100 nm) contacts were deposited onto the exposed n-type GaN layer to serve as the n-type electrode. The fabrication of the blue LED was finished and the scheme diagram is shown in Figure 20 (Nguyen, 2010):

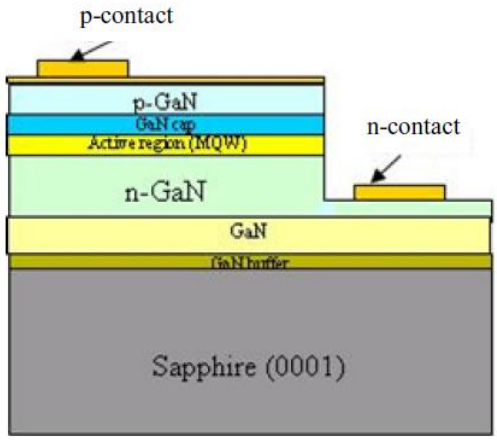


Figure 20: Scheme diagram of a blue LED chip. (Nguyen, 2010)

The performance and efficiency of LED is growing up at an incredible speed recently. Different architectures had been built to increase the photon extraction efficiency which make the LED brighter. There are three kinds of architectures now available in the market. Few years ago, the most popular LED package is LLED (Lateral LED structure) and it is also the most established LED design. The second LED structure is called TF (thin film) LED and it also called VLED, because of its vertical architecture. The third and also the latest is called FCTF LED. FCTF

standards for flip chip thin film. This structure is the combination of TF technology and FC technology. This kind of design is produced by bonding an FC-LED chip that has an anode and cathode on the same side to a package with two interconnects. Competition has fueled the creation of novel device architectures with improved photon-extraction efficiencies, which have in turn increased the chip's brightness and output power. This has opened up the range of applications for these devices, and brought their characteristics more closely in line with the requirements for widespread deployment in solid-state lighting. Vertical thin film InGaN/GaN design is one of the famous among the many LEDs structures. Figure 21shows the scheme diagram of the thin film vertical structure.

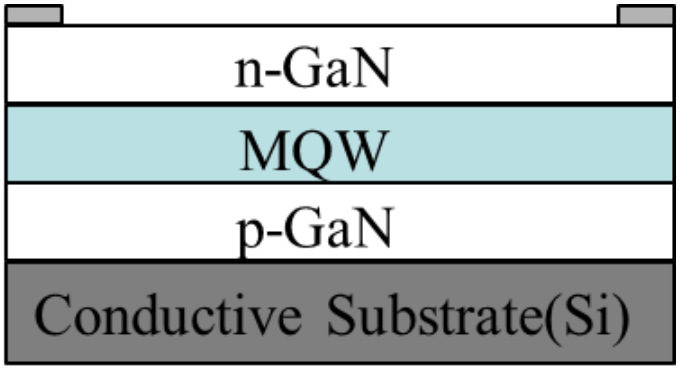


Figure 21: Vertical Thin Film LED.

During the construction of the VLED, the epitaxial layer was grown on the sapphire substrate]. Usually the epitaxial layer has three parts. The bottom layer is n-type GaN. On the top of n-type GaN, multiple layer of quantum well (MQW) active region was built. P-type GaN was on the top of the epitaxial layer. After the growth of the epitaxial layer, a high reflective metal contact was deposited on the p-side of the wafer as p contact by electron-beam evaporation. After that, the p side was bonded to an intermediate conductive substrate. Laser assisted lift off help to

remove the sapphire substrate and expose the n-type GaN surface. Now, the epitaxial layer is totally upside down with n-type GaN of the top. Wire bond and patterned metallic n contact was added to connect the chip with the substrate. Figure 22 shows the fabrication process of vertical thin film LED.

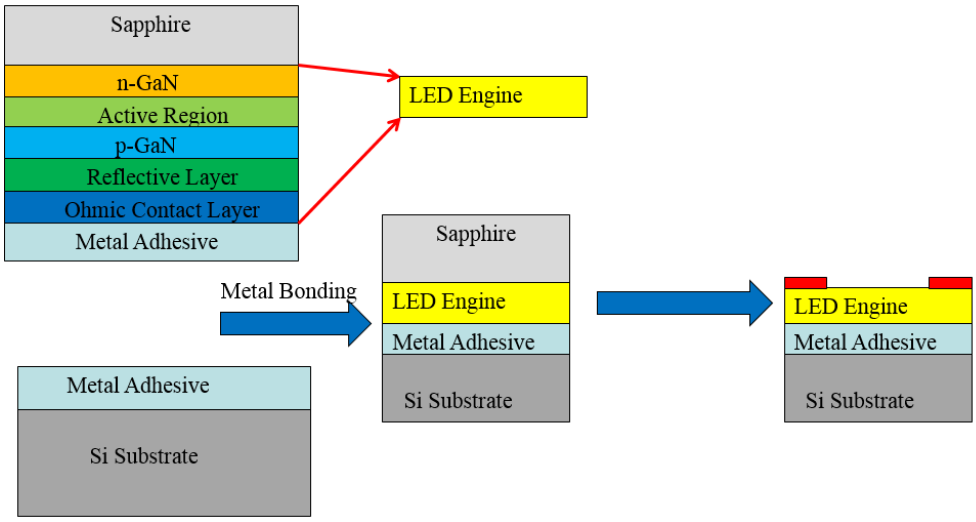


Figure 22: Fabrication process of vertical thin film LED.

Compared with the lateral structure, the vertical thin film LED structure does not have the wire bond, and the solder balls used for internal connection have better heat conductivity. The disadvantages of the vertical thin film LED are the consequence of its structure. The vertical thin film LED is usually produced by depositing a high-reflective metal contract onto the p-type GaN. After the deposition, the whole substrate is bonded to an intermediate conductive substrate to maintain the device integrity in the following fabrication process. Laser-lift-off helps remove the sapphire substrate. The result structure has two major drawbacks. The first is the intermediate substrate increase the thermal resistance of the package. Also, it must be carefully chosen to match with thermal expansion coefficient of GaN. Otherwise, the thermal stress will cause device failure.

The other disadvantage of the vertical thin film structure is the wire bound used in the n-contact. The patterned n-contact reduces the chip's effective emitting area, while the wire bonds obstruct light emission. These wire bonds are particularly irksome in the tightly packed chip arrays used in projection displays and some illumination systems, as they increase the distance from the surface of the LED to the primary optic. The greater distance either increases the size, weight and cost of the optic, or it decreases the system's efficiency.

The newest LED structure is called thin film flip chip LED. This structure units the thin-film and flip-chip technology. It combines the manufacturing merits of both approaches, and is produced by taking an FC-LED chip that has an anode and cathode on the same side and bonding it to a sub mount or package using via. Figure 23 shows the scheme diagram of a TFFC LED structure

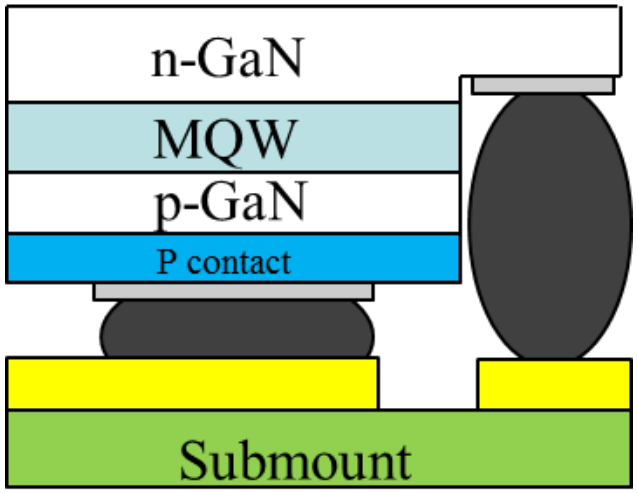


Figure 23: Thin film flip chip LED.

A laser lift-off process removes the sapphire substrate before photo-electrical-chemical etching of the top GaN layer. The process will roughen the top surface and create patterns which

will disrupt wave-guiding in the high refractive index epitaxial layers and increase the extraction efficiency. Compared with the vertical thin film LED, the distance between the surface of the LED and the silicone lens are much smaller. Therefore, the thin film flip chip LED can allow compact package, as electrical connections are removed to the bottom of the device.

## 1.7. WHITE LIGHT

White light is the most used commercial color of light industry. There are various spectrums that can be preserved as white light by human's eyes (Schubert, 2006) (CREE, 2013). The Planckian black body radiation spectrum is treated as the base line and standard for the white light source. The unique characteristics of the Planckian black body radiation is the color temperature. It allows to describe the spectrum with just on parameter, namely the color temperature. Also, the Planckian's radiation spectrum is similar with the natural light. The sun light is actually Planckian's radiation. White light usually has a wide spectrum which includes both visible spectrum and invisible spectrum. The black-body spectrum was first derived by Max Plank and is given by:

$$I(\lambda) = \frac{2*h*c^2}{\lambda^5 * (\exp(\frac{h*c}{\lambda * K_B * T}) - 1)} \tag{72}$$

The inside of the human's eyeball is clad by the retina which is very sensitive to the light. The retina cell includes light-sensitive rod cell and cone cells. Rod cells are more light-sensitive than the cone cell. Rods cell are sensitive over the whole visible spectrum. On the other side, cone cell only has three types and each type is sensitive to one color. Cone cells are sensitive to red, green, and blue spectrum range. At high ambient light level, the vision is dominated by cones. At low ambient light levels, the vision is mediated by rods. Therefore, rod cell has higher sensitivity

than cone cells. However, the sense of color is essentially lost in the low ambient light, because rods is not very sensitive to color compared with cone cells.

The eye has different sensitivity over the whole visible spectrum. CIE introduced the photopic sensitivity function V(λ) in 1931 and revised it in 1978 known as the CIE 1978 V(λ) function (Zukauskas, 2002). The photopic sensitivity function is shown in Figure 24.

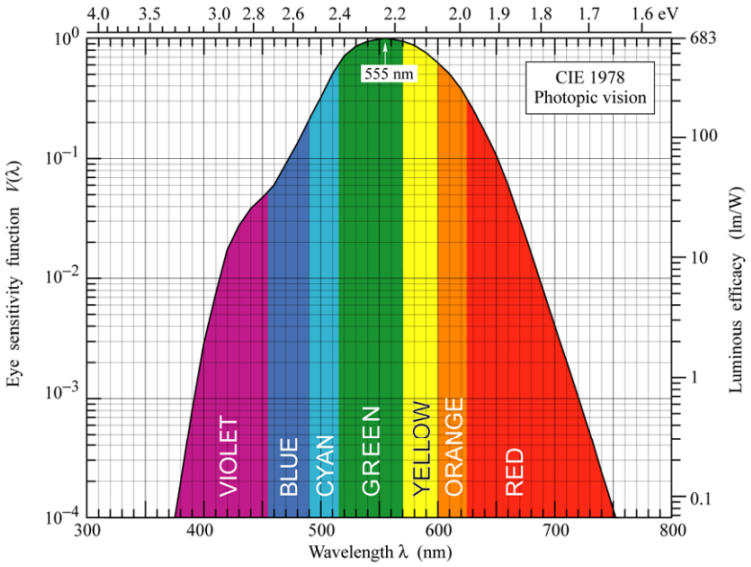


Figure 24: Eye Sensitivity Function. (Zukauskas, 2002)

LED market began to open up in the 1960 with low brightness red LED working as red indicator in electrical products. As the technology develops especially high power LEDs become more and more efficient. The number of possible applications increases dramatically. A highly interesting area with huge potential market is based on white light source. The share of LED in the backlighting market is expected to peak soon, at close to 100 percent in 2016. The market is then likely to shift from LCD TV to OLED TV, which does not use backlighting. Also, LED is now penetrating general lighting which is the mainstream of the lighting market.

It is set to become the next standard in the general lighting source market. There are several ways to generate daylight illumination spectrum from LED. The general daylight illumination source has some request to be satisfied. It should be more efficient than the current general light source such as incandescent lamp and compact fluorescence lamp. Also, the light source should have high color rendering index to reveal the true color of objects. Due to the massive production, the new standard light source should have low cost manufacturability and be environmental benignity. This unique property allows LED to compete with conventional illumination source, in particular incandescent and fluorescent lamps.

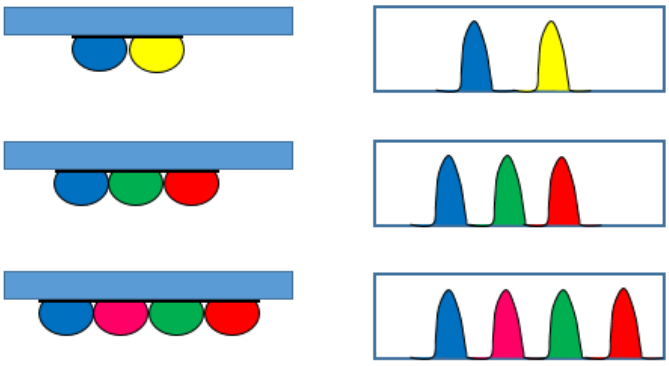

Figure 25: Color Mixing LEDs.

Light is perceived as a white light source is the spectrum of the illumination is perceived as white by cones in the retina. The generation of white light spectrum can be achieved in several possible spectra. LEDs are inherently monochromatic light source which means that LEDs can only emit the spectrum of one color. The creation of white LED requires at least two LEDs which have different colors. Based on the number of LED used in one package, there are three types of color mixing method. Figure 25 shows the combination of color mix LEDs.

The first method requires two LEDs. One emits blue color and the other LED emits yellow color. The white color can also be obtained by three LEDs, blue, green and red LED. The last method requires four LED which are blue, cyan, green and red LED. Each configuration has different luminous efficiency and color rendering properties. High luminous flux and high color rendering index are always desirable. There is fundamental disadvantage of color mix LEDs. It is very difficult to achieve both high luminous efficacy and high color render index. Usually two color mixing white LED has the highest luminous efficacy and poorest color rendering index. Three color mixing white LED has acceptable color render index and luminous efficacy. The four-color mixing white LED has the best color rendering index.

High quality white is usually generated with the three-color mixing method (Schubert, 2006). Thronton (1971) showed that mixing of three monochromatic LED with peak wavelength of 450nm, 540nm and 610 nm can generate high quality white color source. There is various possible combination for the three-color mixing method. To obtain a high luminous efficiency of radiation, the wavelength within the visible spectrum should not be used. The color render index is very sensitive to the peak wavelength used for the color mixing.

White spectrum generated by color mixing is very sensitive to the ambient temperature, since the emission power and peak wavelength of the device have a different temperature dependence. As a result, the chromaticity point of a multi-LED white source changes with temperature. It is shown that the chromaticity point will shift towards higher color temperature as temperature increases. This can be explained by the stronger temperature dependency of red LED device. This color chromaticity shift that caused by temperature can be fixed with a power control circuit of each LED. The temperature of ambient environment is monitored and the electric power

of each LED can be adjusted using the known temperature dependency. However, this method can't adjust the shift of spectrum caused by the degradation of devices.

## 1.8. PHOSPHOR CONVERTED LED

The commercial method generating white light is to apply phosphor. Partial light of monochromatic emitting LED is used to excite one or several phosphors. The combination of residue light and the excited light will form the white spectrum. There are several different methods to generate white light spectrum based on phosphors excited by semiconductor LED (Schubert, 2006). These approaches use either blue LED or UV LED as the excitation source. Figure 26 shows the recombination of excitation source and applied phosphor.

The luminous efficiency decrease with increasing of the thickness and concentration of the phosphor, because the excitation process is not 100% efficient. The color rendering index could reach 100% for the UV LED with four different phosphors. The conversion process of the short wavelength to the long wavelength light is called fluorescence. Fluorescence is the emission of light by a substance that has absorbed light or other electromagnetic radiation. It is a form of luminescence. In most cases, the emitted light has a longer wavelength, and therefore lower energy, than the absorbed radiation. Compared with phosphorescence, the fluorescent materials would cease to glow immediately, if the excitation source is moved away.

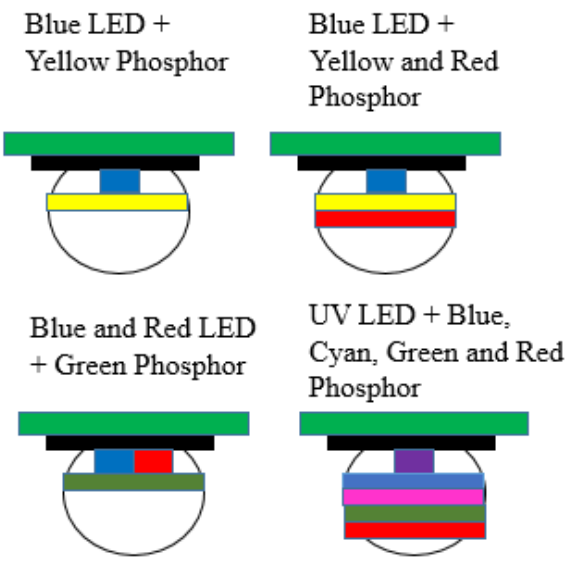


Figure 26: White Source LED with Phosphor excited by Blue or UV LED.

The conversion efficiency of the fluorescent is determined by two factors, namely the external quantum efficiency and the inherent energy lose during the wavelength conversion. The external quantum efficiency of the conversion is the product of internal efficiency and the extraction efficiency (Rohwer, 2003).

$$\eta_{external} = \eta_{internal} * \eta_{extraction} \tag{73}$$

The internal quantum efficiency depends on the inherent conversion loss of the material, whereas the extraction efficiency depends on the spatial distribution of the material. In general, the thin film structure has higher extraction efficiency. Therefore, it is desirable to deploy the phosphor coating in the form of thin film. The emission wavelength is usually higher than the excitation spectrum wavelength. The inherent conversion loss is called Stokes shift when converting a photon with wavelength $\lambda_1$ to a photon with a higher wavelength $\lambda_2$.

$$\Delta E = \frac{hc}{\lambda_1} - \frac{hc}{\lambda_2} \tag{74}$$

The inherent wavelength-conversion loss is the fundamental reason that phosphor converted LED is less efficient than the color mix LED for white spectrum. The Stokes shift is the highest when UV LED is used as the excitation source and red phosphor is applied on the top of the die. Most white LED use short wavelength as the excitation source and a phosphor that can generate longer wavelength. Some of the light emitted by short wavelength emitter is absorbed in the phosphor and then re-emitting as longer wavelength light. As a result, the phosphor converted LED has at least two different peak wavelengths. During the design of phosphor converted LEDs, there are two parameters that need to be considered, namely luminous efficiency and color render index. In some application, the luminous efficiency is the primary criterial of design such as road light. However, for illumination application, both the luminous efficiency and color render index are important. A white light source with sun's spectrum would have the best color rendering index. The sun's spectrum has very high relative intensity at the boundary of visible spectrum (390nm and 780nm). Thus, exact duplication of sun's spectrum is not an excellent choice for white LED.

When the chip is driven under certain current, blue light is emitted by the InGaN chip through electron–hole recombination in the p–n junctions. Some of the blue light from the LED excites the YAG:Ce phosphor to emit yellow light, and then the rest of the blue light is mixed with the yellow light to generate white light. There has been extensive research and development for phosphors. Many traditional phosphors used in compact fluorescence lamp don't work for LED, because those phosphors don't absorb violet or blue LED radiation. Most of the needs for LED phosphors have been met by the development of new materials. During last 10 years, various phosphors have been discovered. LED phosphors has moved from a single phosphor composition $Y_3Al_5O_{12}:Ce^{3+}$ (YAG:Ce) to various nitride, sulfide phosphor, This development has helped white LED cover a full range of correlated color temperature .

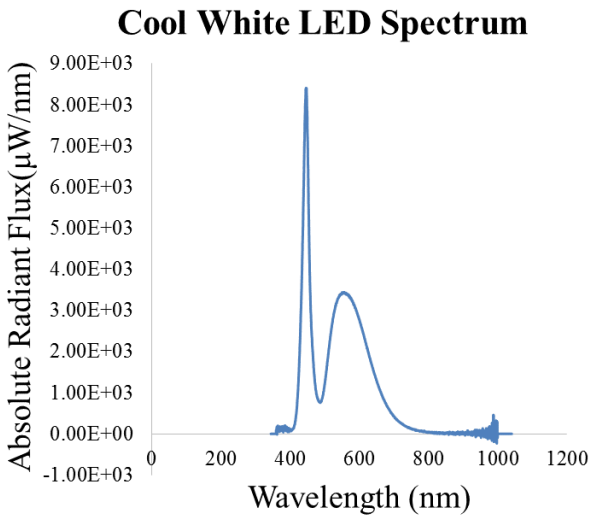


Figure 27: Typical Cool White LED Spectrum.

For cool white LED, YAG:Ce phosphor is the most used one. YAG:Ce absorbs blue LED radiation and emits yellow light via the fluorescence process (Rohwer, 2003). The yellow emission from YAG:Ce and the blue radiation that "bleeds" through a YAG:Ce coating combines to give white light with a daylight-like color temperature (CCT > 4000 K) and reasonable color rendering (CRI ~70- 80), enabling pcLEDs to be used in many applications where color quality is not a key requirement, including backlights for portable displays and indicators. Figure 27 shows a typical YAG:Ce phosphor converted LED spectrum.

However, pc-White LEDs made by means of blue-LED + YAG:Ce yellow phosphors suffer some weaknesses, such as poor color rendering index and low stability of color temperature. The reason is that only YAG:Ce phosphor is applied on top of the blue emitter. Therefore, the emitted spectrum is limited to high CCTs and lower CRIs, due to a lack of a red spectral component. Since the white light is generated by the combination of blue light emitted by an LED chip and yellow light emitted by YAG:Ce phosphors, deterioration of the chip or YAG:Ce phosphors would cause some significant color changes.

The sulfide phosphors could increase the red component of the spectrum. On the other hand, there are drawbacks that prevents sulfide phosphor from being used in the pc-LED industry. The synthesis process of sulfide phosphor requires toxic $H_2S$ atmospheres or may create $H_2S$ as a by-product. Sulfide product could damage the optical parts of the LED package and lead contamination. Besides, sulfide phosphors are very sensitive to ambient humidity which is very common for general light application. Compared with sulfide phosphor material, nitride phosphors doped with $Eu^{2+}$ have several advantages. Many of these nitride phosphors could match the quantum efficiency of YAG:Ce at room temperature.

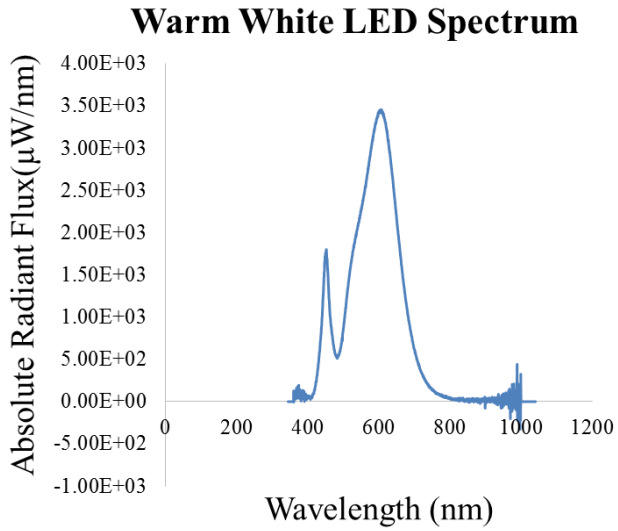


Figure 28: Warm White LED spectrum.

The $Eu^{2+}$ doped nitride phosphor could be blended with YAG:Ce phosphor to generate warm white spectrum. For example, phosphor blends of YAG:Ce and CaAlSiN3:Eu2+ combined with blue LEDs can be used for high CRI, warm white lamps (Rohwer, 2003). There are some disadvantages of nitride phosphor. It is much more difficult to synthesize nitride phosphor than the normal phosphors. Higher temperature is required during the synthesis. Compared with cool

white, the warm white LED has relative larger red spectrum content and thus have higher CRI value. Also, the emission spectrum peak wavelength is higher than cool white LED spectrum. Figure 28 shows a typical spectrum of warm white LED.

# 2. LITERATURE REVIEW

This chapter will depict the current reliability issues that related to the LED. Also, available lifetime prediction models are illustrated. The major causes of failures can be divided into three groups, die failure, interconnect failure, and package-related failure. The LED device reliability section will summarize previously reported failure mechanisms that related to the semiconductor device region of LEDs (Lafont, 2012) (Chang, 2012). The package reliability section will illustrate previously published researches related to the degradation of the package components (Philips Lumileds Lighting Company, 2006) (Fu, 2012). The lifetime model section will discuss the current available methods and techniques for the prediction of the remaining useful life.

During the last years, many efforts have been done in order to improve the luminous flux. As a result, LED with an output of several watts are now commercially available on the market. High Power LED means high light output, as well as high temperature. Therefore, the importance of devices and package thermal management become more obvious. Thermal resistance and capacity must be optimized to obtain longer life time. The development of high power LED necessitates the understanding of the fundamental failure mechanisms of LEDs.

The LED industry is facing changelings while attracting widespread consumption of LEDs. One issue of concern is price, and another is lack of information regarding reliability. The life of LED can be very long and it is very difficult to report the lifetime based on a short experiment. Another reason is that LED is a point source which means each LED can only cover a limited area. If one single LED failures, the final product is sometimes treated as failed. The failure of LEDs in an LCD display is critical, even when only a single LED package experiences changes in optical properties. The failure of an LED or LEDs in an LCD display can cause a dark area or rainbow-

colored area to appear on the LCD screen. Therefore, reliability of LED is very crucial for the LED industry.

A LED package is consisted of two major parts, namely semiconductor device and package. Literature is available on a wide variety of aspects, such as the semiconductor device, encapsulation materials, phosphors and LEDs. All these degradations will lead the decrease of the luminous flux and modification of the spectral properties. The degradation of the semiconductor device and package were found to have different origin and physics. These indicates that the optical power output decrease is not based on one single failure mechanisms. During the last period, many works on LEDs degradation have been published. Most of the papers described the behavior of LEDs subjected to either high forward current or high ambient temperature. However, in the real situation, no commercial LEDs will be running at such high temperature and current. It is not either power efficient or luminous efficient at that condition. Most of the degradation comes from two contributing factors: high junction temperature and moisture ingress. However, there is no published literatures that investigate the failure mechanisms that related to high temperature and high humidity which is essential to understanding the long-term reliability of commercial LES.

## 2.1. LED SEMICONDUCTOR DEVICE RELIABILITY

The LED semiconductor device is composed of p-n junction, multiple hetero barrier. LEDs emit light due to the minority carrier injection and electroluminescence effects. When the p-n junction is forward biased, electron in the n-junction will be injected to the quantum well and recombine with the hole. The active region of perfect LED will emit one photon for every electron injected. Thus, an ideal LED hashe internal quantum efficiency of unity. The LED die is a semiconductor device and the fabrication process is similar with the process of microelectronics. However, there are some unique process involved. The fabrication process, material used and

unique of LED lead to different failure mechanisms. GaN based compounds semiconductors are great candidates for applications of high energy optical electrons, because of their large direct band gap. These materials are appropriate for short wavelength LED, such as blue and UV LED. High-brightness GaN-based LEDs are commercially available on the market now. The progress in the GaN-based LEDs and laser diodes is remarkable. In the ideal LEDs, the light output should be proportional to the forward current (Lu G. S., 2009). However, in real case, the output power will saturate as the forward current increase. There are several reasons that could leads the saturation of the output light power at high ambient temperature and high injection current, such as joule heating and leakage current.

The most often failure mode caused by die degradation is the decrease of light output (Meneghini M. P., 2006) (Meneghini M. T., 2010) (Meneghini M. T., 2008) (JEDEC, 2006). The light output degradation is due to the increase of non-radiative recombination. Thermal stress increases the number of defects in the crystal which will lead to SRH recombination and shift the electrical properties of the semiconductor device. Dislocation is one of the common defects in the crystals. It acts as non-radiative recombination centers cause limitation of stable operation for optical devices under high injected current density. It is widely recognized that high density of dislocations which act as nonradioactive recombination centers, are introduced during the epitaxial layers growth process. Even moderate dislocation densities can impose an upper limit to minority carrier lifetime. These recombination centers reduce the efficiency of LEDs and lasers by effectively competing with radiative recombination paths. Dislocations migrate during device operation under high injected current density and ambient temperature, and result in limited state operation of optical devices.

Another effect that reduces the internal quantum is the dark spot effects during the high injected current density. The emitted light power of the GaN-based LED strongly depends on the injected current density and the radiative recombination rate. Therefore, either the defects or the dark sport effects will reduce the light output and reduce the lifetime of LEDs. During the operation of LED based illumination source, high current density and temperature stress could lead to the formation of defects and reduce the internal quantum efficiency dramatically. Figure 29 shows the light output vs injected current curve of InGaN/AlGaN LED on the sapphire substrate under dc operation at 30°C (Egawa, 1997).

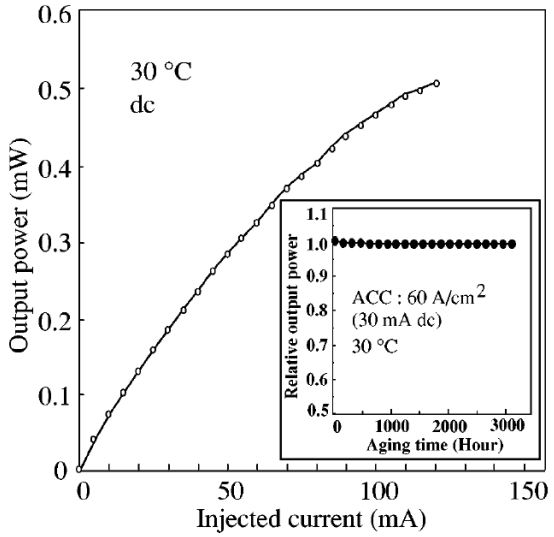


Figure 29: Light output injected current characteristic of the InGaN/AlGaN LED on sapphire under dc operation at 30 °C. The inset shows the aging result under a constant curren density of 60A/cm$^2$ at 30 °C. (Egawa, 1997)

The light output power increases linearly with the increase of forward current, and saturated at a high injected current due to joule heating and leakage current. This test results also confirmed the stable operation of GaN LED at relatively low current density, which is up to 3000 hours under aging condition. However, GaN-based LED exhibited electrical and optical

degradation under high injection current density and ambient temperature. The instability can be examined by the measurement of the emitted spectrum at different injection current. The emission spectra at various dc currents are shown in Figure 30 (Egawa, 1997).

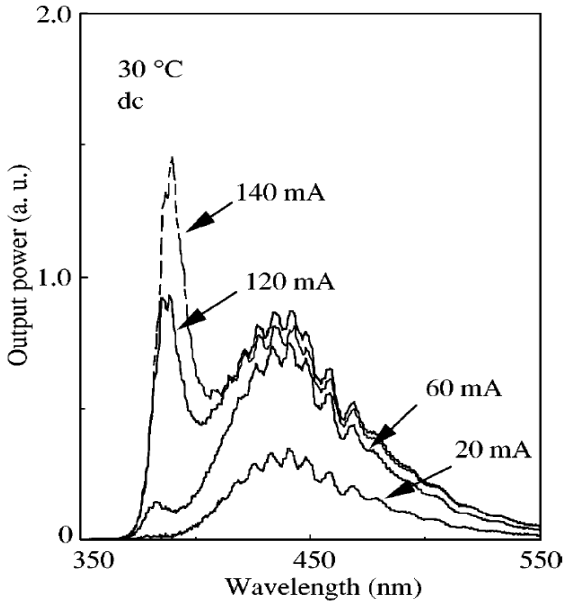


Figure 30: Emission Spectrum of GaN based LED at various injected current. (Egawa, 1997)

At low injected current, the emitted spectrum is centered at 443nm wavelength and has a broad spontaneous emission. However, when the injected current increases, the emission spectrum increased and a new emission is observed at 380nm. In order to study the optical degradation process, electroluminescence images were token on the GaN based LEDs. It was confirmed that the degraded characteristics of GaN based LED arise from the generation of dark-spot defects. Figure 31 shows the expansion of the dark-spot defects during the aging test (Egawa, 1997).

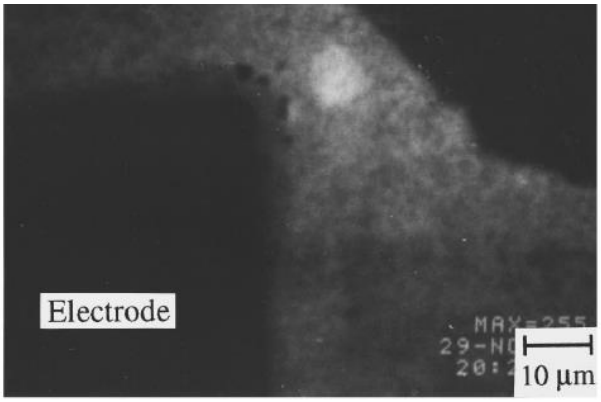


Figure 31: EL image of 67 hours of degradation. (Egawa, 1997)

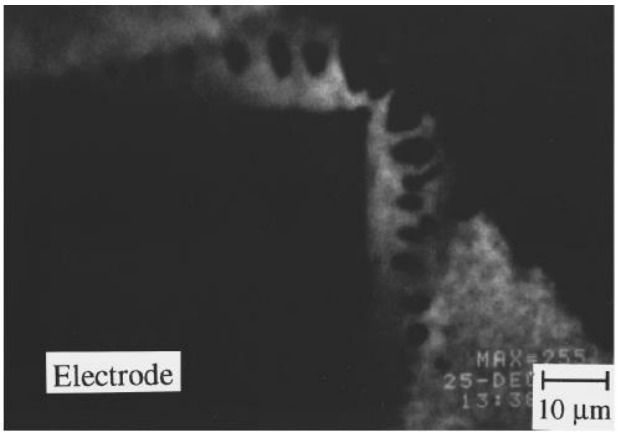


Figure 32: EL images of 310 hours of degradation. (Egawa, 1997)

These dark sports act as the non-radiative recombination centers which will reduce the internal quantum efficiency. The dark sports become darker and the size become larger with the aging process. Figure 32 shows the EL image of 310-hour aging (Egawa, 1997).

The reason why the dark spots and region were observed at the corner of the electrode is that the injected current density concentrates at that location. Therefore, the decease of the light output at high injection current and temperature is caused by the formation of the dark region, which act as non-radiative recombination region.

Dark sport effects are rapid degradation and can be reduced in the state of the art LEDs as a result of continuous improvement of material growth and device process techniques. GaN based LED also exhibit a slow degradation of luminous flux. This slow degradation is generally related to the generation and diffusion of point defects. Those defects act as non-radiative recombination centers and carrier tunneling channels. The forward I-V characteristics of the LED before and after stress are shown in Figure 33 (Cao, 2003).

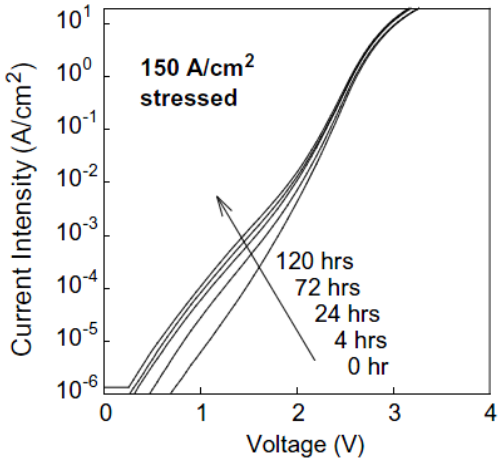


Figure 33: Forward I-V characteritics of GaN based LED. (Cao, 2003)

The low injection characteristics are dominated by carrier tunneling to the active region. This tunneling behavior has been extensively observed in GaN based LED, because of the highly-doped junction and high density defects in the space charge region. The degradation of the I-V curve is a manifestation of slow generation of defects. At high current density, large amounts of heat generated in the active layer where the majority of the carriers recombine. As a result, the temperature in the junction will be high. Hot carriers can transfer enough energy to the lattice. This energy will displace the atoms and break the metal bonds. Those thermal energy assisted defects

occur in the InGaN layers where the bonding energy is the smallest. The defect formation could also be enhanced by a non-radiative recombination process in the active region

Figure 34 shows the EL spectra of the LEDs measured at pristine condition and the 120 hours stressed condition (Cao, 2003),

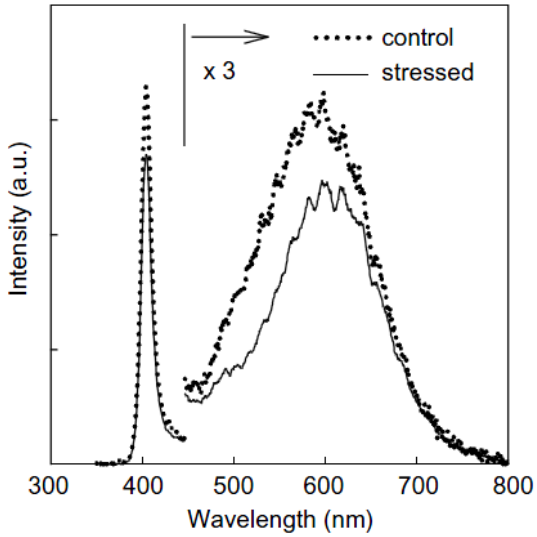


Figure 34: EL Spectrum of GaN based LED. (Cao, 2003)

The EL spectra of the control LEDs show two luminescence bands centered at about 405 and 580 nm, which correspond to the band-edge emission and defect related yellow emission, respectively. The relative intensity of the two bands is a strong function of the injection current. The emission band associated with pre-existing defects in the LEDs offers us the chance to observe defect migration and generation during the stress tests. The intensity of the yellow band is strongly affected by the defects in the active layer. As the stress continues, more and more defects are generated in the active region.

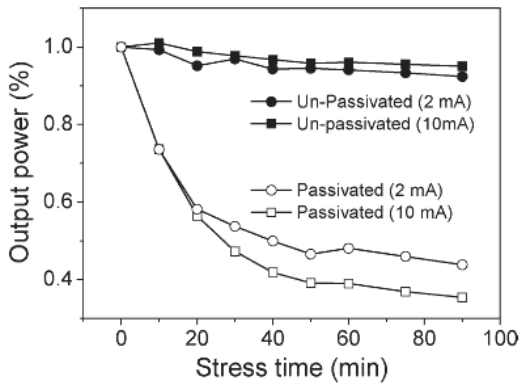


Figure 35:Optical power measurment of the passivated and unpassivated LED at 250°C. (Meneghini M. P., 2006)

During the fabrication process, p-type GaN layer was obtained using magnesium as acceptor. Hydrogen is introduced during growth process in compensating acceptor doping. After the growth, the doping can be activated by means of low-energy electron-beam irradiation and high temperature annealing. GaN LEDs can fail after high-temperature stress (250°C- 300°C) even without bias. The main identified degradation mechanism was emission crowding and series resistance increase. The failure mechanism is the presence of hydrogen which at high temperature can diffuse in the p-layer and generate Mg-H bonds. As a result, this reaction will ruin the active doping and reduce the device performance. The experiment was carried out by comparing the behavior of GaN LEDs with and without a hydrogen-rich SiN passivation layer during thermal stress by means of a combined electrical and optical characterization.

The devices with and without passivation were subjected to thermal storage at 250°C for 90hours at different electrical bias. Figure 35 shows the optical power measurement of the LED with and without hydro-rich SiN passivation layer ( (Meneghini M. P., 2006). It can be shown that the high temperature stress introduces a strong optical power degradation only in the samples with passivation layer, which lost the 65% of their efficiency at 10 mA after the 90-min test. On the

other side, the unpassivated samples lost only the 5% of their efficiency at 10 mA during the 90-min test.

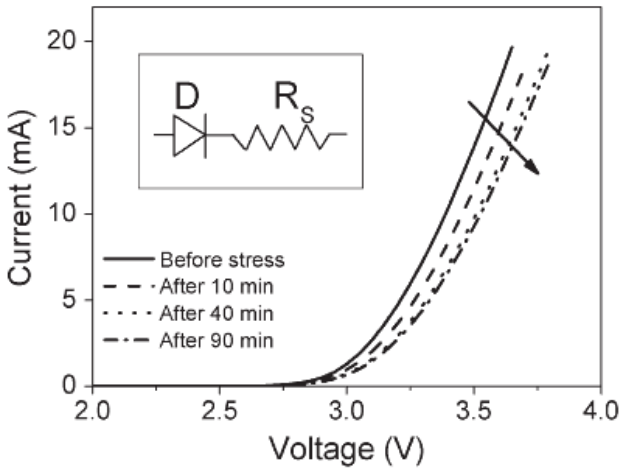


Figure 36: I-V curves measurements of LED with passivation layer at 250°C. (Meneghini M. T., 2006)

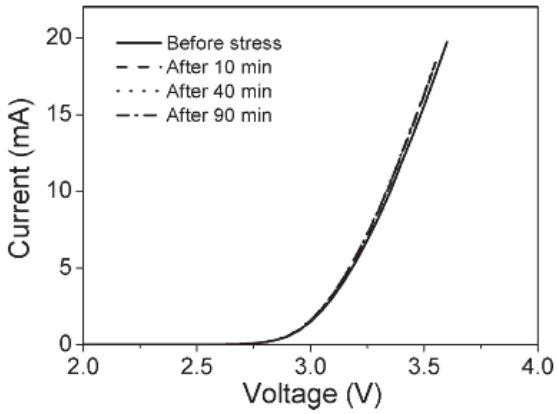


Figure 37: Current-Voltage Curves of the LED without the passivation layer. (Meneghini M. T., 2007)

Figure 36 shows the forward current forward voltage characteristics of one passivated sample (Meneghini M. T., 2006). It can be concluded that thermal stress inducted an increasing of

series resistance in the diode. On the other hand, thermal stress didn't introduce significant changes in the current-voltage of the LED who doesn't have the hydrogen-rich passivation layer. Figure 37 shows the I-V curve of the LED without the passivation layer (Meneghini M. P., 2006).

It can be seen from the above results that high temperature can change the electrical and optical performances of the GaN based LED. The optical power will decrease and the operation voltage will increase. This process can be related to the degradation of the p-type region of the diode, due to the hydrogen-induced compensation of the acceptor dopant (Meneghini M. T., 2007).

The growth of InGaN/GaN multiple quantum well is complex due to the lattice mismatch and the different thermal expansion coefficient of the two material. The optical spectrum of the GaN based LED is strongly influenced by the quality of the quantum well structure which can be easily varied by the minor change of the growth condition. The degradation of the multiple quantum well structure was caused to the interaction of In and Ga between the InGaN and the GaN layer (Yang S. C., 2010) (Horng, 2012) (McCluskey P. M., 1999) (McCluskey M. D., 1998). GaN based LED was fabricated with InGaN/GaN multiple quantum well by metal organic chemical vapor deposition. The optical performance of the LED was correlated with the activation temperature of doped Mg. Photoluminescence and electroluminescence was used to perform the analysis. Figure 38 shows the photoluminescence spectrum of the GaN based LED with Mg as the p-layer dopant (Youn, 2003). The device was activated at the temperature that ranges from 750°C to 925°C in N2 for 30 seconds.

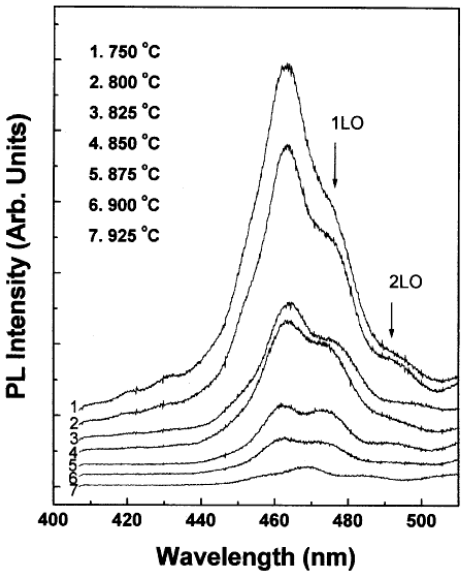


Figure 38: Photoluminescence spectra obtained from the GaN based LED at with the Mg-doped p-GaN layer activated at the temperatures range from 7501C to 9251C fo 30 s in a N2 ambient. (Youn, 2003)

It can be seen that the peak of the spectrum tends to decrease with the increasing of the activation temperature. Among all the samples, the LED that activated at 750°C has the heighted photoluminescence intensity. When temperature goes up across 825°C, the devices showed a significant decrease in the photoluminescence intensity (Youn, 2003). Figure 39 shows the high-resolution transmission electron microscopy (HRTEM) image for the active layers of InGaN/GaN MQW annealed at 8251C. The image show that there are some dark lumps formed in the InGaN quantum well structure. Therefore, the activation process of Mg-doped p-GaN layer should be performed at the lowest temperature to obtain better optical properties of InGaN/GaN multiple quantum well structures (Youn, 2003).

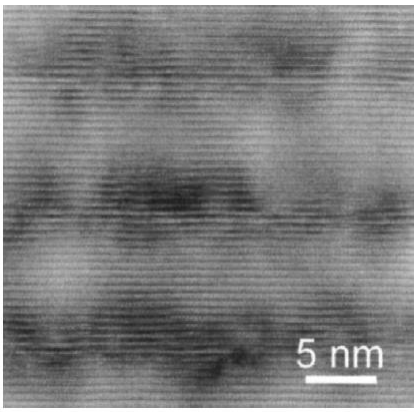


Figure 39: TEM Image of the InGaN/GaN MQW annealed at 8251C for 30 s. (Youn, 2003)

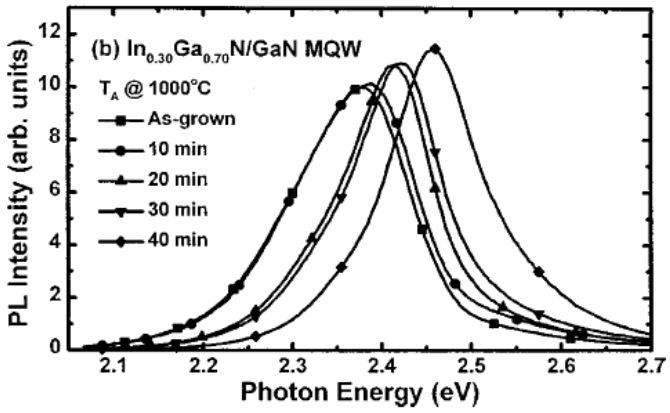


Figure 40: Photoluminescence spectra of annealed samples with various annealing durations. (Chuo, 2001)

Figure 40 shows the Photoluminescence spectra of annealed samples with different annealing durations (Chuo, 2001). A blue shift can be observed with the increasing of annealing temperature from 900°C to 1050°C. This is attributed to the decrease of indium content in the quantum well after the intermixing between InGaN quantum wells and GaN barriers. The test result also indicates that higher diffusivity will happen with high-indium quantum well structure.

## 2.2. LED PACKAGE RELIABILITY

It is important to select the right materials for the optical parts in the LED package, such as lens, encapsulation. Improper materials will lead thermal stresses to the electrical package, due to CTE mismatches and reduce the rate of heat transfer from the semiconductor devices inside the package (Philips Lumileds Lighting Company, 2006) (Hsu, 2008) (Luo, 2010) (Hewlett Packard, 1997) (Lu G. M., 2015) (Lin, 2006) (McCluskey P. M., 1999) (Zhang, 2012) . Figure 41 shows a LED package with various optical parts.

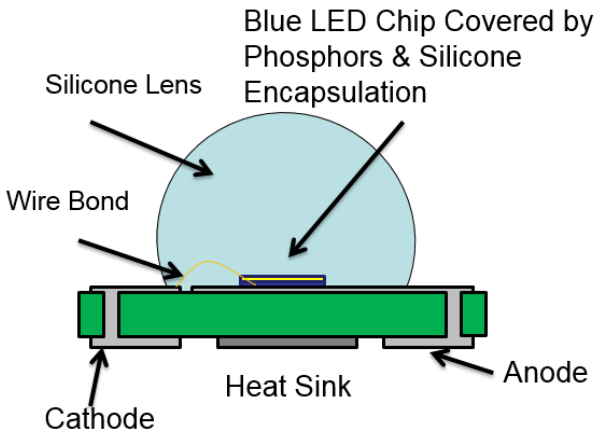


Figure 41: LED package with various optical parts.

The majority of high-power and mid-power LEDs use an epoxy or silicone based systems to make the optical parts of the package. Epoxy was used as the lens and package material when LEDs were first developed. The semiconductor-epoxy can increase the light extraction efficiency, because epoxy has larger refractive index compared with air. Figure 42 shows the light extraction efficiency as a function of epoxy refractive index (Lin, 2006).

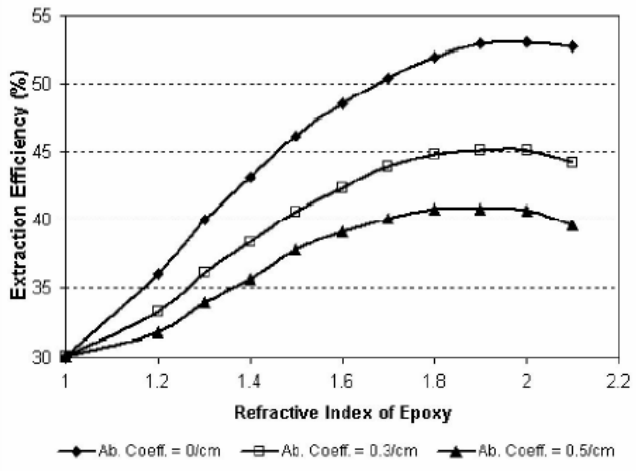


Figure 42: Extraction efficiency of epoxy as a function of refractive index. (Lin, 2006)

It is can be shown from Figure 42 that a higher refractive index and lower absorption coefficient can increase the light extraction efficiency of epoxy. LEDs are encapsulated to prevent the fragile wire bond and semiconductor inside the package from outside mechanical stress. Transparent epoxy resin was used as the encapsulation material for lower power LED for a long time. However, epoxy resins has two disadvantages as the encapsulation material for modern high power white LEDs (McCluskey P. M., 1999) (McCluskey P. M., 2000). Cured epoxy is usually very rigid due to the cross-lined networks. The other disadvantages is that epoxy material tends to degrade very fast when exposed to high temperature or ultraviolet light. This degradation will cause the yellowing of encapsulation. The yellowing of epoxy comes from the formation of thermos-oxidative cross-link. Encapsulation yellowing will decrease the encapsulation transparency and discolored the optical parts. Consequently, the degraded epoxy optical parts work as a light filter which will reduce the light output and shift the light spectrum. The poor thermal and ultraviolet resistance of epoxy encapsulation material can be enhanced by adding anti-oxidants, UV stabilizers. The thermal stability of bisphenol-A, cycloaliphatic, and a new kind of

enhanced epoxy resin, have been studied by constant temperature aging. The performance of each material is shown in Figure 43 (Lin, 2006).

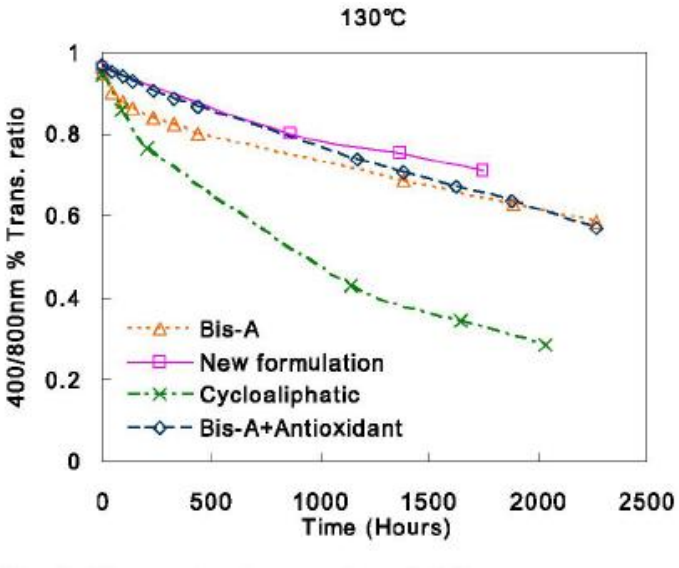


Figure 43: Thermal Performance of different epoxies. (Lin, 2006)

With expectation of higher luminous flux output, higher forward current and better life-long reliability, silicone materials has been introduced to be new generation of encapsulation materials for LED (Narendran N. G., 2004) (Baillot, 2010) (Mehr, 2013b) (Meneghini M. P., 2006). The chemical structure of silicone provides several advantages over epoxy encapsulation used in the optoelectronic products. The advantage includes the thermal and ultraviolet stability of silicone, which are the main characteristics needed for new generation LED products. Figure 44 shows the 200h thermal aging test results of epoxy and silicone (Clapp, 2015) (DeShazer, 2014).

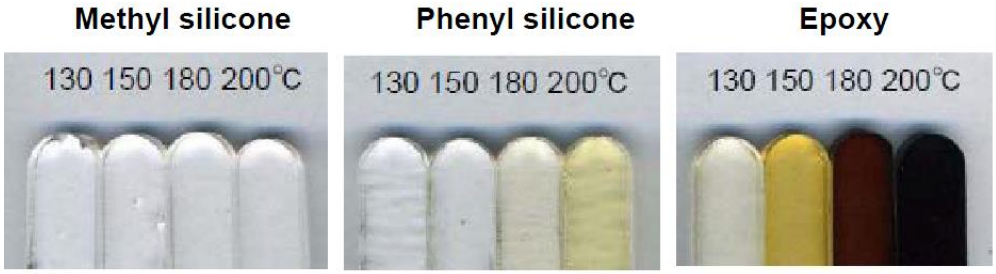


Figure 44: 200 hours thermal aging at different aging temperature. (DeShazer, 2014)

High ultraviolet and thermal stability minimizes the yellowing effects at high heat (150°C+) and withstands high lumen density, especially for high power LED with the blue emitting die. Also, ultraviolet resistance can enhance the long-term reliability for outdoor application (Meneghini M. P., 2006) (Meneghini M. T., 2008).

Silicone can be formulated in different hardness properties, which can be gel, elastic, and hard types. Silicone used in LED encapsulation is generally elastic type to give the flexibility to encapsulated wire bound and die attach. This characteristic provides the ability to absorb thermal stress during the soldering process and during operation at high power as well.

Silicone elastomers, gels, thixotropic gels, and fluids not only perform extremely well in high temperature applications, but also offer refractive index matching so that silicone can transmit light with admirable efficiency. Silicone has a wide variety of material compositions which makes it a potential option for various applications. The optical industry widely uses silicone for various applications such as fiber optical cable potting. Due to these optical advantages, silicone materials have been used in the phosphor binder, encapsulation and lens of LED package.

However, silicone compound as an LED encapsulation material can also have defects, such as larger thermal expansion coefficient, and high permeability to humidity. Silicone resins may

out-gas at extreme high temperatures or the ingress of moisture, releasing acetic acid which is very corrosive to the elements inside the LED package. The catalysts used to prepare silicones can also be harmful to the LED package (Dow Corning Corporation, 1997). Such reactions can result in the degradation of thermal stability or optical stability.

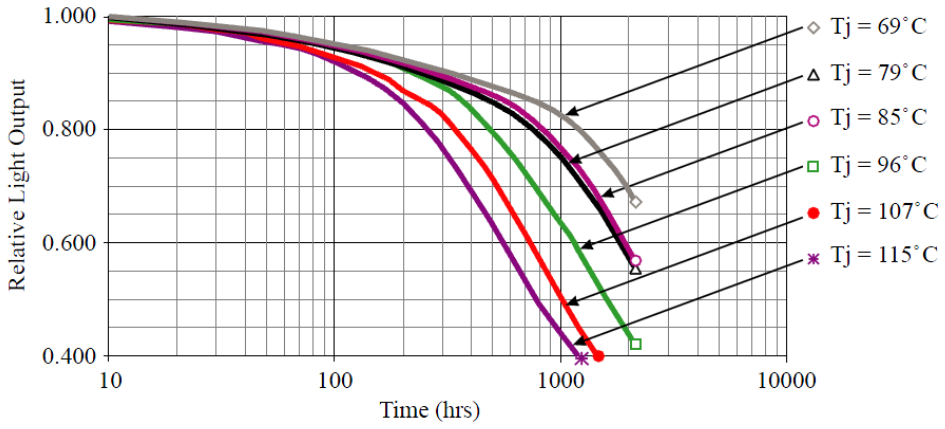


Figure 45: Light output variation as a function of aging time at different temperature. (Narendran N. G., 2004)

The thermal effects associated with high junction temperature also play an important role in the yellowing effects of encapsulation material. Yellowing Effects is related to the combination of ambient temperature and the self-heating. A portion of the emitted light will circulate between the phosphor layer and the reflector cup and increases the temperature of the package. Exposure to high temperature will reduce the luminous output. Figure 45 shows the relative light out as a function of aging time at different ambient temperature (Narendran N. G., 2004).

The light output decrease over time in an exponential pattern. Therefore, the relative light output, L, can be expressed as:

| | |
|---|---|
| $L = e^{-\alpha * t}$ | (75) |

Where a is the light output degradation rate or the decay constant, and t is the operation time measured in hours. Exponential curve fitting of the experimental data yielded the decay constants for each junction temperature. With increasing junction temperature, the decay constant increased exponentially also. Therefore, the light output degradation rate increase with the increasing of junction temperature. Figure 46 illustrates the variation of the decay constant as a function of junction temperature (Narendran N. G., 2004).

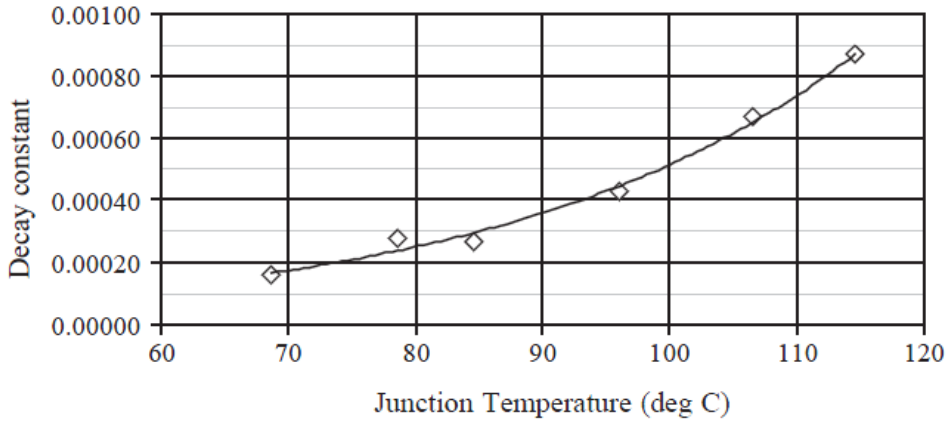


Figure 46: Decay Constant as a function of junctin temperature. (Narendran N. G., 2004)

## 2.3. PHOSPHOR RELIABILITY

The function of phosphor material in LEDs is to absorb the primary wavelength emitted by the LED chip (near ultraviolet or blue light) and convert it to long wavelength spectrum. The requirements of phosphor material used in LEDs includes: high absorption in the region of blue spectrum, high quantum efficiency, resistant to extreme environment such as high temperature and humidity.

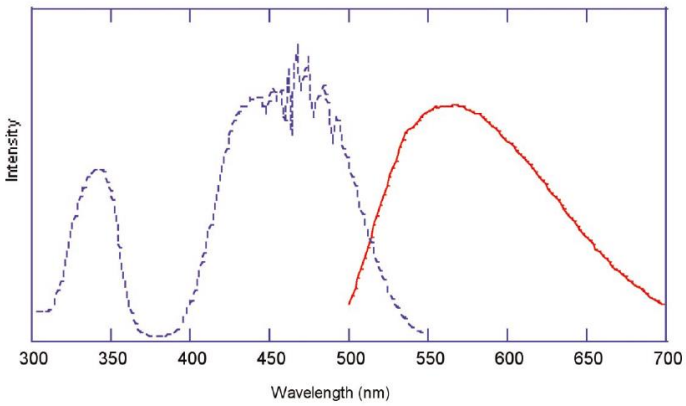


Figure 47: Room temperature excitation (left) and emission spectrum (right) of $Y_3Al_5O_{12}:Ce^{3+}$ phosphor. (Pust, 2014)

Fluorescent lamp phosphors convers the ultraviolet discharge of mercury plasma into visible light. The primary wavelength of the plasma is 254nm and the converted spectrum is 555nm. The efficiency of the conversion process is approximately 45% which is relatively low. There are nearly 55% energy loss during the conversion process in the fluorescent lamp. Therefore, the efficiency of a lighting devices would increase as the excitation spectrum moves closer to the visible spectrum. For example, the energy conversion efficiency of a 370 nm UV and a 450 nm blue radiator into visible light would be about 65 percent and 80 percent, respectively. There are two available semiconductor devices, namely UV emitter (emission at 370nm) and blue emitter (450nm-470nm).

To generate white spectrum, the blue emission from the LED emitter can be mixed with the complementary yellow emission that can be generated by a yellow phosphor. The yellow flour luminescence emission mixed with the residue blue light can generate white light with a range of correlated color temperature form 3000K to 6000K. Figure 47 shows the excitation spectrum and the emission spectrum of $Y_3Al_5O_{12}:Ce^{3+}$ phosphor at room temperature (Rohwer, 2003) (Pust, 2014).

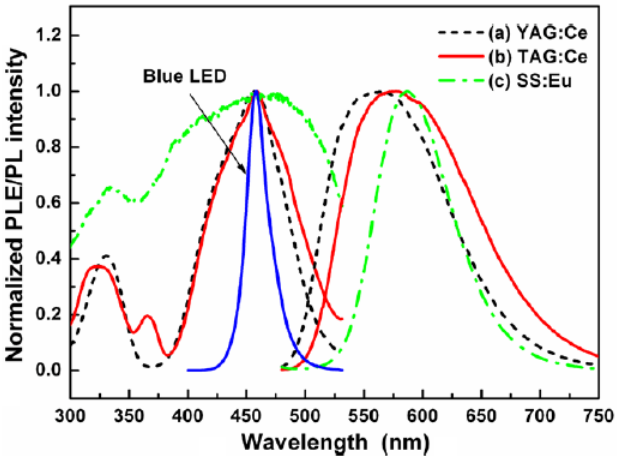


Figure 48 Normalized spectra of various yellow-emitting phosphors: (a) YAG:Ce, (b) TAG:Ce, and (c) $Sr_3SiO_5:Eu^{2+}$, respectively. (Jang, 2009)

By careful control of the garnet phosphor chemical component, the emission spectrum can be tuned to cover a large range of white color temperature. However, there are some drawbacks of YAG:Ce phosphor. The color rendering index of the white LED is very low due to the lack of red emission spectrum. Researchers are developing new phosphor material that can increase the color rendering index of white LED. Among all the new phosphor systems, nitride phosphor material has drawn a lot attention. Divalent europium-activated $M_2Si_5N_8$ (M can be Ca, Sr, Ba) materials display strong absorption in the blue and exhibit efficient emission of red spectrum which can increase the color rendering index significantly. Figure 48 shows the excitation and emission spectrum comparison of YAG:Ce, $Tb_3Al_5O_{12}:Ce^{3+}$and $Sr_3SiO_5:Eu^{2+}$ phosphor system (Jang, 2009)

.

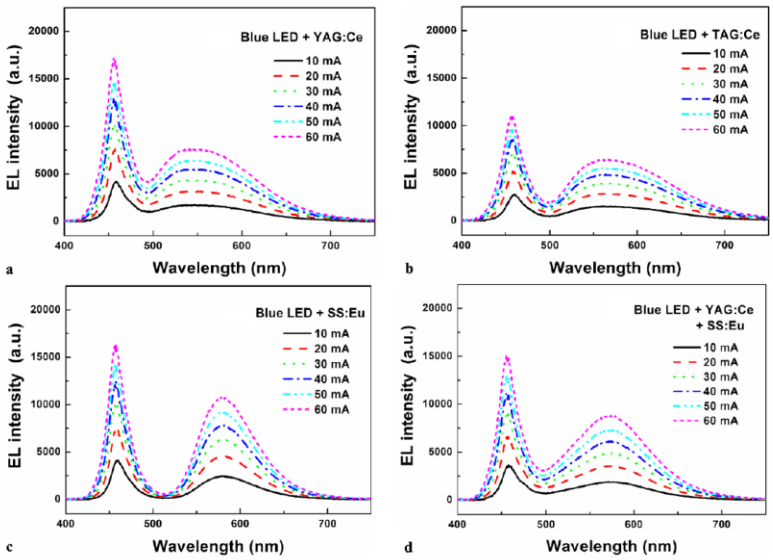


Figure 49: Light Spectral of white LEDs using (a) YAG:Ce, (b) TAG:Ce, (c) SS:Eu, and (d) YAG:Ce+SS:Eu under various currents (DC 10, 20, 30, 40, 50 and 60 mA). (Lunia, 2014)

The emission spectrum of one phosphor system is different from those of the other phosphors. Therefore, a white light can be tuned by combining a blue LED with various available yellow emitting phosphor. The operational current of LED usually has a wide range that can change from 150mA to 1000mA. When the applied current increases, the intensity of the blue and yellow spectrum of white LED increase, because the higher the applied current, the stronger the blue emission. The blue emission will be absorb by the yellow emitting phosphors, and the yellow emissions will increase accordingly. The spectrum of the white light will change with the applied current, so do the color coordinates in the CIE diagram. Figure 49 shows the light spectrum of the white LED under the following applied currents: 10, 20, 30, 40, 50, and 60 mA (Jang, 2009) (Lakshmanan, 2011) (Lunia, 2014).

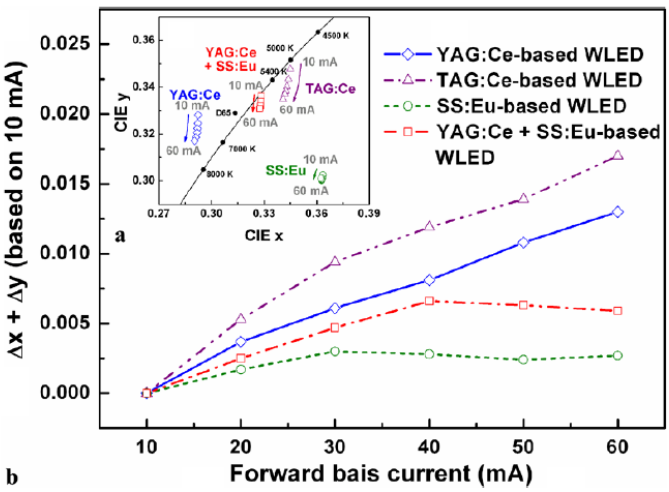


Figure 50: (a) The CIE color coordinates of the pc-LEDs and (b) the variation of the CIE color coordinates of the pc WLEDs as a function of the applied current (DC 10, 20, 30 40, 50, and 60 mA). (Jang, 2009)

Figure 50 shows the color coordinates of the white LED under different applied current (Jang, 2009). It can be shown that the color coordinates shifted to the blue region as the applied current was increased. It indicates that the rate of the increase in blue emission is higher than the rate of increase in yellow emission. In addition, when the forward current was increased, the mixed phosphor (YAG:Ce + SS:Eu)-based white LED showed more stable color stability than single phosphor based white LED. Therefore, by applying mixed phosphors on a blue LED chip, the color stability of different current is improved, as well as the color rendering index (Jang, 2009) (Narendran N. G.-N., 2005).

Although phosphor binder layers are a necessary component for white LEDs, the presence of phosphors can cause a decrease in reliability of LED packages (Tran N. T., 2008) (Meneghini M. T., 2008). Figure 51 shows the light output power of phosphor based LED with different phosphor concentration (Tran N. T., 2008) (Tran N. T., 2009).

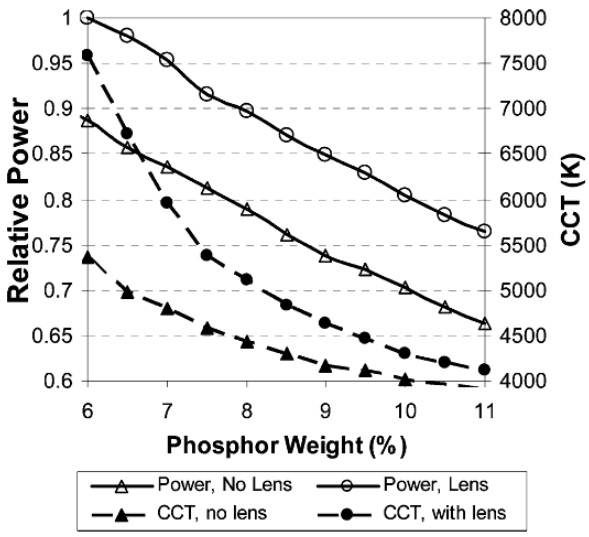


Figure 51: Relative Power output of phosphor based LED at different phosphor concentration. (Tran N. T., 2009)

Phosphor particles are embedded inside the silicone resin. The brightness and luminous efficacy of a LED package depends on the phosphor particles concentration and phosphor binder thickness (Tran N. T., 2008) (Tran N. T., 2009). The package with low phosphor concentration and high phosphor- composite thickness has higher luminous efficacy compared with the package having higher concentration and lower phosphor-composite thickness. Increased phosphor concentration increase the probability of blue light being absorbed and converted to yellow light. Therefore, the correlated color temperature is decreasing with the increase in the phosphor particles concentration. Also, the luminous efficacy will decrease, because the conversion efficiency of phosphor is always less than 100%. Moreover, an increase of phosphor concentration increase the probability of light being trapped inside the package. In conclusion, the power output of LED decrease with the increasing of phosphor concentration.

It is shown that different particle sizes scatter and trap different amount of light inside the package or reduce the amount of light propagating in forward direction (Tran N. T., 2008) (Tran

N. T., 2009). Different phosphor sizes also have different spatial distribution that can be a result of settling effect. Figure 52 shows the light distribution when a blue photon hits the phosphor particle (Tran N. T., 2008) (Tran N. T., 2009).

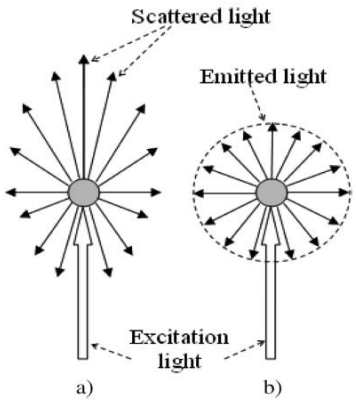


Figure 52: Interaction of excied light and a phosphor particles. (a) scattering light distribution (b) isotropic emission of yellow light. (Tran N. T., 2009)

Light loss in the LED package is dominated by scattering and reflection of excited light by semiconductor chip. There is a large amount of light energy reflected back to the package by the phosphor particles in the binder layer. Also, backscattering of phosphor particles also decrease the extraction efficiency of LED packages. Only 40% of the light will transmit through the phosphor layer, while 60% of them is either reflected back or backscattered (Narendran N. G., 2004). Backscattering and back reflection of light by phosphor particles can be minimized by optimizing phosphor particle sizes.

In a phosphor based white LED, phosphor particles can be applied on the top of the blue emitter. The thin layer of phosphor is dispensed on the chip by a clear encapsulation material, such as silicone. In any phosphor binder geometries, the size of the phosphor particles is expected

to influence the luminous efficacy of the LED package. Figure 53 shows the lumen output of LED package with different phosphor particles size (Tran N. T., 2009).

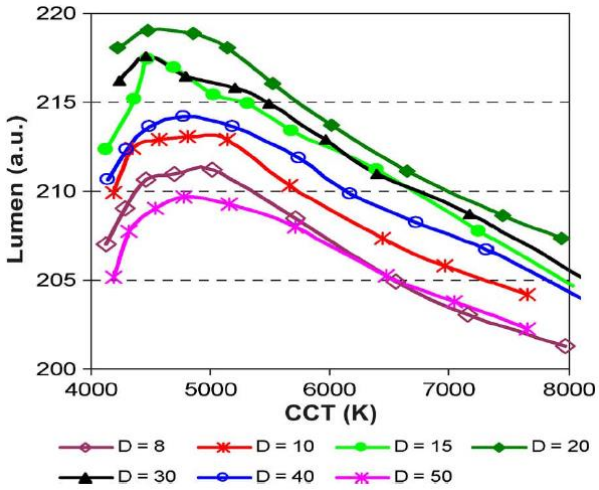


Figure 53: Lumen ouput of phosphor LED with different particle sizes. (Tran N. T., 2009)

In the micro-size region, the lumen output reaches its maximum value at the particle size of 20µm, and decrease when the particles size keeps increasing. This observation can be explained by using the extent of light scattering. In the phosphor binder, the process of light scattering is complicate. The light scattering process depends on the particle size, the degree of refractive index mismatch between the phosphor particles and encapsulate, the concentration of suspended particle, and the wavelength of light.

## 2.4. DIAGNOSTIC AND LIFETIME PREDICTION

Prognostics and health management (PHM) is a method that permits the reliability of a system to be evaluated in its actual life-cycle conditions, to determine the advent of failure, and minimize the system risks (Vichare, 2006) (Pecht, 2009). It requires the diagnostic tools integrated inside the system being monitored. Thanks to the development of sensor system and integrated

circuit, most of the safety crucial mechanical or electrical system has a compact self-diagnostic and monitor system, such as aircraft, submarine. Knowing the health of each components in a system provides better knowledge of making important decisions related to safety. Usually, there are many sensors running inside the system to monitor the system states and health condition in-situ. As a result, a large amount knowledge is available for the health management of mechanical and electrical system such as aviation system. For a long time, prognostic health management has been employed to provide advanced warning of safety and mission critical system to allow necessary maintenance. Some existing PHM technologies have been applied to critical infrastructures, such as nuclear power plant, bridge, railways (Swanson D. C., 2000) (Swanson D. C., 2001) (Batzel, 2009) (Jarrell, 2002), (Coble, 2010), (Ko, 2005).

PHM is also proven an efficient method to monitor and access the health of electronics system (Lall P. B., 2008d) (Lall P. C., 2006a) (Lall P. C., 2007a) (Lall P. C., 2008a) (Lall P. G., 2007b) (Lall P. H., 2007e) (Lall P. H., 2008c) (Lall P. H., 2007c) (Lall P. H., 2006b) (Lall P. I., 2005a) (Lall P. I., 2008f) (Lall P. I., 2004a) (Lall P. I., 2006d) (Lall P. I., 2004b) (Lall P. I., 2004c) (Lall P. L., 2010b) (Lall P. L., 2010a) (Lall P. L., 2011c) (Lall P. L., 2009a) (Lall P. L., 2009b) (Lall P. L., 2011b) (Lall P. L., 2011a) (Lall P. W., 2012a) (Lall P. P., 2005b) (Lall P. P., 2008b) (Lall P. P., 2006e) (Lall P. P., 2004d) (Lall P. S., 2014) (Lall P. S., 2012b) (Lall P. S., 2008e) (Lall P. S., 2013a) (Lall P. Z., 2013b)This method has been widely used in various products, since most products contain some electronics to provide functionality and performance in recent days. The increasing usage of electronic system for mission and safety critical situation has motivated the development of new technologies that can monitor the health of the electronics system and give warming in advance. Assessing the extent of deviation or degradation from expected normal operation condition for electronics system can help to prevent catastrophic failure of critical

system. PHM can provide warning of the failure and extend maintenance cycle which will reduce the life cycle cost. It requires the diagnostic tools integrated inside the system being monitored. Therefore, it should consume minimal resource and be able to provide long enough warning time to allow maintenance to be performed. The health management of electronic package is difficult compared with the mechanical system, since all the components inside the electrical package is in micro scale or nano scale. Electronic package is a highly-intergraded system with complicate architecture inside. Therefore, there are some challenges in the in-situ monitoring, and remaining useful life prediction. For now, there are several methods have been developed to implement the PHM method inside electric package, such as built in test (BIT) and using of expendable devices (Kulkarni, 2010) (Vichare, 2006).

### 2.4.1. BUILD-IN TEST

Built-in test (BIT) is a method that involves on-board hardware. That hardware consists of circuit that built inside the package. Software are used to read the output of the built-in test circuit. The manufacturer of BIT system provides a package which allows the user to access the internal components. The output of the BIT system can be compared with the know characteristics to monitor the health states of the system. Based on the application, the BIT can be separated into several levels, such as circuit-level, module-level and system-level. The working pattern of BIT system depends on its function. Some of the BIT system works continuously, while other BIT systems only work when it is required to do so. Depending on the diagnostics method, BIT technology can also be divided into two categories: direct and indirect method. The direct method diagnoses the system through a sensor attached directly to the components whereas the indirect method evaluates other peripheral parameters that reflect the condition of the component. A system with BIT is characterized by its ability to monitor and diagnose its health condition by itself. BIT

has been deployed in many areas of the industry, such as manufacturing, aerospace, automobile, large-scale integrated circuit (IC), power system (Barke, 2005) (Goebel, 2008) (Gao, 2002) (Mishra S. P., 2002). This trend is primarily due to the need for highly integrated and automated system which requires high level of system reliability.

The increasing number for smart factories with high automation, high productivity and low cost has stimulated the development of innovative BIT applications in all kinds of industry products. IC industry is one example. IC products have high integration density which has lots of reliability issues such as current leakage, cross talk and electro-magnetic compatibility. These problems reduce the reliability of the system and it is very difficult to access the single component for individual test due to the high density. Also, off-line testing procedures are time and resource consuming, presenting a bottleneck for time and resource efficient productivity. It is necessary to have a BIT system to assess the states of each component and provide health management. In this application, the BIT components are embedded inside the function circuits, enabling the quality controller to diagnose the system by comparing BIT signals with a set of reference or threshold values. If the output of BIT doesn't match the reference signature, an error happens which means the degradation of the IC. This method has led to the emergence of BIT in the semiconductor industry as a cost effective and efficient technique. Figure 54 shows the test scheme of IC (Gao, 2002).

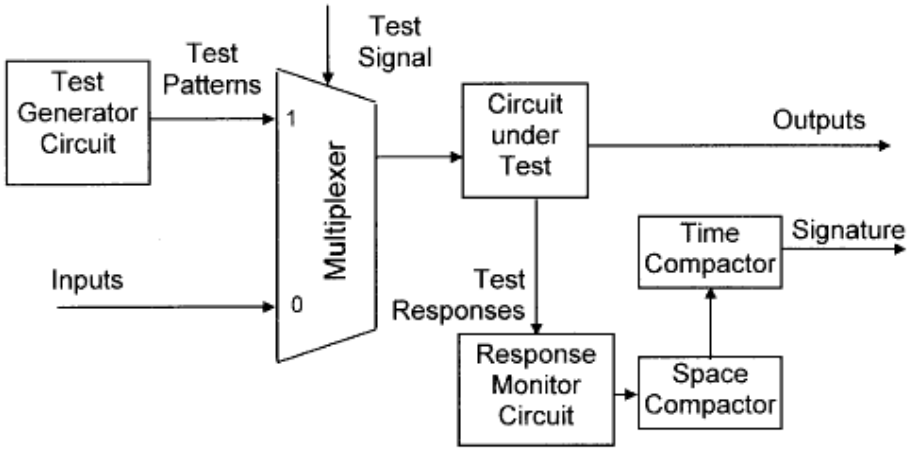


Figure 54: BIT test scheme of IC. (Gao, 2002)

Another application of BIT in IC is to monitor the temperature of the die region. The accurate temperature measurement of the die region can be obtained by measuring the voltage of a constant forward current biased diode. The most important characteristics of aircraft is its safety critical. Disaster could happen if a smallest component fails during the operation. The need for high reliability of aircraft has resulted in the adoption of BIT systems at various levels, such as component level and system level (Zourides, 1989).

The nature of BIT system determines that it can identify the failure modes that closes to the component levels. It helps achieve significant cost reduction by reducing the need for system disassembly during the system diagnostic and maintenance. Another advantage of BIT system is that it can record the time and the environmental stress data of the failure event which will help to identify the cause of failure. Failure analysis and future diagnostics can be much easier with the data from BIT system.

Despite the advantages of BIT systems, there are some concerns. The BIT system is an extra to the original system. It should monitor the mechanical or electrical system without affecting

the normal operation at minimum source consumption. For example, it takes up space and adds extra weight to the aircraft system which will reduce the efficiency of commercial operation. Also, BIT technology is still being developed to achieve high accuracy. The spurious fault detection and indication rate is high. Several studies has been performed on the high fault detection rate which can results excessive replacement, loss of system reliability. BIT system can only be applied in big volume systems, since the extra circuit and interface are going to consume some extra space. BIT system primarily serves as a health monitoring and diagnostics tool and is not be able to provide the prediction of remaining useful life. Those disadvantages greatly restrict its applications scope (Allen, 2003). However, the BIT will ultimately become a wide adopted diagnostics tool in both manufacturing and consumer electronics with the development of wireless data communication and advanced sensors, such as microelectromechanical systems (MEMS). It can be expected that the development of BIT system will integrate many other frontier technologies and bring new challenges that needed to be addressed in the future.

### 2.4.2. RELIABILITY CANARY

Reliability canaries is another traditional method to protect the key structure of mission critical system. Fuses and circuit breakers are examples of reliability canaries that used in electronic system to protect the sensitive components. In some other system, temperature sensors are deployed to sense the ambient temperature, and shut down the system if the temperature go across the limited threshold. Like the BIT system, self-checking circuit can be incorporated in the system and sense the abnormal conditions. (Vichare, 2006). The circuit will fail earlier than the critical functional components, which will gratly reduce the risk of the whole system and save replacement cost. Also, reliability canary circuit embedded in the safety critical system can be used to provide warnings prior the real failure. Semiconductor-level reliability canaries are available

with pre-tuned circuits that can be placed in the same package with the functional chip to monitor the health states of the electronic package. The canary circuit can be used to monitor various semiconductor devices failures, such as dielectric breakdown, hot carrier aging or electro migration (Mishra U. K., 2002). The reliability canary is subject to the same manufacturing process and environmental stress with the actual functional circuits inside the package. By incorporating these monitors as a part of the electrical package, it can assure that the canary circuit components see the same operational environment as the real product. It also assures that any parameter that affects the product reliability will also affect the reliability canary.

If both the functional circuits and the reliability canaries are designed and manufactured with the same technology, both circuits will have the same mean life time. In order to provide the advanced warning for the critical system, the canary circuit should fail earlier than the functional circuit. Although both the circuits are in the same environmental stress, the aging stress of the reliability canary can be altered in a controlled way, such as increasing the electrical stress. Increasing of the electrical stress can be achieved by increasing the current density passing through the reliability canary. Current passing through the functional circuits and the canary circuit are the same in order not to disrupt the functionality of the key system. With the same amount of current passing through both circuits, the cross-sectional area of the canary components can be reduced to achieve higher electrical stress. Another method of increasing the current density is to increase the voltage applied to the canary components. A combination of previous techniques can also be used to increase the electrical stress on the canary components. Higher current density will cause higher internal heating which will cause higher thermal stress on the canary components. When higher electrical stress applied to the canary components, they are expected to fail earlier than the

functional circuit. Figure 55 shows the reliability curves for functional circuit and canary circuit (Mishra S. P., 2002).

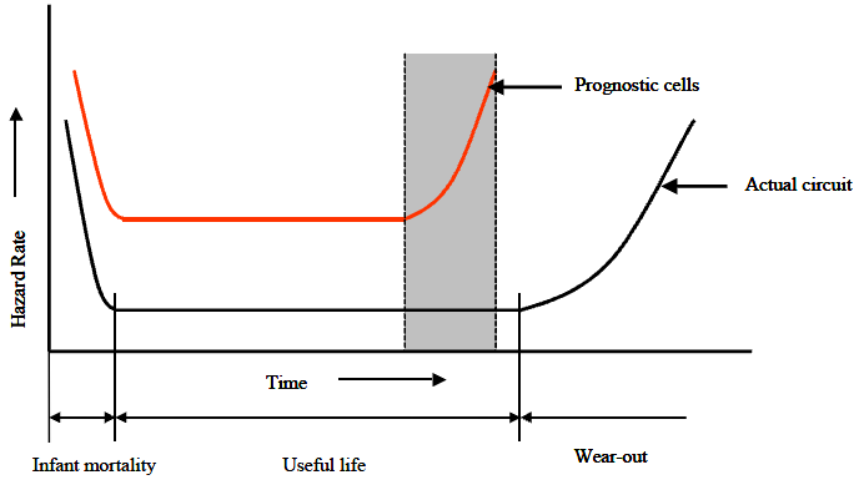


Figure 55: Idealized bathtub reliability curves for the functional circuit and canary components. (Mishra S. P., 2002)

### 2.4.3. ACCELERATED LIFE TEST

The improvement of BIT and reliability canary systems can be achieved by the accelerated life test (ALT). A large amount of failure date could be gathered through the accelerated life test which provides the insight of the failure mechanisms (Nelson, 1990) (Su, 2012). The BIT and reliability canary could be rearranged with the failure mechanisms found in the accelerated life test, which will greatly improve the accuracy of prediction and reduce spurious fault detection (Suhir, 2002) (Hallberg O. a., 1991). The main purpose of ALT is to reveal and understand the physics of the expected and unexpected failure mechanism of a product during the operation. Usually, there are several failure mechanisms of a product. The ALT can also help to accumulate the failure mechanism statistical distribution in a very short time compared with tradition BIT or reliability canary methods. It player an important role in the evaluation and assurance of reliability of products.

Reliability is usually defined as the ability of a product to perform the required function without failure. Reliability engineering studies failure modes and mechanisms, causes of various failures, and methods to prevent failures (Suhir, 2002). It is important for a company to assure its product to have a worthwhile lifetime and reliability of the customer's expectation. In order to be successful in the marketplace, a manufacturer must understand the physics of the failure mechanisms and the method to prevent the failure in the lifetime. The manufacture usually guarantee the lifetime threes time larger than the expected lifetime of a product.

Commercial microelectronics and photonics products present poor reliability control and have lots of challenges during the design and manufacture process, due to the high density of components (Suhir, 2002). The micro-scale or nano-scale size of the components also increase the uncertainty during the manufacture process. It is important to reduce the cost and time to market if a company want to compete in the global market. Accelerated life test plays an important role in the designing of reliable products in a short time range. In some cases, especially for new products of new technologies, where no experience has been yet accumulated, the general qualification standards will no long work. Even the new products pass the similar qualification standards, which is based on the previous accumulated knowledge of similar component or technology, they still have the high chances to fail during the lifetime. It is also unclear what could be done to improve the quality of the new products. Well-designed ALT can dramatically facilitate the company and reduce time-to-market time, without compromising the products quality.

The lifetime of an electronics product is very long, typically on the order of hundred thousand hours and it is impractical and uneconomical to wait for the failure. ALT uses reasonable increases in stresses to improve the efficiency of reliability test. The stresses can be electrical stress, thermal stress, high humidity or mechanical stress. ALT may also be combined stress.

Examples are: temperature/humidity bias (65°C/90%RH, 75°C/75%RH, 85°C/85%RH), vibration tests at elevated temperature condition, etc. The accelerated test conditions must be specifically designed for the product under test, particularly considering the use conditions. For example, before a new model of cell phone is released, several accelerated mechanical tests will be performed such as vibration and shock test (Tan, 2008).

The design of ALT should consider all the possible failure mechanism caused by a particle stressing environment (Trevisanello, 2008) (Tarashioon, 2012). The acceleration factor and stress should change with the changes of the materials and technologies in the products. Also, the market demand should also be considered. For example, the military ALT standard is much harsher than the normal commercial market. The most common accelerated test conditions are shown in Table 1 (Suhir, 2002):

Table 1: Accelerated Test Conditions (Suhir, 2002)

| | |
|---|---|
| Mechanical Stress | Fatigue test |
| | Mechanical shock |
| | Drop shock |
| | Sinusoidal vibration test |
| | Random vibration test |
| Thermal Stress | High temperature storage (Steady state) |
| | Lowe temperature storage |
| | Temperature cycling |
| | Thermal shock |
| Other Stress | Power cycling |

| | |
|---|---|
| | Voltage extremes |
| | High humidity |
| | Radiation |

Typically, a particular failure mechanism will be related with an accelerated test condition. However, accelerated test conditions may lead to other different failure mechanisms. For example, material property could change completely at high temperatures like a phase transition. It is impossible to predict the failure mechanism at a given test condition. Because of the existence of this exception, it is always necessary to identity the right failure mechanisms and understand the underlying physics. Then, the limit of the usage condition can be established. It should be remembered that the defects size, location and stress condition should be considered together as a system. For example, even a large void in the middle of a solder joint might be acceptable and should not be viewed as reliability defect. However, a tiny void or defect at the interface (especially at the solder ball corner) should be taken seriously, it could lead crack initiation and damage the connection. Table 2 shows the common failure mechanism and the corresponding accelerated stress (Suhir, 2002):

Table 2: Failure Mehcanisms and the corresponding acclerated stressed (Suhir, 2002)

| **Failure Mechanisms** | **Accelerated Stresses and Parameters** |
|---|---|
| Corrosion | Corrosive atmosphere, temperature, relative humidity |
| Creep and stress relaxation | Mechanical stress, temperature |
| Delamination | Temperature cycling, relative humidity |
| Dendrite growth | Voltage, humidity |

| | |
|---|---|
| Diffusion | Temperature, concentration gradient |
| Electro migration and thermos migration | Current density, temperature |
| Stress corrosion cracking | Mechanical stress, temperature, relative humidity |
| Contact wear | Contact force, frequency, relative sliding velocity |

The US Department of Defense (DoD) military test standard MIL-STD-810 list a large amount of different accelerated life test methods that can be used for various products which includes microelectronics products. IPC-SM-785 lists the accelerated thermal mechanical stress test standards for the surface mounted electronics which is in mission and safety critical applications. JESD22-B11 and JESD22-B103B list the acceleration test standard for drop and vibration test. Sometimes vibration profile from MIL-STD-810 is used to modify the accelerated vibration test of surface mount electronics (Lall P. L., 2011a). Figure 56 shows a 11gn random vibration profile.

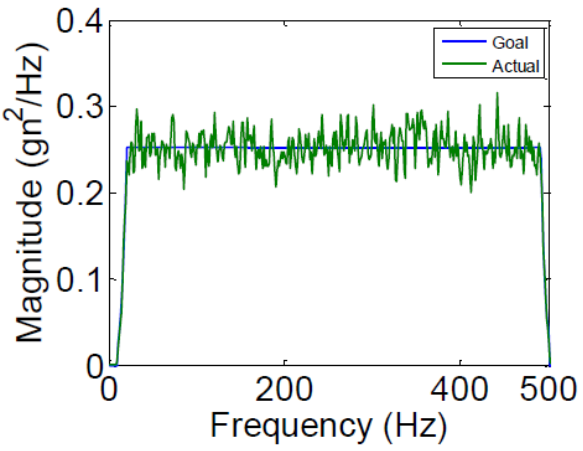


Figure 56: Random Vibration Profile. (Lall P. L., 2011a)

### 2.4.4. TRADITIONAL LIFE PREDICTION MODELS

ALT usually works with a predictive model (Suhir, 2002). This predictive model describes what is changing in the products and what can we get from the ALTs. With the help of the predictive model, the performance of the devices after certain time in service can be predicted at the accelerated test conditions. By considering the fundamental physics of degradation, the performance of the devices at normal operation condition can also be predicted. A good predictive model should clearly include what affects what in a given device, and can be used in new application conditions and new technology developments. There are several PHM methods that can be correlated with the accelerated life test method to predict the remaining useful life of various electronics components. Tradition reliability method predict the lifetime based on the average of a large population, such as Weibull analysis (Kleinbaum, 2005). Weibull distribution is the most common method of statistical analysis being used by researchers to display trends and analyze failure data in electronic packaging today (Lall P. C., 2008a) (Lall P. P., 2008b). The Weibull plot provides failure time estimation for a large population of components. For example, large number of components are thermal cycled in a thermal cycle test. During the cycles, the failure number of component are recorded. The resulting failure data were statistically analyzed using two parameter Weibull models. The standard parameters in such an approach are the Weibull slope β, and the characteristic life η, which is the number of cycles required to cause failure of 63.2% of the samples from a particular leg of the test matrix. The equation used in Weibull plot is list below:

$$R(N) = 1 - F(N) = e^{-(\frac{N}{\eta})^{\beta}} \tag{76}$$

Where N is the number of cycles (time until failure occurs), R is the percentage of parts that remains functional, F is the percentage of parts that failed. η is the characteristics life (where 63.2% of the parts that failed) and β is the Weibull plot slope.

The thermal cycle number when 1% of the devices failed can be calculated with the following equation where F(N) equals 0.01:

$$N(1\%) = \eta * (\ln(\frac{1}{1-F(N)}))^{\frac{1}{\beta}} \tag{77}$$

Figure 57 shows a Weibull distribution plot of a resistor study (John Evans, 2016). This figure plots the number of thermal cycles (x-axis) versus the percentage of occurrence of the cumulative distribution of failures (CDF).

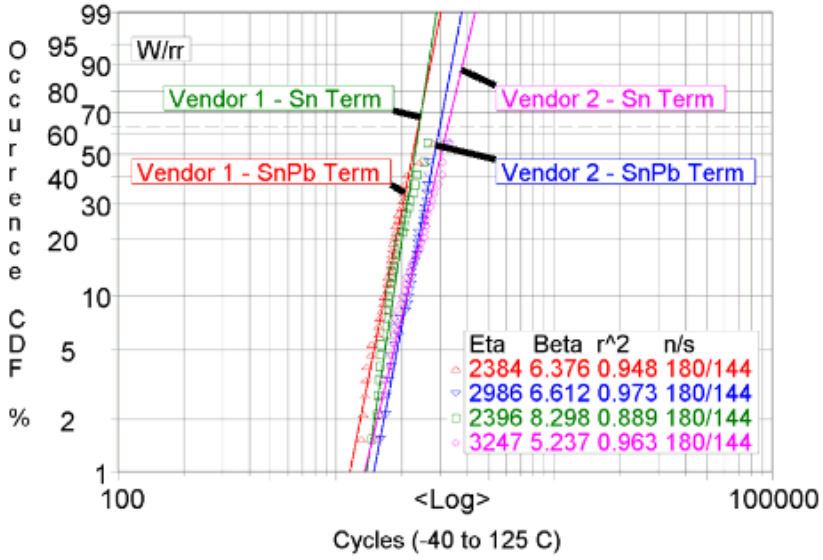


Figure 57: Weibull Plot of a Resistor Termination Study (John Evans, 2016)

Another method to find the mean time to failure is Arrhenius equation. It is one of the earliest and most successful acceleration models predicts how time-to-fail varies with temperature. The Arrhenius equation for reliability is commonly used to calculate the acceleration factor that applies to the acceleration of time-to-failure distributions for microcircuits and other semiconductor devices. The Arrhenius can be expressed:

$$T = A * \exp(\frac{E_a}{K_b * T}) \quad (78)$$

Where T is the lifetime, $E_a$ is the activation energy, $K_b$ is the Boltzmann's constant and T is the absolute temperature. The Arrhenius model can be used with great success if the key factor for the failure is temperature. Most of the physical processes and chemical reactions are temperature dependent. Temperature is the accelerator factor during this degradation. Activation energy ($E_a$) is an empirical value that is the minimum energy required to initiate a specific type of failure mechanism. Material oxidation, electro-migration and contamination are some examples of such failure modes, each with a unique associated $E_a$. The Arrhenius equation can be used to model temperature induced degradation in many electronic and photonic products, such as electronic package, LED (Yang Y. H., 2014). The constant A is a scaling factor that drops out when calculating acceleration factors. The acceleration factor between a higher temperature $T_2$ and a lower temperature $T_1$ is given by:

$$AF = \exp(\frac{E_a}{K} * (\frac{1}{T_1} - \frac{1}{T_2})) \quad (79)$$

When a component has been tested for a number of hours under the stressed condition, the equivalent operation time at the normal use condition can be calculated with the acceleration factor. If the use stress is a less than the stressed condition of an accelerated life test, the acceleration factor will be higher than on.

To add some other stresses in the life predicted model, Eyring model is given as:

$$T = A * \sigma^{-1} * \exp(\frac{Ea}{K_b * T}) \quad (80)$$

The effect of the external stress σ is considered as another term in the Eyring equation. Peck's equation is a modified version of Arrhenius equation. It is designed for the temperature and humidity bias condition which is given below:

$$T = A * RH^{-n} * \exp(\frac{Ea}{K_b * T}) \quad (81)$$

Where RH is the relative humidity percentage.

### 2.4.5. LIFETIME PREDICTION WITH LEADING INDICATOR

There are many drawbacks of traditional reliability modeling. Critics of traditional lifetime prediction methods point to the reliance on large amount of data for statistical analysis (Jang, 2009). The failure of a single component could lead the breakdown of the whole system. Assessing the health of single component provides better information for the system health (Engel, 2009). Another critic of traditional reliability method is the gap between accelerated life test the real usage condition (Smith, 2011)The ALT relies on the large population statistics to get the conclusion. However, the reliability of single component in the system is most relevant to the specific usage condition (Hamada, 2008). During the maintenance, most of the parts are replaced as they fail. Thus, most of the components are replaced at a very low probability of failure. Therefore, the drawbacks of this traditional method is that most components are replaced before they are failed which leads to a large amount of excessive support cost.

Life prediction based on the leading indicator can be used to extrapolate the system information forward with the current data to predicate the remaining useful life. The use of leading indicator can reduce the experimental resource and time dramatically. Also it doesn't require large amount of reliability test data and insight of the variance in manufacturing process (Lall P. L., 2011a) (Lall P. L., 2011b) (Lall P. L., 2011c). Leading indicator based PHM is component based and doesn't affected by various usage conditions. Crack initiation, damage progression can be related to the certain leading indicators of the electronic system, such as resistance, involution of micro-structure, spectral or frequency characteristics of the electronics. Early estimation of remaining useful life (RUL) of a faulty component is at the center of system prognostics and health

management (Celaya, 2011) (Zhou, 2012) (Abdennadher, 2010). It gives operators a potent tool in decision making by quantifying how much time is left until functionality is lost.

A number of environmental stress such as vibration, thermal cycle and many other can cause initiation of cracks of solder balls. Those initiated cracks can propagate through the whole solder ball and damage the connections. Figure 58 shows a crack in a solder ball (Lall P. L., 2011b).

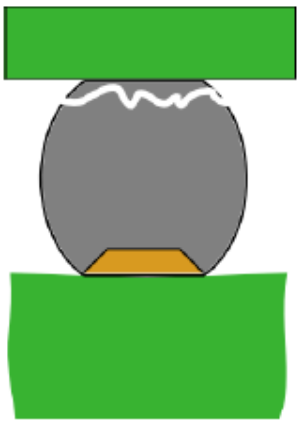

Figure 58: Depiction of a cracked solder joint as the result of applied stress. (Lall P. L., 2011b)

The flip chip and ball grid array package are widely used now. New architectures design further increases the density of interconnects. Each of these new architectures will be limited by the mechanical and environmental stresses. Mission and safety critical electronic applications motivate the development of new technology to diagnostic the health condition. Change of resistance can be related to the cracking initiation and propagation of components in electrical package such as the interface between the solder joint and solder pad (Lall P. P., 2004d) (Lall P. P., 2005b) (Lall P. P., 2006e) (Lall P. P., 2008b). Therefore, this method can be applied to the electronic package and monitor the health condition.

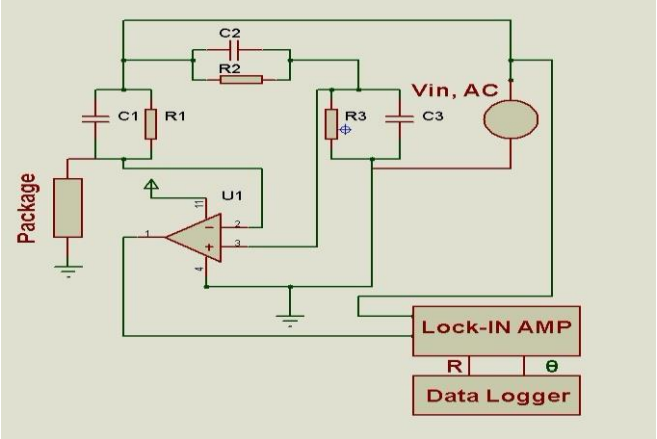


Figure 59: Resistance Spectroscopy sheme diagram.

To complete this task, the method of resistance spectroscopy (RS) was used to detect the small change of resistance. Continuity measurements with measurement devices, such as an oscilloscope, and a traditional DC multiple meter to measure the changes of resistance. Measurement devices usually don't have the adequate resolution to monitor very tiny changes of the contact resistance (Lall P. L., 2011c) (Lall P. L., 2011b) (Lall P. L., 2011a). Resistance spectroscopy is the method that can capture the small change of contact resistance (Stanford Research Systems).

Figure 59 shows the scheme diagram of the resistance spectroscopy. Capacitors C1 and C2 help eliminate stray inductances from wires running between the test board and measurement equipment. Resistors R1, R2 and R3 are used to balance the bridge. The single pole double throw relay has a small but non-negligible resistance that must be balanced out by specifying an appropriate value of resistor R3. Unlike traditional bridges, a AC voltage source drives this bridge, resulting in a sinusoidal output whose amplitude and phase shift are proportional to the resistance of the package. The lock-in amplifier performs the phase sensitive detection which effectively increases the resolution of the RS measurement. The outputs from the lock-in amplifier, the

magnitude and phase shift of the signal V out, AC, are recorded using a data logger. Figure 60 shows the data flow of resistance spectroscopy.

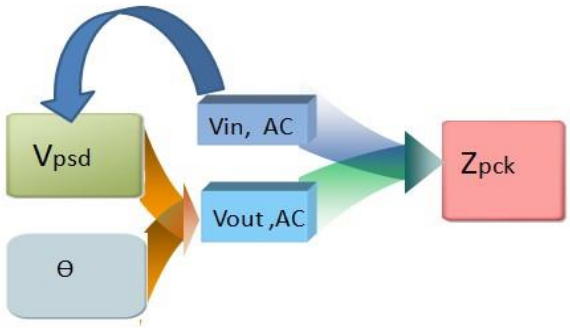


Figure 60: Data Flow of resistance spectroscopy.

Calculating the change in resistance of the package based on the measured output voltage from the bridge follows closely to that of a traditional Wheatstone bridge, but must now incorporate impedances into the calculation. Phase sensitive detection has been used to measure very small changes in resistances which are converted to very small changes in voltage $Vout_{AC}$ by the bridge. Phase sensitive detection is a unique measurement method that allows the interrogation of very small signals corrupted with noise. Detection of signals with signal to noise ratio considerably less one is possible. Implementation involves multiplying a reference signal $Vin_{AC}$, by the measured signal, $Vout_{AC}$.

The resulting signal, Vm passes through a low pass filter to remove frequency components that are not of interest. In practical realization, the low pass filter is higher order filter than depicted in the diagram. The output from the phase sensitive detection, VPSD is a signal that is proportional to the magnitude of the measured signal, $Vin_{AC}$, without noise corruption. See (Lall P. L., 2009b)

for a detailed discussion of phase sensitive detection including the derivation of pertinent equation. Since the components of the Wheatstone bridge are known quantities, the change in resistance of the package can be calculated to the micro-ohm resolution using the phase sensitive detection technique. A lock-in amplifier is traditional method for performing the switch type amplifiers or commercially available generic data acquisition hardware are alternative method. Then the value $Z_{pck}$ which equals $R_{pck}$ can be calculated with the following equation:

$$Zpck = \frac{Vin,\ AC \cdot Z3 \cdot Z1 - Vout,\ AC \cdot (Z2 \cdot Z1 + Z3 \cdot Z1)}{Vout,\ AC \cdot (Z2 + Z3) + Vin,\ AC \cdot Z2} \tag{82}$$

Commonly the leading indicator works with a prognostics algorithm that can implemented through various reiterative filters algorithm. Kalman filter is a recursive filter that can project the state vector forward with the system dynamic function (Kalman, 1960). The Kalman filter (KF) commonly employed by control engineers and other physical scientists has been successfully used in such diverse areas as the processing of signals in aerospace tracking and underwater sonar, and the statistical control of quality such as navigation (Bar-Shalom, 2004) (Bevly, 2007), tracking (Hayward, 1997), dynamic position (Balchen, 1980), auto pilots (Gueler, 1989). More recently, it has also been used in some non-engineering applications such as short-term forecasting and the analysis of life lengths from experiments, such as economic forecasting. The application domain of Kalman filter includes GPS, satellite, aircraft and ships. Kalman filter can smooth the noisy data efficiently and can be used as the noisy filter of various sensors such as accelerometers, radars, and odometer. The general filtering problem shown that, under linearity and Gaussian conditions on the systems dynamics, the general filter particularizes to the Kalman filter.

Kalman filter is a linear, discrete time, finite dimensional time-varying system that evaluates the state estimate that minimizes the mean-square error. When the system state dynamics or the observation dynamics is nonlinear, the non-optimal approach to solve the problem, in the

rage of linear filters, is the Extended Kalman filter (EKF). The EKF implements is the results of the linearization of the original non-linear dynamics around the previous state estimates. As with the original Kalman Filter, the Extended Kalman Filter uses a 2-step predictor-corrector algorithm. The first step involves projecting both the most recent state estimate and an estimate of the error covariance. The second step involves correcting the predicted state estimate calculated in the first step by incorporating the most recent process measurement to generate an updated state estimate. However, due to the non-linear nature of the process being estimated the covariance prediction and update equations use the Jacobian of the transfer function and measurement function.

The Extended Kalman Filter (EKF) has become a standard technique used in a number of nonlinear estimation and machine learning applications. These include estimating the state of a nonlinear dynamic system, estimating parameters for nonlinear system identification (Van Der Merwe R. , 2004) (Julier, 1997) (Tampère, 2007). Due to the linearization, the EKF can be viewed as the "first-order" approximations to the original system. These approximations, however, can introduce large errors in the true posterior mean and covariance of the transformed (Gaussian) random variable, which may lead to sub-optimal performance and sometimes divergence of the filter.

The advantage the UKF is unscented transformation which can calculate the statistics of a random variable which undergoes a nonlinear transformation. With a set of carefully chosen sample points and their weight, UKF can capture the true mean and variance of the state variable when it goes through no-linear system. UKF algorithm has advantages compared to other estimators (Wang, 2006) (Wan, 2000) (Van Der Merwe R. &., 2001). It is easy to implement and has higher accuracy. Due to the unscented transformation, it considers at least second order Taylor

expansion. Also, sigma point sampling is an optimal sampling approach compared with the Monte Carlo random sampling method which used in other estimators.

The particle filter has been used to track the various state vector such as damage of interconnection (Cadini, 2009), capacity degradation of battery (Saha B. &., 2009). The particle filter represents the probability distribution over the current value of each state variable using a discrete probability mass function. The discrete weighted samples of the probability density function are called particles, and the probability of each particle is denoted by its weight. In general, the particle filter is a sequential Monte Carlo technique (Doucet, 2001). The particle filter provides a general solution to the nonlinear filtering problem with arbitrarily accuracy (Saha B. K., 2011) (Jarrell, 2002) (Jiang, 2009). The reason why particle filter is picked is that a lot of methods, like Kalman filters, try to make problems more tractable by using a simplified version of the complex model. However sometimes a simplified model just isn't good enough. Particle filters, which let you use the full, complex model, rather than an approximate solution instead. The approximation of particle filter may be made as good as necessary by choosing the number of samples to be large enough: as the number of sample tends to infinity, this becomes an exact equivalent to the functional form. These random samples are the particles that propagate according to the dynamics and measurement function of the dynamic system. The algorithm of the particle filter is very simple. However, the calculation process can be computationally expensive with the increasing of particles. The advent of cheap, powerful computers over the last ten years has been key to the popular wide spread of particle filters.

# 3. EXPERIMENTAL SETUP AND MEASUREMENTS

This chapter will describe the test vehicles that used in this dissertation, the ALT conditions that are used to accelerate the lifetime test and the test standards that been followed during the measurements. Also, derivation of the math used to process the raw collected data into meaningful results is described in details.

## 3.1. TEST VEHICLES

During the experiments, there were three kinds of high power phosphor converted LED packages were used. Each package had different package structures and size. Different white color temperature LED packages were included for each package structure. All the LED package used in the experiments are commercial available in the market. The Characteristics of XR-C LED is shown in Table 3 (CREE, 2007-2013). The model of the first sample is XR-C from CREE Company.

Table 3: Characteristics of XR-C LED (CREE, 2007-2013)

| **Characteristics** | **Unit** | **Typical Value** | **Maximum Value** |
|---|---|---|---|
| Thermal resistance, junction to solder | °C/W | 12 | |
| Viewing angle | Degree | 90 | |
| Temperature coefficient of voltage | mV/°C | -4 | |
| DC forward current | mA | | 500 |
| Forward voltage (@ 350 mA) | V | 3.5 | 4.0 |
| Forward voltage (@ 700 mA) | V | 3.7 | 4.0 |
| LED junction temperature | °C | | 150 |

This high-power LED package is available in various color such as white (2600 K to 10,000 K CCT), royal blue, blue, green, amber, red‑orange and red. It has high performance and quality of light to a wide range of lighting applications, including color-changing, portable and personal, outdoor, indoor, transportation, stage and studio, commercial and emergency-vehicle lighting. Figure 61 shows the appearance of the XR-C LED package.

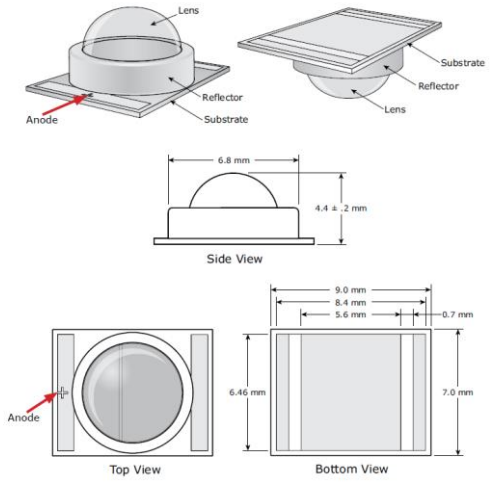


Figure 61: Package configuration of XR-C LED. (CREE, 2007-2013)

This LED package is a typical optical electrical package. It not only has the electrical connections parts, but also has the optical components which helps to extract the light from the package. The whole package is consisted of substrate, reflector, lens, solder pad and die. The die is fixed behind the lens with encapsulation. XR-C LED is a phosphor converted LED. The emitter is a blue semiconductor devices. The partial light of monochromatic emitting LED is used to excite one or several phosphors. The combination of residue light and the excited light will form the white spectrum. Figure 62 shows the white spectrum of XR-C LED with different color temperature (CREE, 2007-2013). Figure 63 (CREE, 2007-2013) shows the light spatial distribution of XR-C LED package. The light spatial distribution is mainly affected by the optical

component of the package. Therefore, different color LED has almost identical light spatial distribution.

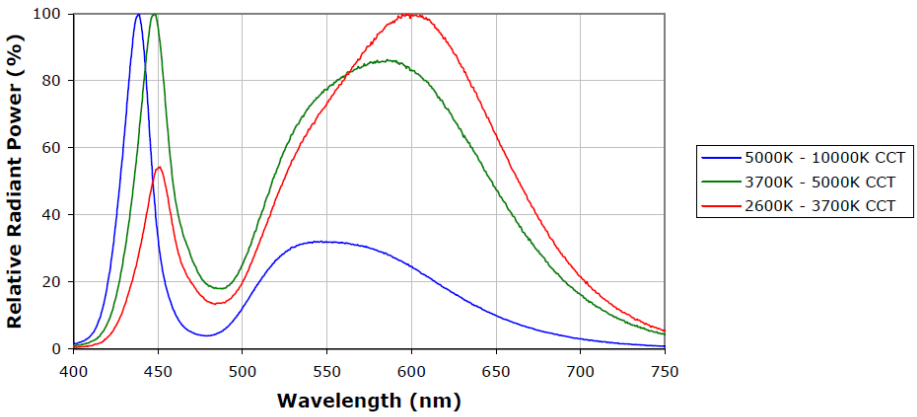


Figure 62: White Spectrum of XR-C LED package. (CREE, 2007-2013)

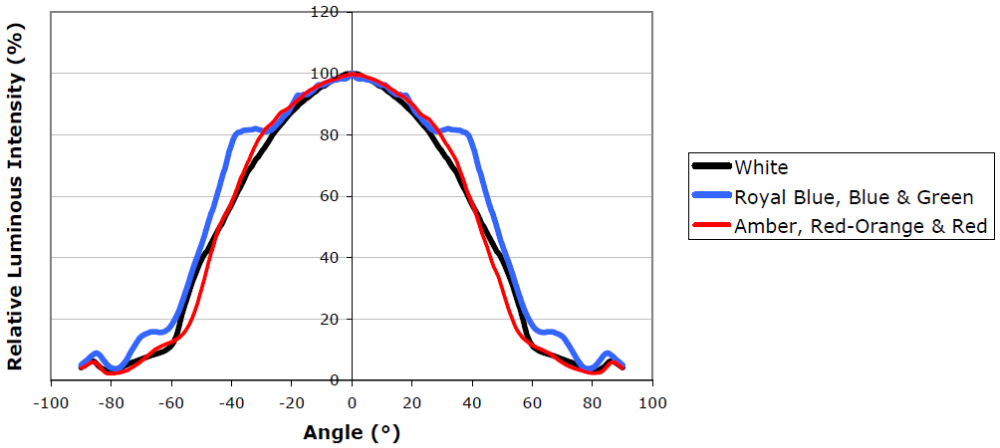


Figure 63: Light Spatical Distribution of XR-C LED Package. (CREE, 2007-2013)

XR-C LED package has lateral structure which requires two wire bonds to connect the die with the outside solder pad. To prevent damage of wire bonds from the mechanical vibration or

shock stress, the whole package was encapsulated with silicone gel-like encapsulate. Figure 64 shows the appearance of XR-C LED package and die region.

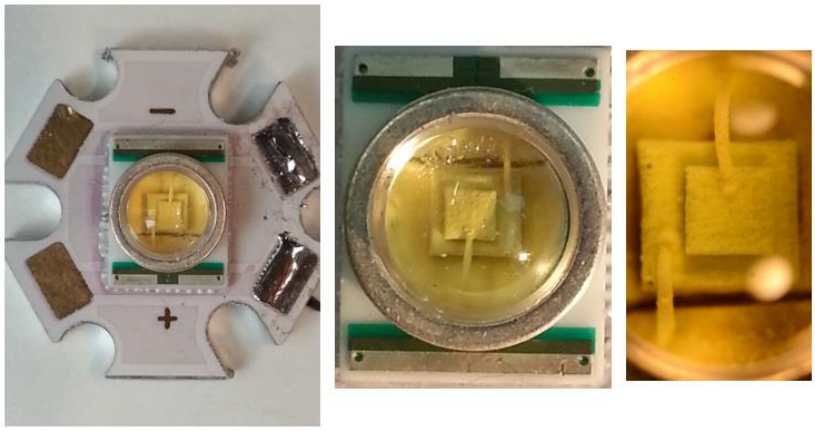

Figure 64: Phosphor converted XR-C white LED Package: Package on star board(left), Package only(Middle), Die region (Right).

Each of the LED packages was pre-soldered on a star board. They can be powered up through the solder pads that connects the electrode inside the package. The star boards can be directly fixed on the aluminum heat sink with screws which will greatly simplify the measurement process.

The second package used in the experiment is XP-G high power LED package. It delivers unprecedented levels of light output and efficacy for a single die LED. XP-G LED packages are the ideal choice for lighting applications where high light output and maximum efficacy are required, such as LED light bulbs, outdoor lighting, portable lighting, indoor lighting and solar-powered lighting. Due to the innovative design, the XP-G LED package can take much high current compared with XR-C LED. The characteristics of XP-G LEDs is shown in Table 4 (CREE, 2009-2012):

Table 4: Electrical and Thermal Characteristics of XP-G LED Package (CREE, 2009-2012)

| **Characteristics** | **Unit** | **Typical Value** | **Maximum Value** |
|---|---|---|---|
| Thermal resistance, junction to solder | °C/W | 4 | |
| Viewing angle | Degree | 125 | |
| Temperature coefficient of voltage | mV/°C | -2.1 | |
| DC forward current | mA | | 1500 |
| Forward voltage (@ 350 mA) | V | 2.9 | 3.75 |
| Forward voltage (@ 700 mA) | V | 3.05 | |
| Forward voltage (@ 1500 mA) | V | 3.25 | |
| LED junction temperature | °C | | 150 |

Compared with XR-C LED package, XP-G LED package has less thermal resistance which can greatly reduce the junction temperature inside the package with the same heat sink. Also, the permitted forward current is three times larger than XR-C LED. At the same forward current, the voltage is less than XR-C LED also. As a result, the luminous efficiency of XP-G package is much higher than XR-C package. XP-G LED is also a phosphor converted white LED package. The phosphor binder layer is dispensed on the top of the blue light emitter. The XP-G LED package has different white temperature and color render index. Typical CRI for cool white (5000 K - 8300 K CCT) is 70. Typical CRI for Neutral White (3,700 K - 5,300 K CCT) is 75. Typical CRI for Warm White (2,600 K - 3,700 K CCT) is 80. The CRI of warm white LED is higher than LED packages of higher CCT value. Figure 65 (CREE, 2009-2012) shows the dimension of XP-G LED package. Figure 66 (CREE, 2009-2012) shows the radiant spectrum of XP-G LED package with different color temperature.

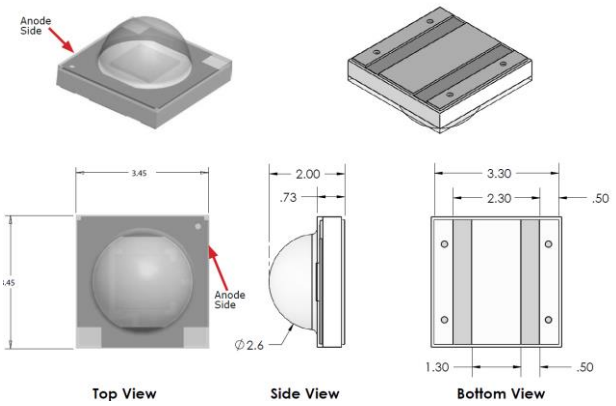


Figure 65: Mechanical Dimension of XP-G LED package. (CREE, 2009-2012)

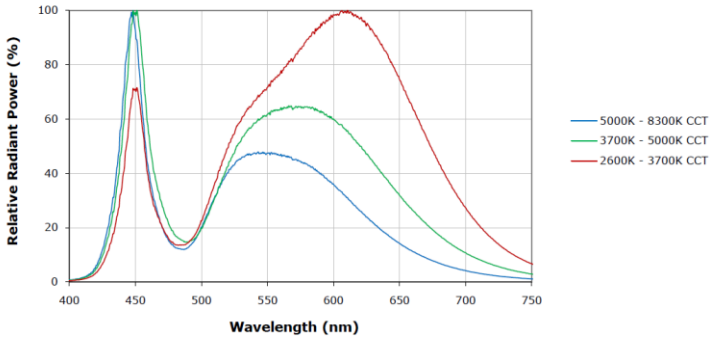


Figure 66: Radiant spectrum of XP-G LED with different color temperature. (CREE, 2009-2012)

The light spatial distribution of XP-G LED package is Lambertian emission pattern. The light intensity of the package in air follows a cosine dependence on the angle. The intensity is the highest for the emission normal to the semiconductor surface. At the angle of 60°C, the intensity decreases to half of its maximum value. The emission pattern of XP-G LED package is shown in Figure 67 (CREE, 2009-2012):

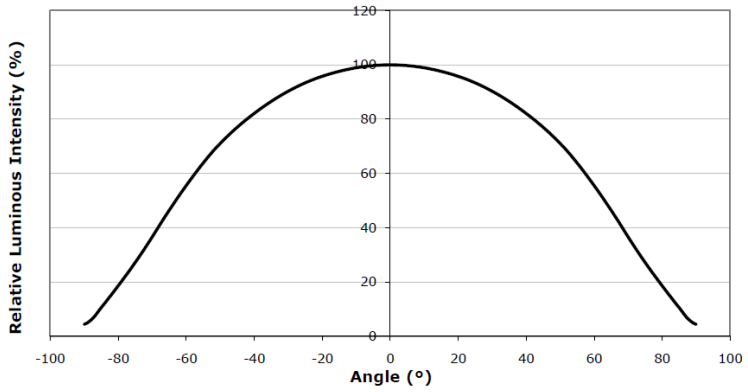


Figure 67: Light emission pattern of XP-G LED package. (CREE, 2009-2012)

XP-G LED is a thin film package which means the real functional die is only 4-5μm thick, because the original epitaxial growth substrate is removed by laser lift-off process. XP-G LED package structure is vertical compared with XR-C LED package whose structure is lateral.. Usually the epitaxial layer has three parts. The bottom layer is n-type GaN. On the top of n-type GaN, multiple layer of quantum well (MQW) active region was built. P-type GaN was on the top of the epitaxial layer. After the growth of the epitaxial layer, a high reflective metal contact was deposited on the p-side of the wafer as p contact by electron-beam evaporation. After that, the p side was bonded to an intermediate conductive substrate. Laser assisted lift off help to remove the sapphire substrate and expose the n-type GaN surface. Now, the epitaxial layer is totally upside down with n-type GaN of the top. Wire bond and patterned metallic n contact was added to connect the chip with the substrate. Figure 68 shows the diagram of the XP-G LED package.

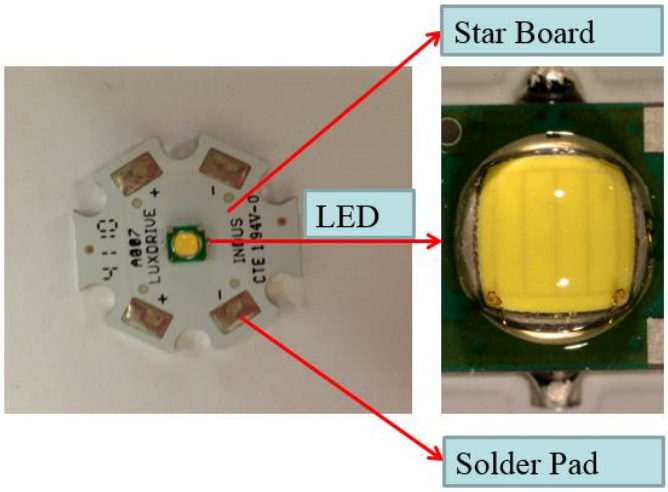


Figure 68: XP-G LED package structure.

The last LED package used in the experiment is XT-E LED package. It is the latest package structure in the market. XT-E White sets the new standard for high performance and dramatically lowers system cost. It offers high performance and quality of light to a wide range of lighting applications, including remote-phosphor, color-changing, portable and personal, outdoor, indoor-directional, transportation, stage and studio, commercial and emergency-vehicle lighting. XT-E white LED package is a phosphor convert LED also. By changing the phosphor thickness and density of phosphor particles. Various white color temperature could be obtained. It is available in high CRI warm white color and the cool white efficiency is up to 148lm/W at 85°C, 350mA. The characteristics of XTE LEDs is shown in Table 5 (CREE, 2011-2016):

Table 5: Electrical and optical characteristics of XTE LED (CREE, 2011-2016)

| **Characteristics** | **Unit** | **Typical Value** | **Maximum Value** |
|---|---|---|---|
| Thermal resistance, junction to solder | °C/W | 5 | |

| | | | |
|---|---|---|---|
| Viewing angle | Degree | 115 | |
| Temperature coefficient of voltage | mV/°C | -2.5 | |
| DC forward current | mA | | 1500 |
| Forward voltage (@ 350 mA) | V | 2.85 | 3.4 |
| LED junction temperature | °C | | 150 |

Figure 69: Spectrial distribution of XTE LED package shows the radiant spectrum of XTE LED package with different whole color temperature.

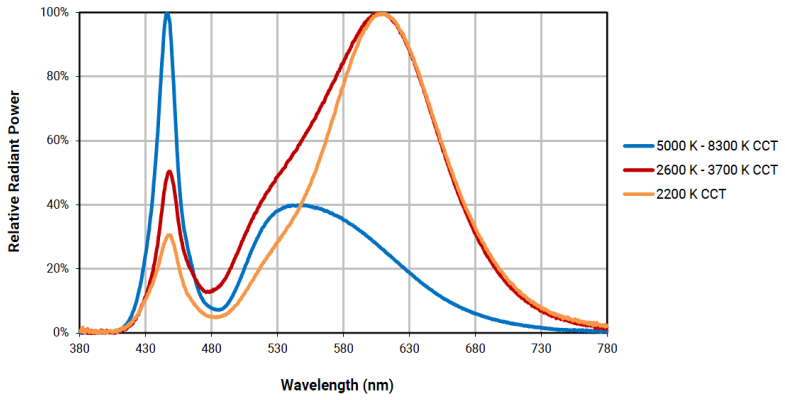


Figure 69: Spectrial distribution of XTE LED package. (CREE, 2011-2016)

XT-E is thin film flip chip (TFFC) package. The TFFC process involves removal of the substrate and roughening of the chip's light-emitting surface to improve light output efficiency. TFFC design is optically and thermally superior to the vertical thin film and lateral structure. The most difference between XT-E and other LED package is that XT-E doesn’t have wire bons. The flip chip structure uses solder bump rather than wire bond to connect the die with the substrate.

Figure 70 (CREE, 2011-2016) shows the size of XT-E LED package and Figure 71 shows the appearance of XTE LED package and the die region.

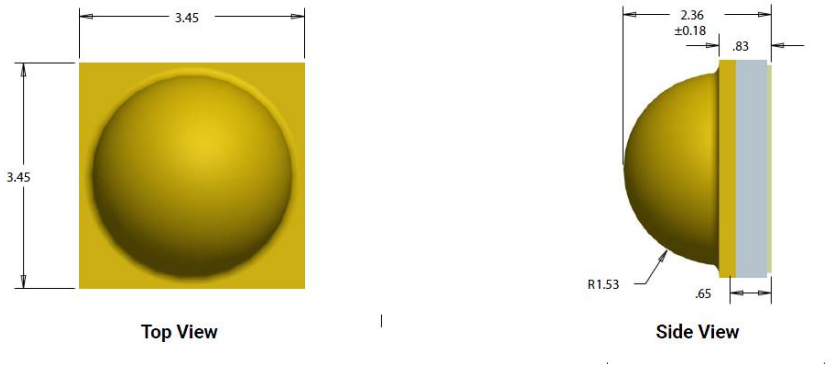


Figure 70: Dimensions of XTE LED package. (CREE, 2011-2016)

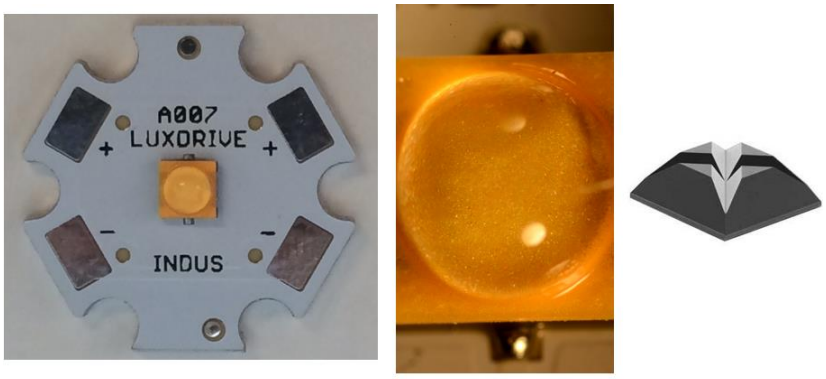


Figure 71: Appearance of XTE LED package. Package and star board (Left), LED package(Middle), Die region (right). (CREE, 2011-2016)

The light spatial distribution of XTE LED package is also Lambertian emission pattern. The light intensity of the package in air follows a cosine dependence on the angle. The intensity is the highest for the emission normal to the semiconductor surface. At the angle of 60°C, the intensity decreases to half of its maximum value. The emission pattern of XP-G LED package is shown in Figure 72 (CREE, 2011-2016):

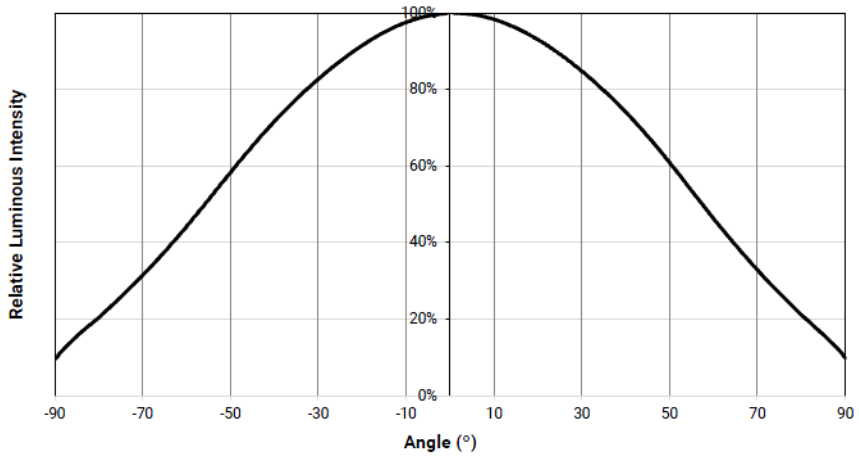


Figure 72: Light spatial distribution of XTE LED. (CREE, 2011-2016)

## 3.2. TEST CONDITIONS

ALT has been adopted to accelerate the degradation process of LED packages in order to accumulate the degradation data for the modeling of lifetime prediction. Also, ALT can capture the failure modes and mechanisms much quicker than normal operational conditions.

### 3.2.1. HIGH TEMPERATURE STORAGE LIFE TEST (HTSL)

The IES LM-80-08 (LM80) (IES, 2008b) is a LED lumen maintenance test method that developed by Illuminating Engineering Society of North America (IESNA). It provides methods of the measurement of lumen maintenance of LED package, arrays and modules. This standard methodology would allow customers to evaluate and compare the lumen maintenance of LED components from different companies. Lumen maintenance is the luminous flux remaining output (typically expressed as a percentage of the initial output) at any elapsed operating time. LM80 requires the testing of LEDs operating at a minimum of three case temperatures (55°C, 85°C and a case temperature selected by the manufacturer), with the same electrical drive current.

During the thermal life test, LED packages were placed in a temperature controlled thermal chamber (55°C, 85°C and third temperature) and powered up with external constant current driver sources. At each readout time, LED packages were taken out of the thermal chamber to cool to room temperature for both colorimetric and photometric measurement. Figure 73 shows the HTSL test condition for this dissertation.

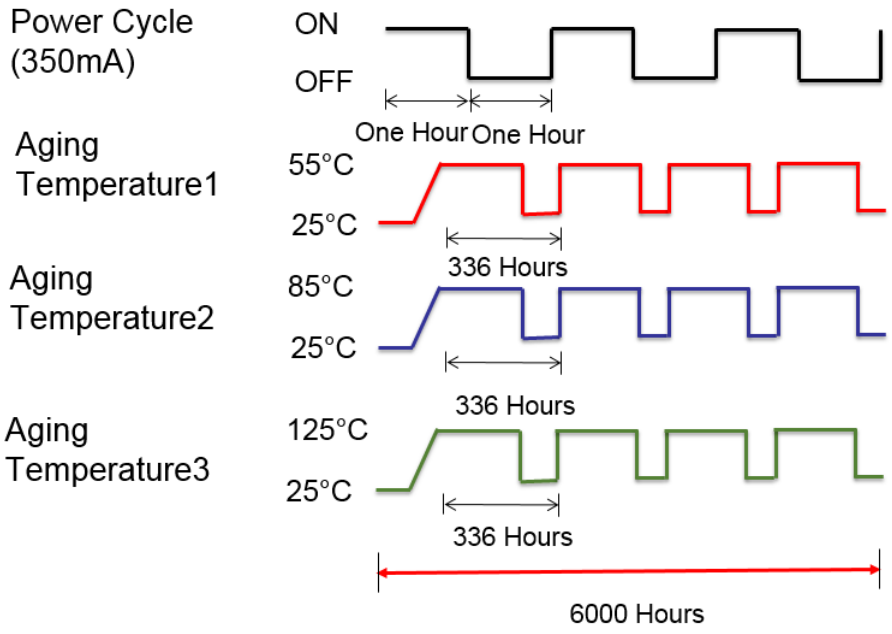


Figure 73: HTSL Test Conditions.

Per the LM80, the case temperature and drive current selected by the manufacturers should represent their expectation for customer's applications and should be within the recommended operating temperature range. In this dissertation, the forward current is selected as 350mA and the highest case temperature is 125°C which is very common to see in the automobile industry. During the test, the ambient temperatures is controlled to ±2°C during life testing by a THERMOTRON thermal environmental chamber. Humidity inside the chamber is maintained less than 65% RH

throughout the life test. LM 80 test requires the test duration of at least 6000 hours with data collection at a minimum of every 1000 hours. In this dissertation, the data was collected every two weeks which is 336 hours which is in the range of requirement. At each readout time, the LEDs are taken out of the thermal chamber to cool to room temperature for photometric measurement. Then LED packages were put back inside the thermal chamber for further life test. Figure 74 shows the thermal chamber and Figure 75 shows the LED packages during the HTSL test.

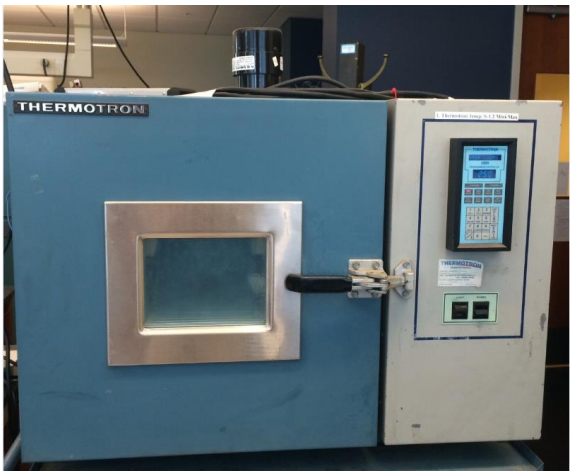


Figure 74: Thrmal Environmental Chamber used in the HTSL.

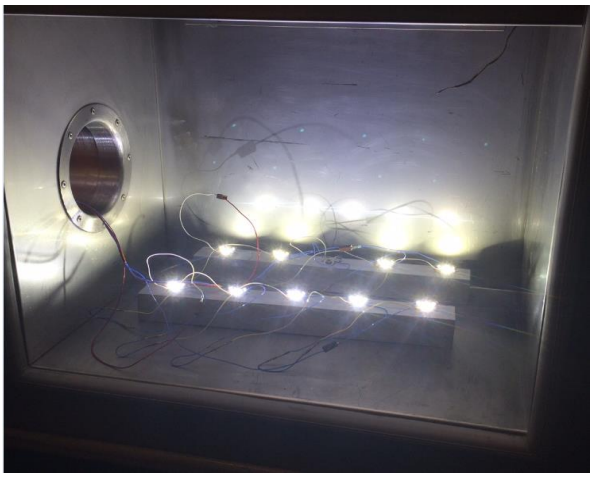

Figure 75: LED packages under HTSL Test.

LM 80 test standard is the base of LM-84 test method which measures the luminous flux and color maintenance of LED lamps, light engines and luminaires. The LM 80 test standard requires that the measurement process should follows LM-79-08 electrical and photometric measurement of solid state light products.

### 3.2.2. WET HIGH TEMPERATURE OPERATING LIFE TEST (WHTOL)

In the LM-80 test, only temperature is involved and relative humidity effect are not considered. In LED-based luminaire applications, some are operated in the harsh environment. During the operation, the LED package not only experiences the high bias current and ambient temperature, but also the humidity around the package, especially for the road lighting and automobile lighting.

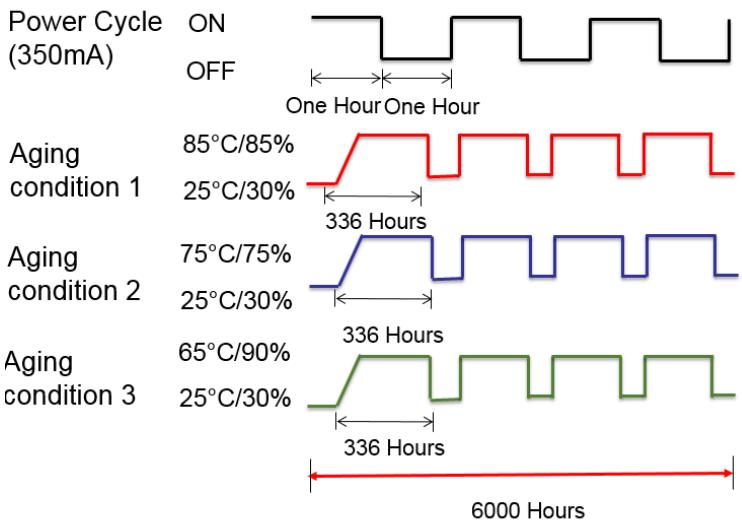


Figure 76: WHTOL Test conditions.

Proper design of LED products for different environment requires the understanding of the various effects on LED package from thermal stress and humidity (Chou, 2012). In this

dissertation, a steady-state temperature-humidity life test with an applied electrical bias was performed to investigate the reliability of the high-power phosphor converted white LED in a humid environment. This ALT test environment consisted of several different temperature and humidity combination in order to investigate humidity related failure mechanisms of the high-power phosphor converted white LED packages. Figure 76 shows the test conditions for WHTOL test.

During the experiment, a temperature and humidity environmental chamber was used to accelerate the life test of the LED packages. LED packages were placed in the temperature and humidity controlled chamber (85°C/85%, 75°C/75% and 65°C/90%). LED packages were biased in series with a constant current power source. At the same time, test samples were electrically power biased on and off at an interval of one hour in the environmental chamber. At each readout time, LED packages were taken out of the thermal and humidity chamber to cool to room temperature for photometric measurement. Then LED packages were put back inside the thermal and humidity chamber for further life test. Figure 77 shows the temperature and humidity chamber and Figure 78 shows the LED packages powered up inside the chamber.

Figure 77: Temperature and Humidity Chamber used in WHTOL Test.

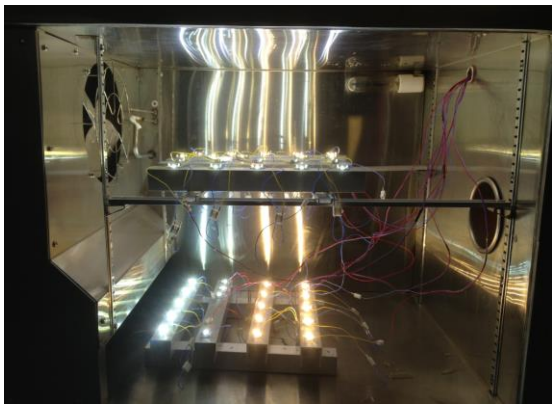

Figure 78: LED packages powered up inside the Temperature and Humidity Chamber.

## 3.3. MEASUREMENT

At each readout time, LED modules were taken out of the chamber and cooled down to room temperature first. In each measurement, LED packages were mounted on a fin heat sink which helps lower the junction temperature during the test in the integrating sphere. At the same time, the LED packages were powered up with the power cord inside the integrated sphere and the forward current is 350mA. The maximum forward current of the tested LED packages range from 500-15000mA and the performed current is among the functional range according to the datasheet.

### 3.3.1. PHOTOMETRIC PROPERTIES

The basic photometric quantities include luminous flux, luminous intensity, etc. Spectroradiometry is the basic method of radiometry to measure the spectral concentration of the given light source. Then the desired photometric quantity such as luminous flux can be calculated. The measurement can be made by a photometer that can be rotated around a lamp. Such an assembly is called a goniophotometer. There are many different designs of goniophotometer that can sampling the points of measurements (Walsh, 1958, Krochmann and Marx, 1969, Jones and Berry, 1970, Brown, 1979) (DeCusatis, 1997). Goniophotometers are usually large instruments, due to its working principle. Another method to measure the radiometric properties of lamp is

called integrated sphere. If a source in placed inside a hollow sphere collated internally with perfect diffusing material, the illuminance on any part of the surface due to the light reflection is the same and proportional to the luminous flux emitted by the measured light sources:

$$E = \frac{\rho * P_0}{4 * \pi * r^2 * (1 - \rho)} \tag{83}$$

Where E is the illuminance which is defined as the total luminous flux received per unit area of sphere wall due to reflection and multiple reflection. P is total luminous flux emitted by the light source inside the sphere. r is the radius of the sphere and ρ is the reflectance of the sphere wall.

The radiometric properties measurement in this dissertation was performed by utilizing integrated sphere and spectroradiometer. Figure 79 shows the integrated sphere, spectroradiometer and connectors of LED package.

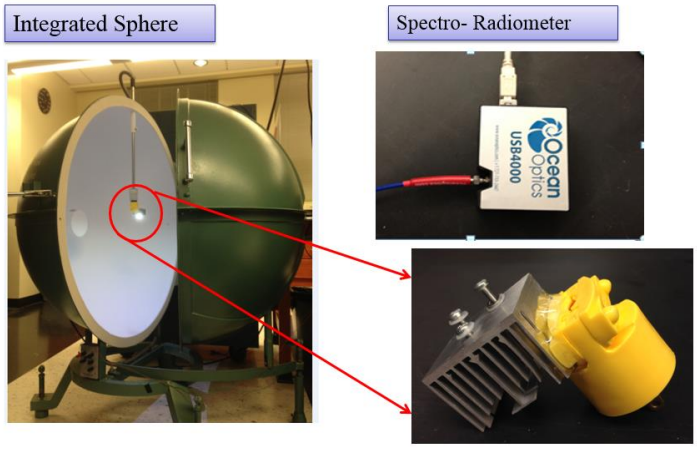


Figure 79: Integrated Sphere Measurement System.

Integrating sphere system has advantage of easy operation and quick measurement. Air movement is minimized and the temperature inside the sphere is not subject to the ambient temperature outside of the sphere. Spectroradiometry is utilized to measure the absolute radiant

flux of the LED packages at each wavelength, from which luminous flux, radiant power, correlated color temperature, chromaticity coordinates in the CIE chromaticity diagram can be calculated.

LM-79-08 “Electrical and Photometric Measurement of Solid State Light Product” (IES, 2008a) has been used as the guideline during the experiment. This approved method gives a detailed description of procedures and precautions to be followed in performing reproducible measurement of absolute radiant flux which can be used to calculate the luminous flux. Also, photometric properties like chromaticity coordinates, color temperature and color shift distance are recoded as well at each readout time. During the measurement, certain conditions must be satisfied, especially the ambient test temperature, because photometric values and electric characteristics of LED product are all sensitive to temperature and air movement. According to the test standard, the ambient temperature during the test should be maintained at 25°C±1°C, measured at a point less than1m from the LED module. The forward current applied to the test LED should be regulated to within ±2percent of the specified value. Before the test, the LED modules should be running long enough to reach luminous output and thermal stabilization.

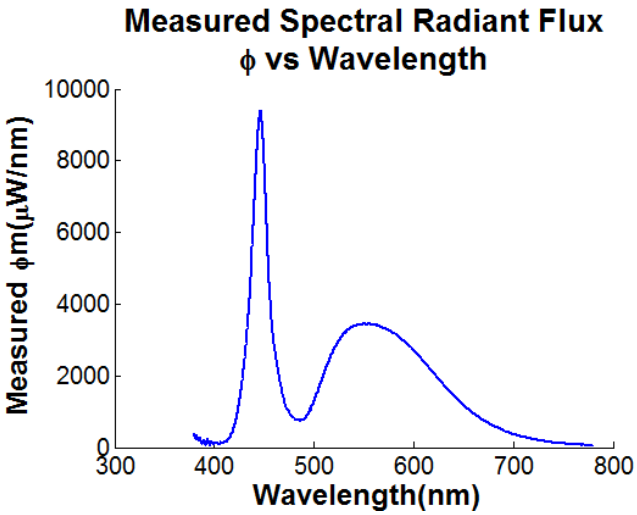


Figure 80: Measured Spectral Radiant Flux.

The integrating sphere uses what is called 4π geometry for SSL devices that emit light omnidirectional or forward directional by utilizing the entire surface of the integrating sphere. The IES LM-79-08 (IES, 2008a) (Wyszecki, 1982) standard states that the total spectral radiant flux, Φtest (λ) [W/nm], of an SSL product under test can be obtained by comparing it to a known reference or calibration standard's. Therefore, before the test, the instrument (integrating sphere plus spectroradiometer) must be calibrated against a reference standard calibrated for total spectral radiant flux (IES, 2008a). Since the integrating sphere is included in this calibration, the spectral throughput of the sphere need not be known. The total spectral radiant flux ΦTEST (λ) of the light emitting diode under test is obtained by comparison to that of a reference standard $\Phi_{REF}$ (λ). The calculation of the absolute radiant flux $\Phi_{TEST}$ (λ) is given:

$$\Phi_{Test}(\lambda) = \Phi_{REF}(\lambda) * \frac{y_{TEST}(\lambda)}{y_{REF}(\lambda)} \tag{84}$$

Where $y_{TEST}$ (λ) and $y_{REF}$ (λ) are the spectroradiometer reading for the LED packages under test and for the standard reference lamp, respectively (IES, 2008a). Figure 80 shows a measurement of absolute radiant flux.

In the calculation, the self-absorption correction shall be considered. Self-absorption is the effect, in which the response of the sphere system changes due to the absorption of light by the lamp itself in the sphere. Errors can occur if the size and shape of the test light source are different from those of the standard light source. The self-absorption correction is critical, since the physical size and shape of the LED packages under test are typically very different from the standard reference lamp in size and shape. The self-absorption can be found through a comparison of an auxiliary lamp. The self-absorption factor is given by:

$$\alpha(\lambda) = \frac{y_{aux,TEST}(\lambda)}{y_{aux,REF}(\lambda)} \tag{85}$$

Where $y_{aux,TEST}(\lambda)$ and $y_{aux,REF}(\lambda)$ are the spectroradiometer reading for the auxiliary lamp when the LED packages in the integrated sphere and for auxiliary lamp when the standard reference lamp in the integrated sphere, and $\alpha(\lambda)$ is the self-absorption factor measured using an auxiliary lamp as described in LM-79 (IES, 2008a). Please note that both the LED packages and standard reference lamp should be turned off during the measurement of auxiliary lamp. Figure 81 shows a sample of absorption factor:

The correlated absolute radiant flux of LED package with self-absorption factor can be calculated by multiplying the measured absolute radiant flux with self-absorption correction factor:

$$\Phi_{Test}(\lambda) = \Phi_{REF}(\lambda) * \frac{y_{TEST}(\lambda)}{y_{REF}(\lambda)} * \frac{1}{\alpha(\lambda)} \quad (86)$$

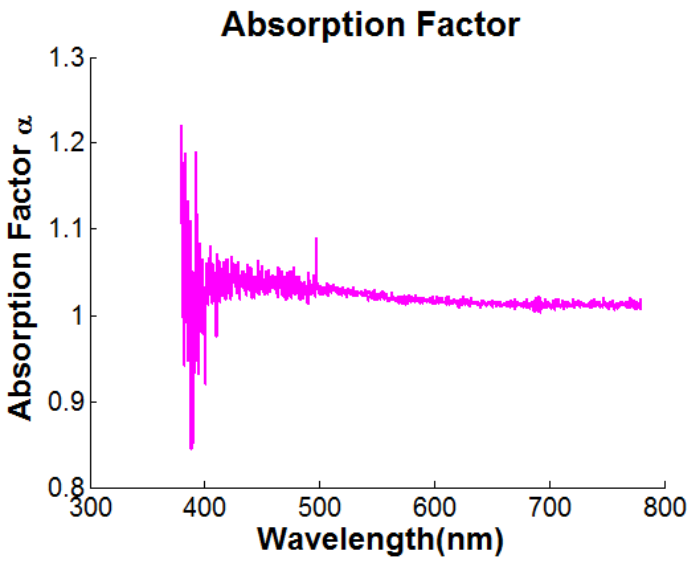


Figure 81: Absorption Factor of LED packages.

### 3.4. LUMINOUS FLUX

The luminous efficiency function describes the average spectral sensitivity of human visual perception of brightness. It is based on subjective judgments of which of a pair of different-colored lights is brighter, to describe relative sensitivity to light of different wavelengths. The CIE

luminous efficiency function is a standard function established by the CIE and can be used to convert radiant energy into visible luminous energy.

The total luminous flux (Lm) of the LED packages can then be calculated by the multiplying the measured absolute radiant flux with the wavelength dependent luminous efficiency function (Eye sensitivity function) V(λ). Then, this wavelength dependent vector is integrated over the visible spectrum range (380nm- 780nm) to get the energy. At last, the result will be scaled by $K_m$ (683 lm/W) which is the maximum spectral luminous efficacy. The total luminous flux can be calculated by (DeCusatis, 1997) (IES, 2008b) (Wyszecki, 1982):

$$\Phi_{TEST}(lm) = K_m * \int_{380}^{780} \Phi_{TEST}(\lambda) * V(\lambda) * d\lambda \tag{87}$$

### 3.5. RADIANT POWER

Radiant power is the amount of power (light) emitted from a source irrelevant of the direction it is emitted, expressed in Watt (W). Applied to the LED packages, it is known as spectral power and defines the total amount of power in Watts emitted for each wavelength in each direction. The radiant power of LED package can be calculated by the integration of the absolute radiant flux over the visible spectrum range (380nm- 780nm). The calculation is given:

$$P = \int_{380}^{780} \Phi_{TEST}(\lambda) * d\lambda \tag{88}$$

Wall-plug efficiency of LED package is the ratio of the radiant power (the total optical output power of the LED package, measured in watts) and the electrical input power which is the product of forward current and forward voltage.

$$\eta = \frac{P}{I * V} \tag{89}$$

The efficiency of a LED package can be measured in a simplified version (lumens per watt). This method calculates how many lumens can be generated in 1 watt energy. The more lumens per watt, the better the light source in terms of energy efficiency.

$$\eta = \frac{\Phi(LM)}{I * V} \tag{90}$$

### 3.5.1. COLORIMETRICAL PROPERTIES

The quantification of color is referred to the science of color (colorimetric). It is the science that is used to describe and quantify the perception of light by the human eye in term of color (Schanda, 2007). Therefore, it associates with the vision of human eyes very closely. The human sense of vision is very different from the human sense of hearing. Mixing two monochromatic color will appear to one color for human vision. Humans are unable to recognize the dichromatic color of that color.

## 3.6. TRISTRIMULUS VALUES

Light creates different levels of excitation of the red, green, and blue cones in the eye. Human has slightly different sensation of color by a particular color source. For this reason, the International Commission for Illumination (Commission Internationale del'Eclairage, CIE) has standardize the measurement of color by means of color matching functions (Wyszecki, 1982) (CIE, 2004a).

The color matching function is obtained by experiment. A visible monochromatic color is matched by the mixing of three colors (red, blue and green). A human subject makes these two colors to appear the same by adjusting the relative intensity of the red, blue and green light. Then, the color matching function could be obtained through the matching process across the whole visible spectrum. The color matching functions reflect the fact that human vision process color in

a way of trichromacy. The color of any light source could be a combination of three colors which are red, blue and green. The red color match function is represented as $\bar{x}(\lambda)$. The green color match function is represented as $\bar{y}(\lambda)$. The blue color match function is represented as $\bar{z}(\lambda)$. Also, the color match function of green is the same with eye sensitivity equation of human $V(\lambda)$. When judging the relative brightness of different colors of equal power, humans tend to perceive light within the green parts of the spectrum as brighter than red or blue light. CIE has two specifications for a standard observer: the original 1931 specification and a revised 1964 specification. In both cases the standard observer is a composite made from small groups of individuals (about 15-20) and is representative of normal human color vision. Figure 82 (Wyszecki, 1982) shows the color match function of these two versions.

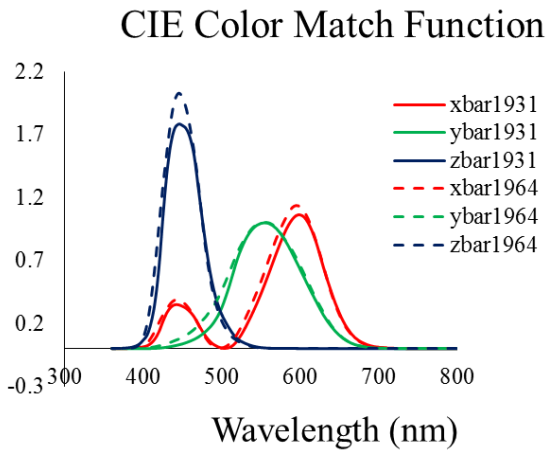


Figure 82: 1931 and 1964 Color Match Function. (CIE, 1924) (Wyszecki, 1982)

For a given light source, the tristimulus values can be calculated with the absolute radiant flux, reflectance spectrum and color match function. The calculated tristimulus values are the intensity of the three-color required to match the color of the tested LED package. (Schubert, 2006) (CREE, 2013) (CIE, 2004a) (Schanda, 2007) (Westland, 2004) (Wyszecki, 1982) (CIE, 2004b)

(CIE, 1995). The CIE 1931 tristimulus values are called X, Y, and Z. CIE XYZ tristimulus values can be calculated by the integration of the product of the absolute radiant flux Φ(λ) with the standard observer functions $\bar{x}$, $\bar{y}$, $\bar{z}$ . The integration is approximated by summation, thus:

$$X = k * \int_{380}^{780} \Phi_{TEST} * \bar{x}(\lambda) * d\lambda = \sum_{\lambda=380}^{\lambda=780} k * \Phi_{TEST} * \bar{x}(\lambda) * \Delta\lambda \quad (91)$$

$$Y = k * \int_{380}^{780} \Phi_{TEST} * \bar{y}(\lambda) * d\lambda = \sum_{\lambda=380}^{\lambda=780} k * \Phi_{TEST} * \bar{y}(\lambda) * \Delta\lambda \quad (92)$$

$$Z = k * \int_{380}^{780} \Phi_{TEST} * \bar{z}(\lambda) * d\lambda = \sum_{\lambda=380}^{\lambda=780} k * \Phi_{TEST} * \bar{z}(\lambda) * \Delta\lambda \quad (93)$$

$$k = \frac{100}{\int_{380}^{780} E(\lambda) \cdot \bar{y}(\lambda) \cdot d\lambda} \quad (94)$$

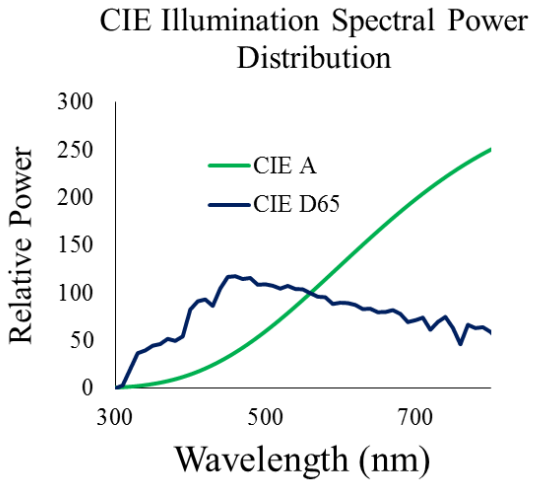


Figure 83: CIE Illumination Spectral power distribution. (CIE, 1931) (Wyszecki, 1982)

The normalizing factor k is introduced such that Y = 100 for a sample that reflects 100% at all wavelengths: recall that Y is proportional to the luminance of the stimulus. The introduction of this normalization is convenient since it means that relative, rather than absolute. In this equation, E (λ) is the relative spectral power distribution of a CIE standard illuminant whose

spectral power distribution is published. Figure 83 shows the spectral power distribution of illuminant A and D65 (CIE, 1995).

During the calculation of tristimulus values, the CIE standard illuminant A was used. Standard illuminants provide a basis for comparing images or colors recorded under different lighting. Illuminants A, B, and C were introduced in 1931, with the intention of respectively representing average incandescent light, direct sunlight, and average daylight. Illuminants D represent phases of daylight, Illuminant E is the equal-energy illuminant, while Illuminants F represent fluorescent lamps of various composition. Once the tristimulus values are calculated out, color coordinates and correlated color temperature can be obtained to describe the colormetric properties of LED packages (Schanda, 2007) (Westland, 2004) (Wyszecki, 1982).

## 3.7. COLOR SPACE

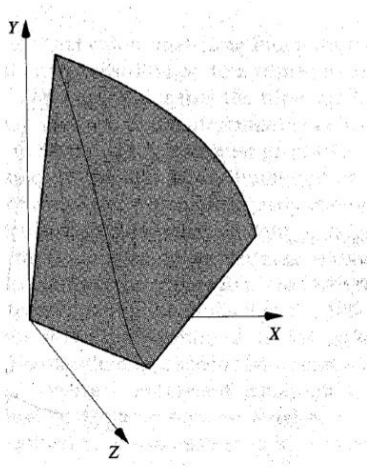


Figure 84: CIE XYZ Color Space. (Wyszecki, 1982)

The three-dimensional color space CIE XYZ is the basis for all color management systems. This color space contains all perceivable colors - the human gamut. Many of them cannot

be shown on monitors or printed whose gamut is smaller than the human gamut (Wyszecki, 1982). Figure 84 shows the 3D chromaticity diagram.

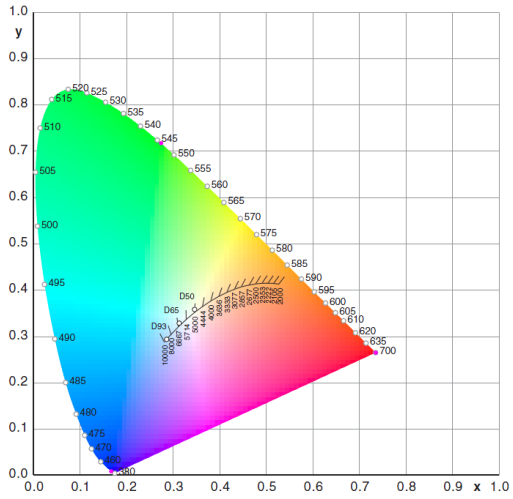


Figure 85: 1931 Chromaticity Diagram with the Planckian locus and isothermal lines.

CIE XYZ is based on a direct graph of the signals from each of the three types of color sensors in the human eye. These are also referred to as the X, Y and Z tristimulus values. The CIE XYZ tristimulus values are assigned to the red, green and blue curves respectively. XYZ is typically used to report the spectral response of a sample measured by a colorimeter or a spectrophotometer. However, CIE XYZ system is not so useful for humans to describe color, because irregular 3D volume shape is very difficult to understand. It would be much easier if the 3D color system can be transferred into a 2D color space. Figure 85 shows the 1931 chromaticity diagram.

This transformation process can be done by normalizing X, Y, Z with the total light intensity (X+Y+Z).

$$x = \frac{X}{X + Y + Z} \tag{95}$$

$$y = \frac{X}{X + Y + Z} \tag{96}$$

$$z = \frac{X}{X + Y + Z} \tag{97}$$

Since x+y+z=1, all color can be represented in a plane consisted of x and y axis. Each pair of (x, y) coordinate represent a unique color in the 3D X Y Z color space. This transformation transfer the 3D color space into a 2 D color space which is much easier to interpret. The CIE 1931 chromaticity diagram can be used to map a device's color gamut showing the range of colors that can be reproduced against the visible spectrum. Therefore, it can be used to compare different devices.

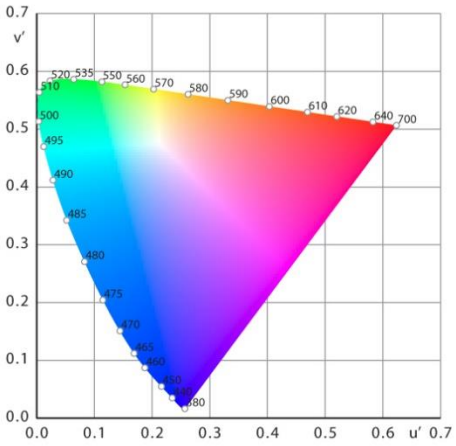


Figure 86: CIE 1976 chromaticity diagram.

Plotting x and y out will give the 1931CIE chromaticity diagram. However, this representation allocates too much area to the greens confining most of the apparent color variation to a small area. The CIE 1976 chromaticity diagram is the transformation of CIE 1931 chromaticity diagram. After the transformation, the color is much more uniformly distributed. Figure 86 shows the CIE 1976 chromaticity diagram.

In the 1976 the color space is defined by a pair of coordinates (u', v') which can be calculated from both tristimulus values (X Y Z) and 1931 (x, y):

$$u' = \frac{4*X}{X+15*Y+3*Z} = \frac{4*x}{-2*x+12*y+3} \tag{98}$$

$$v' = \frac{9*Y}{X+15*Y+3*Z} = \frac{9*y}{-2*x+12*y+3} \tag{99}$$

The CIE 1976 chromaticity diagram is mostly used to calculate correlated color temperature, where the isothermal lines are perpendicular to the Planckian locus. All these color space contain the same color information. They are just scaled differently. The big advantage attributed to the 1976 diagram is that the distance between points on the diagram is approximately proportional to the perceived color difference since color in the diagram is much more evenly distributed.

### 3.8. COLOR SHIFT DISTANCE

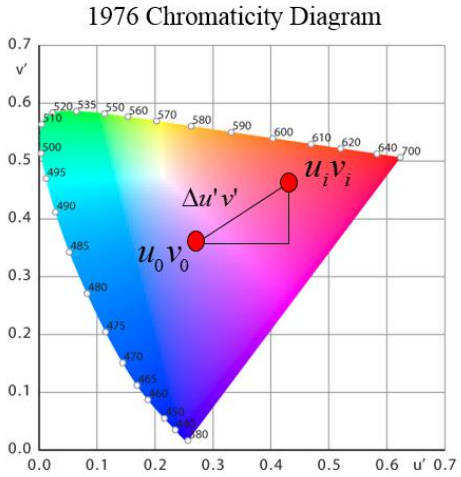


Figure 87: Color shift distance in 1976 Chromaticidy Diagram.

Similar to the 3-D color space, the color difference in 2-D space can be determined using the Euclidean distance between the initial, pristine value and the one obtained at each sampling

period. The 2D color shift distance usually calculated under 1976 CIE chromaticity diagram. Color shift distance calculation is given as:

$$\Delta u'v' = \sqrt{(u_i - u_0)^2 + (v_i - v_0)^2} \tag{100}$$

Where $u_i$ and $v_i$ are the measurement of period I and $u_0$ and $v_0$ are the initial color coordinates in the 1976 chromaticity diagram. Figure 87 illustrates the calculation process of the Euclidean distance.

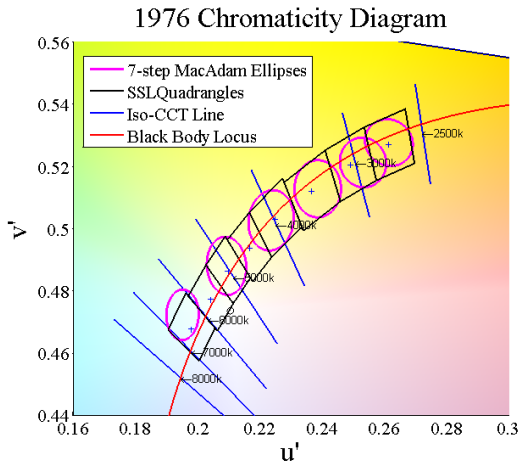


Figure 88: ANSI tolerance for CFL and SSL.

In CIE (International Commission on illumination) 1976 u' v' chromaticity space, each LED color was represented by unique u', v' coordinates. The American National Standard (ANSI) [19] defines the specifications for the chromaticity of solid state lighting products. It specifies the range of the chromaticity recommended for general lighting with SSL products. The existing chromaticity standard (ANSI C78.376) for compact fluorescent lamps (CFL) is based on six nominal correlated color temperatures. For SSL products, quadrangles are used for the chromaticity criteria. If the color coordinates shift out of the designated quadrangle, the color

change is visible for human. Figure 88 shows the ANSI tolerance for CFL and SSL in 1976 chromaticity diagram.

### 3.9. CORRELATED COLOR TEMPERATURE

White light usually has a broad spectrum extending over the entire human visible range. A reference spectrum of white light is the sun light. However, the sun's light changes with time, weather and other reasons. It is desirable to define an independent standard for white light.

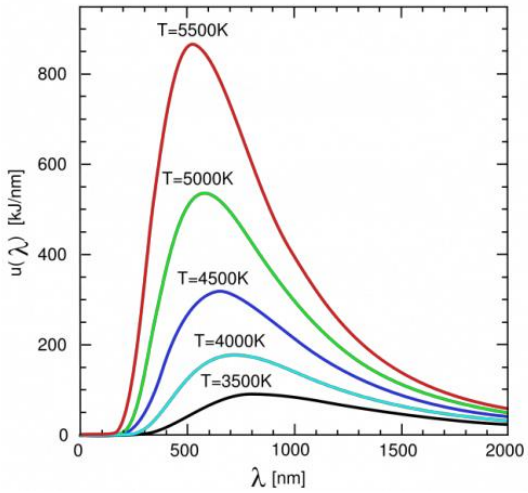


Figure 89: Spectrum of black body with different temperatures. (Wikipedia, 2006)

The Planckian black-body radiant spectrum is used as the standard. The black-body spectrum only depends on the temperature of the body. The black-body spectrum is calculated by Max Plank and is given:

$$I(\lambda,T) = \frac{2 * h * c^2}{\lambda^5 * (\exp(\frac{h * c}{\lambda * K_b * T}) - 1)} \tag{101}$$

Where T is the temperature of the black body, c is the speed of light (2.998 x $10^8$ m/s), h is the Planck constant (6.626 x $10^{-34}$ J·s), k is the Boltzmann constant (1.381 x $10^{-23}$ J/K) and λ is

wavelength. The black body Planckian spectrum of different temperature is shown in Figure 89.The peak wavelength of radiation from a black body at temperature T is given by Wien's law:

$$\lambda_{\max} = \frac{2880\mu m * K}{T} \tag{102}$$

At low temperature, most of the spectrum is located at the infrared region. As the temperature increases, the maximum of radiant shifts to the visible spectrum region. The Tristimulus values of the black body radiant at temperature of T can be calculated as:

$$X(T) = \int_0^\infty I(\lambda, T) * \bar{x}(\lambda) * d\lambda \tag{103}$$

$$Y(T) = \int_0^\infty I(\lambda, T) * \bar{y}(\lambda) * d\lambda \tag{104}$$

$$Z(T) = \int_0^\infty I(\lambda, T) * \bar{z}(\lambda) * d\lambda \tag{105}$$

With the temperature dependent Tristimulus values, the temperature dependent color coordinates in the 1976 chromaticity diagram can be calculated as:

$$u'(T) = \frac{4 * X(T)}{X(T) + 15 * Y(T) + 3 * Z(T)} \tag{106}$$

$$v(T)' = \frac{9 * Y(T)}{X(T) + 15 * Y(T) + 3 * Z(T)} \tag{107}$$

The temperature dependent u'v' values in the 1976 Chromaticity diagram are called the Planckian locus or black body locus. This locus depicts the color of a black body would take in a particular chromaticity space as the blackbody temperature changes. For a tested light source, the color coordinates ($u'_x$, $v'_x$) could be calculated following the procures above. The correlated color temperature can be found by the interpolation between the two closest iso-temperature lines. Figure 90 shows the Planckian locus in the 1976 chromaticity diagram.

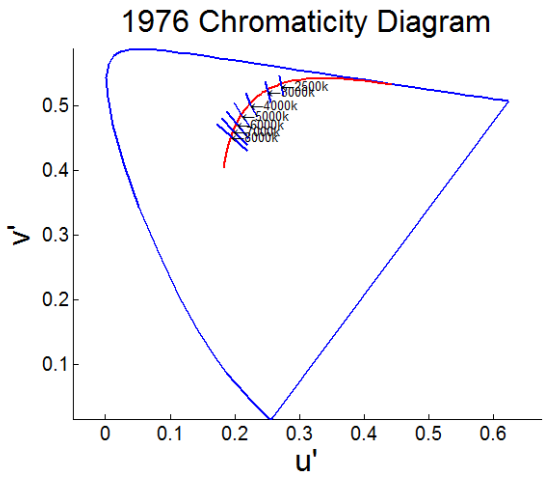


Figure 90: Planckian locus(Red line) in the 1976 chromaticity diagram.

The color coordinates of the black body radiation with various color temperature are given in the following Table 6 (Ohno, 2014) (Hernandez-Andres, 1999) (Hsieh, 2012).

Table 6: Color Distance between Tested Source and Black Body Radiation (Ohno, 2014)

| Temperature(K) (i) | u`(i) | v`(i) | Distance (i) | Sample i |
|---|---|---|---|---|
| 1000.00 | 0.448011 | 0.354625 | 0.230361 | 1 |
| 1010.00 | 0.445681 | 0.354826 | 0.228073 | 2 |
| 1020.10 | 0.443353 | 0.355026 | 0.225787 | 3 |
| : | : | : | : | |
| 4404.38 | 0.218633 | 0.329547 | 0.002536 | m-1 |
| 4448.42 | 0.218016 | 0.329042 | 0.002328 | m |
| 4492.91 | 0.217407 | 0.328537 | 0.002377 | m+1 |
| : | : | : | | |
| 19, 592.54 | 0.183990 | 0.277410 | 0.060959 | 300 |

| | | | | |
|---|---|---|---|---|
| 19, 788.47 | 0.183939 | 0.277254 | 0.061115 | 301 |
| 19, 986.35 | 0.183888 | 0.277100 | 0.061270 | 302 |

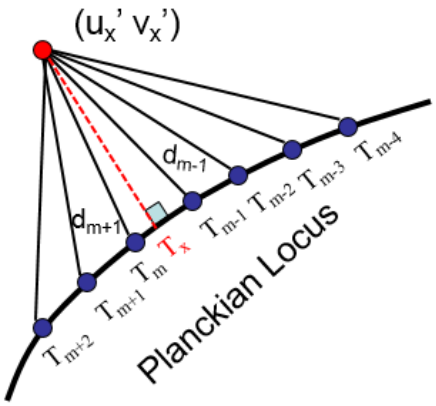


Figure 91: Location of the Corrleated Color Temperature on the Planckian locus. (Ohno, 2014)

CCT calculation starts with a minimum-search for the temperature that gives the smallest color difference between the tested light source and the black body radiation. In this example sample m has the nearest distance with the tested light source. Then a triangle could be plotted with the coordinates of the m-1 sample, m+1 sample and the color coordinate of the tested light source. Figure 91 (Ohno, 2014) shows the constructed triangular.

The Planckian locus could be assumed a line between $T_{m-1}$ and $T_{m+}1$. Draw a vertically line from ($u`_x$, $v`_x$) to the Planckian locus. The intersection $T_m$ is the closest point to the light source ($u`_x$, $v`_x$) and is the CCT value to be obtained. Detailed calculation could be illustrated with Figure 92 (Ohno, 2014):

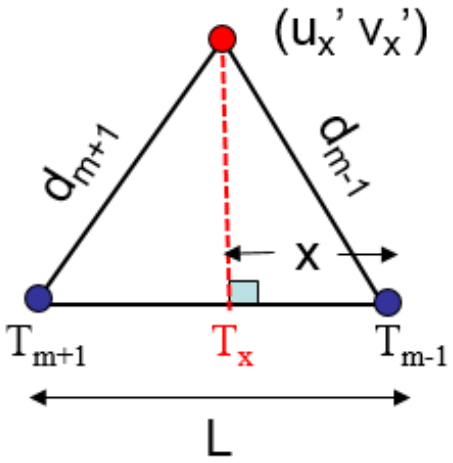


Figure 92: Triangular principle of CCT Calculation. (Ohno, 2014)

The CCT of the test lamp could be calculated as:

$$CCT = T_x = T_{m-1} + (T_{m+1} - T_{m-1}) \cdot \frac{x}{L} \tag{108}$$

Where x and L can be calculated as:

$$x = \frac{d_{m-1}^2 - d_{m+1}^2 + L^2}{2 \cdot L} \tag{109}$$

$$L = \sqrt{(u'_{m+1} - u'_{m-1})^2 + (v'_{m+1} - v'_{m-1})^2} \tag{110}$$

There are three kinds of white based on the correlated color temperature (CCT) of their light spectrum. CCT of 2700-3000 K (kelvin) are defined as the warm white, a yellowish type of white. CCT of 3500-4000k are described as neutral white and above are defined as cool white (blueish white). Color temperature and chromaticity space coordinates are important aspects of light. LED degradation not only results in the decrease of luminous flux output, but also may produce significant color shift which can contribute a failure in critical applications. It is thus necessary to maintain both the luminous flux output and color in acceptable error bound

## 3.10. COLOR RENDER INDEX (CRI)

Color rendering effects of a light source is defined as the effect of an illuminant on the color appearance of objects compared with their color appearance under a reference illuminant (CIE 1974). In this context, the CRI of a lighting source is defined as the measurement of the degree to which the perceived color of objects illuminated by the tested light source compare to a reference illuminant. The CRI of a light source does not indicate the apparent color of the light source. It is understood to be a measure of how well light sources render the colors of objects, materials compared with standard illuminant. Therefore, there must be agree on the standard light source with which to the test lights are compare. The choice of the standard source with which to compare the tested light source should be able to reflect the objects' original color perception. The perceived color of an object in the standard source should be the same with the color it is usually observed. In most practical case, the standard source is the natural day light.

The CIE 1974 has recommended the method to specify the color rendering properties of a light source. The CIE color render index is based on a color shift method, because it evaluates the average colorimetric shift in a color space. The CRI is calculated by comparing the color rendering of the test source to that of a standard illumination source. The reference illuminant source is different for different light source. If the CCT value of light source is below 5000K, the reference illumination source should be Planckian radiator. The reference illumination should be the same or nearly the same chromaticity as the light source to be tested.

CRI is measured only with respect to a reference source which is either the blackbody curve below 5000K or a CIE Daylight source above 5000K. The reference must be the closest in chromaticity (color) to the source being tested. Otherwise the comparison makes little sense. Comparing the CRI of two very different color temperature sources is meaningless but in general,

higher CRI mean less deviation from the reference source. For the calculating of CRI, a set of specific colors is used to measure the color difference between a reference source and the source under test in the interest of international standard. This is termed the General Color Rendering Test and represents a calculation using color sample numbers R1 through R14. A $15^{th}$ color sample is defined by the Japanese Industrial Standard JIS-Z872 that pertains to Japanese complexion under daylight conditions. Their approximate Munsell notations and color appearance under day light is given in Table 7 (CIE, 1995) (Schanda, 2007) (Zukauskas, 2002):

Table 7: Standard CIE Test Color Samples (CIE, 1995)

| **Standard Test Color NO.** | **Approximate Munsell Notation** |
|---|---|
| 1 | 7.5R 6/4 |
| 2 | 5Y 6/4 |
| 3 | 5GY 6/8 |
| 4 | 2.5G 6/8 |
| 5 | 10BG 6/4 |
| 6 | 5PB 6/8 |
| 7 | 2.5P 6/8 |
| 8 | 10P 6/8 |
| 9 | 4.5R 4/13 |
| 10 | 5Y 8/10 |
| 11 | 4.5G 5/8 |
| 12 | 3PB 3/11 |
| 13 | 5YR 8/4 |
| 14 | 5GY 4/4 |
| 15 | 1YR 6/4 |

By convention, the Planckian black-body reference source is assumed to have a CRI of 100, because natural daylight resembles a black-body radiation. Light source other than the standard illumination reference source will have a CRI lower than 100, because the reference illumination source has a CRI of 100. Emission of incandescent lamp follows the pattern of black

body radiation. Therefore, incandescent lamp has the highest CRI compared with fluorescent lamp or LED lamp.

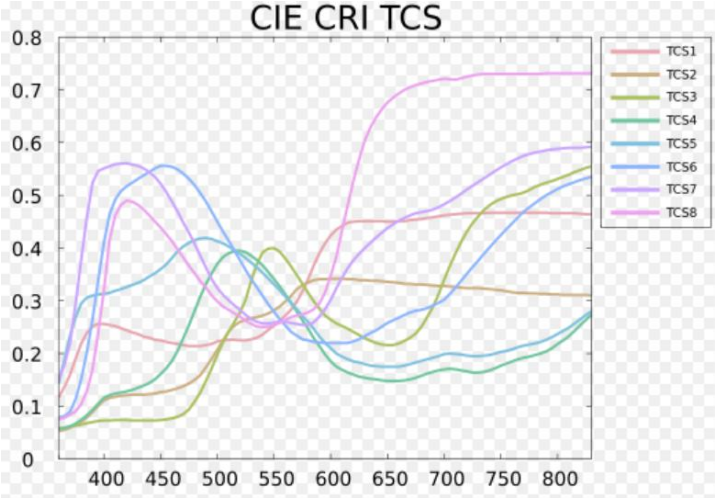


Figure 93: CIE Test color sample reflectivity. (CIE, 2004a)

The general CRI is calculated based on the first 8 test color samples and is an average of the first 8 samples:

$$CRI_a = \frac{1}{8} * \sum_{i=1}^{i=8} CRI_i \tag{111}$$

Where $CRI_i$ are the special CRIs for a set of eight test-color samples. The special color render index can be calculated by:

$$CRI_i = 100 - 4.6 * \Delta E_i^* \tag{112}$$

Where $\Delta E_i^*$ is the quantitative color change of the test-color sample when it is illuminated with the reference illumination source and with the test light source. The CRI will have a value of 100 if there is no difference in color appearance when illuminated by tested light source and standard illumination source. $\Delta E_i^*$ plays an important role during the calculation of CRI. The quantitative value of $\Delta E_i^*$ not only depends on the tested light source, but also has a strong

dependence of the picked standard illumination source. The 14 test color samples are defined in terms of their spectral reflectivity. The reflectivity curves of the international standard test colors are shown in Figure 93 (CIE, 2004a) (CIE, 2004b):

There are several steps during the calculation of CRI. The first step is find the right reference illumination source. Generally, when the correlated color temperature of the test lamp is less than 5000K, the black body radiator with the same color temperature should be used as the reference illumination source. In this case the color change of $\Delta E_i^*$ which is the difference in appearance of a test color when illuminated by the test lamp and the reference lamp, can be calculated as:

$$\Delta E_i^* = \sqrt{(\Delta L^*)^2 + (\Delta u^*)^2 + (\Delta v^*)^2} \tag{113}$$

Where

$$\Delta L = L^*_{ref} - L^*_{test} = [116 * (\frac{Y_{ref,i}}{Y_{ref}})^{\frac{1}{3}} - 16] - [116 * (\frac{Y_{test,i}}{Y_{ref}})^{\frac{1}{3}} - 16] \tag{114}$$

$$\Delta u^* = u^*_{ref} - u^*_{test} = [13 * L^*_{ref} (u_{ref,i} - u_{ref})] - [13 * L^*_{test} (u_{test,i} - u_{ref})] \tag{115}$$

$$\Delta v^* = v^*_{ref} - v^*_{test} = [13 * L^*_{ref} (v_{ref,i} - v_{ref})] - [13 * L^*_{test} (v_{test,i} - v_{ref})] \tag{116}$$

$$u = \frac{4 * X}{X + 15 * Y + 3 * Z} \tag{117}$$

$$v = \frac{6 * Y}{X + 15 * Y + 3 * Z} \tag{118}$$

Where X, Y and Z are tristimulus value. If they are the tristimulus values of the reference source spectrum, they will be calculated with spectrum of reference illumination source S(λ) that reflected from the test color sample $TC_i$ (λ). If they are the tristimulus values of the tested light source, they will be calculated with the spectrum of the tested light Φ(λ) source that reflected from the test color sample $TC_i$ (λ). The tristimulus values of the reference illumination source and tested light source can be calculated as:

$$X_{ref} = \frac{\int_{380}^{780} S(\lambda) * \bar{x}(\lambda) * d\lambda}{\int_{380}^{780} S(\lambda) * \bar{y}(\lambda) * d\lambda} * 100 \quad (119)$$

$$Y_{ref} = \frac{\int_{380}^{780} S(\lambda) * \bar{y}(\lambda) * d\lambda}{\int_{380}^{780} S(\lambda) * \bar{y}(\lambda) * d\lambda} * 100 = 100 \quad (120)$$

$$Z_{ref} = \frac{\int_{380}^{780} S(\lambda) * \bar{z}(\lambda) * d\lambda}{\int_{380}^{780} S(\lambda) * \bar{y}(\lambda) * d\lambda} * 100 \quad (121)$$

$$X_{test} = \frac{\int_{380}^{780} \Phi(\lambda) * \bar{x}(\lambda) * d\lambda}{\int_{380}^{780} S(\lambda) * \bar{y}(\lambda) * d\lambda} * 100 \quad (122)$$

$$Y_{test} = \frac{\int_{380}^{780} \Phi(\lambda) * \bar{y}(\lambda) * d\lambda}{\int_{380}^{780} S(\lambda) * \bar{y}(\lambda) * d\lambda} * 100 \quad (123)$$

$$Z_{test} = \frac{\int_{380}^{780} \Phi(\lambda) * \bar{z}(\lambda) * d\lambda}{\int_{380}^{780} S(\lambda) * \bar{y}(\lambda) * d\lambda} * 100 \quad (124)$$

The tristimulus values for test color sample i (i= 1,2,3…15) illuminated by the reference illumination source can be calculated as:

$$X_{ref}(TCi) = \frac{\int_{380}^{780} S(\lambda) * TC_i(\lambda) * \bar{x}(\lambda) * d\lambda}{\int_{380}^{780} S(\lambda) * \bar{y}(\lambda) * d\lambda} * 100 \quad (125)$$

$$Y_{ref}(TCi) = \frac{\int_{380}^{780} S(\lambda) * TC_i(\lambda) * \bar{x}(\lambda) * d\lambda}{\int_{380}^{780} S(\lambda) * \bar{y}(\lambda) * d\lambda} * 100 \quad (126)$$

$$Z_{ref}(TCi) = \frac{\int_{380}^{780} S(\lambda) * TC_i(\lambda) * \bar{x}(\lambda) * d\lambda}{\int_{380}^{780} S(\lambda) * \bar{y}(\lambda) * d\lambda} * 100 \quad (127)$$

The tristimulus values for test color sample i (i= 1,2,3…15) illuminated by the tested light source can be calculated as:

$$X_{test}(TCi) = \frac{\int_{380}^{780} \Phi(\lambda) * TC_i(\lambda) * \bar{x}(\lambda) * d\lambda}{\int_{380}^{780} S(\lambda) * \bar{y}(\lambda) * d\lambda} * 100 \quad (128)$$

$$Y_{test}(TCi) = \frac{\int_{380}^{780} \Phi(\lambda) * TC_i(\lambda) * \bar{x}(\lambda) * d\lambda}{\int_{380}^{780} S(\lambda) * \bar{y}(\lambda) * d\lambda} * 100 \quad (129)$$

$$Z_{test}(TCi) = \frac{\int_{380}^{780} \Phi(\lambda) * TC_i(\lambda) * \bar{x}(\lambda) * d\lambda}{\int_{380}^{780} S(\lambda) * \bar{y}(\lambda) * d\lambda} * 100 \quad (130)$$

To get high CRI value, the tristimulus values of the tested lamp should be as close as the tristimulus values of the reference illumination source. The calculation of CRI shows that it not only account for the ability of a light source to render the chromaticity of a physical object, but also account for the ability of a test source to render the lightness of a physical object. However, when the CCT of a light source is high than 5000k, Planckian black body radiator can't be used as the reference illumination source any more.

When the light source chromaticity is far from the Planckian locus, the CRI should be very low according to the calculation above. However, in the real situation, colors can be vivid and natural even for illumination sources slight off the Planckian locus due to the chromatic adaption. Chromatic adaptation is the human visual system's ability to preserve the appearance of objects' colors under different illuminations system. An object may be viewed under various conditions.

For example, it may be illuminated by daylight, the light of a fire, etc. In all of these situations, human vision perceives that the object has the same color: an apple always appears red, whether viewed at night or during the day. On the other hand, a camera with no adjustment for light may register the apple as having varying color. This feature of the human visual system is called chromatic adaptation, or color constancy. CIE 1995 introduced an alternative method to calculate the CRI in a more realistic way. This method considers the human ability of chromatic adaption by introducing the concept of adaptive color shift. The change in chromatic adaption caused an adaptive color shift for each test sample which can be estimated by making use of a Von Kries-type linear transformation of the CIE tristimulus values.

### 3.11. PEAK WAVELENGTH

Spectrum data are the finger print of a tested light source. There are two peaks of the spectrum of phosphor converted LEDs. One peak is caused by the semiconductor blue emitter. The other peak is the emission spectrum of the phosphor. Monitoring the wavelength of these two peaks help to understand the degradation mechanisms of LED packages. If the peak wavelengths have no shift during the operation, the degradation is probably caused by the degradation of optical parts. However, if peak wavelengths shifted during the operation, it is for sure that some physical properties of the LED packages degraded. For example, yellow peak wavelength shift may mean the chemical property degradation of phosphor particles.

### 3.12. PHOTON NUMBER

The radiant energy of n photon at specific wavelength (λ) is given by the following equation:

$$Q = n * \frac{h * c}{\lambda} = n * \frac{1.99 * 10^{-16}}{\lambda} \tag{131}$$

Where Q is the photon energy in joules and h is the Planck's constant (joules*second) which equal 6.626*10-34. c is the speed of light (meter / second) and equals 3*108. If the total energy is known, the number of photon at a specific wavelength can be calculated as:

$$n = 5.03*10^{15}*\Phi*\lambda \tag{132}$$

With the measured absolute radiant flux, the total number of photon emitted by LED at each readout time can be calculated with:

$$TotalNumberofPhotons = \int_{350}^{800} 5.03*10^{15}*\Phi*\lambda*d\lambda \tag{133}$$

### 3.13. VI CURVE

LED is a semiconductor device form from a p-n junction. When it is forward biased, it will pass current. The forward current and forward voltage is exponential relation in an active device such as an LED. Measuring the characteristics curve of the LED package helps to monitor the p-n junction inside the package. During the accelerated life test, at each readout time, VI curve of the samples were taken. The test result can be used to check if there is any material or electric degradation of the semiconductor device. In this dissertation, all VI curves were taken with a source meter. During the measurement, forward current was changed from 0mA to 700mA and forward voltage of LED packages were taken. Figure 94 shows a measurement of VI curve.

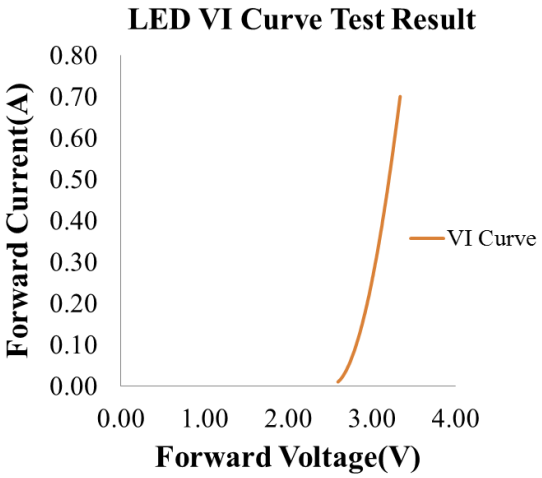


Figure 94: LED VI Curve Test Result.

# 4. EXPERIMENTAL RESULTS AND FAILURE MECHANISM ANALYSIS

Development of failure distributions in absence of accelerated test methods presents a huge challenge to testing the life of LED systems. Life and reliability of the LED system may change with the change of the condition of operation. However, standardized accelerated life test methods for fast-turn testing of LED failure mechanisms are not available. In this section, various accelerated life test conditions were performed on the high-power pc-LED packages. Test results are presented in three groups: WHTOL test without electrical bias, HTSL test with electrical bias and WHTOL test with electrical bias.

## 4.1. WHTOL TEST WITHOUT ELECTRICAL BIAS

A set of test samples of XRC from CREE Lighting were used for this experimental measurement. This unique package allows very precise failure analysis to be performed. The test samples feature electrically neutral thermal path, low thermal resistance (12°C/W) and support for a wide range of drive currents (maximum to 500 mA). Usually in the LED driver, Flyback converter is used in DC/DC conversion with galvanic isolation between the input and outputs. The PWM control of the Flyback converter can be integrated in one chip with the high voltage MOSFET and only a few external components are required which allows a small profile in the Light emitting diode driver design. The test samples were mounted on the cold side of TE technology TE-2-(31-12)-1.0 Thermoelectric Module (Peltier Module). The hot side of this thermoelectric module was mounted on a heat sink. Test samples were subjected to 85°C temperature stress and 85% relative humidity in thermal and humidity chamber. The samples were not powered during temperature humidity testing. Samples were taken out for forward voltage, forward current measurement and luminous flux measurement at regular times. When taking the

lumen measurement, the forward voltage is set to 2.3 V and the initial forward current is 135mA. The working condition for thermoelectric module is 2.5 Volts and the current is 550mA.

During the VI curve measurement, forward voltage has been programmed to go up slowly at an interval of 0.01 V and forward voltage and forward current are recorded by Agilent 34970A data logger. The LED was powered by square wave pulse, in order to reduce the heat generated in the P-N junction. The Agilent 33220A function generator produces a small current square wave and this wave was amplified by TIP125 Epitaxial Darlington Transistor to give a big current square wave source which powers up the light emitting diode. Detailed test set up is given in Figure 95.

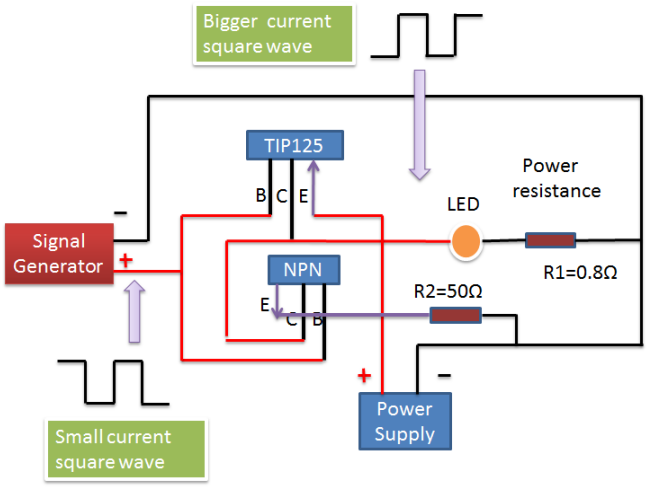


Figure 95: PWM Setup.

To monitor both forward voltage and forward current, a power resistor has been put in series with the LED. The second channel was deployed to monitor the voltage of power resistor and with the power resistance value. The forward current was calculated from these values. Data logger deployment configuration is shown in Figure 96. In this experiment, three data channel need to be recorded automatically, forward voltage, forward current and reference point

temperature. An Agilent 34970A data acquisition system has been deployed to communicate with the CPU with a GPIB card. The data logger is used to monitor multiple signals over extended periods of time to identify irregularities. Figure 97 shows the Labview virtual instrument used for data acquisition.

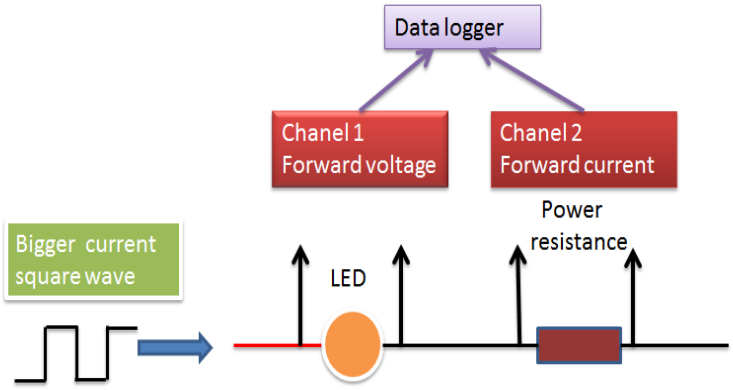


Figure 96: Data Logger Set Up.

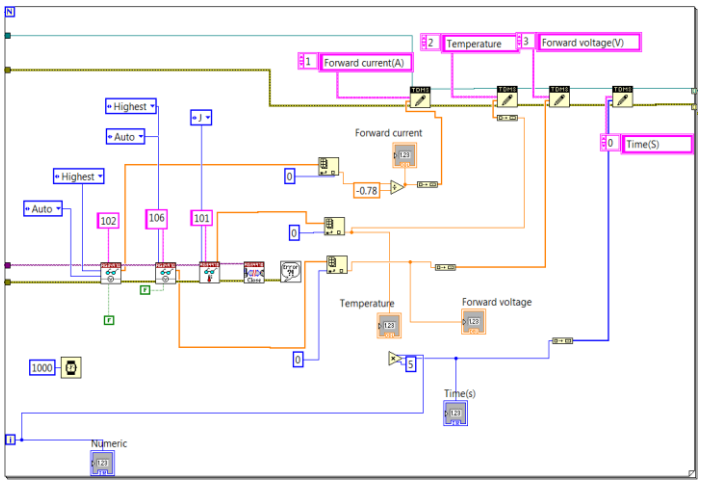


Figure 97: LabVIEW program for the data acquisition.

A CPU has been used to record the data with aid of a LabVIEW program. A LabVIEW program has also been built to connect between the data logger and CPU. Another LabVIEW program has been built to control the programmable Agilent E3631A power supply.

Modified PWM (pulse width modulation) has been used in this experiment to power the LEDs. PWM is a powerful way of controlling analog circuits and systems, using the digital outputs of microprocessors. PWM provides a way to control a digital signal, through the alteration of state and frequency. This modulation affects the magnitude, frequency and duty cycle of square wave pulse. By changing the magnitude of the square wave, the forward voltage can be changed. Figure 98 gives an output example.

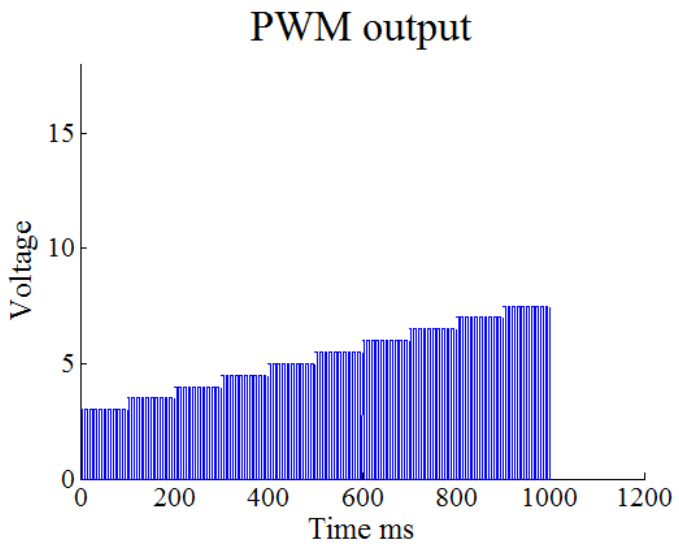


Figure 98: Modified PWM Output.

In this experimental set up, the output of power supply can be programmed to change according to certain path. The second parameter is the duty cycle, which can be changed by adjusting the duty cycle of the function generator. With these two parameters, this experimental set can give out any square wave the light emitting diode needs.

In this experiment, three parameters have been recorded for the further study of light emitting diode failure theory. The first pair was forward voltage and forward current. Test result was used to plot the IV curve. The third parameter is luminous flux of the LEDs, which can be correlated with the change of IV curve to identify onset of LED failure. Figure 99 shows the shift of IV curve with time. Notice how forward current changes at constant forward voltage. It changes prior to the traditional definition of failure of light emitting diode. The advance warning of failure validates the use of forward current as the leading indicator in the prognostics health management of light emitting diode.

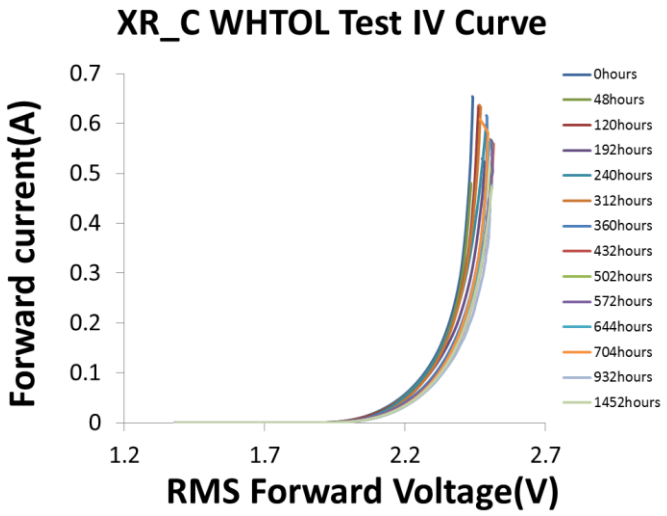


Figure 99: XRC RMS IV Curve for WHTOL test without bias.

At the same time, luminous flux measurement has also been measured. The following table gives the test result for 1296 hours. According to the IES LM-79 for the Electrical and Photometric Measurement of Solid –State Lighting Product, luminous flux was test at the forward voltage at RMS 2.3 V and at the initial state forward current was RMS 126 mA. The test condition is

consistent with usage, typically in range of 250mA peak value. The test reference temperature is 22°C. The junction temperature is related to the dissipated power as follows:

$$T_j = T_{Ref} + R\Theta_{j\text{-}Ref} * P_D \quad (134)$$

Where RΘJ-Ref is thermal resistance (°C/W) from LED P-N junction to a reference point (which can be air, heat sink, etc.). PD is power dissipation (W) can be calculated by LED forward current multiply by forward voltage. TRef can be measured with a thermocouple. From the XR_C specification, RΘJ-Ref is 15°C/W and the P-N junction temperature is approximately 25°C which qualify the test standard. Figure 100 shows the scheme diagram of the thermal resistances.

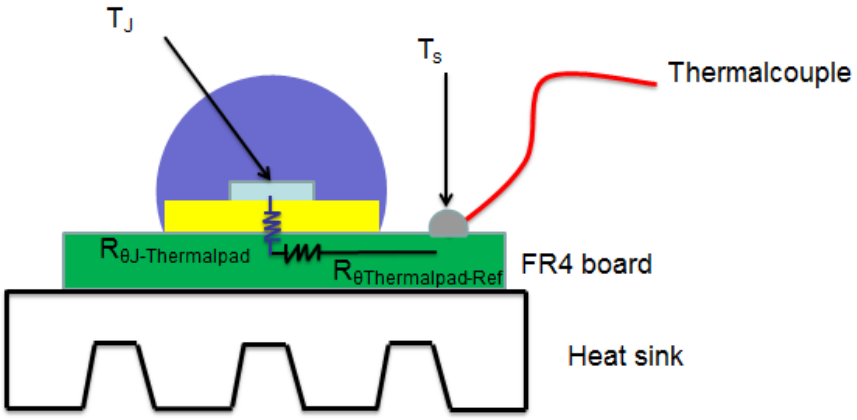


Figure 100: Thermal Resistance set up at the initial state.

In this experiment, 5-test samples have been used. Experimental data indicates that forward current can be used as the leading indicator in the prediction of remaining useful life of light emitting diode. Figure 101, and Figure 102 show the change in current, and luminous flux for different samples tested.

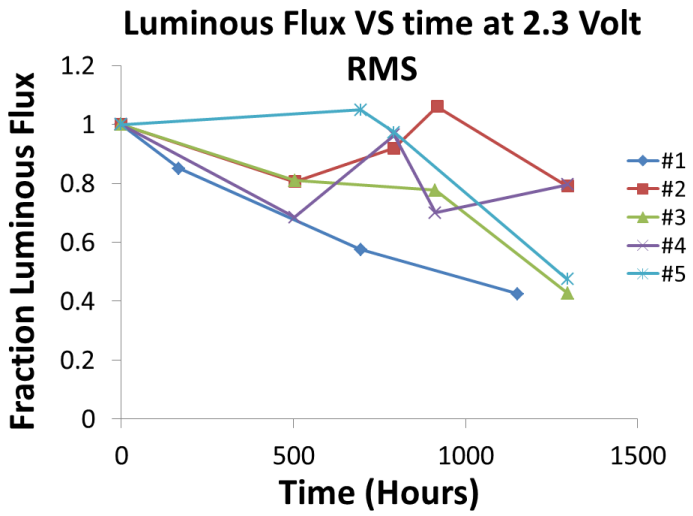


Figure 101: Change of Luminous flux vs aging time at forward voltage 2.3 V RMS.

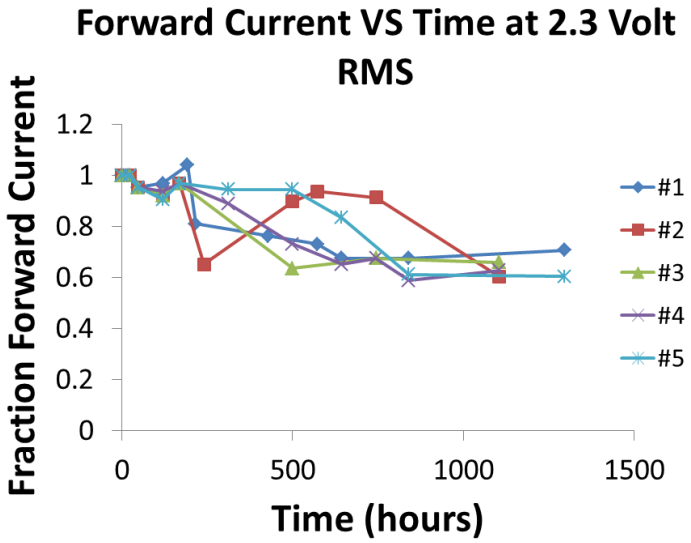


Figure 102: Change of Forward Current vs aging time at 2.3 V RMS.

Figure 103 and Figure 104 shows correlation of lumen degradation with change of resistance at 2.3 V RMS.

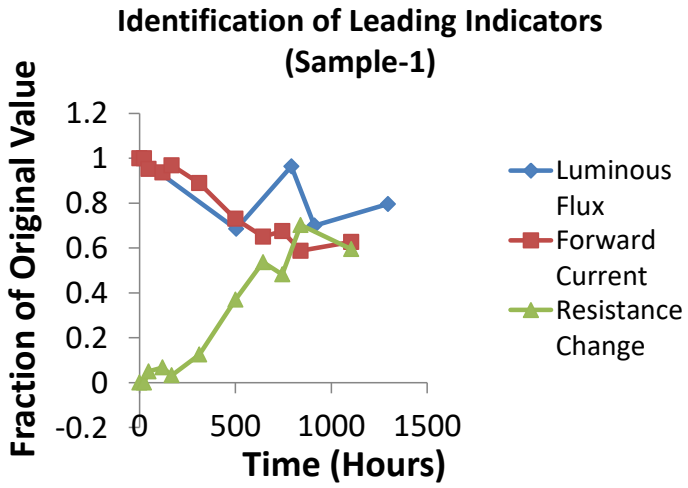


Figure 103: Correlation of forward current, luminous flux and resistance (Sample-1).

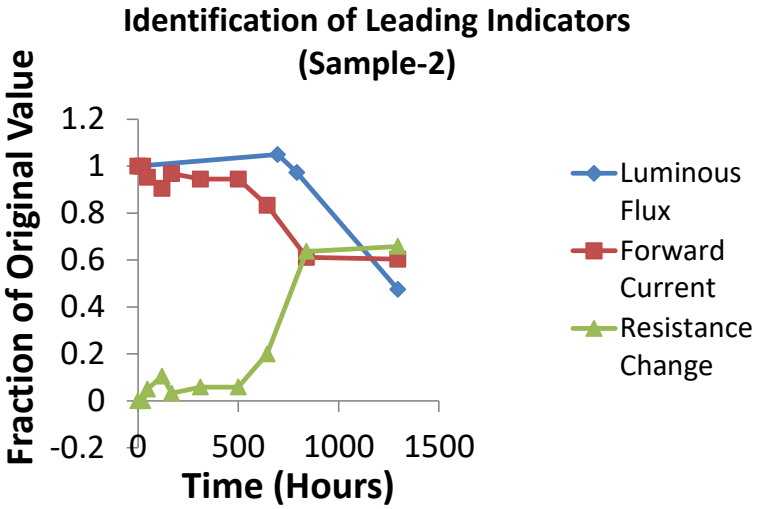


Figure 104: Correlation of forward current, luminous flux and resistance (Sample-1).

Figure 101 and Figure 102 show the degradation of luminous flux and forward current. The degradation indicates that they follow the same pattern and forward current can be used as the leading indicator of the LED package. Figure 103 and Figure 104 test results indicate that, at constant forward voltage, forward current drops because of the increasing of resistance. The

increasing of resistance make the junction temperature higher and more energy will become heat rather than turning into photons. As a result, the luminous flux drops which can be proven by the test result in Figure 101. Figure 105 shows the measured radiant flux.

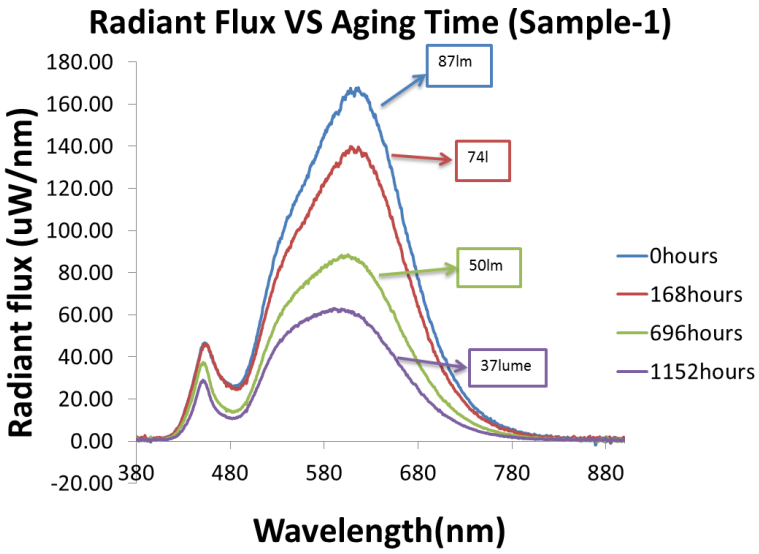


Figure 105: Change of Radiant flux vs aging time.

In Figure 105, there is an obvious drop of the radiant flux of the LED package. There are two peaks in the spectrum. The first pear around 450nm is caused by the emission of the LED chip. After the excitation of the phosphor, the excitation peak is around 560nm. With the combination of blue light and yellow light, the LED package give out white spectrum.

## 4.2. HTSL TEST WITH ELECTRICAL BIAS

In this and the following section, experiments are set up to explore the different effects of the humidity and thermal stress on LED packages. High CRI (Ra=80), commercial available warm white (3000k) LEDs are used to study the degradations caused by temperature and humidity. Each group focuses on either the thermal stress or the combination of thermal stress and humidity.

Extreme condition was intentional picked up to accelerate the life test. If test result is the same, it can be proven that humidity had no effects on LED package. All the damage of the package comes from thermal stress. On the other, if the test results between each group are not same, thermal stress and humidity effects can be concluded from each group.

Two kinds of commercial available phosphor converted warm white LED packages were used for the designed test. Those LEDs were purchased from LED supply. Each of the LED packages was pre-soldered on a star board. They were powered up through the solder pads that connect the electrodes inside the package. Star board can be directly fixed on the aluminum heat sink with screws. LED packages were biased in series with constant current power source. During the experiment, temperature environmental chamber was used to accelerate the life test of LED packages. Test procedures followed the protocols that outlined in JESD22-A101C from the electronics industry (JEDEC, 2010) (JEDEC, 2009). This test standard requires constant temperature. At the same time, test samples were electrical power biased on and off at an interval of one hour in the environmental chamber.

Five groups of samples were prepared for the designed test and each group had a population of five. Detailed test condition for each group are provided in the Table 8.

Table 8: Test Condition of Each Group

| **Group** | **Test Vehicle** | **Current** | **Test Condition** | **Aging Time** |
|---|---|---|---|---|
| 1 | XR_C Warm White | 350mA | 105°C | 6360 hours |
| 2 | XR_C Warm White | 500mA | 175°C | 816 hours |

Each group was powered in series with constant current power source at designated current. Samples were attached to aluminum heat sink and secured with screws. Three constant test

environments were used to check the different effects from temperature and humidity. During the test, each group that mounted on heat sink were placed in their own environmental chamber for accelerated lift test. The LED package were powered up with a constant current drive that was out of the chamber. After two weeks, 336 hours, LED packages were moved out chamber and cooled down to room temperature. Their photometric and colorimetric properties were measured inside an EVERFINE integrated sphere, following the instructions from LM-79 test standard.

Characteristic curve of the diode was measured with KEITHLEY 2401 power source. Sweep current changed from 0mA to 500mA and forward voltage was measured. VI curve of the LED was plotted with the measured data to monitor the electrical properties of the die. After electrical properties measurement, all samples were returned to the environmental chamber for further accelerated life test. The direct measurement is radiant flux. Some other parameters were also calculated based on the measured data, such as color CCT, shift distance, luminous flux and radiant power. All measured and calculated parameters are listed in Table 9.

Table 9: Measured and Calculated Parameters

| **Measured** | **Calculated** |
|---|---|
| • Absolute Radiant Flux (μW/nm)<br>• VI Curve | • Luminous Flux (lumen)<br>• Radiant Power (W)<br>• Color Shift Distance<br>• Photon number (1/s)<br>• Yellowness Index<br>• Yellow to blue ratio<br>• Correlated Color Temperature(K)<br>• Color Coordinates in Chromaticity Diagram (u' v')<br>• |

Figure 106 and Figure 107 illustrate the radiant flux measurement of XRC LED at different temperature. Absolute radiant flux is measured with spectroradiometer and integrating sphere in μW/nm. Absolute radiant flux of each visible wavelength was plot together as a spectrum.

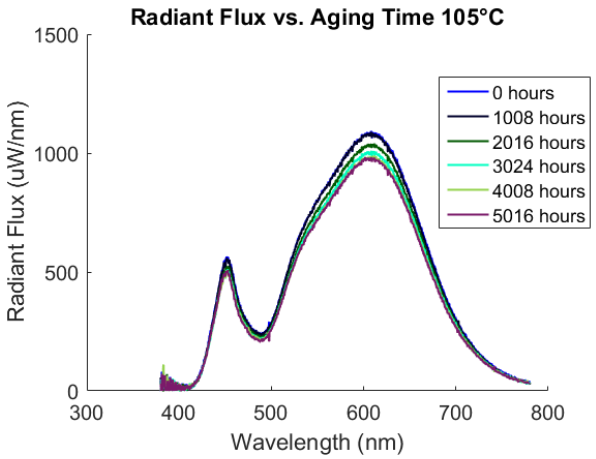


Figure 106: Radiant Flux Measurment of XRC LED at 105°C.

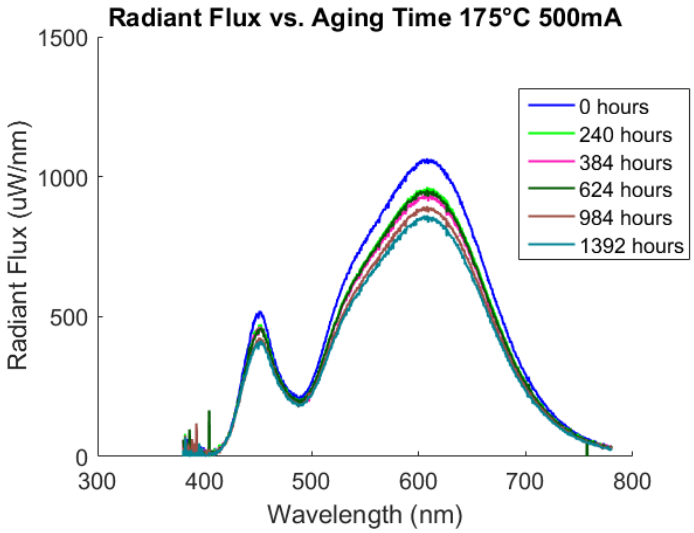


Figure 107: Radiant Flux Measurment of XRC LED at 175°C.

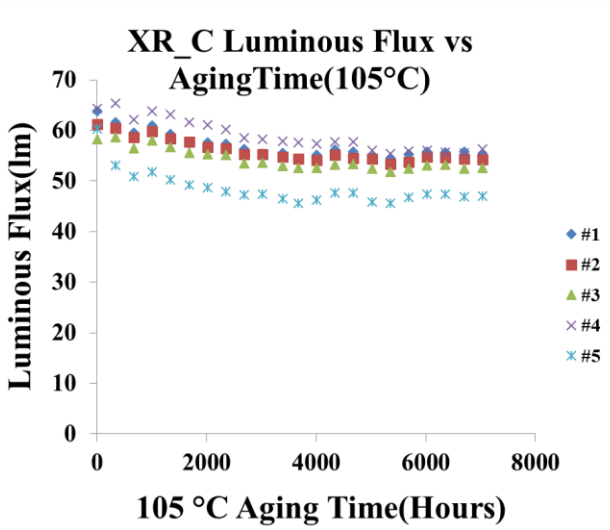


Figure 108: XRC LED luminous Flux measurements at 105°C.

Based on the absolute radiant flux, the luminous flux could be calculated. Figure 108 and Figure 109 shows the luminous flux of XRC LED at different aging temperature.

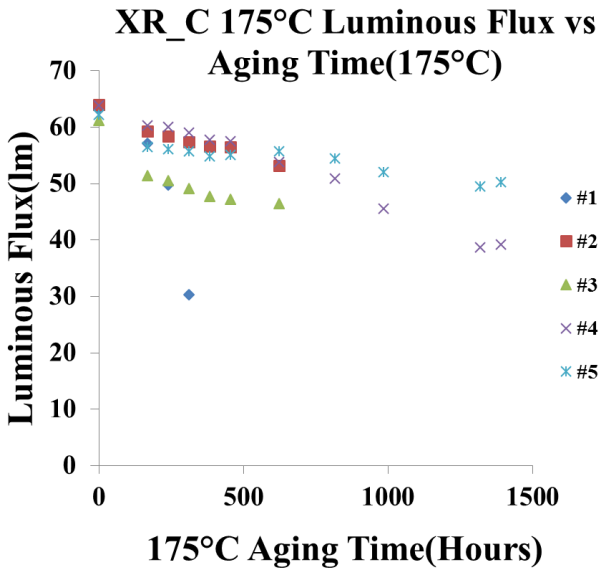


Figure 109: XRC LED luminous Flux measurements at 175°C.

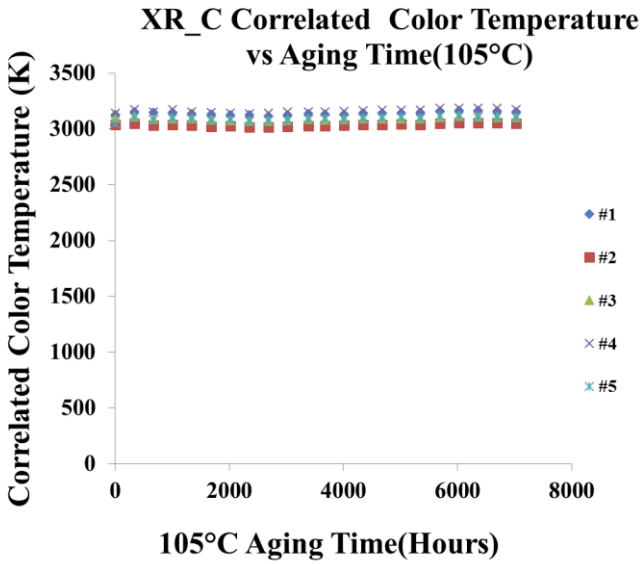


Figure 110: XRC Correlated Color Temperature measurement at 105°C.

Figure 110 and Figure 111 shows the CCT measurements of XRC LED at different aging temperature.

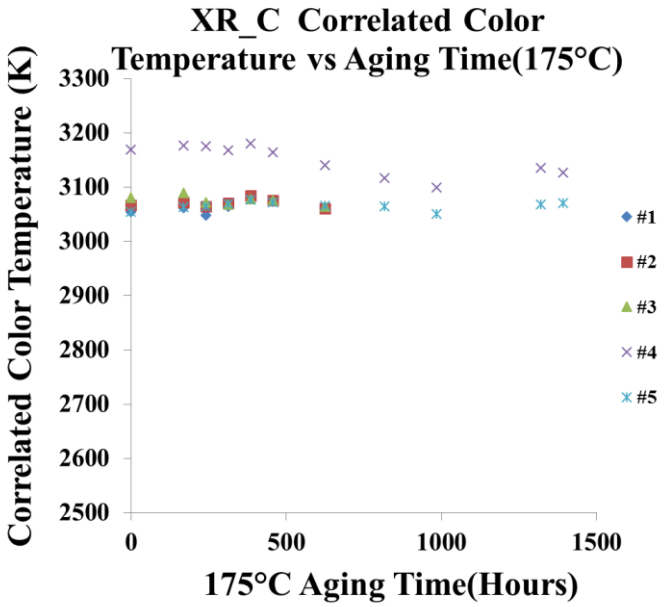


Figure 111: XRC Correlated Color Temperature measurement at 175°C.

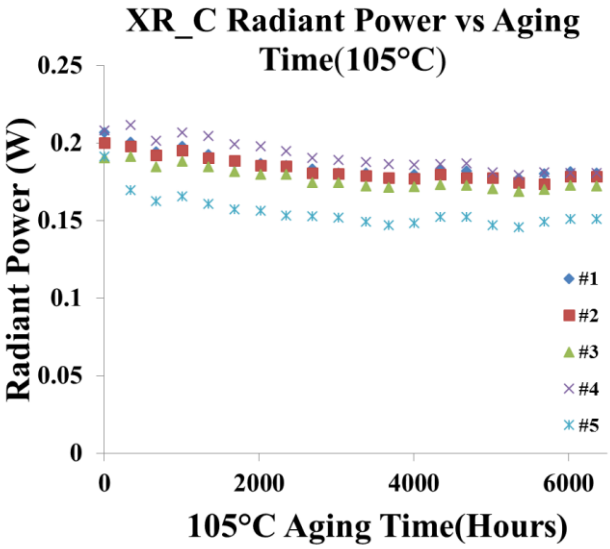


Figure 112: XRC radiant power measurement at 105°C.

Figure 112 and Figure 113 shows the radiant power measurement of XRC LED at different aging temperature.

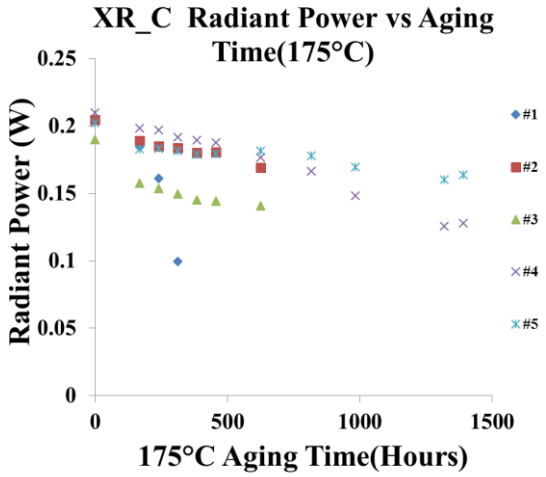


Figure 113: XRC radiant power measurement at 175°C.

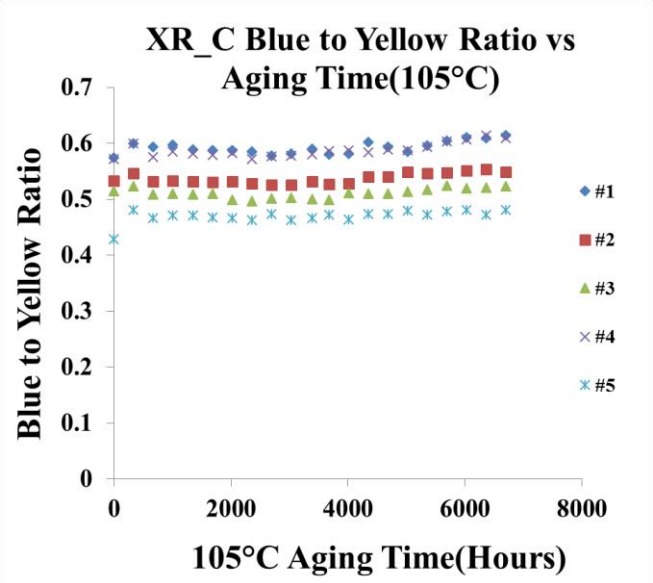


Figure 114: XRC Blue to Yellow Ratio measurement at 105°C.

Figure 114 and Figure 115 shows the blue to yellow ratio measurement of XRC LED at different aging temperature.

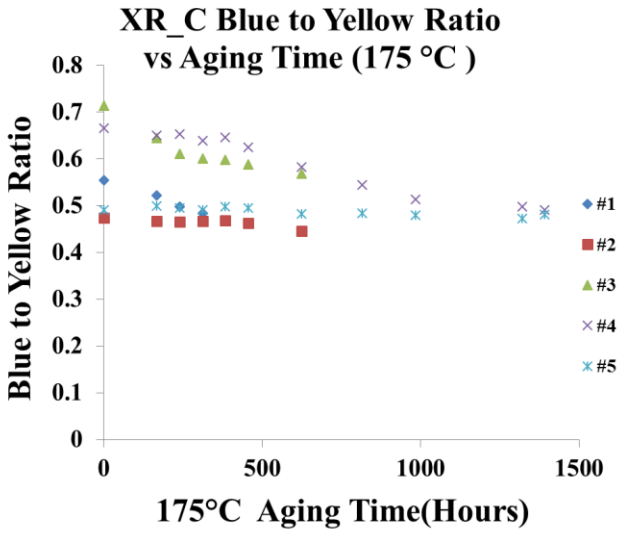


Figure 115: XRC Blue to Yellow Ratio measurement at 175°C.

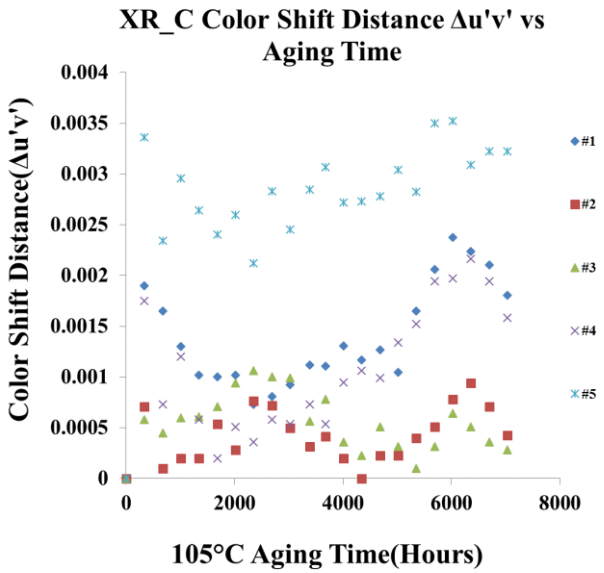


Figure 116: XRC Color shift distance measurement at 105°C.

Figure 116 and Figure 117 shows the color shift distance measurement of XRC LED at different aging temperature.

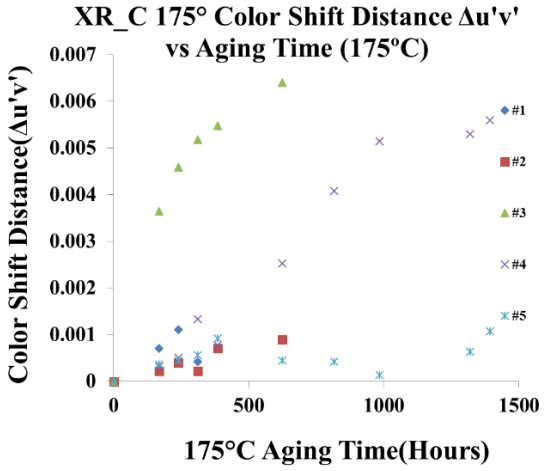


Figure 117: XRC Color shift distance measurement at 105°C.

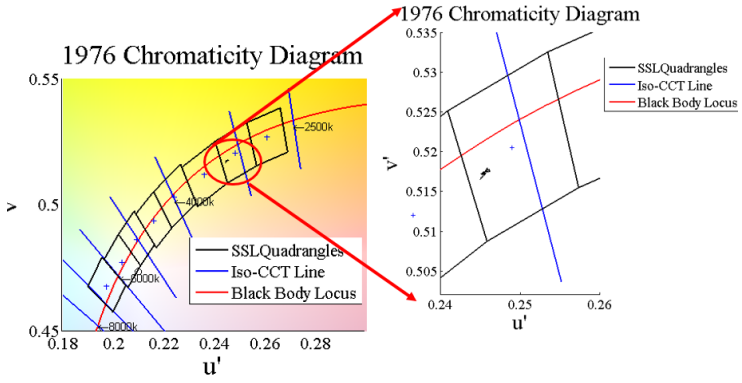


Figure 118: XRC  Color Shift Path measurement at 105ºC.

Color Shift Distance is the absolute distance between the accelerated tested LED modules' chromaticity coordinates and the pristine LED modules' chromaticity coordinate in the CIE 1976 color space. Monitoring the color shift path helps to understand which parts of LED package fails and analysis can be great help for LED designer. Figure 118 shows the test result of color shift path in the 1976 chromaticity diagram.

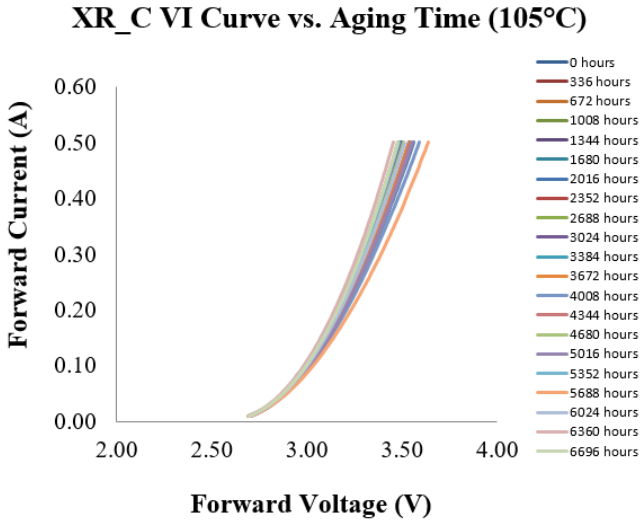


Figure 119: XRC VI curve measurement at 105ºC.

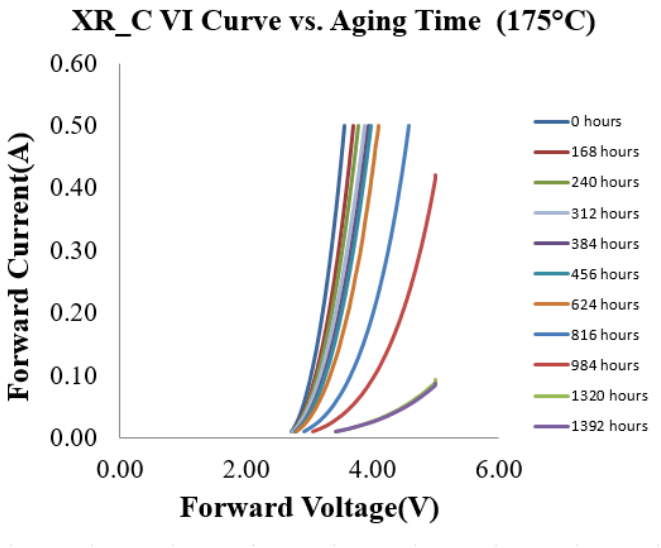


Figure 120: XRC VI curve measurement at 175ºC.

LED is a semiconductor device form from a p-n junction. When it is forward biased, it will pass current. The forward current and forward voltage is exponential relation. Measuring the characteristics curve of the LED package helps to monitor the p-n junction inside the package. During the accelerated lift test, at each readout time, VI curve of the samples had been taken. The test result can be used to check if there is any material or electric change of the diode. Figure 119 and Figure 120 show the test result of one sample from XRC LED at 105ºC. Test results of other samples in each group have the same pattern.

Figure 119 demonstrates that there are no monochromatic pattern of the change of the VI curve during the accelerated life test. It can be concluded that electric properties of the diode were very stable during the high temperature test at 105ºC. The conclusion in agreement with the absolute radiant flux measurement. However, in Figure 120, an obvious VI curve shift can be observed. This is also consistent with the absolute radiant flux measurement of XRC LED at 175ºC. Dramatic change of VI curve means the electric or material change of the diodes inside package. That also explains the big drop of the blue peak intensity of XRC LED at 175ºC.

## 4.3. WHTOL TEST WITH ELECTRICAL BIAS

This chapter focuses on the failure mechanisms and color stability of a commercially available high power LED under harsh environment conditions. The reliability of high power LEDs (HP-LEDs) used for illumination have been studied for the past ten years and major findings are reviewed elsewhere. There has also been previous work on other SSL luminaire components such as drivers, but in general there is a lack of publicly available data on humidity effects on LED packages. IESNA (illuminating Engineering Society of North American) published a test standard LM-80. LM-80 refers to a method for measuring the lumen depreciation of solid-state lighting sources, such as LED packages, modules and arrays. This standard methodology would allow customers to evaluate and compare the lumen maintenance of LED components from different companies. During the test, LED packages are placed in a temperature controlled case (55°C, 85°C and third temperature) and driven with external current sources. At each readout time, LEDs are taken out of the thermal chamber to cool to room temperature for radiometric measurement. However, in the LM-80 test, only temperature is involved and relative humidity effect are not considered. In LED based luminaire applications, some are operated in the harsh environment. During the operation, the LED package not only experiences the high bias current and ambient temperature, but also the humidity around the package, especially for the road lighting and automobile lighting. Proper design of LED products for different environment requires the understanding of the various effects on LED package from thermal stress and humidity. In this section, the pc-LED packages are exposed to high humidity for accelerated life test. During the accelerated life test, the effects of VOC contamination are also studied. Several LED manufacturers have released application notes pertaining to the chemical compatibilities of the LED products. Material selection considerations and chemical compatibility test methods are

outlined in order to increase the overall lifetime of LEDs through the reduction of VOCs during operation. In this dissertation, VLEDs from the same manufacturer have been studied in a contaminated and uncontaminated environment.

### 4.3.1. WHTOL TEST WITH ELECTRICAL BIAS IN THE VOC CONTAMINATED ENVIRONMENT

If a high-power pc-LED package is in the presence of VOCs, then VOCs can diffuse into the gas-permeable silicone lens and encapsulates. The VOCs will occupy the free space in the molecular structure of the silicone. Once exposed to high photonic energy emitted by the LED and heat from the junction temperature, the VOCs start to discolor and deteriorate the pc-LED. The predominant failure mechanism of VOC contamination is the discoloration of the phosphor layer. After VOC contamination occurs, the degradation of luminous flux and the chromaticity shift becomes extremely rapid.

Periodically, luminous flux and CCT were recorded in order to correlate the photometric and colorimetric results to the predominant failure mechanisms previously described. The lighting measurements followed the LM-79-08 test standard. Additionally, the VLEDs were subject to a steady-state temperature humidity life test of 85/85 with an electrical bias based on the JEDEC standard JESD22-A101C and other reports. Upon completion of the accelerated testing, a pristine sample and the contaminated samples was cross-sectioned to further investigate the contamination area of the VLED package. Figure 121 shows the contamination source for this experiment.


Figure 121: Potential Contamination Source.

In this test, there are two potential contamination source. The first is the port stopper of the thermal and humidity chamber and it is made of vulcanized rubber. Sulfur is added to the natural rubber during the vulcanization process. However, sulfur is known to escape from the rubber, although with short chain plasticizing molecules at high temperature.

The second potential source of contamination is the adhesive epoxy used in the thermal and humidity chamber. In order to fix the thermal couple and humidity sensor, a lot of adhesive epoxy were used in the chamber during the maintenance. After the test, an obvious discoloration of the adhesive epoxy can be observed.

During the test, samples of the same XP-G LED packages are separated into two groups. Each group had a population of five. The first group stayed in the contaminated chamber until complete failure. Samples of the second group had been moved into VOCs free chambers after the observation of VOC contamination to monitor the reversibility of contamination. Table 10 shows the test matrix.

Table 10: Test Groups

| **Group** | **Group Attributes** |
|---|---|

| | |
|---|---|
| Groups-1 | Stayed in the contaminated chamber until complete failure due to VOC contamination |
| Groups-2 | Moved into VOCs free chambers after the observation of VOC contamination |

The first group's test result shown that luminous flux of the LEDs degraded dramatically in a short time due to the VOC contamination. The second group's test result shown that the VOC contamination process was reversible, if samples were transferred to a clean environment. During the test, pictures were taken to record the discoloration process at each readout time with digital camera.

Figure 122 show the expansion of the discolored area caused by VOCs contamination for the first group. The black area only appears in the phosphor layer. Detailed analysis is followed in the next phase.

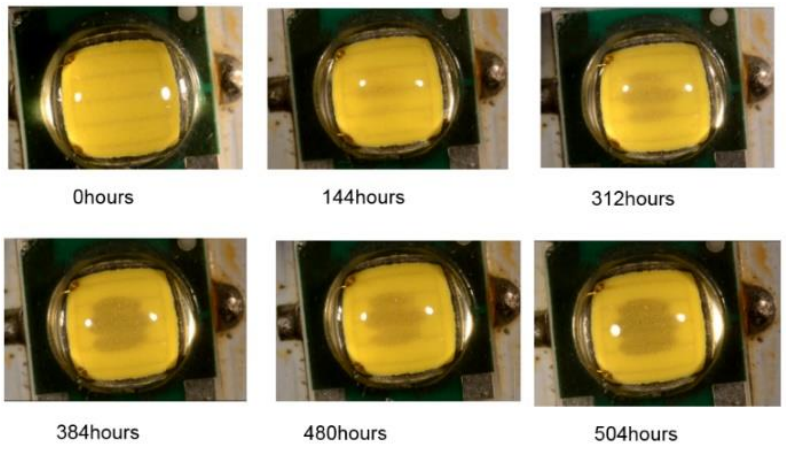


Figure 122: Expansion of Contamination Area.

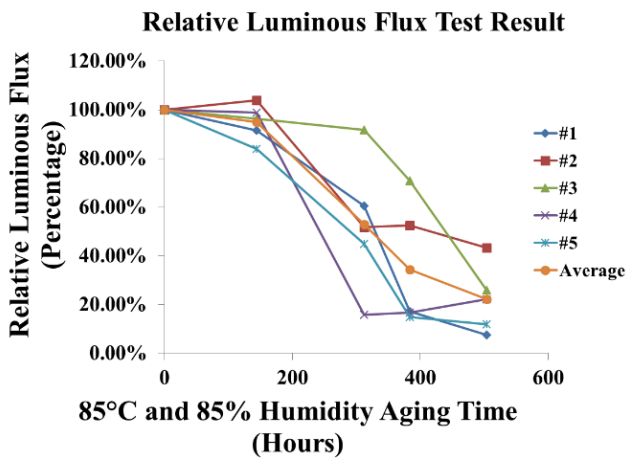


Figure 123:Relative Luminous Flux measurement of Group1.

Figure 123 shows the relative luminous flux of the group1 samples during the test. It is obvious that the luminous flux drops dramatically in a very short time in conjunction with the appearance of discoloration area. Figure 124 shows the recorded data of correlated color temperature. From the result, it can be observed that color shifts from white color to yellow area.

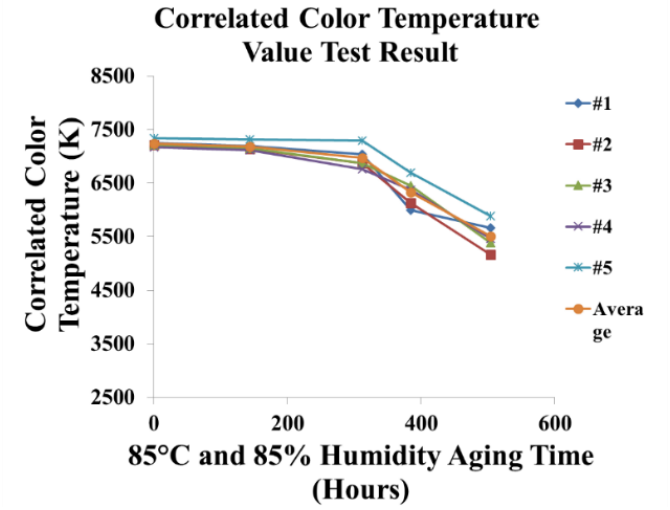


Figure 124: Correlated Color Temperature measurement of Group1.

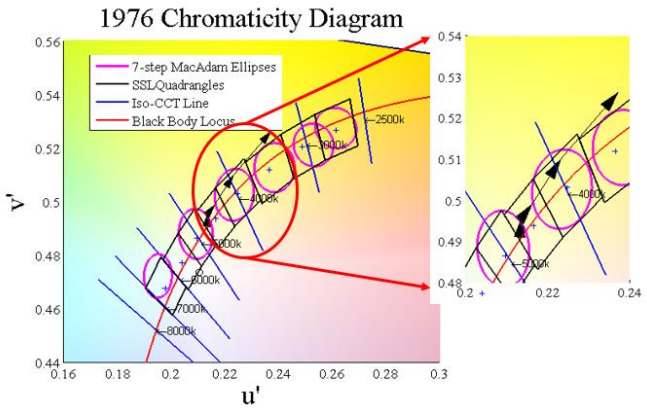


Figure 125: Color Shift in Chromaticity Tolerance of ANSI of Group 1.

It can be shown that the color temperature of the lamp shifts dramatically because of the discoloration of the phosphor. Figure 125 shows the color shift path of Group1 sample in ANSI tolerance for SSL source in the 1976 u', v' chromaticity diagram. The color shift follows the black arrow in the plot. Following the arrow, the color shift from near the Planckian locus to yellow area indicating a filtering of blue emission.

The other group test result shows that the discoloration process is reversible when samples were moved to VOCs free environment. Luminous flux output of the sample can go up again. Also, color coordinates in chromaticity space can shift back to the place that near white point. Figure 126 is the test result of relative luminous flux for the group2 samples. Relative luminous flux goes down dramatically caused by the VOC contamination and then goes up when samples were transferred to clean chamber.

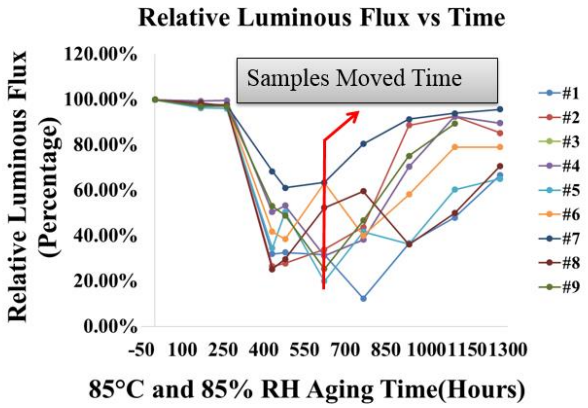


Figure 126: Relative Luminous Flux Measuement of  Group2.

Figure 127 shows the correlated color temperature test result of the second group. From the test result, the CCT value drops first and then starts to increase caused by the disappearance of discoloration area.

Figure 128 shows the color shift distance during the test. In the contaminated chamber, color shift dramatically in short time. When the samples were removed to clean chamber, the color shift distance started to decrease, because of the disappearance of discoloration area.

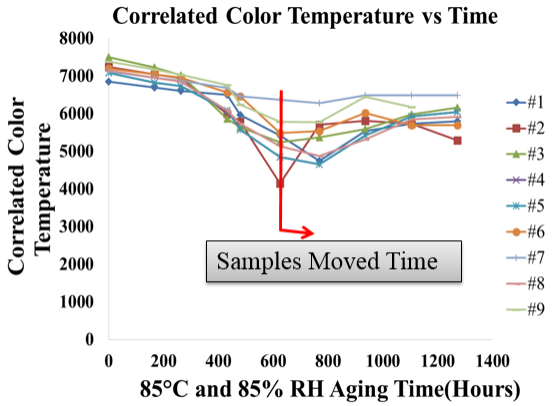


Figure 127: Correlated Color Temperature measurement of Group2.

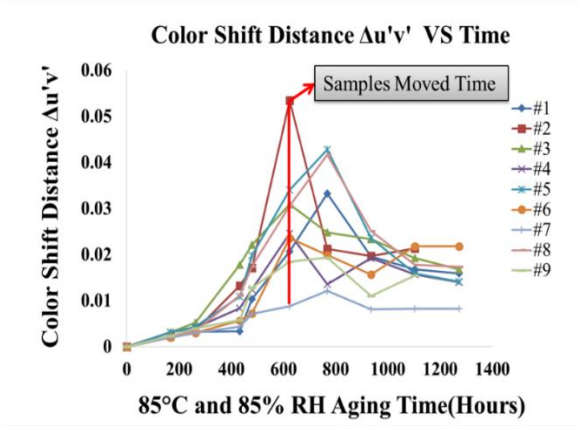


Figure 128: Color Shift Distance Measurement of Group2.

Figure 129 shows the color shift path of a sample from group 2 in ANSI tolerance for SSL source in the 1976 u', v' chromaticity diagram.

The color shift follows the black arrow in the plot. Following the arrow, the color shift from near the Planckian locus to the yellow area after contamination. However, when the sample were moved to VOCs free environment, its chromaticity coordinates started to go back to place that near the Planckian locus.

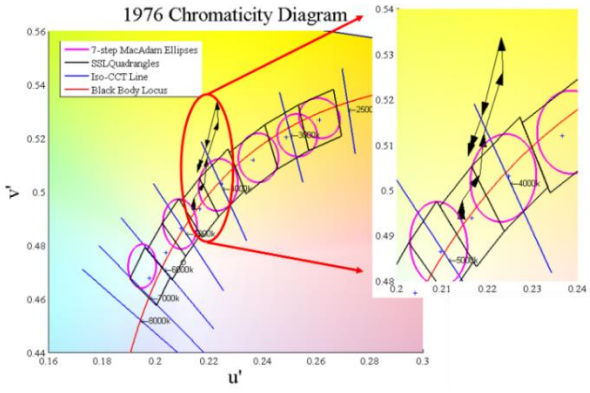


Figure 129: Color Shift in Chromaticity Tolerance of ANSI of Group 2.

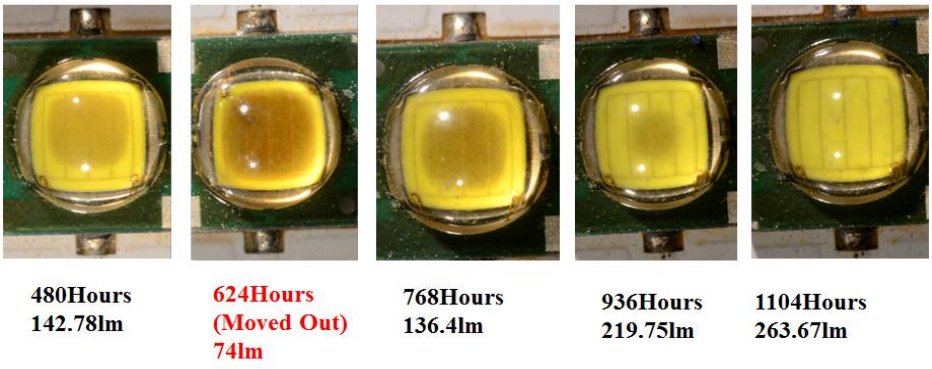


Figure 130: Reversing Process of VOC contamination.

During the reverse process, optical image of LED package was recorded to monitor the change of the contamination area on the phosphor layer. Figure 130 shows the reversing process of VOC contamination. From the following Figure 130, it can be show that VOC contamination is reversible when samples were moved to VOC free environment. After taking measurement for 624 hours in contaminated environment, samples were moved to VOC free environment. The black area on the phosphor is caused by the discoloration of VOCs. Special consideration should be put on the lens of these samples. The lens did not change during the experiment.

The conclusion is that during the accelerated test, high temperature and high percentage relative humidity made the vulcanized rubber and epoxy start to give off volatile organic compounds. Due to the sealed environment, VOCs of high density started to diffuse into the silicone polymer and were trapped into the space between the phosphor particles. When the LEDs went through the power cycle, high junction temperature and radiant power from the chip made the trapped VOCs start to discolor. Thus, the luminous flux degraded dramatically and color coordinates shifted significantly in the yellow direction. However, when the test samples were moved to a VOCs free environment, the VOCs trapped inside the phosphor particles will diffuse

out and the discoloration will disappear. The discoloration process caused by VOCs is reversible under clean environment.

### 4.3.2. WHTOL TEST WITH ELECTRICAL BIAS IN THE CLEAN ENVIRONMENT

The performance of high power pc-LED package under high temperature and high humidity in the VOC free environment is studied with several different warm white LED packages. Each of the LED packages was pre-soldered on a star board. They were powered up through the solder pads that connect the electrodes inside the package. Star board were directly fixed on the aluminum heat sink with screws.

In order to study the effects of package on the reliability of LEDs, several different package configurations were used in the experiment, such as XR-C, XP-G and XT-E. Each of them has different package configuration. XR-C LED package has a lateral package structure which requires two wire bonds to connect the anode and cathode of the die with the outside solder pad. In order to prevent damage of wire bonds from the mechanical vibration or shock stress, the whole package was encapsulated with silicone gel-like encapsulate. XP-G LED package structure is vertical compared with the XR-C LED package whose structure is lateral. The real functional die of XP-G LED is only 4-5μm in thickness. XT-E is thin film flip chip (TFFC) package structure and don't have wire bond any more. Instead, XT-E LED package structure uses solder bump to connect the die with the substrate. All these three LED package structure are phosphor converted based. The phosphor binder layer is dispensed on the top of the blue light emitter.

Test procedures followed the protocols that outlined in JESD22-A101C from the electronics industry. This test standard requires constant temperature and humidity. At the same time, test samples were electrical power biased on and off at an interval of one hour in the

environmental chamber. Six groups of samples were prepared for the designed test and each group had a population of five. Table 11shows the group attributes of each group in the test.

Table 11: Group Attributes

| **Group** | **Test Vehicle** | **Current** | **Test Condition** | **Sample Number** | **Aging Time** |
|---|---|---|---|---|---|
| Groups-1 | XR-C Warm White | 350mA | 85°C/85%RH | 5 | 5708 hours |
| Groups-2 | XP-G Warm White | 350mA | 85°C/85%RH | 5 | 5688 hours |
| Groups-3 | XP-G Warm White | 350mA | 75°C/75%RH | 5 | 4000 hours |
| Groups-4 | XT-E Warm White | 350mA | 85°C/85%RH | 5 | 5688 hours |
| Groups-5 | XT-E Warm White | 350mA | 75°C/75%RH | 5 | 4560 hours |
| Groups-6 | XTE Warm White | 350mA | 65°C/95%RH | 5 | 4824 hours |

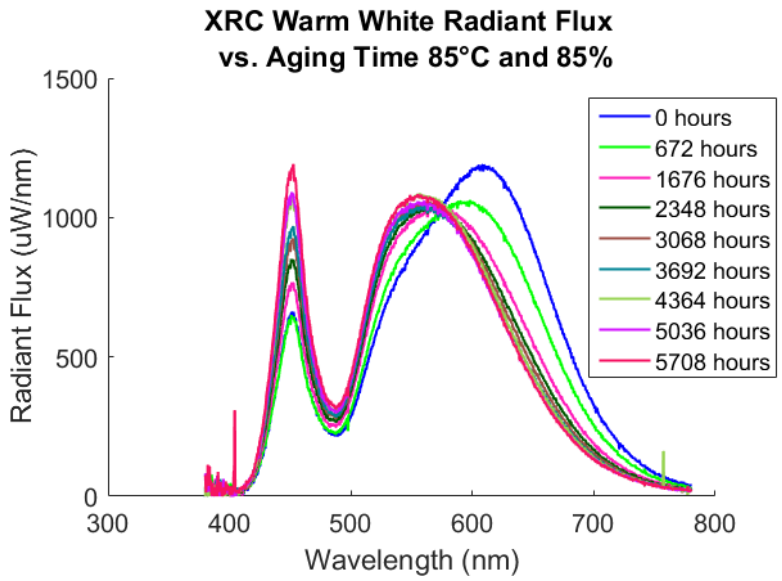


Figure 131: Absolute Radiant Flux Measuremnt of XR-C LED at 85°C/85%RH.

Figure 131 shows the absolute radiant flux measurement of XR-C LED at 85°C/85%RH. Absolute radiant flux is measured with spectroradiometer and integrating sphere in μW/nm. Absolute radiant flux of each visible wavelength was plot together as a spectrum.

Based on the absolute radiant flux, the luminous flux could be calculated. Figure 132 shows the luminous flux of XR-C LED at 85°C/85%RH aging condition. Figure 133 shows the CCT measurements of XR-C LED at 85°C/85%RH aging condition.

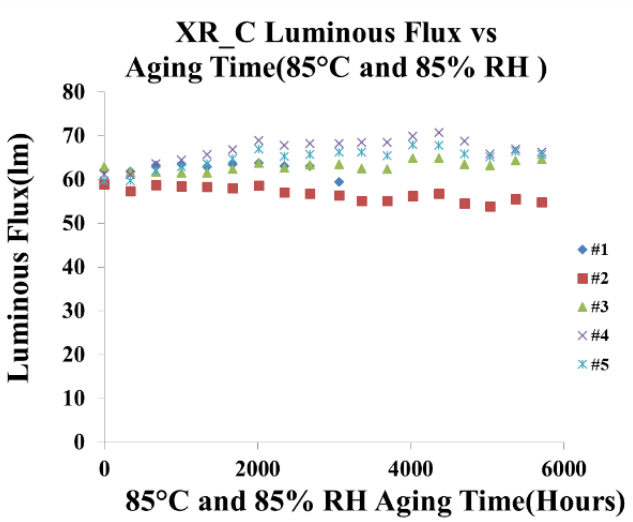


Figure 132: Luminous Flux Measurement of XR-C LED at 85°C/85%RH.

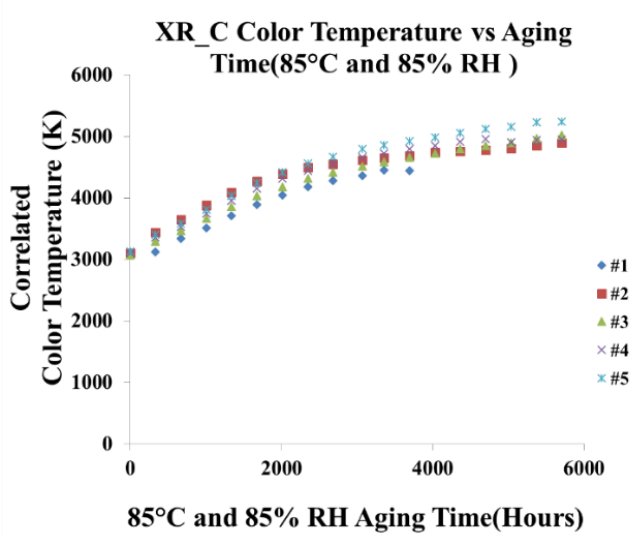


Figure 133: Correlated Color Temperature Measurement of XR-C LED at 85°C/85%RH.

After the integration, the absolute radiant flux, the radiant power can be calculated. Figure 134 shows the radiant power measurement of XR-C LED at 85°C/85%RH aging condition. Figure 135 shows the blue to yellow ratio measurement of XR-C LED at 85°C/85%RH aging condition.

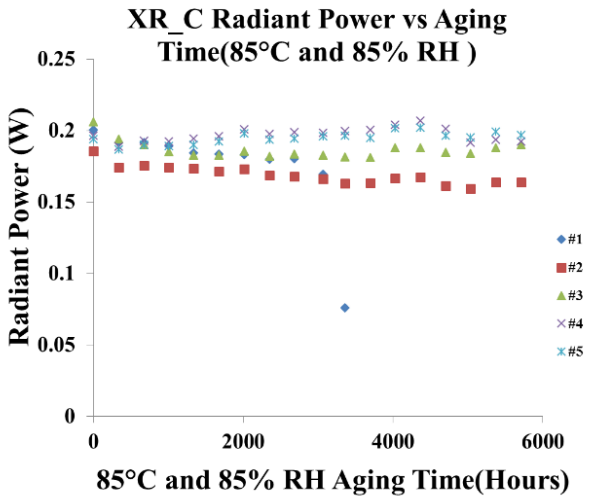


Figure 134: Radiant Power Measurement of XR-C LED at 85°C/85%RH.

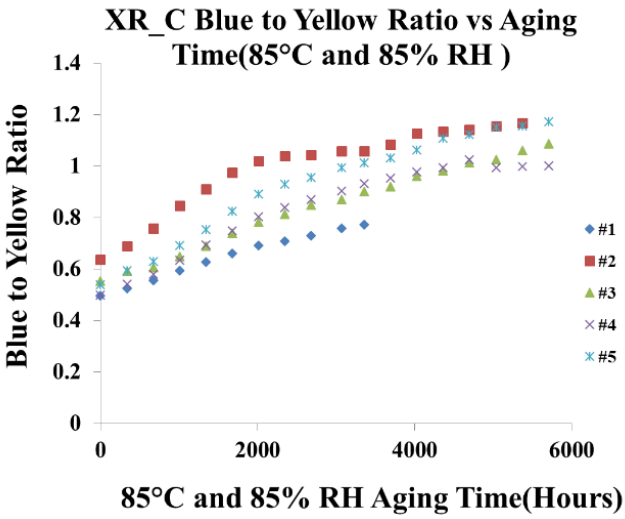


Figure 135: Blue to Yellow Ratio Measurement of XR-C LED at 85°C/85%RH.

Figure 136 shows the yellow peak wavelength. Monitoring the wavelength of the peak wavelength helps to understand the degradation mechanisms of LED packages. Figure 137 shows the color shift distance measurement of XR-C LED at 85°C/85%RH aging condition.

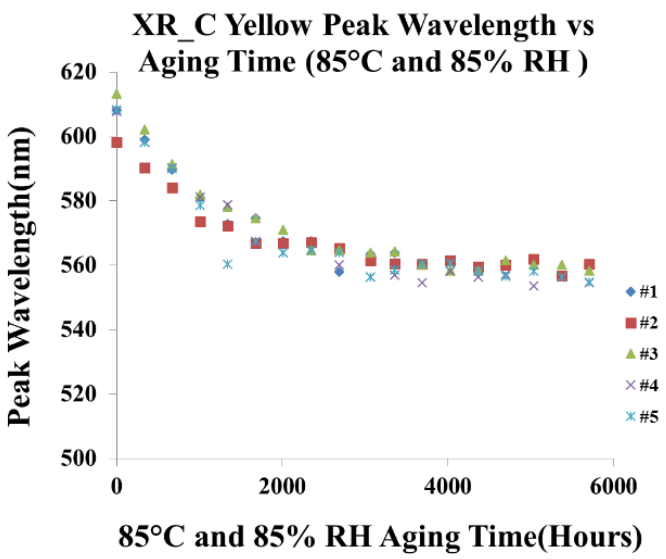


Figure 136: Yellow Peak Wavelength Measurement of XR-C LED at 85°C/85%RH.

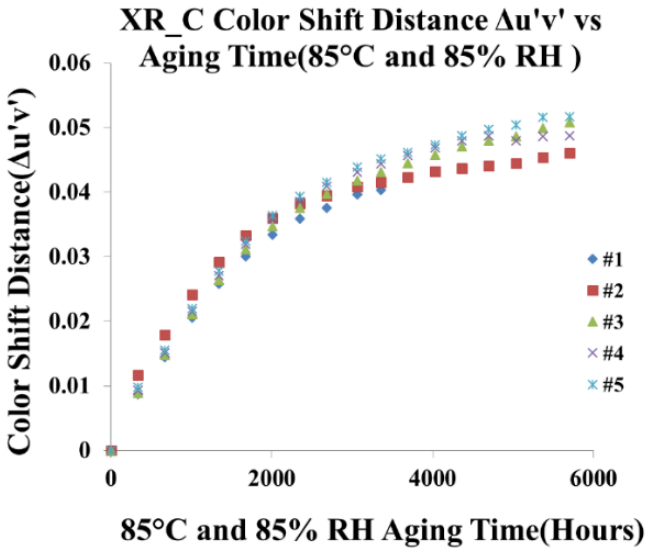


Figure 137: Color Shift Distance Measurement of XR-C LED at at 85°C/85%RH.

Figure 138 shows the color shift path in CIE 1976 Chromaticity diagram. Color shift follows the black arrow in the plot. VI curve of the samples had been taken. Figure 139 shows the

VI curve test result of one sample at 85°C/85%RH. Test results of other samples in each group have the same pattern.

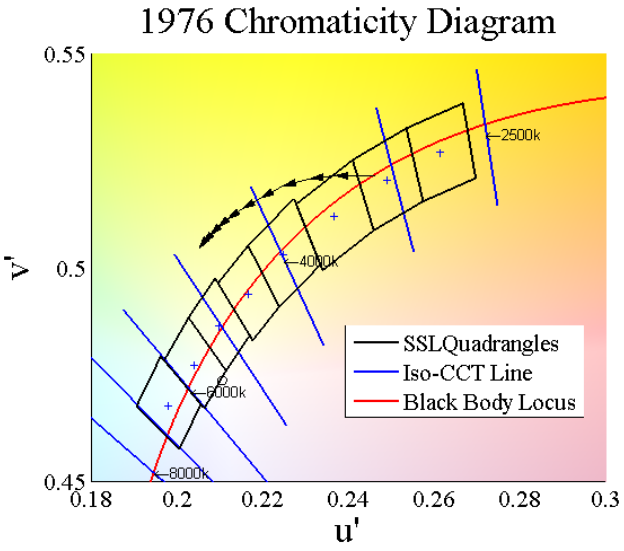


Figure 138: Color Shift Path of XR-C LED at 85°C/85%RH.

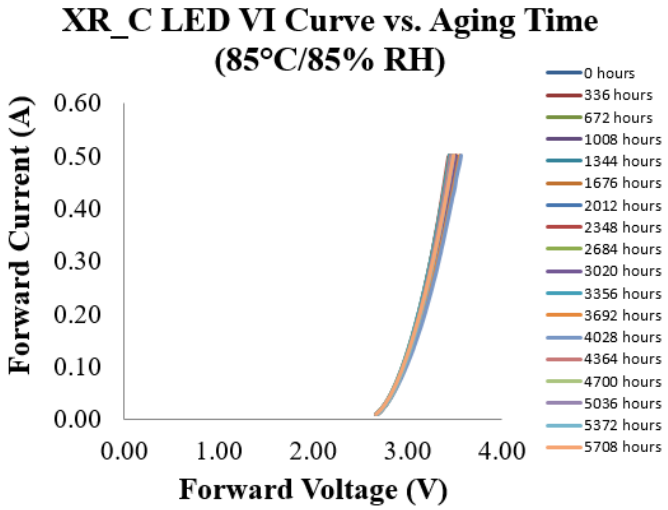


Figure 139: XR-C VI curve measurement at 85°C/85%RH.

Figure 140 shows the absolute radiant flux measurement of XP-G LED at 85°C/85%RH. Based on the absolute radiant flux, the luminous flux could be calculated. Figure 141 shows the luminous flux of XP-G LED at 85°C/85%RH aging condition.

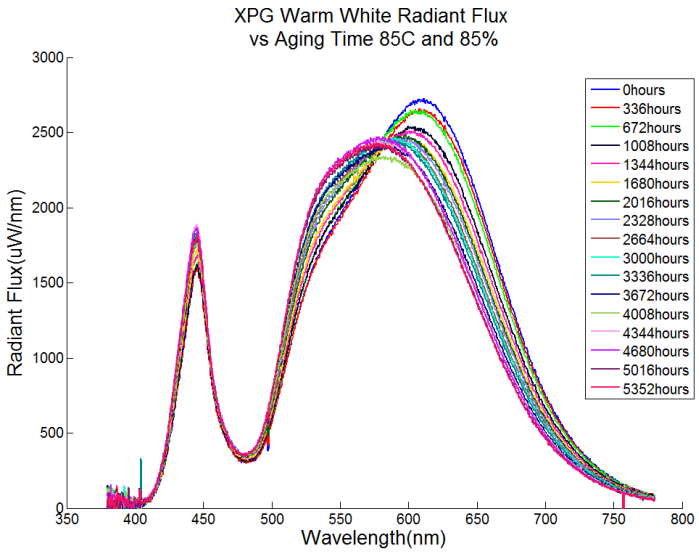


Figure 140: Absolute Radiant Flux Measurement of XP-G LED at 85°C/85%RH.

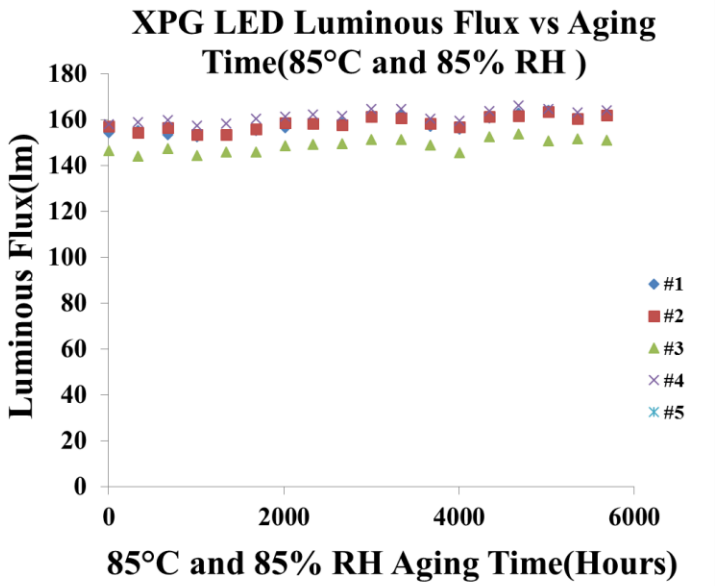


Figure 141: Luminous Flux Measurement of XP-G LED at 85°C/85%RH.

Figure 142 shows the CCT measurements of XP-G LED at 85°C/85%RH aging condition. Figure 143 shows the radiant power measurement of XP-G LED at 85°C/85%RH aging condition, which can be calculated by the integration the absolute radiant flux.

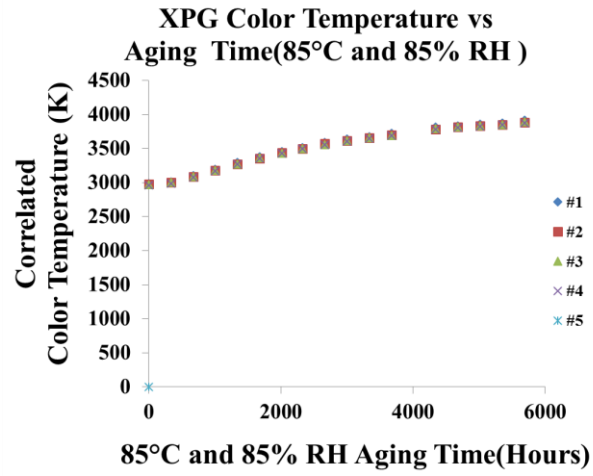


Figure 142: Correlated Color Temperature Measurement of XP-G LED at 85°C/85%RH.

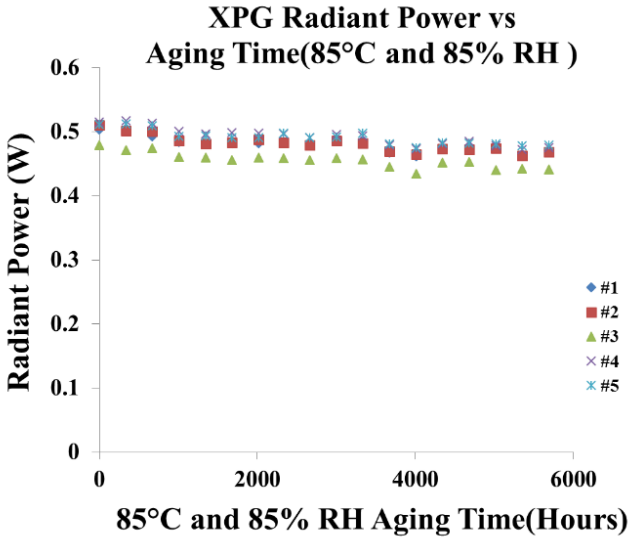


Figure 143: Radiant Power Measurement of XP-G LED at 85°C/85%RH.

Figure 144 shows the blue to yellow ratio measurement of XP-G LED at 85°C/85%RH aging condition. Figure 145 shows the yellow peak wavelength. Monitoring the wavelength of the peak wavelength helps to understand the degradation mechanisms of LED packages.

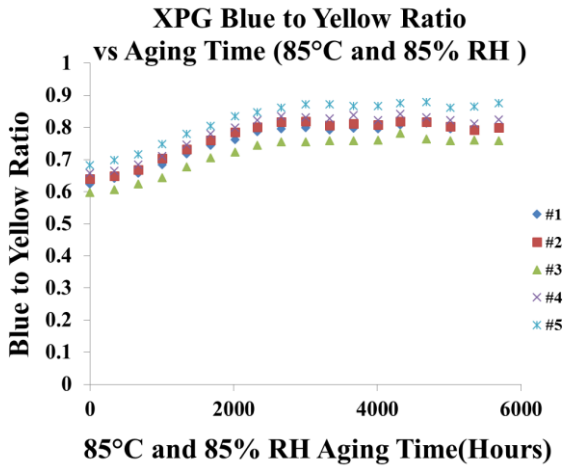


Figure 144: Blue to Yellow Ratio Measurement of XP-GLED at 85°C/85%RH.

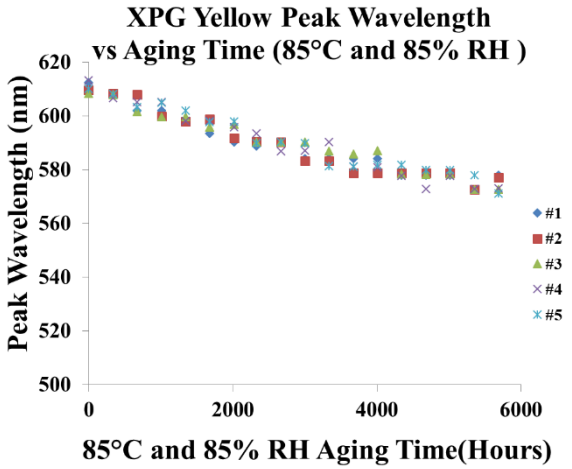


Figure 145: Yellow Peak Wavelength Measurement of XP-G LED at 85°C/85%RH.

Figure 146 shows the color shift distance measurement of XP-G LED at 85°C/85%RH aging condition. Figure 147 shows the color shift path in CIE 1976 Chromaticity diagram. Color shift follows the black arrow in the plot.

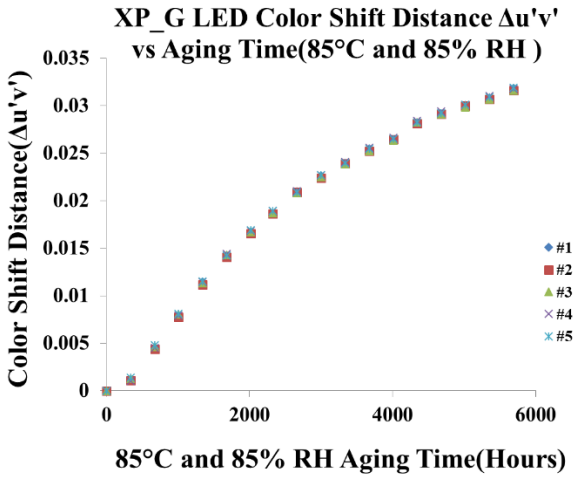


Figure 146: Color Shift Distance Measurement of XP-G LED at 85°C/85%RH

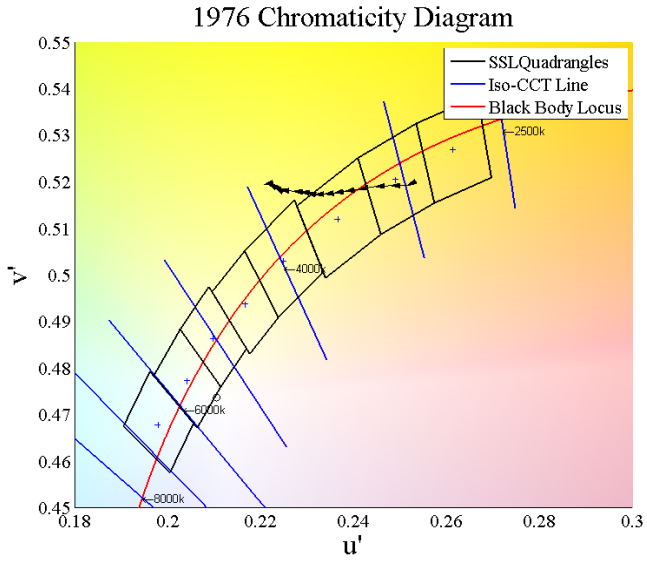


Figure 147: Color Shift Path of XP-G LED at at 85°C/85%RH.

Figure 148 shows the VI curve test result of one sample at 85°C/85%RH. Test results of other samples in each group have the same pattern. Figure 149 shows the CCT measurements of XP-G LED at 75°C/75%RH aging condition.

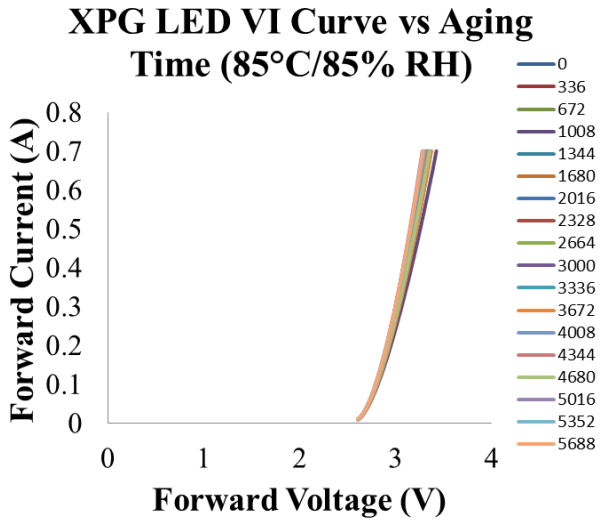


Figure 148: XP-G VI curve measurement at 85°C/85%RH.

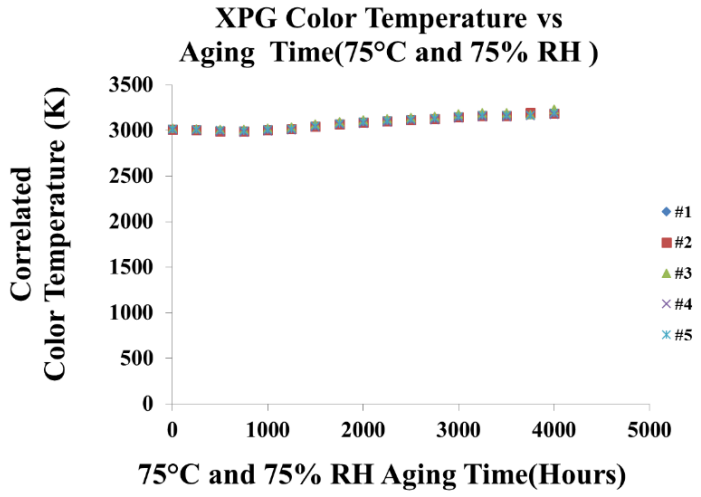


Figure 149: Correlated Color Temperature Measurement of XP-G LED at 75°C/75%RH.

Figure 150 shows the color shift distance measurement of XPG LED at 75°C/75%RH aging condition. Figure 151 shows the absolute radiant flux measurement of XT-E LED at 85°C/85%RH.

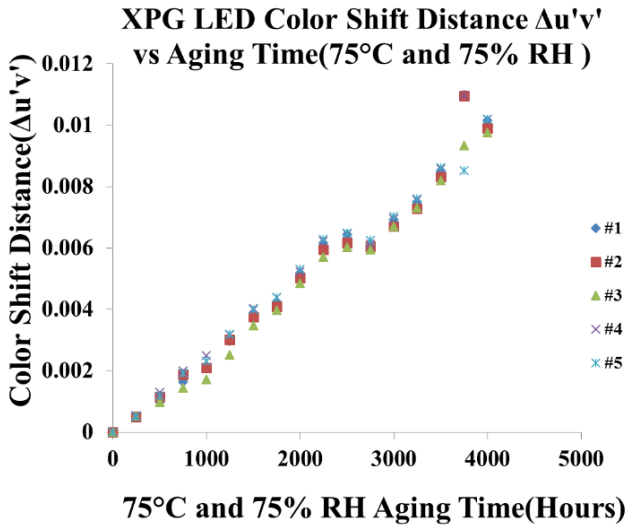


Figure 150: Color Shift Distance Measurement of XP-G LED at 75°C/75%RH.

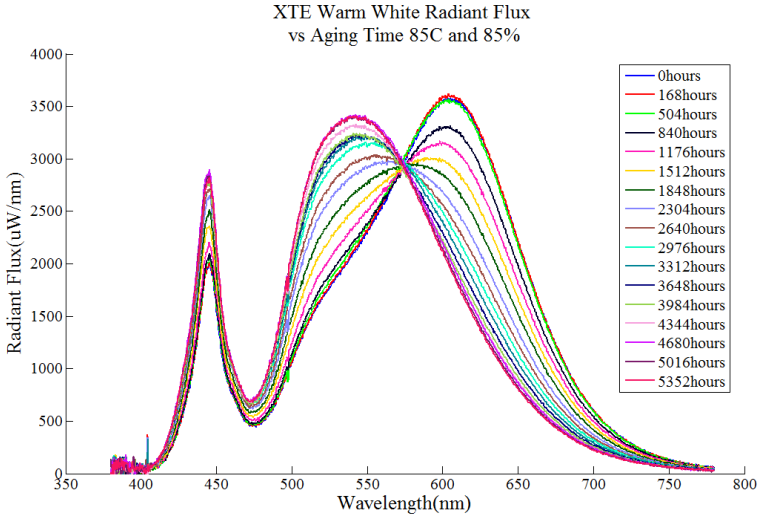


Figure 151: Absolute Radiant Flux Measurement of XT-E LED at 85°C/85%RH.

Based on the absolute radiant flux, the luminous flux could be calculated. Figure 152 shows the luminous flux of XT-E LED at 85°C/85%RH aging condition. Figure 153 shows the CCT measurements of XT-E LED at 85°C/85%RH aging condition.

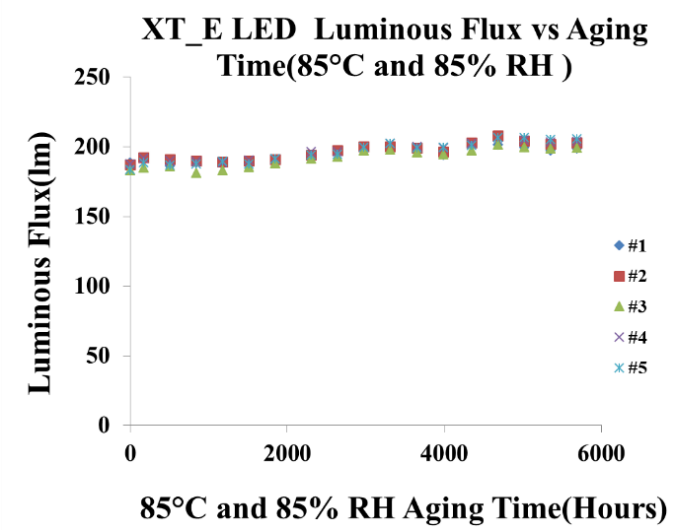


Figure 152: Luminous Flux Measurement of XT-E LED at 85°C/85%RH.

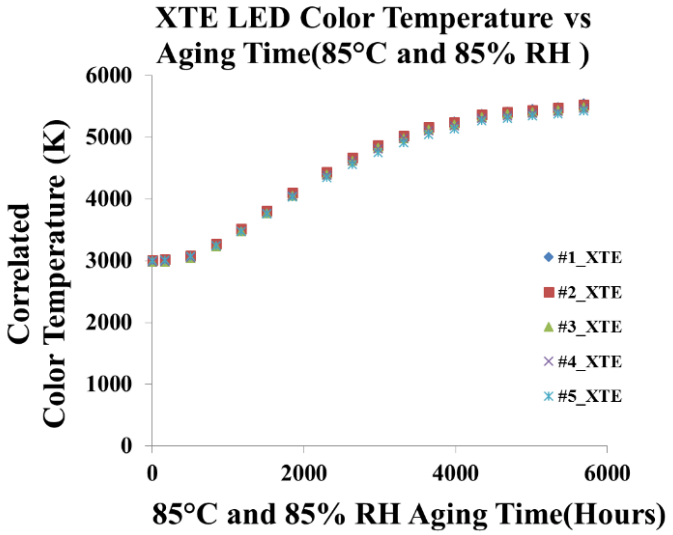


Figure 153: Correlated Color Temperature Measurement of XT-E LED at 85°C/85%RH.

Figure 154 shows the radiant power measurement of XT-E LED at 85°C/85%RH aging condition, which can be calculated by the integration the absolute radiant flux. Figure 155 shows the blue to yellow ratio measurement of XT-E LED at 85°C/85%RH aging condition.

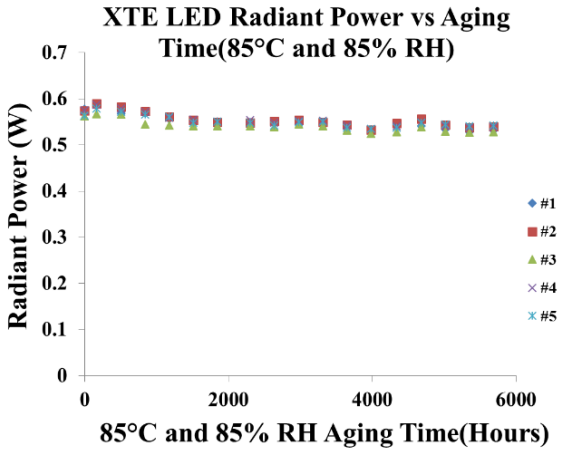


Figure 154: Radiant Power Measurement of XT-E LED at 85°C/85%RH.

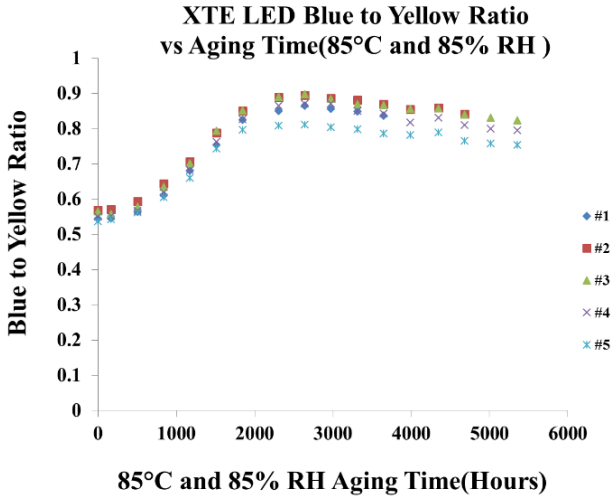


Figure 155: Blue to Yellow Ratio Measurement of XT-E LED at at 85°C/85%RH.

Figure 156 shows the yellow peak wavelength. Monitoring the wavelength of the peak wavelength helps to understand the degradation mechanisms of LED packages. Figure 157 shows the color shift distance measurement of XT-E LED at 85°C/85%RH aging condition.

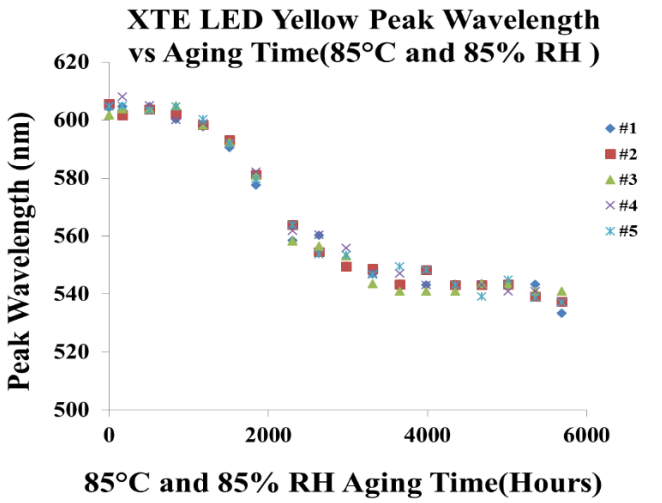


Figure 156: Yellow Peak Wavelength Measurement of XT-E LED at 85°C/85%RH.

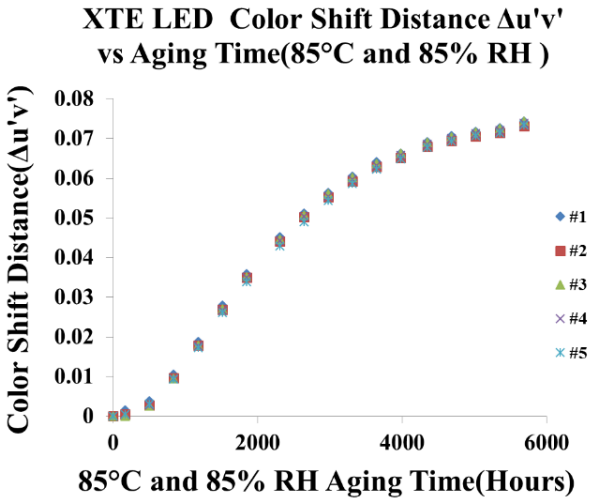


Figure 157: Color Shift Distance Measurement of XT-E LED at at 85°C/85%RH.

Figure 158 shows the color shift path in CIE 1976 Chromaticity diagram. Color shift follows the black arrow in the plot. Figure 159 shows the VI curve test result of one sample at 85°C/85%RH. Test results of other samples in each group have the same pattern.

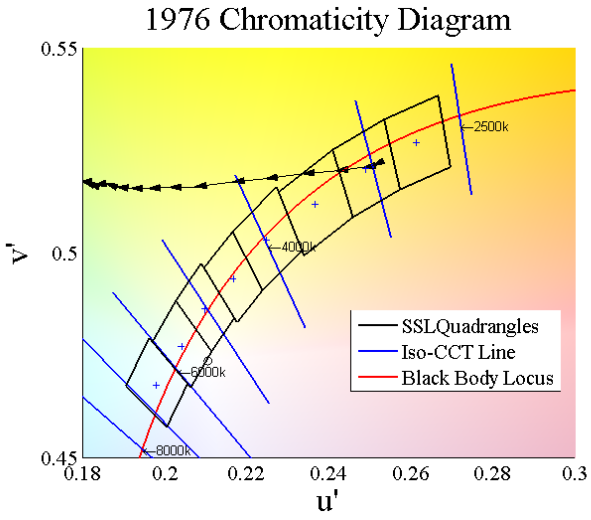


Figure 158: Color Shift Path of XT-E LED at at 85°C/85%RH.

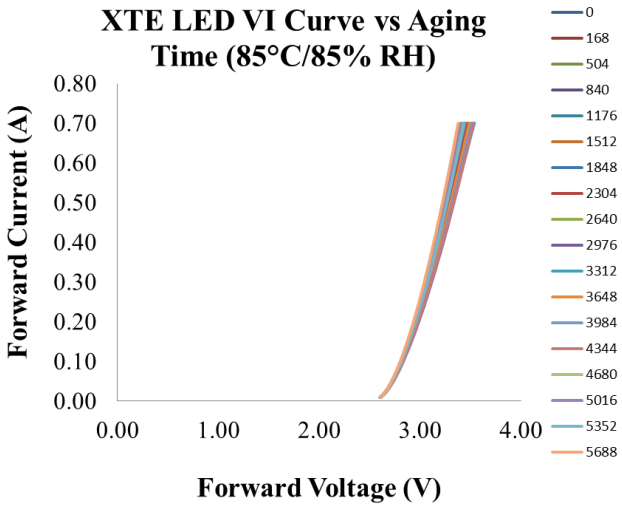


Figure 159: XTE VI curve measurement at 85°C/85%RH.

Figure 160 shows the absolute radiant flux measurement of XT-E LED at 75°C/75%RH. Based on the absolute radiant flux, the luminous flux could be calculated. Figure 161 shows the luminous flux of XT-E LED at 75°C/75%RH aging condition.

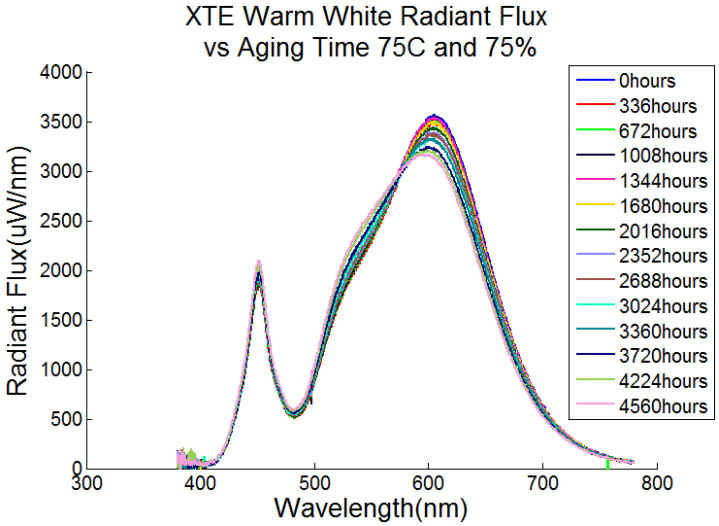


Figure 160: Absolute Radiant Flux Measurement of XT-E LED at 75°C/75%RH.

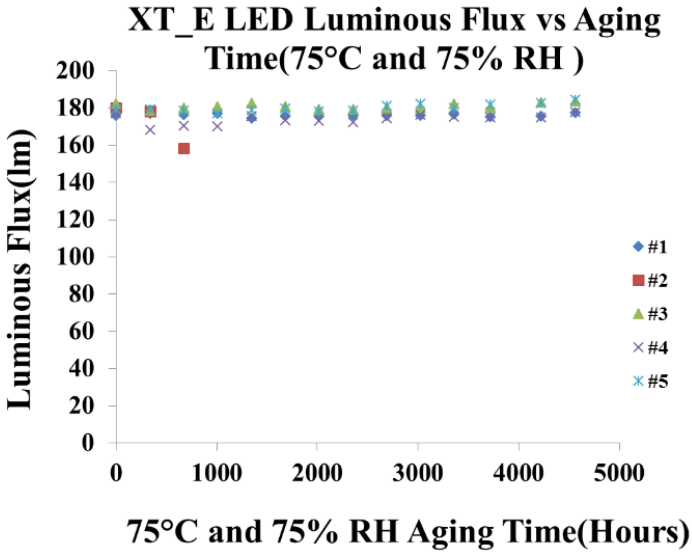


Figure 161: Luminous Flux Measurement of XT-E LED at 75°C/75%RH.

Figure 162 shows the CCT measurements of XT-E LED at 75°C/75%RH aging condition. Figure 163 shows the radiant power measurement of XT-E LED at 75°C/75%RH aging condition, which can be calculated by the integration the absolute radiant flux.

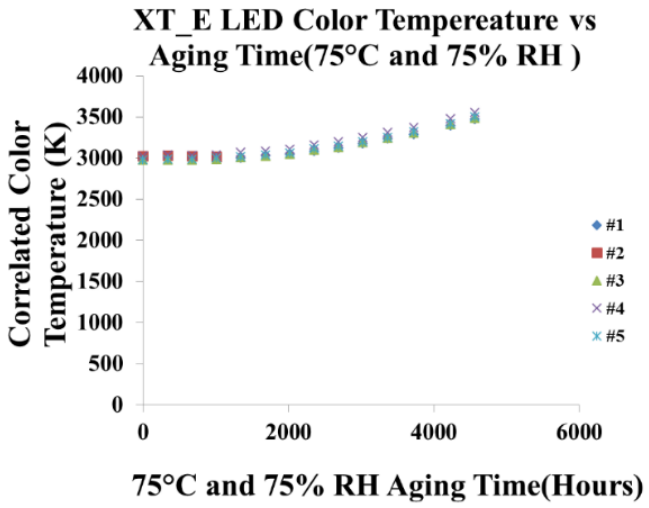


Figure 162: Correlated Color Temperature Measurement of XT-E LED at 75°C/75%RH.

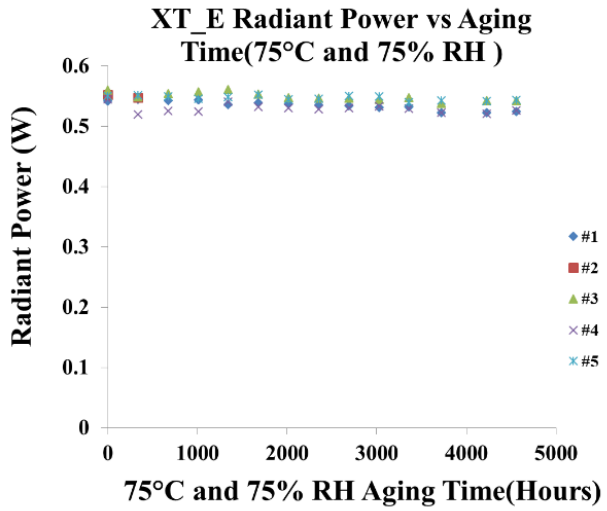


Figure 163: Radiant Power Measurement of XT-E LED at 75°C/75%RH.

Figure 164 shows the blue to yellow ratio measurement of XT-E LED at 75°C/75%RH aging condition. Figure 165 shows the yellow peak wavelength. Monitoring the wavelength of the peak wavelength helps to understand the degradation mechanisms of LED packages.

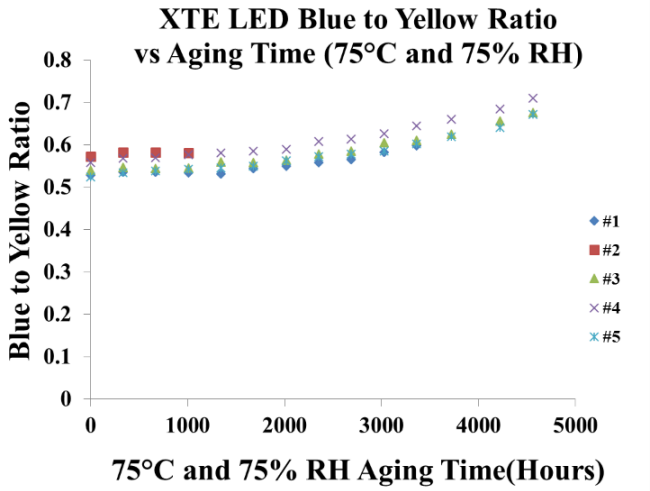


Figure 164: Blue to Yellow Ratio Measurement of XT-E LED at at 75°C/75%RH.

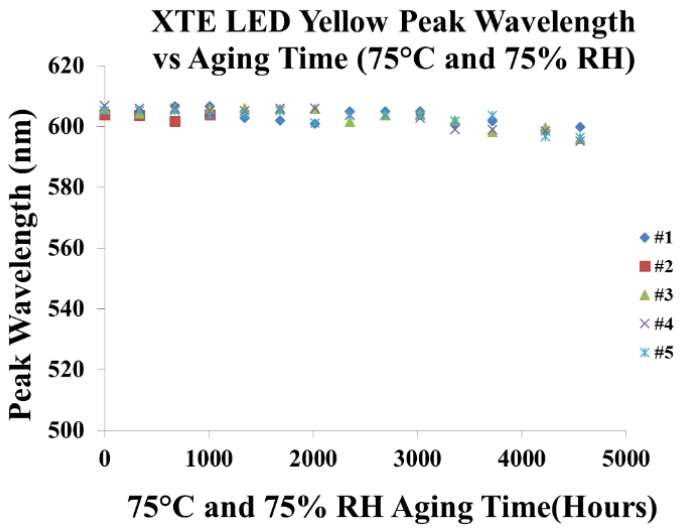


Figure 165: Yellow Peak Wavelength Measurement of XT-E LED at 75°C/75%RH.

Figure 166 shows the color shift distance measurement of XT-E LED at 75°C/75%RH aging condition. Figure 167 shows the color shift path in CIE 1976 Chromaticity diagram. Color shift follows the black arrow in the plot.

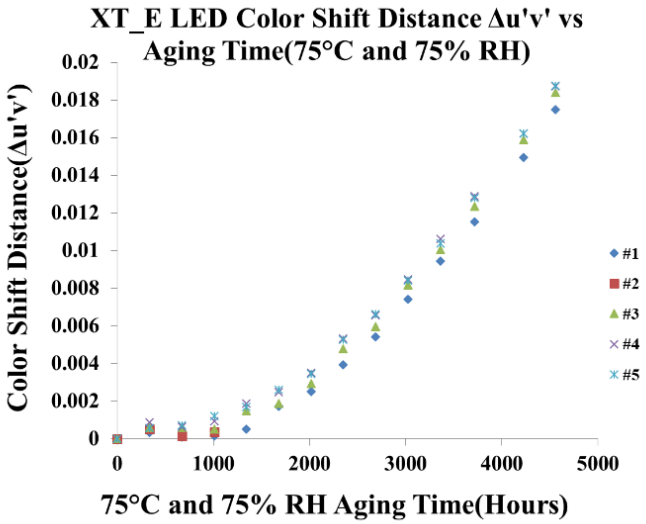


Figure 166: Color Shift Distance Measurement of XT-E LED at 75°C/75%RH.

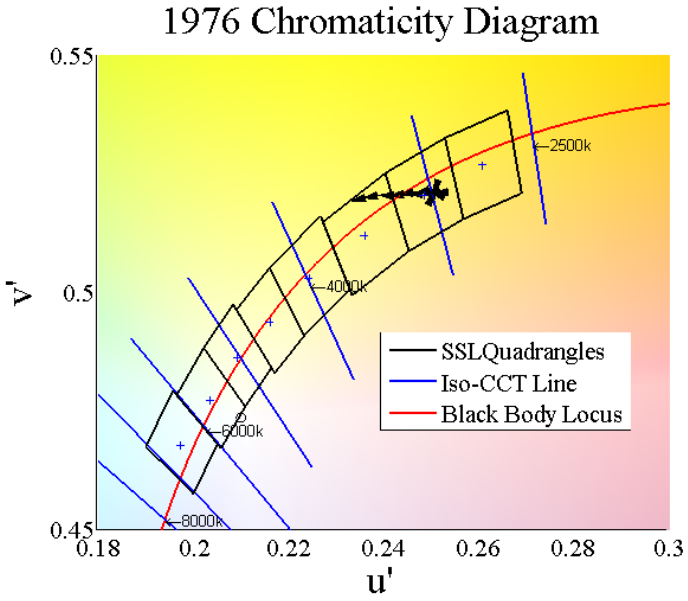


Figure 167: Color Shift Path of XT-E LED at 75°C/75%RH.

Figure 168 shows the VI curve test result of one sample at 75°C/75%RH. Test results of other samples in each group have the same pattern. Figure 169 shows the absolute radiant flux measurement of XT-E LED at 65°C/90%RH.

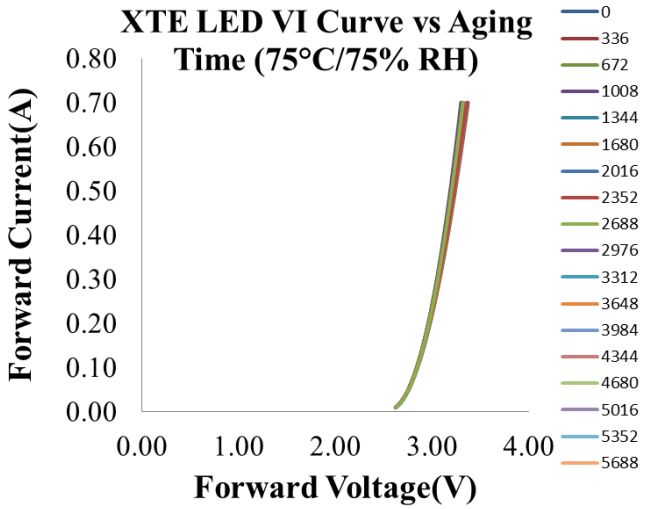


Figure 168: XT-E VI curve measurement at 75°C/75%RH.

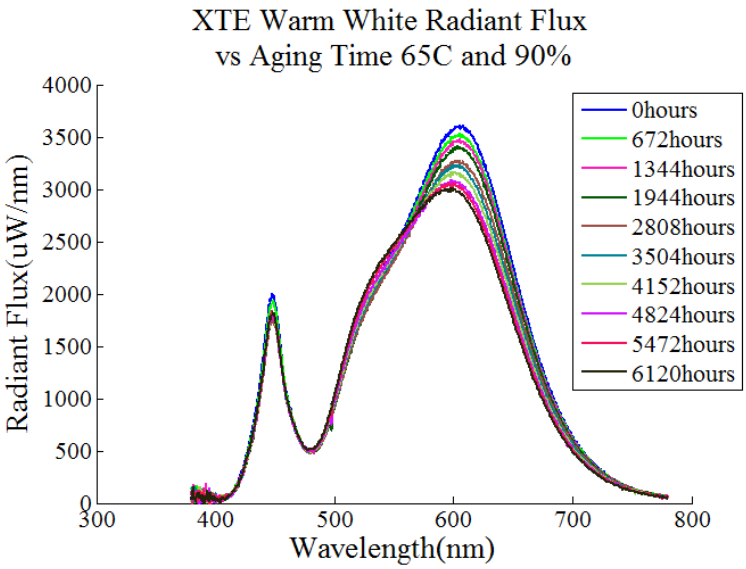


Figure 169: Absolute Radiant Flux Measurement of XT-E LED at 65°C/90%RH.

Based on the absolute radiant flux, the luminous flux could be calculated. Figure 170 shows the luminous flux of XT-E LED at 65°C/90%RH aging condition. Figure 171 shows the CCT measurements of XT-E LED at 65°C/90%RH aging condition.

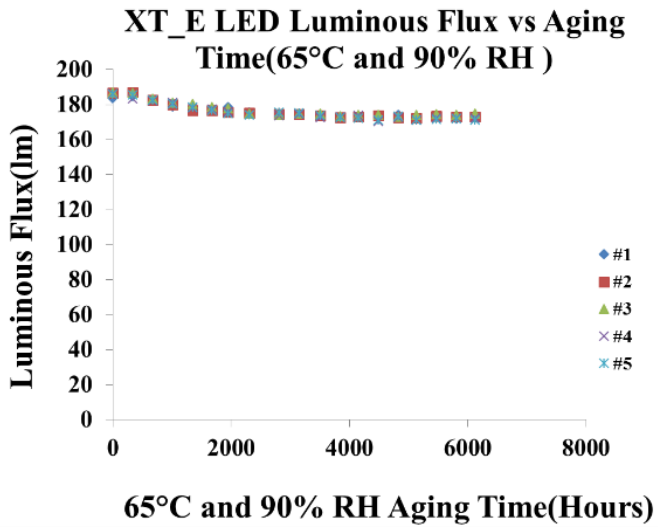


Figure 170: Luminous Flux Measurement of XT-E LED at 65°C/90%RH.

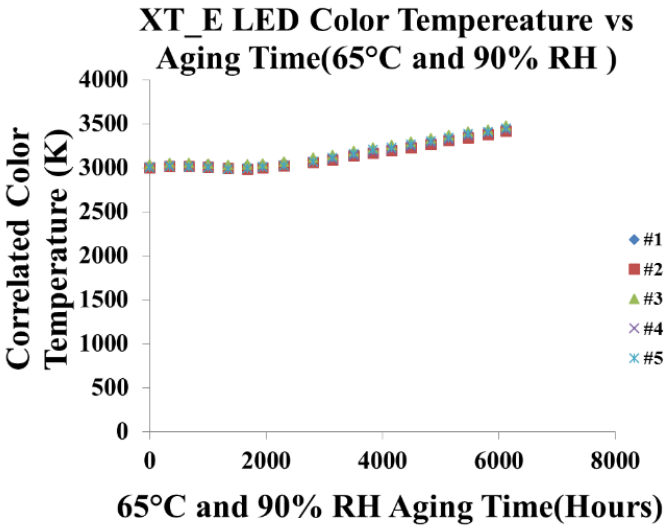


Figure 171: Correlated Color Temperature Measurement of XT-E LED at 65°C/90%RH.

Figure 172 shows the radiant power measurement of XT-E LED at 65°C/90%RH aging condition, which can be calculated by the integration the absolute radiant flux. Figure 173 shows the blue to yellow ratio measurement of XT-E LED at 65°C/90%RH aging condition.

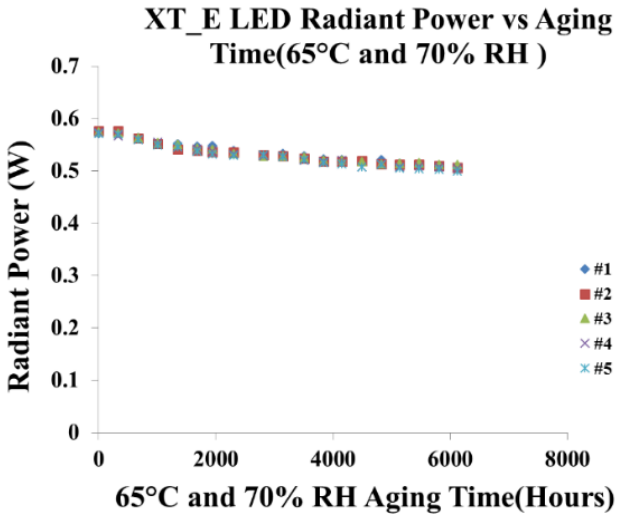


Figure 172: Radiant Power Measurement of XT-E LED at 65°C/90%RH.

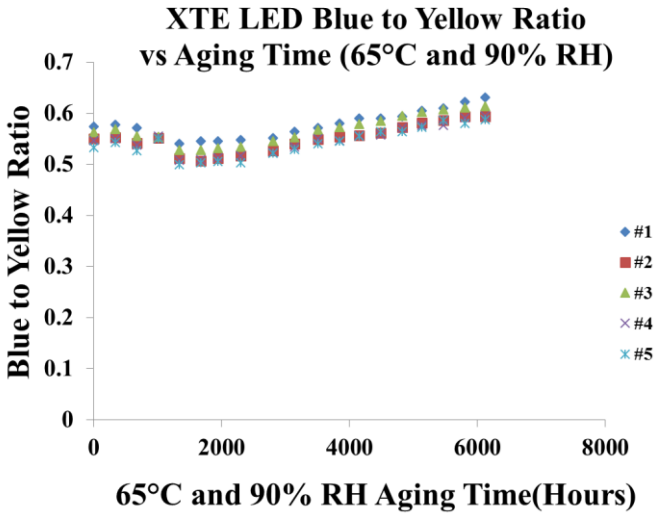


Figure 173: Blue to Yellow Ratio Measurement of XT-E LED at 65°C/90%RH.

Figure 174 shows the yellow peak wavelength. Monitoring the wavelength of the peak wavelength helps to understand the degradation mechanisms of LED packages. Figure 175 shows the color shift distance measurement of XT-E LED at 65°C/90%RH aging condition.

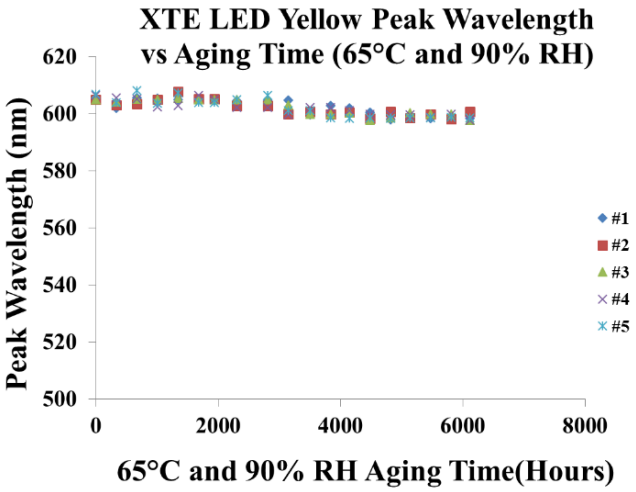


Figure 174: Yellow Peak Wavelength Measuremnt of XT-E LED at 65°C/90%RH.

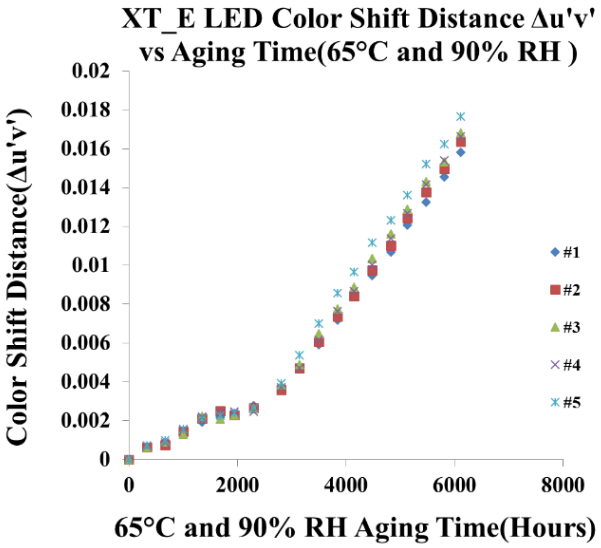


Figure 175: Color Shift Distance Measuremnt of XT-E LED at 65°C/90%RH.

Figure 176 shows the color shift path in CIE 1976 Chromaticity diagram. Color shift follows the black arrow in the plot.

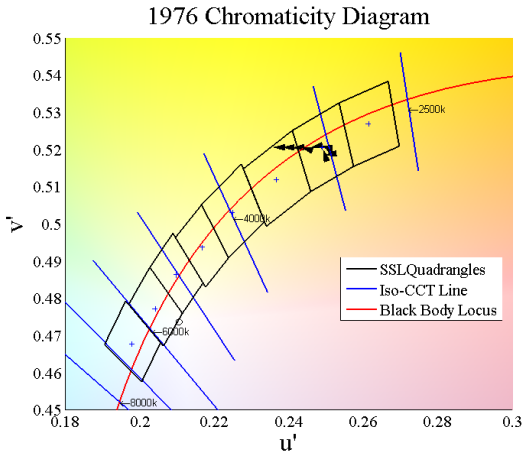


Figure 176: Color Shift Path of XT-E LED at 65°C/90%RH.

## 4.4. TEMPERATURE HUMIDITY EFFECTS COMPARISON

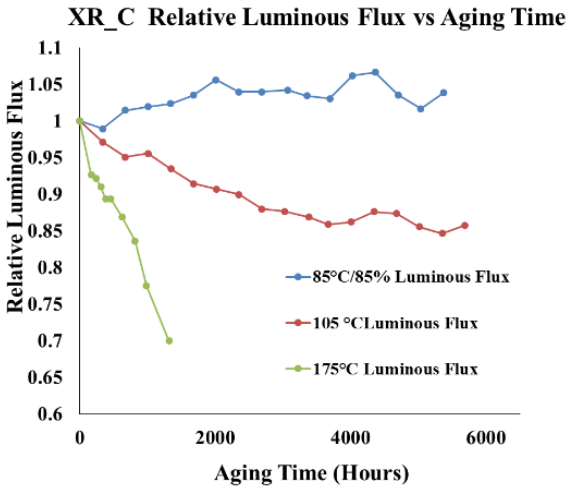


Figure 177: XR-C LED luminous flux maintenance measurement at various aging conditions.

Degradation of the absolute radiant flux over the aging time can be observed from the above measurements. Also, from the observation, there is no sign of a shift in the yellow peak

spectrum in the high temperature test, which means that the phosphor is still functioning well after high temperature aging.

Absolute radiant flux measurement at 175°C demonstrates a dramatic drop in the blue peak compared with the measurement at 105°C, which indicates a degradation of the blue emitter during the extreme high temperature aging. It can also be concluded that higher temperature will lead to a higher decay ratio of the absolute radiant flux spectrum by comparing the measurement from 175°C and 105°C. The luminous flux maintenance of XRC LEDs at different aging condition is plotted as a function of aging time in Figure 177.

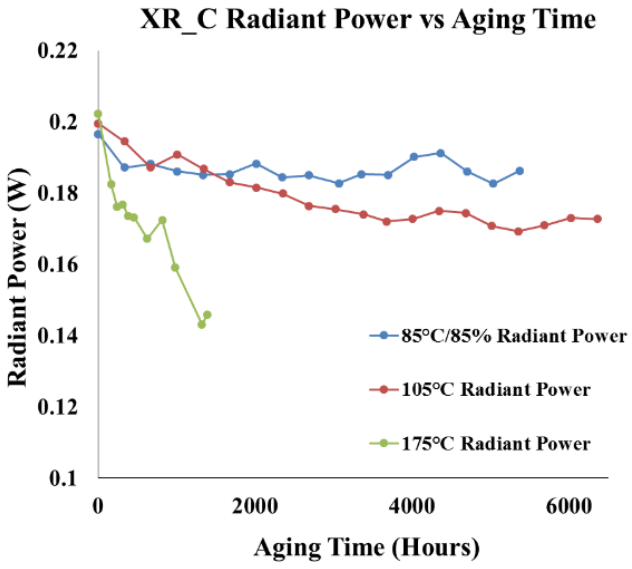


Figure 178: Radiant Power Measurements of XR-C LED.

All samples under 175°C failed after a short time (less than 2000 hours), due to the extreme high junction temperature. Test result demonstrates that the luminous flux actually increases during the 85C/85% aging condition. The absolute radiant flux spectrum of shifted to the left

during the accelerated life test and it will be scaled more by the photopic sensitivity equation. As a result, the calculated luminous flux will increase.

In contrast, a decline in luminous flux was observed for the LEDs under pure high temperature aging. The result is in agreement with the measurement of the absolute radiant flux also. Another way to examine this is to check the radiant power of LED package. Figure 178 demonstrates the change of radiant power over the aging time.

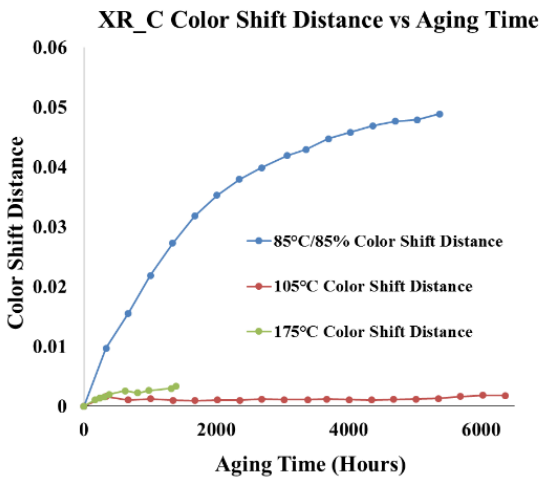


Figure 179: Color Shift Distance Measuremnt of XR-C LED under various aging conditions.

Radiant power is calculated by the integration of absolute spectral radiant flux without the scale of photopic sensitivity equation. The radiant power of all three groups should decrease, due to the degradation of optical parts and the blue light emitter. The test result shows that high temperature will lead to high decay ratio of the radiant power. The blue emitter of the package will degrade according to the ambient temperature. Less photons will be emitted by the degraded emitter at higher junction temperature.

Color Shift Distance is the absolute distance between the accelerated tested LED package's chromaticity coordinates and the pristine LED package's chromaticity coordinate in the CIE 1976

color space. Monitoring the color shift distance helps to monitor the color stability of the LED package and build the health management system. Figure 179 shows the color shift distance test result of XR-C LED under various aging conditions.

Test result from above analysis demonstrates that humidity can alter the phosphor and binder layer that sit on top of the blue photon emitter. Also, analysis in this study and the previous study show that high ambient temperature degrades the optical parts of the package and leads to the reduction of luminous flux. If the junction temperature goes across the limit, the contact resistance of the diode will go up and lead to a VI curve shift. Consequently, the package will fail catastrophically, due to the accumulated heat.

## 4.5. Failure Mechanism Analysis

### 4.5.1. Failure Analysis of VOC contamination

To further study the VOC contamination area of the XP-G LED packages, a pristine sample and a contaminated sample were cross sectioned as depicted by the red line in Figure 180.

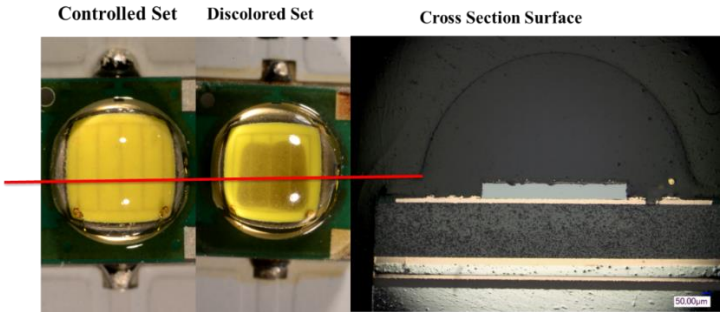


Figure 180: Cross-Section Analysis of the VOC Contamination Area.

Additionally, an image of the polished surface of the pristine XP-G LED package is shown in Figure 181 as well as the zoomed in picture.

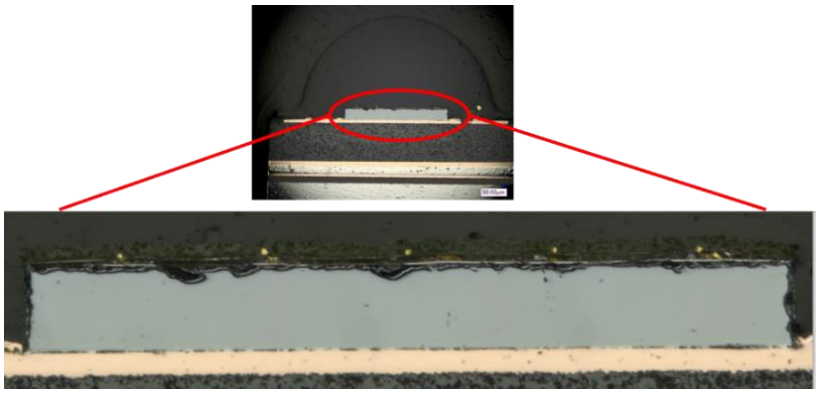

Figure 181: Prinstine XP-G LED Package Cross-Section.

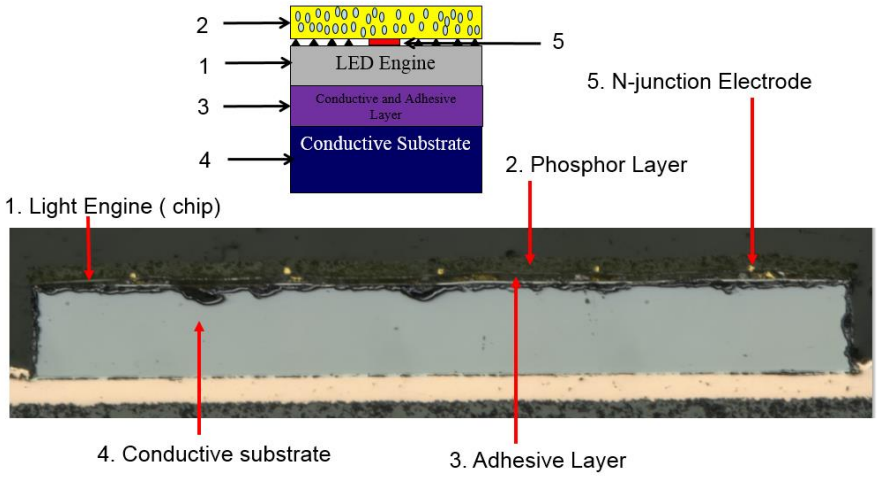


Figure 182: LED Package Structure.

Details analysis have been down on the area near the LED chip in the package. The following Figure 182 shows the magnified view of the chip area. From the image, different layers can be seen clearly. Each layer will be analyzed in the next phase. During the fabrication of LED package, each layer is combined together with different method. In the Figure 182, 5 layers have been identified to help understanding the VOC contamination process and place. Also, a diagram has been draw on the top to help understanding the vertical structure of LED chip.

SEM image of the chip area have been taken to further observe the details of the chip area which can be shown in Figure 183. From the image, surface pattern and n electrode can be see very clearly. The thickness of the thin film chip is about 2-3 µm.

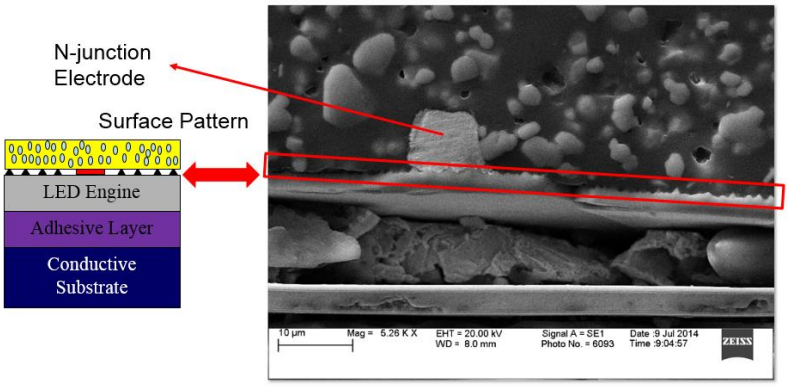


Figure 183: SEM View of the Chip Area.

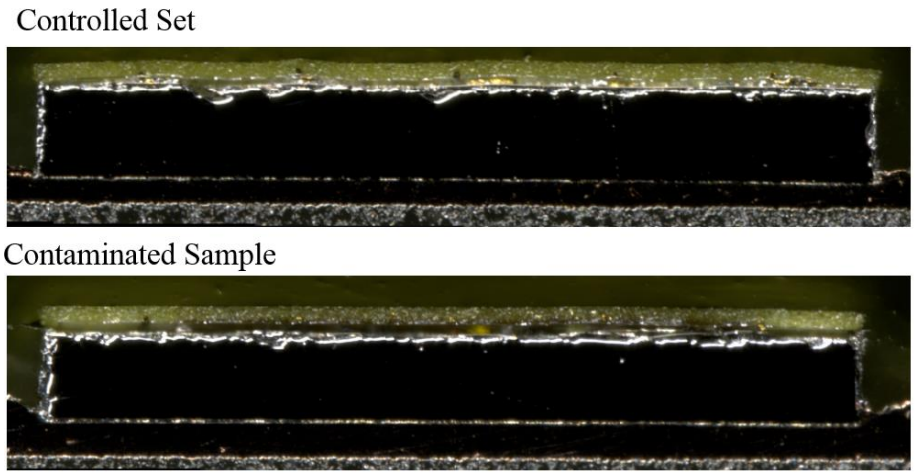


Figure 184:Optical Image of the VOC Contamination.

Optical image of high magnification of both controlled and contaminated samples have been recorded to see how and where the VOC contamination happened. Figure 184 shows the comparison between the controlled sample and contaminated sample. There is an obvious color

change in the phosphor layer and adhesive layer. From the comparison, it is possible that both layers are discolored by VOCs contamination. However, from the VOCs contamination theory, the contamination should only happen in phosphor binder layer. In the following phase, detailed analysis was performed on the adhesive layer with SEM (Scanning electron Microscopy) and EDX (Energy-dispersive X-ray) technology to explain the reason for discolored adhesive layer. There will be detailed analysis of these two layers to see which layer domination the appearance of contamination area.

During the analysis of the conductive and adhesive layer, SEM image had been taken and EDX analysis have been performed to decide what changed in that layer. Energy-dispersive X-ray spectroscopy (EDS, EDX, or XEDS), which also called energy dispersive X-ray analysis is an elemental analysis technique. This technique based on an interaction of X-ray excitation and samples. Each element has unique atomic structure and allows unique set of peaks on its X-ray spectrum. In order to stimulate the sample to emit X-ray, an electron beam generates a beam of high energy electrons that induce X-ray emission from the sample. The incident beam may excite an electron in an inner shell of an atom and spout it out of shell. Electron from the outer, high energy shell fills the hole. The energy difference between the outer shell and the inner shell will be released in the form of X-ray. Energy dispersive spectrometer is utilized to measure the number and the energy of the X-ray emitted from the samples being studied. The emitted energy varies as the structures of the elements are different. This allows the elemental composition analysis of the specimen. Figure 185 shows the SEM pictures and EDX analysis of the adhesive layer:

From the test result, it can be shown that gold is the main component of the conductive material and it is very stable. There are supposed to be no change of that layer. The reason why it

become black is the optical illusion. Figure 186 shows that the adhesive layer is not continuous and most part of the layer is empty which make sense considering the high cost of gold.

| Element | Weight % | Atomic% |
|---|---|---|
| B K | 4.42 | 25.04 |
| C K | 6.38 | 32.54 |
| N K | 2.94 | 12.84 |
| Al K | 0.71 | 1.62 |
| Ga K | 2.39 | 2.10 |
| Au M | 83.15 | 25.85 |
| Totals | 100.00 | |

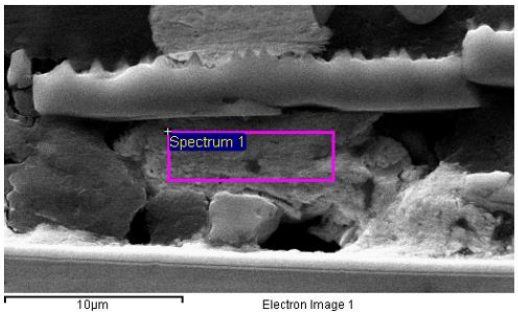


Figure 185: SEM view and EDX Analysis of Adhensive and Conductive Layer.

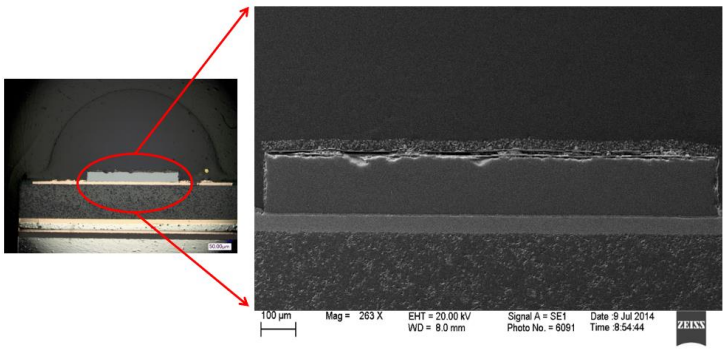


Figure 186: SEM View of the Whole Chip Area.

Because of the discoloration of the phosphor layer, the light goes into the space will be trapped by the phosphor layer and this process makes the adhesive layer looks black. The contamination area only appears in the phosphor layer which can also be proved by the following sample whose optical lens were removed in Figure 187. It is obvious that only the phosphor layer become black.

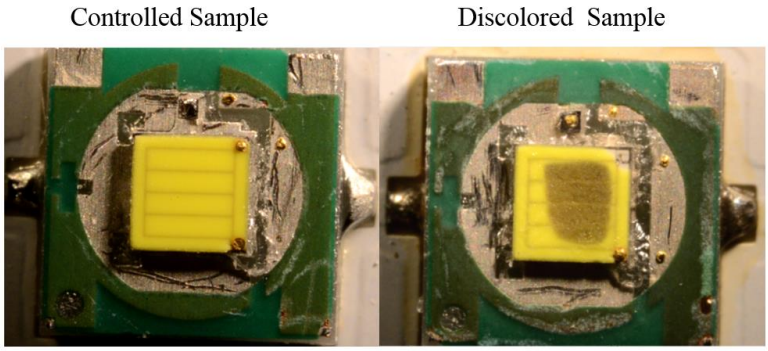


Figure 187: Lens Removed XP-G LED Package Samples.

The experiment process and result show that materials around the LED-based product may lay off volatile organic compound and effect the luminous flux output of the product dramatically. In critical application, prior tests about the construction material are required to perform before they go to mass production. Special attention should be paid to glues, gaskets and plastic covers which are often utilized during the assembly procedures of LED package. In high temperature environment they may lead VOC contamination. Therefore, high temperature test, at least operating temperature test of these materials should be performed. Due to the easy VOC contamination of LED modules, the importance of choose a right fixture and sealing is as important as the design of drivers, heat management for a good LED-based product.

### 4.5.2. Analysis of Humidity Effects on the Phosphor Layer

Figure 188 provides the optical comparison between the pristine sample and the XR-C LED package that under 85°C/85% aging condition for 5780 hours.

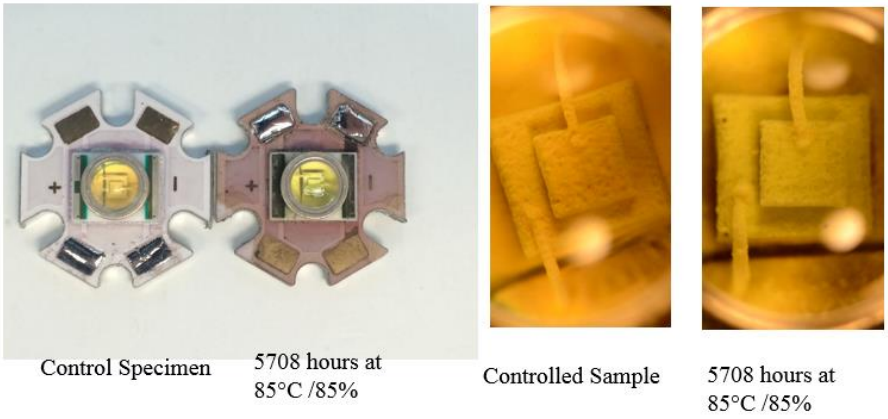


Figure 188: Comparison Between the Controlled Sample and the Failure Sample.

The die region of the two samples are examined in the right part of Figure 188. All the optical images were taken under the same light condition. As shown above, the color of the phosphor binder layer changed from reddish yellow to light yellow. The color change of the phosphor binder caused the dramatic shift of chromaticity coordinates. In order to further study the failure mechanism of warm white LED package under accelerated lift test, a pristine sample and a failed sample from each group were cross sectioned in the middle of the package. On the cross-section surface, die, phosphor binder, encapsulation and the lens can be observed clearly under optical microscope and scanning electronic microscope (SEM). Figure 189 depicts the cross-section surface of the controlled sample, the sample under 85°C/85% and the sample under 105°C aging conditions.

An obvious color change of the phosphor binder was observed for the samples that exposed to 85°C/85%. The most possible area of failure is the phosphor binder area. Detailed analysis of the phosphor binder in each package was performed under the SEM. Higher magnification images of the phosphor binder area were taken to examine the degradation. Figure 190 provides the 273 magnification images from SEM.

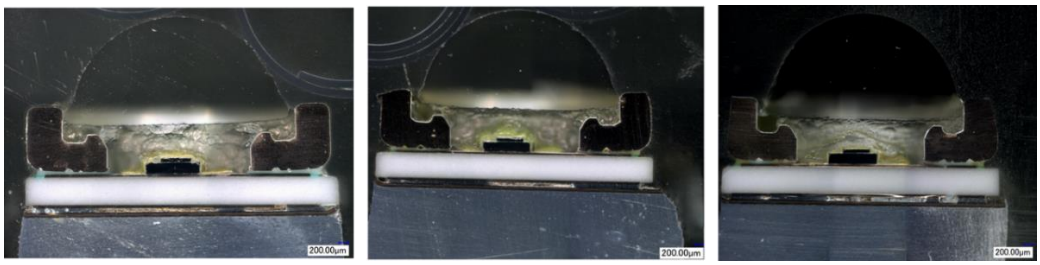

Figure 189: Optical Picture of the Cross Section Surface. The left image is for pristine sample. The middle one is the optical image of the samples under 85°C/85% for 5708 hours. The right image is for the samples under 105°C for 6360 hours.

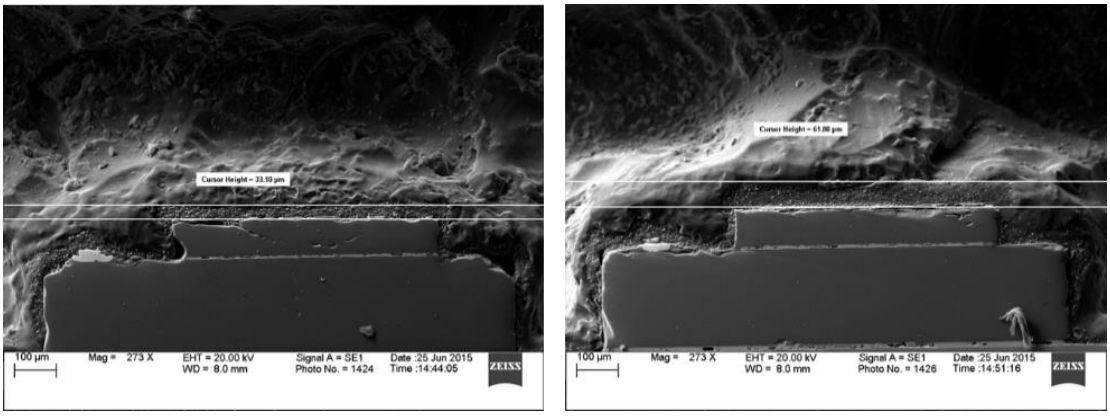


Figure 190: SEM Images of 273 magnification. The left image is for the pristine sample. The right one is the image of the sample under 85°C/85% for 5708 hours.

The measurement of the phosphor layer marked by the white line in the Figure 190 indicates the expansion of the phosphor binder layers. The thickness of the phosphor binder changed from 33.10 µm to 61.80µm. To observe the phosphor particles, SEM image of 2580 magnification were taken. Figure 191 provides higher resolution SEM images.

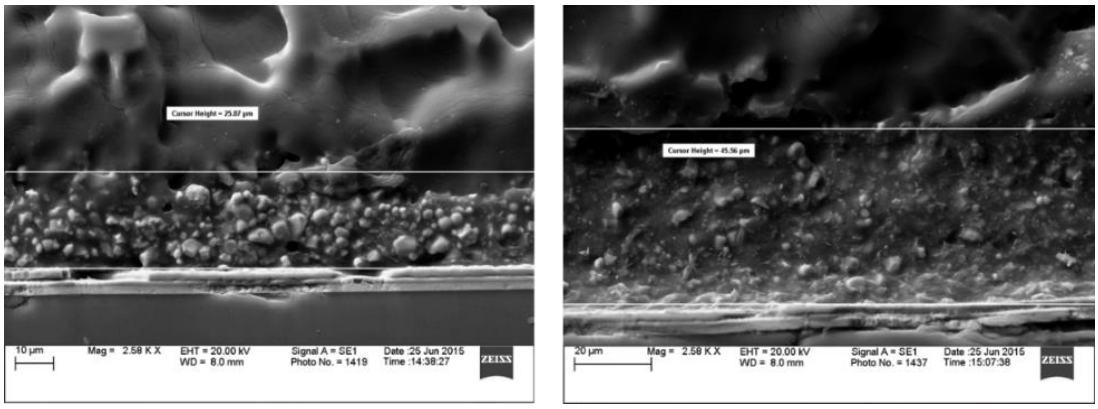


Figure 191: SEM Images of 2580 magnification. The left image is for the pristine sample. The right one is the image of the sample under 85°C/85% for 5708 hours.

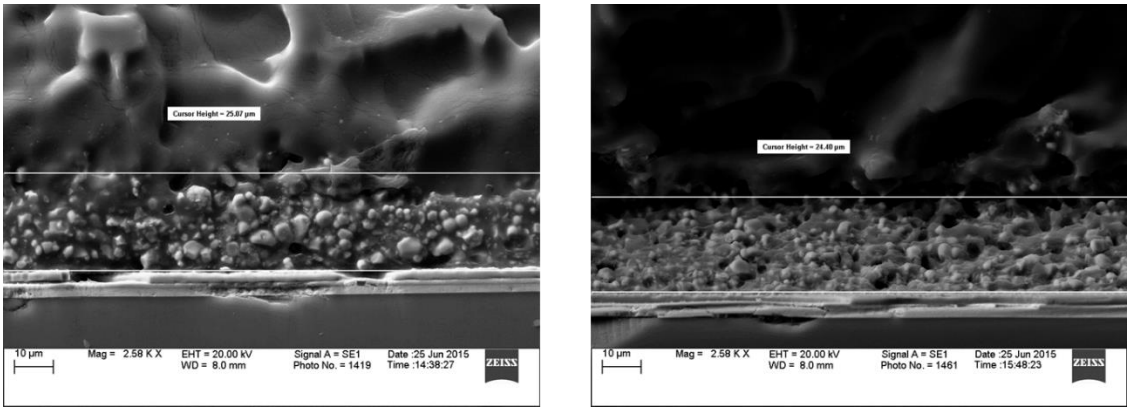


Figure 192: SEM Images of 2580 magnification. The left image is for the pristine sample. The right one is the image of the sample under 105°C for 6360 hours.

Figure 191 shows a variety of the changes of the phosphor particles had been observed. The most obvious one is the density change of the phosphor particles. All the images were taken under the same working distance and magnification. Phosphor particles are evenly distributed on the top of the thin film die which located on the sub mount. After exposed to 85°C/85% for 5708 hours, the phosphor binder layer start to expand and the density of the phosphor particles start to reduce. This observation agrees with the expansion of phosphor binder layer that been observed before.

To further compare the different effects between the humidity and thermal stress. A comparison of the cross-section surface between the controlled sample and the group2 sample were done under the SEM. Figure 192 provides the SEM image of 2580 magnification. It can be observed from the above image that the high temperature test environment aging did not change the density of the phosphor particles. Additionally, there is no sign of expansion in the phosphor binder layer. The aged sample have similar thickness of the phosphor binder compared with the pristine sample.

# 5. LIFETIME PREDICTION AND MODELING

Various PHM approaches had been proposed by other researchers for the estimation of unknown states and the prediction of remaining useful life. The very common used one is based on the physical model of failure. The prediction of RUL depends on the mathematical dominant governing equation which describes the physical failure process. The second one use state estimator to estimate the true unknown states and predict the RUL based on the parameters got from the estimator. There are also some other techniques that use mathematical fitting of the experimental data to get the RUL. However, the fitting method is very sensitive to the experimental value. If the experimental noise is high, the error between the real model and the fitted model will be gigantic. For now, there is not published physics based failure model for LED lumen degradation. Therefore, the best option is to adopt the state estimation method to predict the RUL. In this dissertation, the data driven technique with various state estimator will be employed to predict the RUL based on the observed luminous flux and color shift distance. Also, a physics based model will be proposed to perform the life maintenance of LED packages.

## 5.1. PHM METHODOLOGY

Data driven method is very powerful and it can extrapolate the current measured data forward and make prognostics prediction of failure which is quite useful for a mission critical user. It is a statistically defendable method and actions can be taken based on these predictions. There are many ways can be used to do the prediction and extrapolation, such as Kalman filter, Extended Kalman filter, particle filter and Unscented Kalman filter. The basic methodology can be illustrated by the following Figure 193.

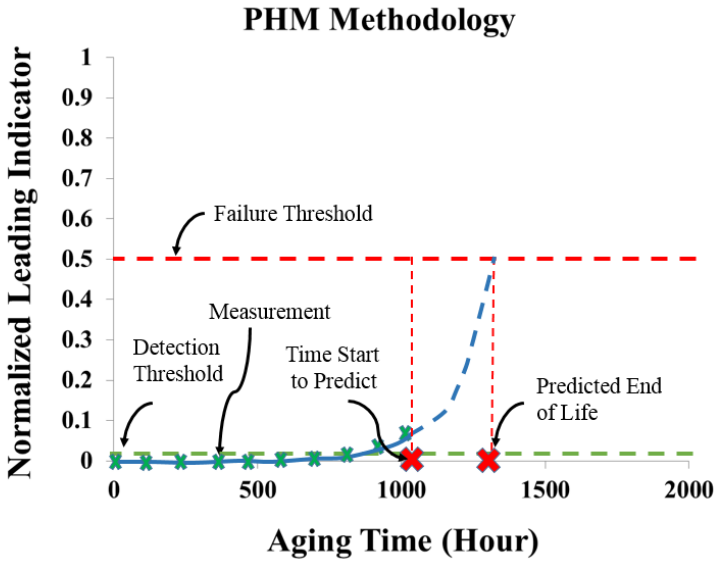


Figure 193: Scheme Graph of PHM Methothology.

Figure 193 illustrate the PHM methodology of a typical system. The y axis represents the measured leading indicator of a system such as the luminous flux, color shift distance which can be any variable that characterize the health of the system. The x axis represent the accelerated life test aging time. The green line in Figure 197 is the detection threshold. It defines a regime when nothing is change in that area, such as the measurement noise of the equipment used during the measurement. Measurement result of leading indicator under the detection threshold can't be used to predict the end of life for this system. After the leading indicator, has gone cross the detection threshold, prediction can be made based on the measured leading indicator measurement. The end of life is defined as the time when the leading indicator goes across the failure threshold which is the red line in Figure 193. At the end of life, the system no longer works. The PHM method focuses on the prediction which can predict the time in the future when the leading indicator cross the failure threshold. There are several methods that can be used during the projection of the leading indicator until the leading indicator cross the failure threshold. To increase the accuracy of the

prediction, the predicted failure time usually have a statistical distribution. Figure 194 illustrate a Gaussian distribution. However, it is not restricted to a close form statistics.

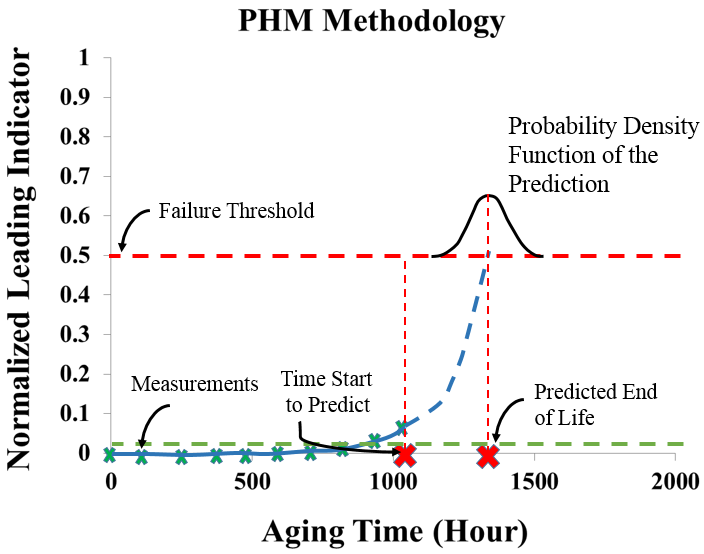


Figure 194: Prediction Distribution.

Given certain amount of leading indicator measurement, the prediction of the time when the leading indicator cross the failure threshold can be challenging. There are many variables that can affects the projection of the leading indicator, such as temperature, relative humidity, current stress and mechanical stress. With so many variables, it is important to have an empirical model that includes all these parameters. Then a meaningful prediction result can be supplied to the users of the system. In order to make the prediction result easy to understand for any users, the concept of remaining useful life is defined. It is the duration between the time when prediction is started and the failure time. Figure 195 illustrates the remaining useful life at certain time x.

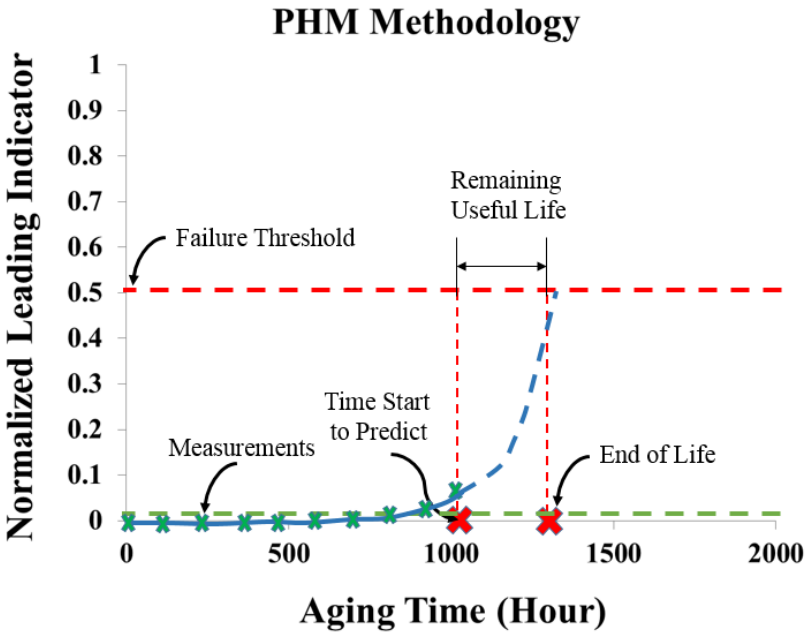


Figure 195: Illustration of Remaing Useful life.

There are many challenges during the prediction of the failure time. The predicted result from the projection method is a distribution around the predicted failure time. It is necessary to have a method that can interprets the predicted result for a user. Risk based decision making is a methodology that can help the end user of a system. It is a statistically defendable method that helps user of a system making decisions using the prediction data. Risk based decision making uses the information output from a prognostic method to help the user making decisions under uncertainty, especially for the safety and mission critical system. There are several algorithms that can be used in the prognostics methods which will be described in the following sections.

Risk based decision making requires several acceptable levels of risking that a system user can tolerate. These risks include maximum allowable probability of failure and maximum probability of proactive maintenance. Maximum allowable probability of failure defines the user's tolerance for unplanned failure. For safety and mission critical application, the maximum

allowable probability of failure is usually a very small number. The maximum probability of proactive maintenance represents the user's tolerance for replacing the components before it fails. For safety, critical system, this value is small. However, for resource limited system, the maximum probability of proactive maintenance should be as large as possible to save the operation cost.

Integration of the whole probability function is unity. The window of opportunity, where action can be taken to replace the components, can be calculated by the subtraction of maximum probability of proactive maintenance from the maximum probability of failure. Figure 196 shows the calculation of the time window where action can be taken.

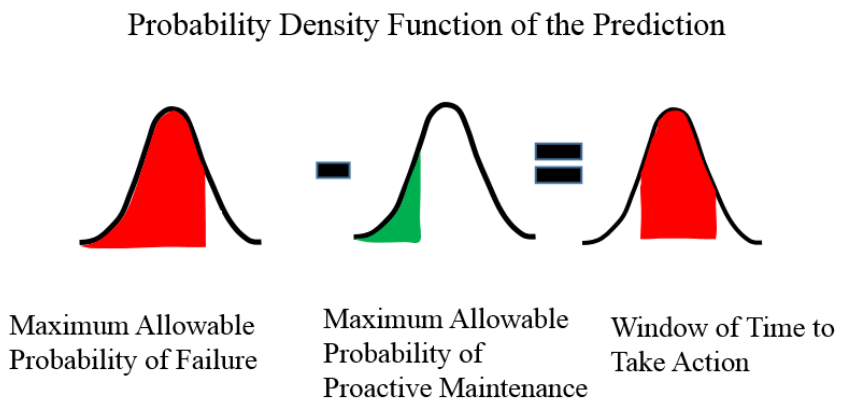


Figure 196: Risk Based Decision Making Method.

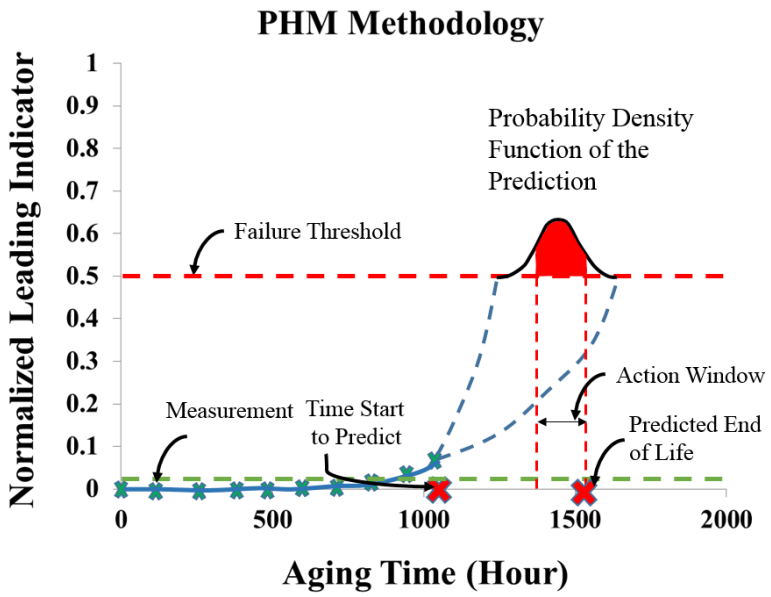


Figure 197: Predicted Time Range to Take Action.

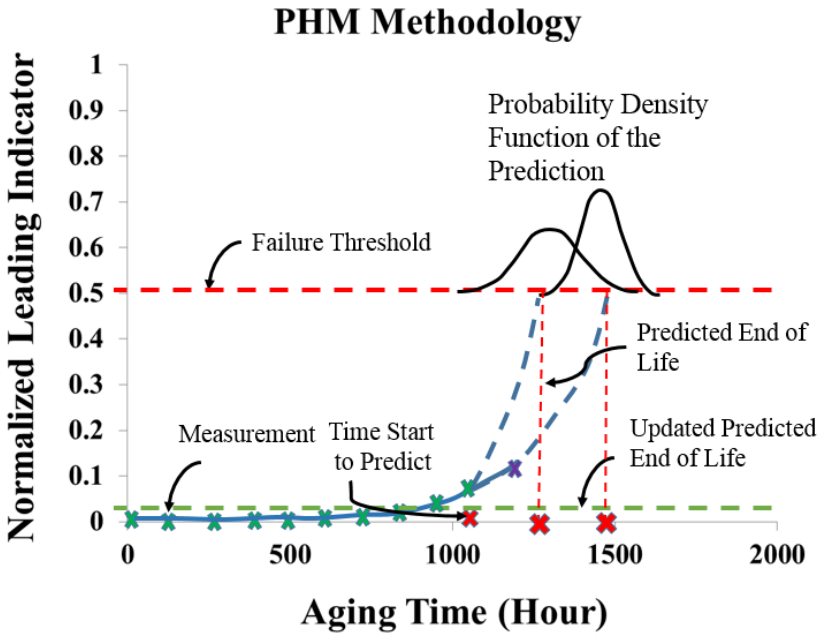


Figure 198: Updated Prediction of Failure Time.

Figure 197 illustrate the time window where proper proactive action can be taken in a system. It shows a range of time where it is in the user's tolerance to replace the components which has high probability of failed.

The prediction of failure time can be updated after each measurement. The new measured information of the leading indicator can be used by the PHM framework to update the extrapolation process. The process of incorporating new measurement of the leading indicator and updating the prediction repeats after each measurement and until the end of life. Figure 198 shows the updating process of the prediction.

The risk based decision making method can be applied for the case of high power LED package to estimate the remaining useful life. During the prediction, new available measurements recursively update the predicted failure time.

## 5.2. STATE ESTIMATION

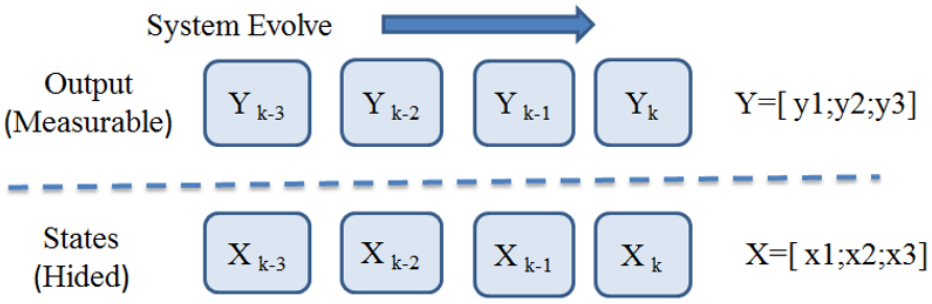


Figure 199: State Estimation Framework.

The State Estimation method includes both discrete time state estimation and continuous time state estimation. In this paper, discrete time estimation has been adopted and discussed. In control theory, a state observer is algorithm that provides an estimate of the internal state of a given

real system, from measurements of the input and output of the real system. The basic framework of discrete state estimation is shown in Figure 199.

The mathematical model used in the state estimation usually has two master equations for the discrete state estimation. The first is called state transfer equation and the second is output equation which describes the relationship between the state variables and the output variable.

$$X_k = f(X_{k-1}, U_{k-1}, V_{k-1}) \tag{135}$$

In this equation, $X_k$ is state variable matrix. k stands for current time and k-1 is the previous time. $U_{k-1}$ is the previous step known input to the system and $V_{k-1}$ is the process noise of the mathematical model applied to the practical model.

$$Y_k = h(X_k, U_k, N_k) \tag{136}$$

The output equation has three parameters, state variables, known input, and the measurement noise. In practical situation, $X_k$ represented the unobservable states of the system and $Y_k$ is the observable signal. A lot of state estimation techniques have been developed for now. In this dissertation, Extended Kalman Filter, Unscented Kalman Filter and the particle filter will be employed for the state estimator.

There are two steps during the estimation process. The first step is to perform the filter to the measured data and the second step project the state vector forward with the transfer function. Figure 200 shows the estimation process. The state estimator estimates the true states under noise and error. After long enough training, the estimator can understand the system and works independently without the measured data. The advantage of the estimator over other techniques is the no need for the specified dominant model from the undying physics. By observing the measurement data from the measurement, the undying model can be picked. It is generally

accepted that luminous flux output of LED package changes in exponential pattern with aging time.

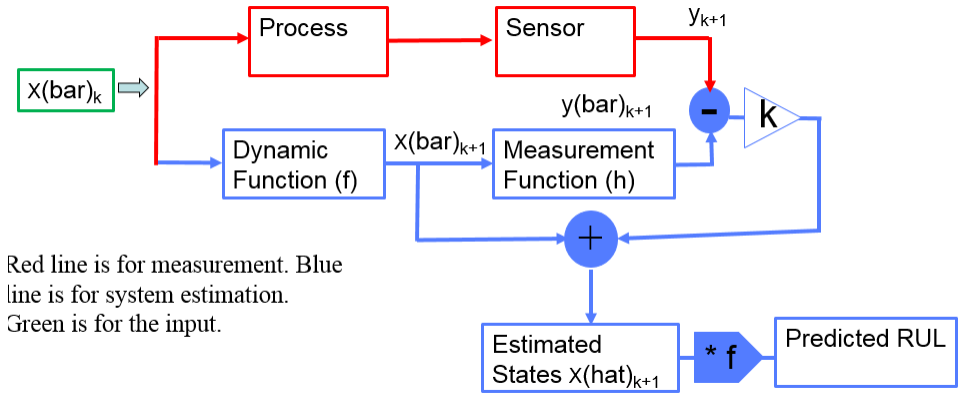


Figure 200: State Estimation Process.

### 5.2.1. EXTENDED KALMAN FILTER

The Extended Kalman filter is typically derived using vector algebra as a minimum mean squared estimator and it applies a first order linearization in the Riccatic equations (Balakrishnan, 1987) (Grewal, 2001) (Zarchan, 2000). The extended Kalman Filter was developed for non-linear discrete time process is not optimal in any sense. And further, if the process model is inaccurate then due to the use of the Jacobians -- which essentially represent a linearization of the model -- the Extended-Kalman Filter will likely diverge leading to very poor estimates. However, in practice, and when used carefully, the Extended-Kalman Filter can lead to very reliable state estimation. This is particularly the case when the process being estimated can be accurately linearized at each point along the trajectory of the states. The luminous flux of LED usually degrades exponentially with time in the following equation (IES, 2008b):

$$\Phi(t) = B * \exp(-a * t) \tag{137}$$

Where B is the pre-exponential constant which is very close to unity, if the luminous flux is normalized. α is the decay constant and t is the aging time.

During the estimation, the state vector of the system were chosen as X[x ẋ b] where x is the luminous flux, ẋ is the derivative of the luminous flux and b is the decay constant. Then, a set of nonlinear systems could be acquired to describe the system:

$$\dot{X} = f(X) + w \tag{138}$$

Where X is the state vector of the system, f(X) is the non-linear function of the system and w is the system noise which is a Gaussian noise. Similarly, the measurement equations can be expressed as:

$$\dot{Z} = h(X) + v \tag{139}$$

Where h(X) is the measurement function of the system which describes the relation between the measurement variables and the system state vector X. v is the measurement noise which is another Gaussian noise. The system dynamic matrix F and measurement matrix H could be calculated by the following equations:

$$F = \frac{\partial f(X)}{\partial X} \tag{140}$$

$$H = \frac{\partial h(X)}{\partial X} \tag{141}$$

Then, the fundamental matrix Φ could be calculated as:

$$\Phi = I + F * t + \frac{(F * t)^2}{2} \tag{142}$$

The higher terms of the fundamental matrix are neglected. From the above equations, the system dynamic equation could be written as:

$$\dot{x} = -b * x \tag{143}$$

$$\ddot{x} = b^2 * x = -b * \dot{x} \tag{144}$$

$$\dot{b} = 0 \tag{145}$$

The state evolution equation could be written as:

$$\begin{bmatrix} \Delta\dot{x} \\ \Delta\ddot{x} \\ \Delta\dot{b} \end{bmatrix} = \begin{bmatrix} \frac{\partial\dot{x}}{\partial x} & \frac{\partial\dot{x}}{\partial\dot{x}} & \frac{\partial\dot{x}}{\partial b} \\ \frac{\partial\ddot{x}}{\partial x} & \frac{\partial\ddot{x}}{\partial\dot{x}} & \frac{\partial\ddot{x}}{\partial b} \\ \frac{\partial\dot{b}}{\partial x} & \frac{\partial\dot{b}}{\partial\dot{x}} & \frac{\partial\dot{b}}{\partial b} \end{bmatrix} * \begin{bmatrix} \Delta x \\ \Delta\dot{x} \\ \Delta b \end{bmatrix} \tag{146}$$

The system dynamic based on equation 9, 10, 11 and 12 is given by:

$$F = \begin{bmatrix} -b & 1 & -x \\ b^2 & -b & 2*b*x \\ 0 & 0 & 0 \end{bmatrix} \tag{147}$$

The fundamental matrix could be calculated as follows:

$$\Phi = \begin{bmatrix} 1 & 0 & 0 \\ 0 & 1 & 0 \\ 0 & 0 & 1 \end{bmatrix} + \begin{bmatrix} -b & 1 & -x \\ b^2 & -b & 2*b*x \\ 0 & 0 & 0 \end{bmatrix} * t = \begin{bmatrix} 1-b*t & t & -x*t \\ b^2*t & 1-b*t & 2*b*x*t \\ 0 & 0 & 1 \end{bmatrix} \tag{148}$$

During the filtering and prediction, the Extended Kalman Filter was repeated recursively until the state vector cross the failure threshold. The recursive procedure is given as:

Initialization:

Initially, the only available information is the initial state vector $\widehat{X_0}$ and the covariance P0.

Model Forecast:

Project the state vector forward with the fundamental matrix $\Phi_{k:}$

$$\overline{X}_k = \Phi_{k-1} * \hat{X}_{k-1} + Q \tag{149}$$

Project the error covariance forward:

$$M_k = \Phi_{k-1} * P_{k-1} * {\Phi_{k-1}}^T + Q \tag{150}$$

Data Assimilation and Correction

Calculate the Kalman gain:

$$K_k = M_k * H_{k-1}^{\ T} * (H_{k-1} * M_k * H_{k-1}^{\ T} + R)^{-1} \quad (151)$$

Update the state vector with the measurements:

$$\hat{X} = \Phi_{k-1} * \hat{X}_{k-1} + K_k * (Z_k - \overline{X}_k) \quad (152)$$

Update the covariance with the Kalman gain:

$$P_k = (I - K_k * H_{k-1}) * M_k \quad (153)$$

Project the state vector forward until it crosses the failure threshold

$$\hat{X}_{k+n} = \Phi_{k+n-1} * \hat{X}_{k+n-1} \quad (154)$$

Report the predicted Remaining useful life

Iterate to step 2 for next measurement to predict the remaining useful life again.

The data driven approach relies on the analysis of the in situ monitored data obtained from the experiment which can eliminate the noise by passing the data through the filter first. Figure 201 shows the Extending Kalman Filter filtered data vs the experimental data. Luminous flux is changing exponentially with aging time, however, remaining useful life is linear function in terms of the thermal aging time. Figure 202 shows the projection of luminous flux and the calculation of remaining useful life (RUL).

The RUL can be calculated by projecting the state vector forward at each measurement point until it across the threshold. The time between the start point of the projection and the intersection is the RUL which is shown in Figure 202. Figure 203 shows the RUL prediction with the station estimation method.

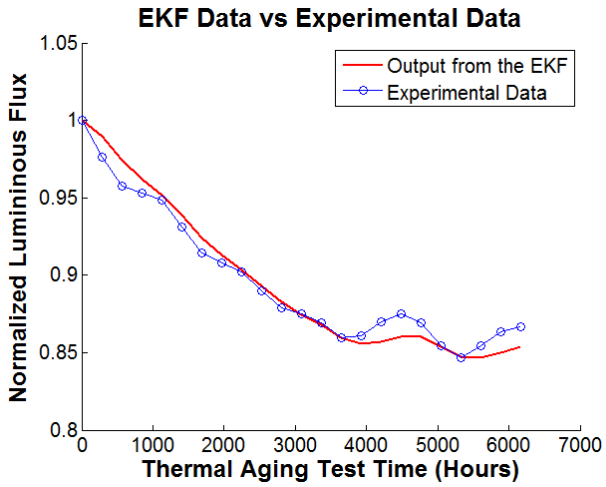


Figure 201: Comparision between the Filtered Data with the Experimental Data.

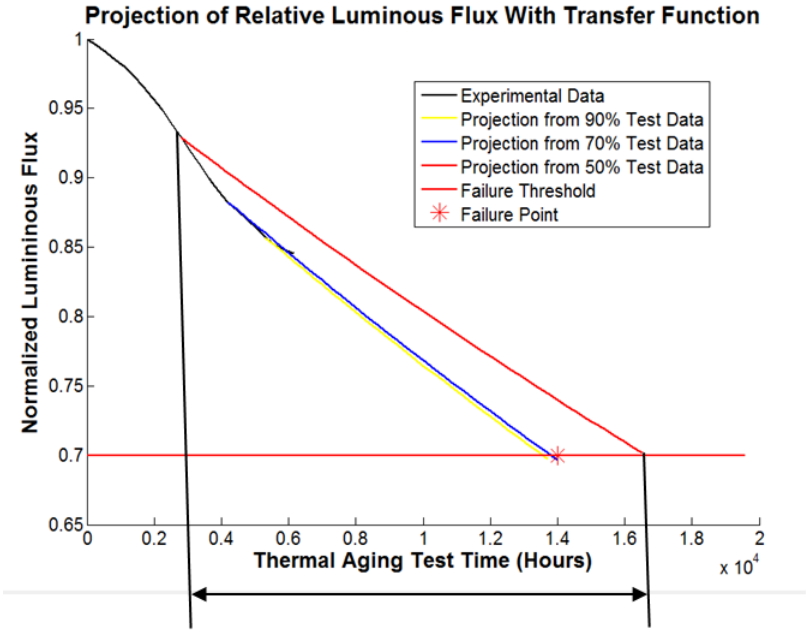


Predicted RUL from 50% of the Experimental Data

Figure 202: Projection of Relative luminous flux and the Calculation of RUL.

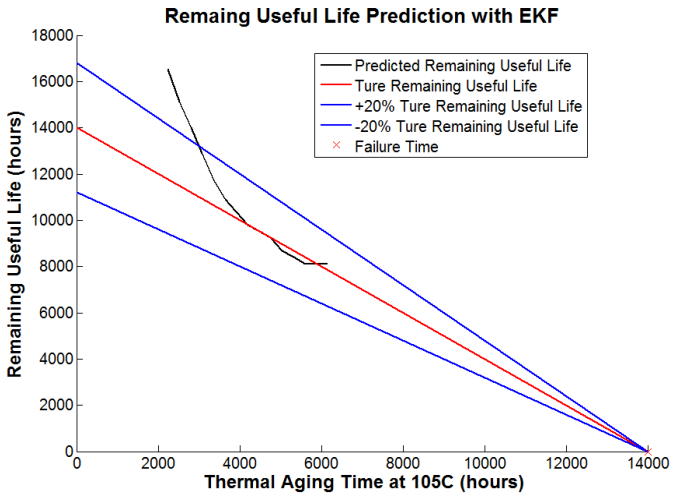


Figure 203: Predicted RUL vs the Ideal RUL.

Plot the ideal RUL in terms of thermal aging time will give a straight line with a slop of 135°. The red line is the ideal RUL and the black line is the predicted RUL. The blue line is the ± 20% error boundary. The result shows that all prediction result can fall into the 20% boundary of the goal after 3000 hours. Also, the prediction aligns with the ideal data after 4000 hour's data which means 4000 hour's experiment is good enough to get the decent result. The implement of state estimator is easier than the TM21 protocol. However, there are several disadvantages of state estimation. It is not be able to predict the luminous flux at the other test conditions, while, the TM21 can predict the luminous flux at any given condition with two given test conditions. The possible solution for this tradeoff is to combine the TM21standard with state estimation. State estimation method can predict the decay constant and projected initial constant with very less data, comparing with 6000 hours' data required by TM21. Then, the predicted decay constant can be used to calibrate the activation energy. The last part of TM21 method can be finished with the calculated activation energy.

### 5.2.2. UNSCENTED KALMAN FILTER

The advantage the UKF is unscented transformation which can calculate the statistics of a random variable which undergoes a nonlinear transformation. With a set of carefully chosen sample points and their weight, UKF can capture the true mean and variance of the state variable when it goes through no-linear system. UKF algorithm has advantages compared to other estimators [Eric 2000]. It is easy to implement and has higher accuracy. Due to the unscented transformation, it considers at least second order Taylor expansion. Also, sigma point sampling is an optimal sampling approach compared with the Monte Carlo random sampling method which used in another estimator.

#### 5.2.2.1.Unscented Transformation

Assume state vector x has L variables and goes through a non-linear function y=g(x). The mean of x is $\bar{x}$ and covariance is $P_x$. To calculate the statics of y, a combined matrix X of 2*L+1sigma state vector x has been created according to the following equation. In the following equation, subscript stands for the column number.

$$X_0 = \bar{x} \tag{155}$$

$$X_i = \bar{x} + (\sqrt{(L+\lambda)*P_x})_i \quad \text{i=1,2,…L} \tag{156}$$

$$X_i = \bar{x} - (\sqrt{(L+\lambda)*P_x})_i \quad \text{i=L+1,L+2,…2*L} \tag{157}$$

$$\lambda = a^2*(L+k) - L \tag{158}$$

In the above equation, the variable determines the spread of the sigma points around $\bar{x}$ is usually set to a small positive number. K is a second scaling number which usually set to 0. Different weight factor of each column of the combined matrix have been assigned in the following equation and subscripts stands for the column number.

$$W_0^m = \frac{\lambda}{L+\lambda} \tag{159}$$

$$W_0^c = \frac{\lambda}{L+\lambda} + (1 - a^2 + \beta) \tag{160}$$

$$W_i^m = W_i^c = \frac{1}{2*(L+\lambda)} \quad \text{i=1,2,3,…2*L} \tag{161}$$

In the above equation, β is employed to incorporate prior knowledge of the distribution of x and for Gaussian distribution β equals 2. The combined sigma vectors propagate forward through the state transfer equation.

$$Y = g(X) \tag{162}$$

The mean and variance of the y are calculated with the weighting factor Wm and Wc in the following equation.

$$\bar{y} = \sum_{i=0}^{2*L} W_i^m * Y_i \tag{163}$$

$$P_y = \sum_{i=0}^{2*L} W_i^c * \{Y_i - \bar{y}\} * \{Y_i - \bar{y}\}^T \tag{164}$$

The unscented Kalman filter is the recursive expansion of the unscented transformation. The nonlinear function g will be replaced by the state transfer function F. Combined state vector matrix is the unscented transformed previous estimated state $X_{k-1}$ and the output $X_k$ is the next estimated state. From the measurable output signal, the true state variable can be calculated.

**5.2.2.2.Unscented Kalman Filter Algorithm**

In this dissertation, Unscented Kalman Filter as the discrete control method will be employed for the state estimation. Figure 204 shows the framework of UKF.

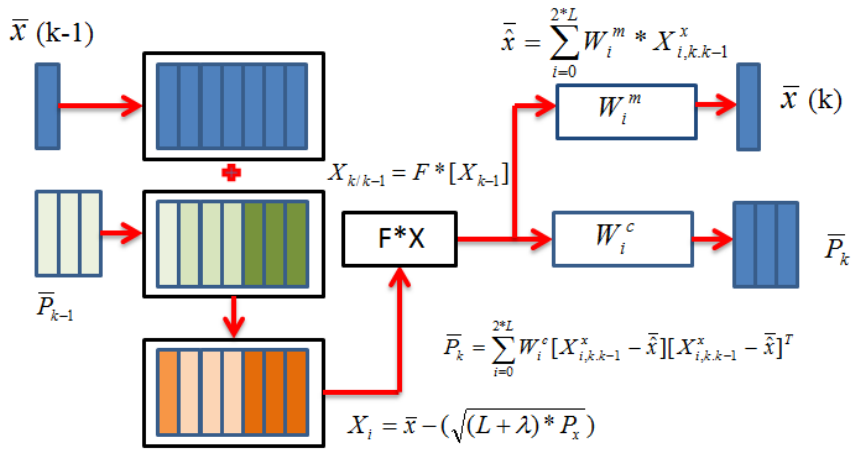


Figure 204: UKF Frame work.

The UKF algorithm is given in four steps. First, algorithm stars with initialization of state variable at zero time.

$$\hat{x}_0 = E[x_0] \tag{165}$$

$$P_0 = E[(x_0 - \hat{x}_0)*(x_0 - \hat{x}_0)^T] \tag{166}$$

Augment state vector and covariance matrix are followed:

$$\hat{x}_0^a = E[x_0^a] = [\hat{x}_0^T \; 0 \; 0]^T \tag{167}$$

$$P_0^a = E[(x_0^a - \hat{x}_0^a)*(x_0 - \hat{x}_0^a)^T] = \begin{bmatrix} P_0 & 0 & 0 \\ 0 & P_v & 0 \\ 0 & 0 & P_n \end{bmatrix} \tag{168}$$

Second, perform unscented transformation and calculate the sigma point:

$$X_{k-1}^a = [\hat{x}_{k-1}^a \quad \hat{x}_{k-1}^a \pm \sqrt{(L+\lambda)*P_{k-1}^a}] \tag{169}$$

Third, time updating according to the state transfer function, updates state variables first, then update output.

$$X_{k/k-1}^a = F*[X_{k-1}^x, X_{k-1}^v] \tag{170}$$

$$\bar{\hat{x}} = \sum_{i=0}^{2*L} W_i^m * X_{i,k.k-1}^x \tag{171}$$

$$\bar{P}_k = \sum_{i=0}^{2*L} W_i^c [X_{i,k.k-1}^x - \bar{\hat{x}}][X_{i,k.k-1}^x - \bar{\hat{x}}]^T \tag{172}$$

Output update

$$Y_{k/k-1} = H * [X_{k-1}^x, X_{k-1}^n] \tag{173}$$

$$\bar{\hat{y}} = \sum_{i=0}^{2*L} W_i^m * Y_{i,k.k-1}^x \tag{174}$$

The last step uses the covariance of output and state variable updates the measurement equation.

$$P_{\bar{\hat{y}},\bar{\hat{y}}} = \sum_{i=0}^{2*L} W_i^c [Y_{i,k.k-1}^x - \bar{\hat{y}}][Y_{i,k.k-1}^x - \bar{\hat{y}}]^T \tag{175}$$

$$P_{\bar{\hat{x}},\bar{\hat{y}}} = \sum_{i=0}^{2*L} W_i^c [X_{i,k.k-1}^x - \bar{\hat{x}}][Y_{i,k.k-1}^x - \bar{\hat{y}}]^T \tag{176}$$

$$K = P_{\bar{\hat{x}},\bar{\hat{y}}} * P_{\bar{\hat{y}},\bar{\hat{y}}}^{-1} \tag{177}$$

$$\hat{x}_k = \bar{\hat{x}} + K * (y_k - \bar{\hat{y}}) \tag{178}$$

$$P_k = \bar{P}_k - K * P_{\bar{\hat{y}}*\bar{\hat{y}}} * K^T \tag{179}$$

In the estimation of RUL, both luminous flux and color shift distance had been used with the same estimator. From observation and fitting method, fourth order polynomial fits both the measured data. The only difference is that luminous flux degrades and color shift distance increase with the aging time. However, that does not confuse the algorithm, since both of them follow the same dynamic function.

The test data from five test periods will be select to train the algorithm and then the prediction of the failure time will be performed without the experimental data. The period was chosen as the 30%, 40%, 50%, 60%, 70% test data of the entire test time. Figure 205 and Figure 206 shows the projection data of the algorithm after training. The convergence of the projection can be observed form the following Figure 206 for both luminous flux and color shift distance.

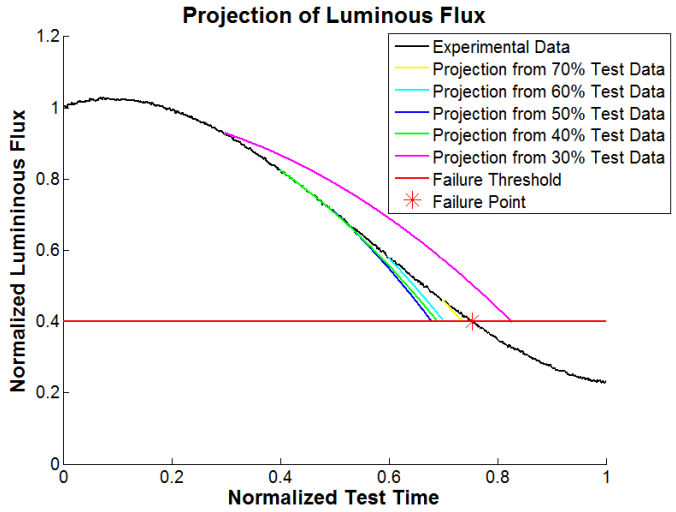


Figure 205: Projection of Luminous Flux with Trained Estimator.

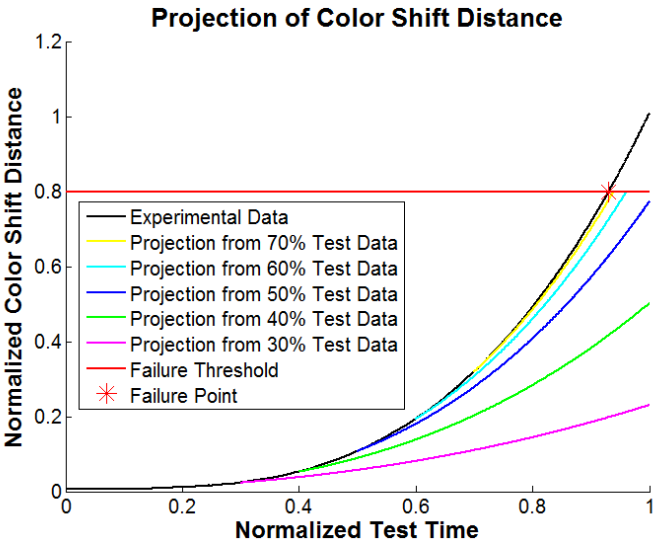


Figure 206 : Projection of Color Shift Distance with Trained Estimator.

In order to quantify and validate the PHM method above, a comparison between the observed luminous flux and color shift distance and the predicted values had been done. The validation procedures follow the algorithm assessment metrics proposed in (Saxena A. C., 2008) (Saxena A. C., 2009a) (Saxena A. C., 2009b). The validation method usually involves four steps.

First, calculate the alpha-lambda performance and see whether the prediction converge to the true value. Second, calculate the statistics of the beta equation to see the precision of the algorithm. The third step is to calculate the relative accuracy. The last step of the validation depends on the demands of the algorithm. The alpha-lambda metric compares the actual remaining useful life against the predicted RUL. The actual RUL can be found from the experimental data after the component had been stressed to failure. The alpha bounds are determined by the application and they provide a goal region for the algorithm. In this paper α (±20) % of the actual RUL are chosen. If the predicted RUL falls within the alpha bounds, then it is counted as a correct prediction. It should be noticed that the alpha bounds is different from the confidence interval of the predicted mean value. It defines the acceptable error bound of the prediction.

Figure 207 and Figure 208 show the predicted remaining useful life from each test point with the measurement of luminous flux and color shift distance. At the very beginning of the test, approximately 30% of the test time, the algorithm is not able to do the prediction, because the size of the input data is not enough to make the algorithm converge. However, after about the 38 percent of the test time, the algorithm is good enough to make the prediction fall into the 20% boundary of the true remaining useful life. The most important is that, after it falls into the 20% boundary, it does not go out of the boundary which means that the algorithm converges.

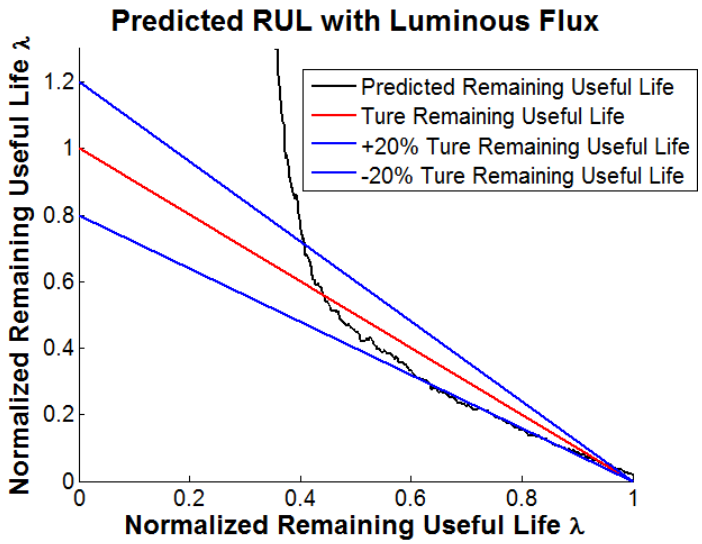


Figure 207: Predicted RUL with Luminous Flux.

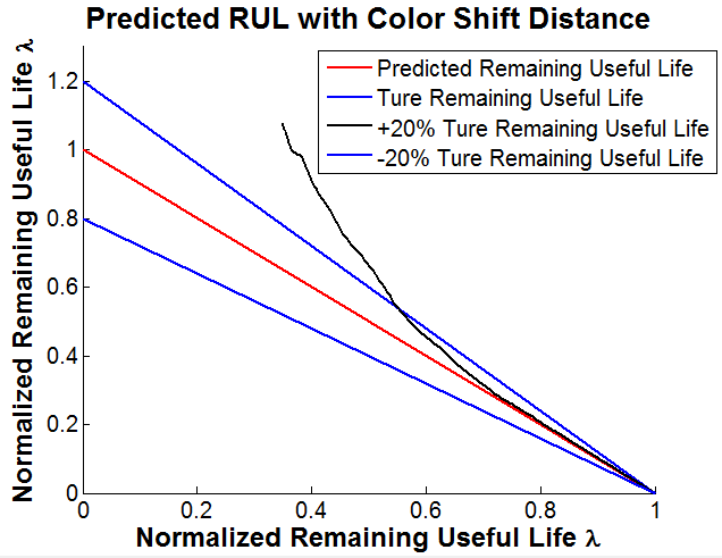


Figure 208 : Predicted RUL with Color Shift Distance.

In the prediction, all the time value had been normalized by the failure time. In the picture, λ is defined as the normalized time and it can be calculated by $t/t_f$ where f stands for failure. Normalized time is plotted on the x-axis. When lambda equals 0, the part is pristine and when lambda is equal to 1, the part fails. Beta metric is the second criteria and is defined as how much

of the area under the probability density function falls within the alpha bounds at each specific time. With this definition, it can be calculated by the following equation.

$$\beta = \int_{-a}^{+a} p(\mathrm{RUL}(t) \mid z_{0:t}) dt \tag{180}$$

Since the probability density function defines the distribution of the predicted remaining useful lift, the more area fall into the alpha boundary, the more confidence of the prediction. The whole property density function falls into the 20% boundary when beta equals1.The following Figure 209 shows the beta metric of the algorithm. After the convergence of the algorithm, the beta values jump around 1.

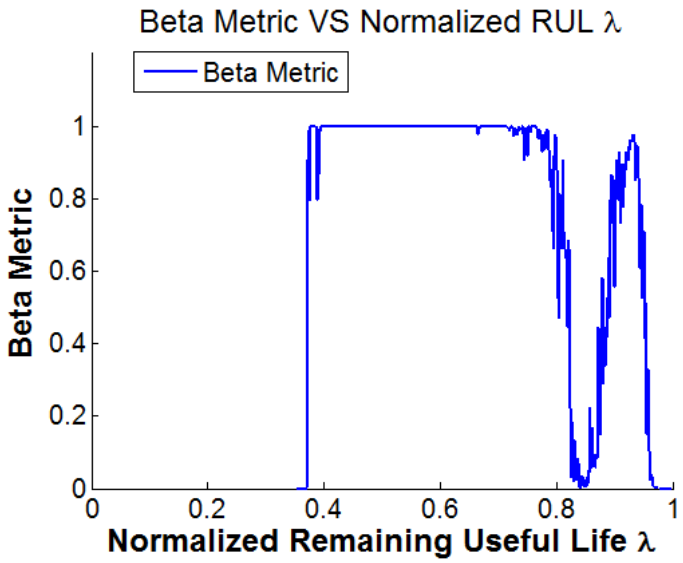


Figure 209: Beta Matric.

Relative accuracy is defined as a metric to indicate how closer the predicted remaining useful life to the actual remaining useful life. It can be calculated by the following equation.

$$RA_{\lambda} = 1 - | RUL_{actual} - RUL_{predicted} | / RUL_{actual} \tag{181}$$

From the equation, relative accuracy equals 1 when predicted value is equal to the true state. The following Figure 210 shows the calculated relative accuracy of the prediction result. The relative accuracy of the algorithm is very close to one after the convergence of the algorithm. It can also be seen from the prediction of the remaining useful life in Figure 210.

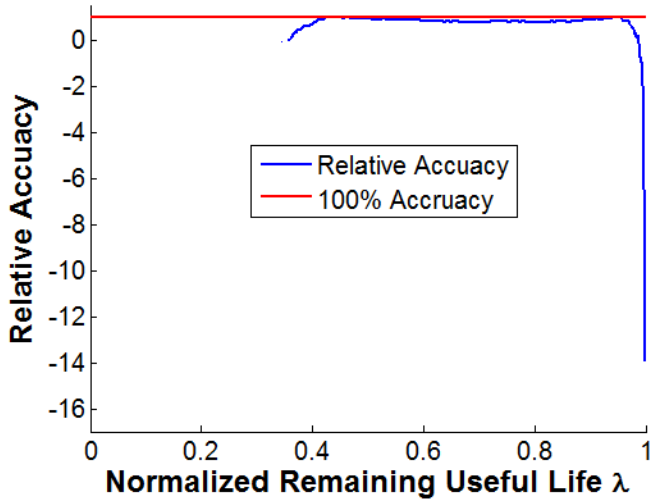


Figure 210: Relative Accuracy of Prediction.

To summarize the result of the prognostic algorithm into a single function, the performance function used the average Beta metric value and Relative accuracy value. Different weight of them can be assigned based on the demand. Taking the performance function as an equal weight of both accuracy and the RA metric is usually utilized.

## 5.3. PHYSICS BASED MODELING

### 5.3.1. TM21

Usually LM 80 report requires 6000 hours' test data. Then, TM-21 (IES, 2011) long term lumen maintenance projecting method can be used to extend the test data to the desired time. TM-

21 method requires at least two test condition which make the test very lengthy and tedious. The following procedures provides the methods of lumen maintenance projections based on the curve-fit method.

Before the curing fitting, all test data of luminous flux should be normalized to a value of 1. The first step is to perform an exponential least square curve-fit through the averaged value at each measurement with the following equations:

$$\Phi(t) = B * \exp(-\alpha * t) \tag{182}$$

Where t is the operating time in hours; Φ (t) is the averaged normalized luminous flux output at time t; α is the decay constant derived by the lease square curve-fit; B is the projected initial constant derived by the lease squares curve-fit.

The second step is to calculate the pre-exponential factor and the activation energy based on the Arrhenius equations listed below:

$$\alpha_i = A * \exp(\frac{-E_a}{K_b * T_{s,i}}) \tag{183}$$

Where A is the pre-exponential factor, Ea is the activation energy in eV; Tsj is the in-situ absolute temperature in Kelvin; Kb is the Boltzmann's constant (8.6173*10^-5 eV/K).

Obtain α1, α2 from the two-aging temperature ($T_{s,1}$, $T_{s,2}$) test result and then, calculate the radio of Ea/Kb with the following equation:

$$\frac{E_a}{K_B} = \frac{\ln \alpha 1 - \ln a2}{\frac{1}{T_{s,2}} - \frac{1}{T_{s,1}}} \tag{184}$$

With the activation calculated above, the pre-exponential factor can be get using the following equation:

$$A = \alpha_1 * \exp(\frac{E_a}{K_b * T_{s,1}}) \tag{185}$$

The predicted luminous flux output as a function of aging time t is:

$$\Phi(t) = \sqrt{B_1 * B_2} * \exp(-A * \exp(\frac{-E_a}{K_B * T_{s,i}}) * t) \quad (186)$$

Figure 211 provides the least square curve fit of the experimental data from 105°C and 175°C aging conditions. The black line shows the prediction of the luminous flux at 140°C with the measured data.

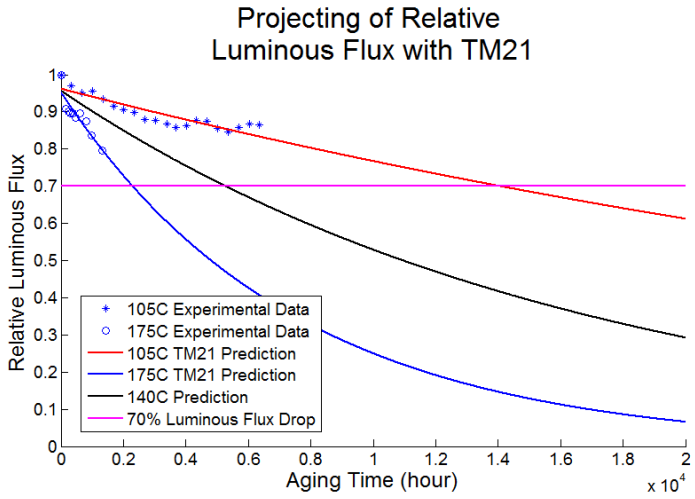


Figure 211: Projection of Relative Luminous Flux with TM21 Method.

To calibrate the activation energy, TM21 method can only work with two finished tests that been performed under different aging temperatures. These estimation and information then, can be used to assess the expected useful life of other using condition. As shown above, this method is tedious and require long test data compared with state estimation methods (Fan, 2011) (Sutharssan, 2011).

### 5.3.2. Color Shift Distance Modeling

Figure 212 shows the test result of color shift distance of six groups. It can be found that higher temperature and higher humidity will lead to higher color shift distance for the same LED package. Also, different LED package has different color shift distance under the same test

condition which could be either caused by the package structure or the chemical recipes of the phosphor particles used in the package. Apparently, Δu dominate the color shift distance during the degradation of color stability.

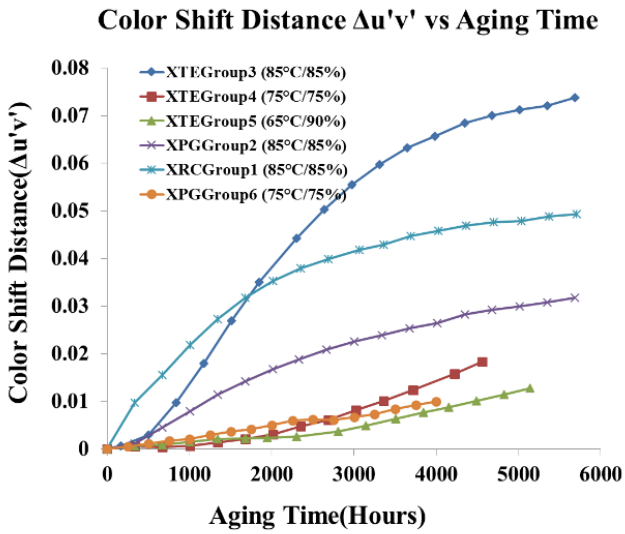


Figure 212: Color Shift Distance Measurement.

As show in Figure 213 , humidity will lead to an increase of the CCT value of LED packages due to the yellow emission spectrum shift and increase of blue peak intensity. The CCT test result under both temperature and humidity is different form the test result from TM80 report in which only thermal stress is considered. Most of TM80 test reports show that color shift to the yellow area and CCT value decreases.

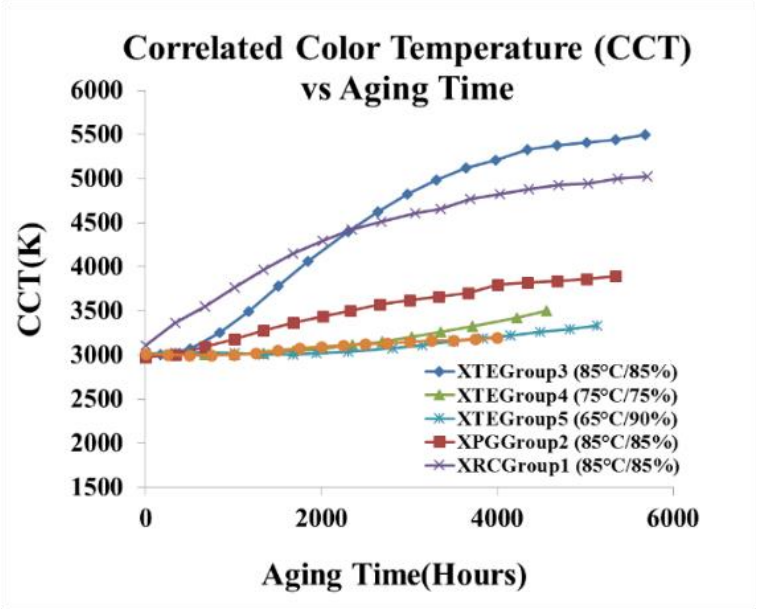


Figure 213: Correlated Color Temperature.

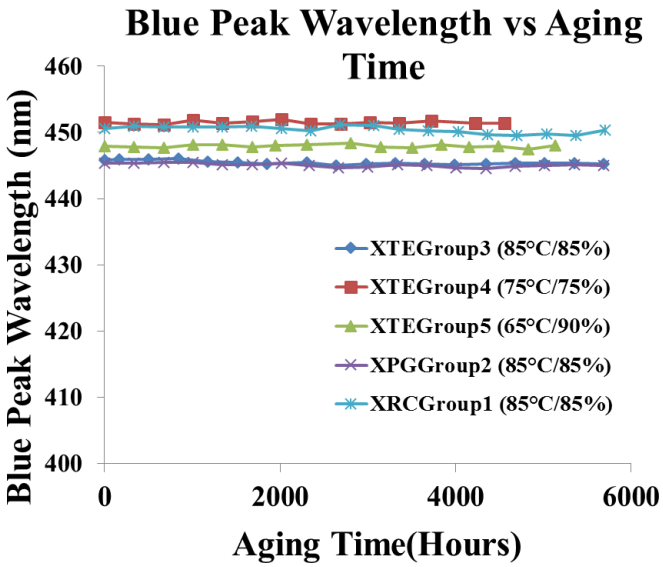


Figure 214: Blue Peak Intensity Wavelength.

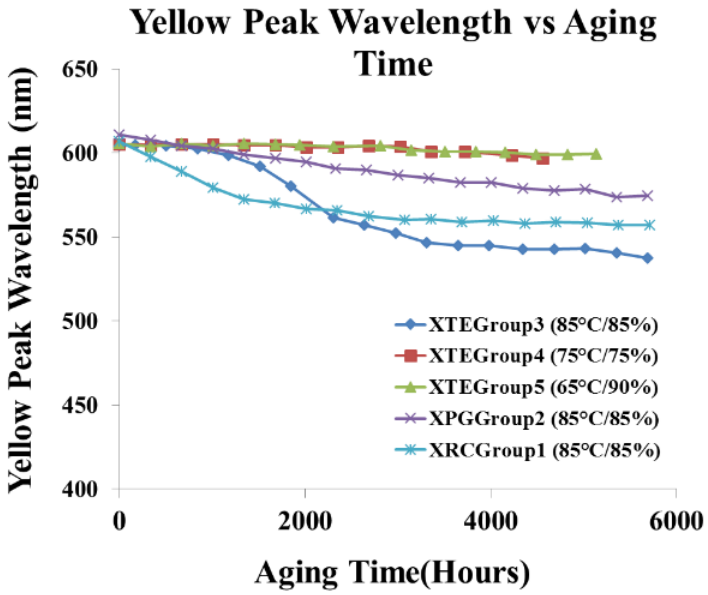


Figure 215: Yellow Peak Intensity Wavelength.

Spectrum power distribution test result shows that the yellow emission spectrum shifts to the lower wavelength area. Figure 214 and Figure 215 demonstrate the blue peak intensity wavelength and yellow peak intensity wavelength measurement during accelerated life test. It can be observed that there is no wavelength shift for the blue peak wavelength. However, the wavelengths of blue peak intensity are not the same for all groups, which means that different semiconductor device parameters are used during the fabrication process. Figure 215 shows that all groups have a shift of yellow emission spectrum to the lower wavelength which is caused by the oxidation of phosphor particles. A higher temperature will lead to higher shift for the same package structure.

In the industry, LM-80 test reports luminous flux maintenance data under a given set of experimental conditions. Then, the TM-21 method can project the luminous flux measurement forward to a desired time within a limited projection window. TM21 projection standard uses the Arrhenius relationship to calibrate the activation energy for LED packages as a function of

temperature and aging time only. However, there are two failure criteria for LED packages and they are luminous flux degradation and color shift. Both of them have specific failure threshold. It can be shown that color shift distance cross the failure threshold earlier than the luminous flux when the LED packages are exposed to the operation environment with both thermal and humidity stress. TM21 is the method can project the luminous flux measurement forward and there is no method that is available for the color shift distance. It is necessary to have a color shift modeling that can project the color shift distance forward and estimate the remaining useful life (RUL).

To introduce additional stresses with the Arrhenius relationship, there are some proposed models. A well-known model that includes both the thermal and humidity is Peck's model which is shown in Equation (187).

$$t_f = A_0 \cdot RH^{-N} \cdot \exp\left[\frac{E_a}{k_b \cdot T}\right] \tag{187}$$

Where RH is relative humidity, T is the ambient temperature, A0 is the model constant, Ea is activation energy and Kb is Boltzmann constant 1.38064852 × 10-23 m2 kg s-2 K-1. Arrhenius model is the basis for the Peck's model and corrosion models that include stresses due to moisture ingress. Peck's model is widely used in industry for moisture ingress in epoxy encapsulated ICs with a high degree of accuracy. However, Peck's model didn't account for the additional stress, such as package geometries. Another well-known model that account for additional stress is Peck's Power Law which is shown in Equation (188):

$$t_f = A_0 \cdot f(\Psi) \cdot RH^{-N} \cdot \exp\left[\frac{E_a}{k_b \cdot T}\right] \tag{188}$$

Peck's Power Law uses f(Ψ) function to produce additional stress function to account for the variety of stresses LED packages may encounter during the operation. Typically, the unknown-function f(Ψ) is considered a constant with no impact on the time-to-failure predictions. In this

paper, Peck's model and Peck's Power Law have been used in the closed-form modeling of color shift distance in terms of aging time and physical package parameters.

From observation of the measurement, the color shift distance changes linear first and they it starts to increase following the logarithm form. Therefore, two equations are used to model the color shift distance in term of aging time. The first is logarithm function with two parameters a and b. The second function is a linear function with only on parameters c, consider the color shift distance is 0 at the initial time. Equation (189) and (190) describe the color shift distance and aging time.

$$y = \frac{\ln(\frac{x}{a})}{b} \tag{189}$$

$$y = c * x + 0 \tag{190}$$

Where y is the color shift distance, x is the aging time, a, b and c are model constant. In order to incorporate accelerated life test temperature, humidity and package structure parameters, a, b and c should be a function of various stresses and geometry parameters of the LED package. Peck's Power Law uses an extra f(Ψ) function to compensate additional stress that LED packages may encounter during the operation. f(Ψ) function should be a time invariant constant that related to the geometry of the package structure. In order to properly determine additional unknown stresses to accurately characterize the color shift distance in terms of aging time, some of the potential parameters were investigated for possible inclusion into the color shift distance model as part of the function f (Ψ). The following Table 12 shows all the potential parameters that related with the model constant.

Table 12: Potential Parameters of Color Shift Distance Model

| **Parameters Classification** | **Description** |
|---|---|

| | |
|---|---|
| Ambient Temperature | Aging Temperature (T) |
| Humidity | Relative Humidity (RH) |
| Geometry Parameters | Particle Size(PS) |
| | Thermal Resistance (TR) |
| | Phosphor Thickness (PT) |
| | Power(P) |
| | Chip length(CL) |
| | Package Length(PL) |

Assuming that each of the parameters a, b, and c can be fit to a power law of various components which is easy for regression process, additional geometry parameters are related with the color shift distance model constant in the following equations.

$$a = RH^{m_1} * \exp(\frac{m_2}{T}) * PS^{m3} * TR^{m_4} * PT^{m_5} * P^{m_6} * CL^{m_7} * PL^{m_8} \quad (191)$$

$$b = RH^{n_1} * \exp(\frac{n_2}{T}) * PS^{n3} * TR^{n_4} * PT^{n_5} * P^{n_6} * CL^{n_7} * PL^{n_8} \quad (192)$$

$$c = RH^{l_1} * \exp(\frac{l_2}{T}) * PS^{l3} * TR^{l_4} * PT^{l_5} * P^{l_6} * CL^{l_7} * PL^{l_8} \quad (193)$$

Similar to what was done with the general form of Peck's model, each LED package's geometry size has been used with the initial function of f (Ψ) to investigate a generalized color shift model. Package structure parameters are related to the function of f (Ψ) in the power form. M, n and l are the coefficients of the power function. The independent variables of each package are given in the

Table 13:

Table 13: Independent Variables of Each LED Package

| | **PS (um)** | **TR (°C/W)** | **PT (um)** | **CL (um)** | **PL (um)** |
|---|---|---|---|---|---|
| XRC | 6 | 12 | 33 | 600x600 | 6880 |
| XPG | 8 | 4 | 50 | 980x980 | 3400 |
| XTE | 15 | 5 | 180 | 1000x1000 | 3400 |

In order to solve for the unknown parameters in Equation (191), (192) and (193), a multivariate analysis was performed on the independent variables. Multiple linear regression methods assume the model's parameters to be linearly independent. If there is a linear dependency of the independent variables, erroneous prediction will be produced due to the correlation, instability and variability. In this paper, the multivariate technique of principal component regression (PCR) has been applied to eliminate linear dependency. PCR is a technique for analyzing multiple regression data that suffer from multi-collinearity. This technique can use eigenvectors to transform a set of standardized dependent variables to a new set of linearly independent variables. The new orthogonal principal components are ranked in order of importance to decrease the number of variables needed to explain most of the variance in the model. This is accomplished by looking at the proportion of total variance explained by each principal component from a Scree plot of the eigenvalues.

All collected data have been placed together as a dependent matrix and an indecent matrix. The regression equation could be written in matrix form as:

$$Y = X * \beta + e \tag{194}$$

Where Y is the dependent variable, X represents the independent variables, β stands for the regression coefficients to be estimated and e represents the error or residues. All the independent variables are placed together as the matrix X. The column of the matrix is independent variables

and each row stands for one sample. There could be several samples in each group. The following matrix shows the structure of X:

$$X = \begin{bmatrix} 1 & x_{1,1} & x_{1,2} & . & . & x_{1,n} \\ 1 & x_{2,1} & x_{2,2} & . & . & x_{2,n} \\ . & . & . & . & . & . \\ . & . & . & . & . & . \\ 1 & x_{30,1} & x_{30,2} & . & . & x_{30,n} \end{bmatrix} \quad (195)$$

Where n represents the total independent variables and 30 is the total sample numbers. The structure of depend matrix Y is as follows:

$$Y = \begin{bmatrix} a_1 & b_1 & c_1 \\ a_2 & b_2 & c_2 \\ . & . & . \\ . & . & . \\ . & . & . \\ a_{29} & b_{29} & c_{29} \\ a_{30} & b_{30} & c_{30} \end{bmatrix} \quad (196)$$

Where a, b and c are the dependent variables for the color shift model. According to the regression equation, β matrix is a n*3 matrix. The independent and dependent matrixes must be centered and scaled in order to obtain the proper form of the regression equation. Centering and scaling requires the mean and standard deviation of each column vector from the predictor matrix. Equation (197) and (198) shows the centering and scaling process:

$$Y^* = \frac{Y - \overline{Y}_i}{\sigma_i} \quad (197)$$

$$X^* = \frac{X - \overline{X}_i}{\sigma_i} \quad (198)$$

Where I is the column number. Then the regression model becomes:

$$Y^* = X^* * \beta^* \quad (199)$$

The next step is to calculate the correlation matrix of X* and eigenvalue and eigenvector of the correlation matrix as show in Equation (200):

$$C = X^* * X^{*T} \tag{200}$$

$$[C] - \lambda * [I] * V = 0 \tag{201}$$

With the orthogonal eigenvectors V solved, the standardized predictor matrix in equation (199) can be transformed into principal components as shown in Equation (202):

$$Y^* = X^* * V * V^T * \beta^* \tag{202}$$

V is the eigenvector matrix of C and it is orthogonal so that V'*V is unity matrix. Assume Z=X*V and a=VT * β*. The regression model becomes:

$$Y^* = Z * a \tag{203}$$

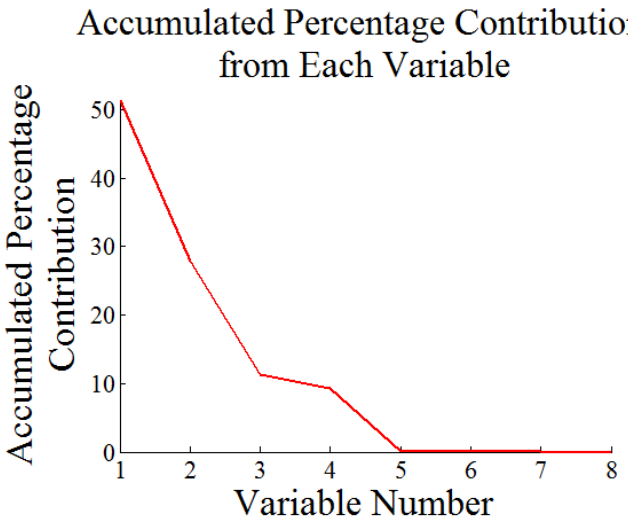


Figure 216: Accumulated Percentage Contribution from Each Variable.

We have created a new variable Z as weighted averages of the original variable X. The new variable Z contains principal components, their correlations with each other are all zero. Severe multi-collinearity will be detected as very small eigenvalues. To get rid of the data with multi-collinearity, the components of the Z matrix will be omitted if they are associated with small eigenvalues. The following Figure 216 shows the accumulated percentage contribution from each

variable. It can be shown that the first five parameters is enough for the color shift distance modeling which are temperature, humidity, particle size, thermal resistance, and phosphor layer thickness.

The strategy of elimination of principal components should be to begin by discarding the component associated with the smallest eigenvalue. The rationale is that the principal component with smallest eigenvalue is the least informative. Using this procedure, principal components are eliminated until the remaining components explain some pre-selected percentage of the total variance (for example, 85 percent or more). Multi-collinearity is no longer a problem after we eliminate the components with small eigenvalues. The regression coefficients are estimated, using the formula of ordinary least squares:

$$a = \left[Z^T * Z\right]^{-1} * Z^T * Y^* \tag{204}$$

After the regression, the coefficient should be transformed back to the original independent variables. With the retention of all component in equation (203), the coefficient for the centered and scaled independent variables are obtained as:

$$\beta^* = V * a \tag{205}$$

Note that β* is the vector of estimated coefficient of the centered and scaled independent variables. Transformation to the coefficients of the non-centered and scaled variables is done as follows:

$$\beta = \frac{\beta_j^*}{\sigma_j} \tag{206}$$

$$\beta_0 = \overline{Y}_j - \frac{\beta_j^* * \overline{X}_j}{\sigma_j} \tag{207}$$

Table 14 and Table 15 shows the least square fitted model constant and the prediction from the color shift distance model.

Table 14: Predicted Color Shift Distance Model Constant a and b

| Test Sample | Sample # | a | b | Prediction of a | Prediction of b |
|---|---|---|---|---|---|
| XRC Warm White 85°C/85% | 1 | 114.1427 | 78.52824 | 172.6949 | 69.82958 |
| | 2 | 213.4707 | 64.44623 | 172.6949 | 69.82958 |
| | 3 | 150.3943 | 71.80848 | 172.6949 | 69.82958 |
| | 4 | 83.6113 | 65.42725 | 172.6949 | 69.82958 |
| XPG Warm White 85°C/85% | 1 | 559.9458 | 73.39709 | 481.6001 | 72.28404 |
| | 2 | 565.4478 | 73.23455 | 481.6001 | 72.28404 |
| | 3 | 557.4734 | 73.76634 | 481.6001 | 72.28404 |
| | 4 | 554.9393 | 73.29065 | 481.6001 | 72.28404 |
| | 5 | 557.1857 | 73.30335 | 481.6001 | 72.28404 |
| XTE Warm White 85°C/85% | 1 | 501.1881 | 31.97777 | 603.8959 | 32.22898 |
| | 2 | 512.8953 | 32.1938 | 603.8959 | 32.22898 |
| | 3 | 520.7767 | 31.5109 | 603.8959 | 32.22898 |
| | 4 | 522.4266 | 31.65729 | 603.8959 | 32.22898 |
| | 5 | 545.1661 | 31.36641 | 603.8959 | 32.22898 |
| XTE Warm White 75°C/75% | 1 | 1335.609 | 77.34122 | 1064.398 | 74.51866 |
| | 2 | 1292.521 | 75.23646 | 1064.398 | 74.51866 |
| | 3 | 1247.757 | 75.78247 | 1064.398 | 74.51866 |
| | 4 | 1255.291 | 75.4858 | 1064.398 | 74.51866 |
| XTE Warm White 65°C/90% | 1 | 1669.44 | 84.10501 | 1662.375 | 80.15227 |
| | 2 | 1685.871 | 80.63428 | 1662.375 | 80.15227 |
| | 3 | 1657.109 | 79.73188 | 1662.375 | 80.15227 |
| | 4 | 1680.737 | 78.99925 | 1662.375 | 80.15227 |
| | 5 | 1619.567 | 77.4431 | 1662.375 | 80.15227 |
| XPG Warm White 75°C/75% | 1 | 846.701 | 153.4122 | 848.8454 | 167.1325 |
| | 2 | 865.2427 | 153.1933 | 848.8454 | 167.1325 |
| | 3 | 780.98 | 177.654 | 848.8454 | 167.1325 |
| | 4 | 820.137 | 156.4893 | 848.8454 | 167.1325 |
| | 5 | 711.236 | 184.8977 | 848.8454 | 167.1325 |

Table 15: Predicted Color Shift Distance Model Constant c

| Test Sample | Sample # | c | Prediction of c |
|---|---|---|---|
| XRC Warm White 85°C/85% | 1 | 2.37E-05 | 2.28E-05 |
| | 2 | 2.19E-05 | 2.28E-05 |
| | 3 | 2.25E-05 | 2.28E-05 |
| | 4 | 2.31E-05 | 2.28E-05 |

| | | | |
|---|---|---|---|
| XPG Warm White 85°C/85% | 1 | 8.84E-06 | 8.95E-06 |
| | 2 | 8.63E-06 | 8.95E-06 |
| | 3 | 8.76E-06 | 8.95E-06 |
| | 4 | 8.88E-06 | 8.95E-06 |
| | 5 | 8.86E-06 | 8.95E-06 |
| XTE Warm White 85°C/85% | 1 | 1.21E-05 | 1.11E-05 |
| | 2 | 1.13E-05 | 1.11E-05 |
| | 3 | 1.13E-05 | 1.11E-05 |
| | 4 | 1.12E-05 | 1.11E-05 |
| | 5 | 1.09E-05 | 1.11E-05 |
| XTE Warm White 75°C/75% | 1 | 2.73E-06 | 2.97E-06 |
| | 2 | 2.88E-06 | 2.97E-06 |
| | 3 | 3.02E-06 | 2.97E-06 |
| | 4 | 2.99E-06 | 2.97E-06 |
| XTE Warm White 65°C/90% | 1 | 1.99E-06 | 2.11E-06 |
| | 2 | 2.02E-06 | 2.11E-06 |
| | 3 | 2.16E-06 | 2.11E-06 |
| | 4 | 2.06E-06 | 2.11E-06 |
| | 5 | 2.34E-06 | 2.11E-06 |
| XPG Warm White 75°C/75% | 1 | 2.48E-06 | 2.39E-06 |
| | 2 | 2.38E-06 | 2.39E-06 |
| | 3 | 2.41E-06 | 2.39E-06 |
| | 4 | 2.42E-06 | 2.39E-06 |
| | 5 | 2.46E-06 | 2.39E-06 |

Figure 217, Figure 218 and Figure 219 shows the prediction error in terms of sample numbers. It can be shown that the all prediction falls into the ±20% error boundary.

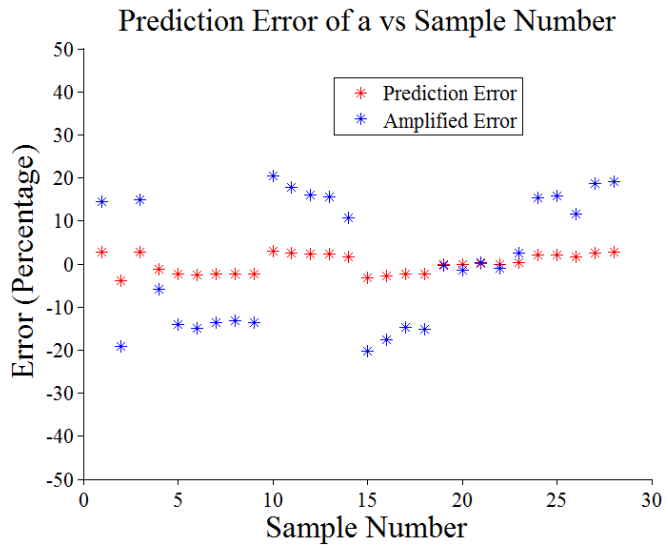


Figure 217: Prediction of Model Constant a.

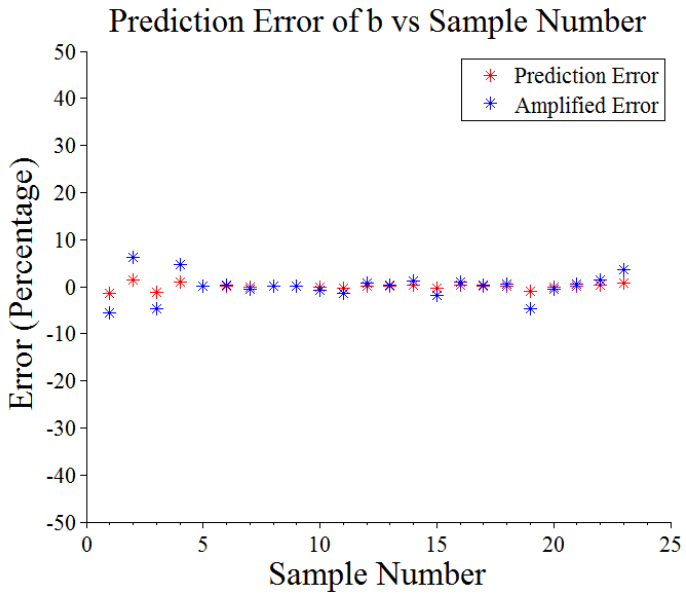


Figure 218: Prediction Error of Model Constant b.

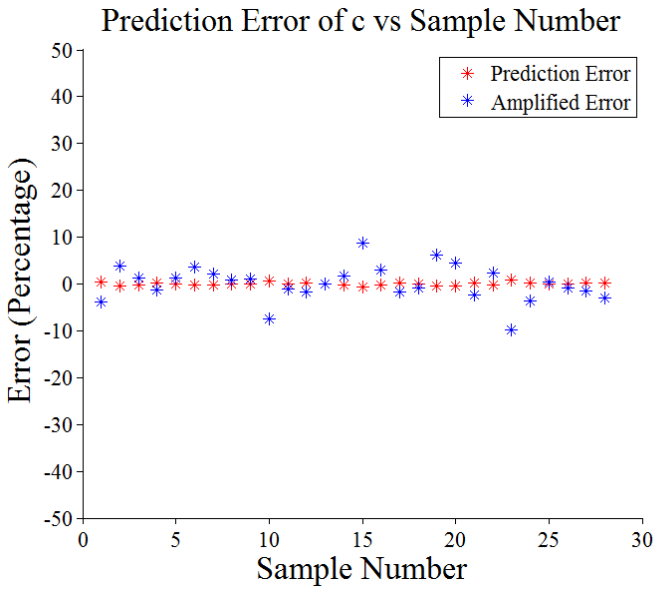


Figure 219: Prediction Error of Model Constant c.

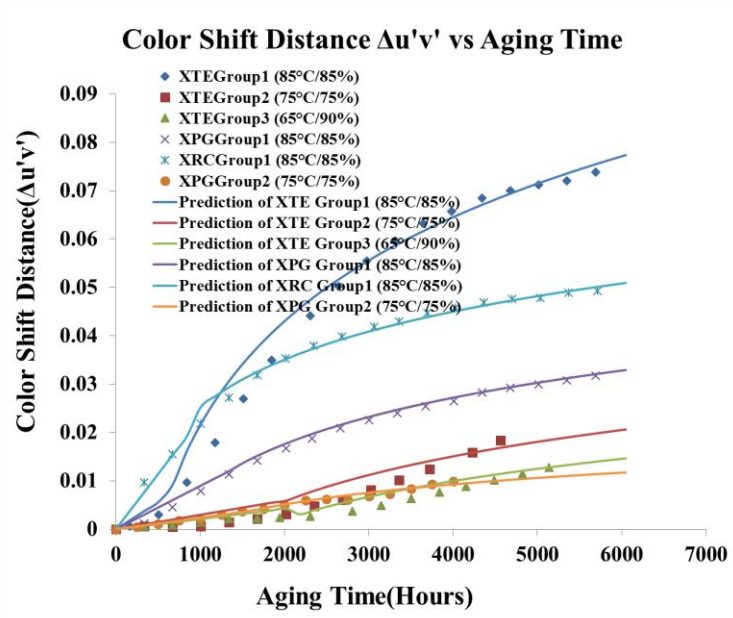


Figure 220: Predicated Color Shift distance vs Experimental Data.

Figure 220 shows the model prediction vs the experimental data for all three LED packages under several different accelerated life test conditions. It can be shown that the proposed model

can predict the color shift distance for different LED package structure at various test condition with acceptable error boundary.

# 6. FUTURE WORK AND CONCLUSIONS

## 6.1. FUTURE WORK

This work can be expanded beyond what has been demonstrated. The generalized acceleration model can be used as a starting point to produce a more accurate lifetime prediction model that utilizes non-thermally driven failure modes. Additional test conditions and the inclusion of additional LED packages will give valuable luminous flux degradation data to determine decay rates. This will allow for a curve-fit of decay rate versus temperature/humidity to produce a generalized decay rate model. With the addition of more ALT conditions and test vehicles, the collected degradation data and the generalized acceleration model can be used towards the achievement of a robust lifetime model for all high-power LED packages.

## 6.2. CONCLUSIONS

LED packages with combined YAG:Ce and GaAlSiN3:Eu2+ phosphor layers are able to deliver higher CRI white spectrum with low CCT. However, nitride phosphor are easy to oxide in the presence of humidity. While previous studies and test standards only focused on the degradation mechanisms caused by high temperature, this paper analyzed the relative humidity effects on the color stability of LEDs. In this paper, three different LED package structures are used during the accelerated life test under both high temperature and humidity. The measurements of different parameters show that high temperature and humidity will deteriorate the color stability of LED packages in a short operation time. Failure analysis from this study demonstrates that humidity can alter the phosphor and binder layer that sit on top of the blue photon emitter. It can be found that oxidized phosphor particles will shift the phosphor emission spectrum to the lower wavelength, and the expanded phosphor binder layer will reduce the density of the phosphor particles. As a result, redistributed emission spectrum shift the chromaticity point of the LED

package. However, this failure mechanism only impacted the color stability properties of the LED. The luminous flux actually tended to increase due to the shift of the phosphor emission peak toward green. A closed-form color shift distance model was built based on the aging time, operation conditions and LED package characteristics. This model can project the color shift distance forward to the desired time. In conclusion, a perspective that takes into account the effects of both relative humidity and thermal stress is essential for understanding the reliability of LED packages.

## REFERENCES


Abdennadher, K. V. (2010). A Real-Time Predictive-Maintenance System of Aluminum Electrolytic Capacitors Used in Uninterrupted Power Supplies. *IEEE Transactions on Industry Applications*, *46*(4), 1644-1652.

Allen, D. (2003). Probabilities associated with a built-in-test system, focus on false alarms. *IEEE Systems Readiness Technology Conference* (pp. 643-645). IEEE.

Baillot, R. D. (2010). Effects of silicone coating degradation on GaN MQW LEDs performances using physical and chemical analysis. *Microelectronics Reliability, 50*, 1568-1573.

Balakrishnan, A. V. (1987). *Kalman Filtering Theory (Series in Communication and Control Systems)1987.* New York: Optimization Software.

Balchen, J. G. (1980). A dynamic positioning system based on Kalman filtering and optimal control.

Barke, D. &. (2005). Structural health monitoring in the railway industry: a review. *Structural Health Monitoring*, 81-93.

Bar-Shalom, Y. L. (2004). *Estimation with applications to tracking and navigation: theory algorithms and software.* John Wiley & Sons.

Batzel, T. D. (2009). Prognostic health management of aircraft power generators. *Aerospace and Electronic Systems*, 473-482.

Bevly, D. M. (2007). Cascaded Kalman filters for accurate estimation of multiple biases, dead-reckoning navigation, and full state feedback control of ground vehicles. *Control Systems Technology*, 199-208.

Cadini, F. Z. (2009). Monte Carlo-based filtering for fatigue crack growth estimation. *Probabilistic Engineering Mechanics*, (pp. 367-373).

Cao, X. A. (2003). Defect generation in InGaN/GaN light-emitting diodes under forward and reverse electrical stresses. *Microelectronics Reliability*, 1987-1991.

Celaya, J. R. (2011). A model-based prognostics methodology for electrolytic capacitors based on electrical overstress accelerated aging. *Proceedings of the Annual Conference of the Prognostics and Health Management Society*, (pp. 31-39). Montreal, Quebec Canada.

Chang, M.-H. D. (2012). Light emitting diodes reliability review. *Microelectronics Reliability, 52*, 762-782.

Chou, H. Y. (2012). Maintenance of stable light emission in high power LEDs. *Microelectronics Reliability*, 912-915.

Chuo, C. C. (2001). Interdiffusion of In and Ga in InGaN/GaN multiple quantum wells. *Applied Physics Letters*, 78.

CIE. (1924). CIE. (1926). Cambridge: Cambridge University Press.

CIE. (1931). CIE. (1932). Cambridge: Cambridge University Press.

CIE. (1995). *Method of Measuring and Specifying Colour Rendering Properties of Light Sources.* 13.3-1995.

CIE. (2004a). *Colorimetry.* 15-2004.

CIE. (2004b). *A Review of Chromatic Adaptation Transforms.* TC-152.

Clapp, T. V. (2015). *Silicone Solutions for LED.* Dow Corning Corporation.

Coble, J. H. (2010). *Adaptive monitoring, fault detection and diagnostics, and prognostics system for the IRIS nuclear plant. .* TENNESSEE UNIV KNOXVILLE.

Colinge, J. P. (2005). *Physics of semiconductor devices. .* Springer Science & Business Media.

CREE. (2007-2013). *Cree® XLamp® XR-C LEDs.*

CREE. (2009-2012). *Cree® XLamp® XP-G LEDs.*

CREE. (2011-2016). *Cree® XLamp® XT-E LEDs.*

CREE. (2013). *LED Color Mixing: Basics and Backgrounds.* CLD-AP38 REV 1.

Davidson, M. W. (n.d.). *Fundamentals of Light-Emitting Diodes*. Retrieved from ZEISS: http://zeiss-campus.magnet.fsu.edu/print/lightsources/leds-print.html

DeCusatis, C. (1997). *Handbook of Applied Photometry.* New York: AIP Press.

DeShazer, D. J. (2014). *Silicones & Phosphors in Solid State Lighting.* Dow Corning Corporation.

DOE EERE. (2013c). *Gateway Demonstrations: Demonstration of LED Street Lighting.* Kansas City, Missouri: DOE.

DOE: EERE. (2012). *Solid-State Lighting Multi-Year Market Development Support Plan.* Building Technologies Program: Solid-State Lighting Program.

DOE: EERE. (2013a). *Hammer Testing Findings for Solid-State Lighting Luminaires.* DOE.

DOE: EERE. (2013b). *Gateway Demonstrations: Demonstration Assessment of LED Parking Structure Lighting.* Washington D.C.: DOE.

DOE: EERE. (2013d). *Subjective Evaluation of Beam Quality, Shadow Quality, and Color Quality for LED PAR38 Lamps.* Richland, Washington: PNNL.

DOE: EERE. (2014a). *Gateway Demonstrations: Long-Term Testing of LED Luminaires.* Minneapolis, Minnesota: DOE.

Doucet, A. G. (2001). Particle filters for state estimation of jump Markov linear systems. *Signal Processing*, 613-624.

Dow Corning Corporation. (1997). *Silicone Chemistry Overview*. Midland, MI: Dow Corning Corporation.

EERE. (2006). *Office of Energy Efficiency & Renewable Energy*. Retrieved January 12, 2015, from http://energy.gov/eere

Egawa, T. J. (1997). Characteristics of InGaN/AlGaN light-emitting diodes on sapphire substrates. . *Journal of applied physics, ,* 5816-5821.

Engel, S. (2009). PHM Engineering Perspectives, Challenges and 'Crossing the Valley of Death. *Annual Conference of the Prognostics and Health Management Society,* (pp. 1-21). San Diego.

Fan, J. Y. (2011). Physics-of-failure based prognostics and health management for high power white light-emitting diode lighting. *IEEE Transactions on Device and Materials Reliability, 11*(3), 407-416.

Fu, H. K. (2012). nvestigation of dynamic color deviation mechanisms of high power light-emitting diode. *Microelectronics Reliability,* 866-871.

Gao, R. X. (2002). BIT for intelligent system design and condition monitoring. *Instrumentation and Measurement,* 1061-1067.

Goebel, K. S. (2008). Prognostics in battery health management. *IEEE instrumentation & measurement magazine,* 33.

Grewal, M. S. (2001). *Kalman Filtering: Theory and Practice Using MATLAB* (2nd ed.). New York: John Willy & Sons Inc.

Gueler, G. F. (1989). Modelling, design and analysis of an autopilot for submarine vehicles. *International shipbuilding progress,*, 51-85.

Hallberg, Ö. &. (1991). Recent humidity accelerations, a base for testing standards. *Quality and Reliability Engineering International,* 169-180.

Hallberg, O. a. (1991). Recent Humidity Accelerations, A Base for Testing Standards. *Quality and Reliability Engineering International, 7,* 169-180.

Hamada, M. S. (2008). *Bayesian reliability.* Springer Science & Business Media.

Hayward, R. C.-E. (1997). Inertially aided GPS based attitude heading reference system (AHRS) for general aviation aircraft. *In Proceedings of the Institute of Navigation ION-GPS Conference* , (pp. 1415-1424).

Hernandez-Andres, J. L. (1999). Calculating correlated color temperatures across the entire gamut of daylight and skylight chromaticities. *Journal of Applied Optics, 38*(27), 5703-5709.

Hewlett Packard. (1997). *Reliability of precision optical performance AllnGaP LED lamps in traffic signals and variable message signs.* Application Brief I-004.

Horng, R. H. (2012). Failure modes and effects analysis for high-power GaN-based light-emitting diodes package technology. *Microelectronics Reliability, ,* 818-821.

Hsieh, Y. F.-Y. (2012). Determination of optimal converting point of color temperature conversion complied with ANSI C78.377 for indoor solid-state lighting and display applications. *Journal of Optics Express, 20*(18), 20059-20070.

Hsu, Y. L. (2008). Failure mechanisms associated with lens shape of high-power LED modules in aging test. *IEEE Transactions on Electronic Devices, 55*(2), 689-694.

IES. (2008a). *IES LM-79-08 Approved Method: Electrical and Photometric Measurements of Solid-State Lighting Products.* New York: Illuminating Engineering Society.

IES. (2008b). *IES LM-80-08 Approved Method: Measuring Lumen Maintenance of LED Light Sources.* New York: Illuminating Engineering Society.

IES. (2011). *IES TM-21-11 Projecting Long Term Lumen Maintenance of LED Light Sources.* New York: Illuminating Engineering Society.

Jang, H. S. (2009). mprovement of electroluminescent property of blue LED coated with highly luminescent yellow-emitting phosphors. *Applied Physics* , 715-720.

Jarrell, D. S. (2002). Prognostics and condition based maintenance (CBM) a scientific crystal ball. *International Congress on Advanced Nuclear Power Plants (ICAPP)*, (p. Vol. 194).

JEDEC. (2006). *Failure Mechanisms and Models for Semiconductor Devices.* JEDEC.

JEDEC. (2009). *JEDEC Steady State Temperature Humidity Bias Life Test Standard.* JESD22-A101C.

JEDEC. (2010). *JEDEC High Temperature Storage Life Standard.* JESD22-A103D.

Jiang, M. &. (2009). Jiang, M., & Dummer, D. J. (2009, January). Bayesian reliability demonstration test in a design for reliability process. *In 2009 Annual Reliability and Maintainability Symposium.*

John Evans, C. Z. (2016). Long Term Aging Effects on The Reliability of Lead Free Solder Joints in Ball Grid Array Packages With Various Pitch Sizes and Ball Arrangement. *Journal of Surface Mount Technology*, 37-46.

Julier, S. J. (1997). New extension of the Kalman filter to nonlinear systems. *AeroSense'97* (pp. 182-193). International Society for Optics and Photonics.

Kalman, R. E. (1960). A new approach to linear filtering and prediction problems. *Journal of basic Engineering*, 35-45.

Kasap, S. (2001). *Pn junction devices and light emitting diodes.* Retrieved from http://kasap3. usask. ca/samples/PNJunctionDevices. pdf

Kleinbaum, D. G. (2005). Competing risks survival analysis. *Survival Analysis: A self-learning text*, 391-461.

Ko, J. M. (2005). Technology developments in structural health monitoring of large-scale bridges. *Engineering structures*, 1715-1725.

Kulkarni, C. B. (2010). Integrated diagnostic/prognostic experimental setup for capacitor degradation and health monitoring. *AUTOTESTCON* (pp. 1-7). 2010 IEEE.

Lafont, U. v. (2012). Increasing the reliability of solid state lighting systems via self-healing approaches: A review. . *Microelectronics Reliability*, 71-89.

Lakshmanan, A. K. (2011, May). Synthesis, photoluminescence and thermal quenching of YAG:Ce phosphor for white light emitting diodes. *Indian Journal of Pure & Applied Physics, 49*, 303-307.

Lall, P. B. (2008d). Interrogation of system state for damage assessment in lead-free electronics subjected to thermo-mechanical loads. *IEEE Proceedings of the 58th Electronic Components and Technology Conference* (pp. 918-929). Orlando, Florida: IEEE.

Lall, P. C. (2006a). Health monitoring for damage initation & pregression during mechanical shock in electronic assemblies. *Proceedings of the 56th Electronics Components and Technology Conference* (pp. 85-94). San Diego, California: IEEE.

Lall, P. C. (2007a). Statistical pattern recognition and built in reliability test for feature extraction and health monitoring of electronics under shock loads. *Proceedings of the 57th Electronics Components and Technology Conference* (pp. 1161-1178). Reno, Nevada: IEEE.

Lall, P. C. (2008a). Health monitoring for damage initiation and progression during mechanical shock in electronic assemblies. *IEEE Transactions on Components and Packaging Technologies, 31*(1), 173-183.

Lall, P. G. (2007b). Solder-joint reliability in electronics under shock and vibration using explicit finite element sub-modeling. *IEEE Transactions on Electronic Packaging Manufacturing, 30*(1), 74-83.

Lall, P. H. (2006b). Feature extraction and damage data for prognostication of leaded and leadfree electronics. *Proceedings of the 56th Electronics Components and Technology Conference* (pp. 718-727). San Diego, California: IEEE.

Lall, P. H. (2007c). Prognostics health monitoring (PHM) for prior-damage assessment in electronics equipment under thermo-mechanical loads. *Proceedings of the 57th Electronics Components and Technology Conference* (pp. 1097-1111). Reno Nevada: IEEE.

Lall, P. H. (2007e). Feature extraction and damage-precursors for prognostication of lead-free electronics. *Microelectronics reliability*, *47*, 1907-1920.

Lall, P. H. (2008c). Algorithms for prognostication of prior damage and residual life in lead-free electronics subjected to thermo-mechanical loads. *IEEE Proceedings of the 10th Intersociety Thermal and Thermo-mechanical Phenomena* (pp. 638-651). Orlando, Florida: IEEE.

Lall, P. I. (2004a). Leading indicators-of-failure for prognosis of electronic and MEMS packaging. *Proceedings of the 54th Electronics Components and Technology Conference.* Las Vegas, Nevada: IEEE.

Lall, P. I. (2004b). Damage mechanics of electronics on metal-backed substrates in harsh environments. *Proceedings of the 54th Electronics Components and Technology Conference.* Las Vegas, Nevada: IEEE.

Lall, P. I. (2004c). Model for BGA and CSP reliability in automotive underhood applications. *IEEE Transactions on Components and Packaging Technologies*, *27*(3), 585-593.

Lall, P. I. (2005a). Prognostication and health monitoring of leaded and lead free electronic and MEMs packages in harsh environments. *Proceedings of the 55th Electronics Components and Technology Conference* (pp. 1-9). Orlando, Florida: IEEE.

Lall, P. I. (2006d). Damage mechanics of electronics on metal-backed substrates in harsh environments. *IEEE Transactions on Components and Packaging Technologies, 29*(1), 204-212.

Lall, P. I. (2008f). Design envelopes and optical feature extraction techniques for survivability of SnAg leadfree packaging architectures under shock and vibration. *IEEE Proceedings of the 58th Electronic Components and Technology Conference* (pp. 1036-1047). Orlando, Florida: IEEE.

Lall, P. L. (2009a). Prognostication Based On Resistance-Spectroscopy for High Reliability Electronics under Shock-Impact. *ASME International Mechanical Engineering Conferance & Exposition.*

Lall, P. L. (2009b). Resistance spectroscopy-based condition monitoring for prognostication of high reliability electronics under shock-impact. *Proceedings of the 59th Electronic Components and Technology Conference.* IEEE.

Lall, P. L. (2010a). Prognostics Using Kalman-Filter Models and Metrics for Risk Assessment in BGAs under Shock and Vibration Load. *Proceedings of the 60th Electronic Components and Technology Conference.* IEEE.

Lall, P. L. (2010b). Use of Prognostics in Risk-Based Decision Making for BGAs under Shock and Vibration Loads. *11th IEEE Intersociety Conference on Thermal and Thermomechanical Phenomena in Electronic Systems.* IEEE.

Lall, P. L. (2011a). Extend Kalman Filter Models and Resistance Spectroscopy for Prognostication and Health Monitoring of Lead-free Electronics under Vibration. *IEEE Conference on Prognostics and Health Management.*

Lall, P. L. (2011b). Particle Filter Models and Phase Sensitive Detection for Prognostication and Health Monitoring of Lead-free Electronics under Shock and Vibration. *Proceedings of the 61st Electronic Components and Technology Conference.* IEEE.

Lall, P. L. (2011c). PHM of Lead-free Interconnects using Resistance Spectroscopy Based Particle Filter Models for Shock and Vibration Environments. *Proc. Of ASME 2011 Technical Confernce & Exposition On Packaging and Integration of Electronics and Photonic Systems.* ASME.

Lall, P. P. (2004d). Models for reliability prediction of fine-pitch BGAs and CSPs in shock and drop-impact. *Proceedings of the 54th Electronics Components and Technology Conference* (pp. 1296-1303). Las Vegas, Nevada: IEEE.

Lall, P. P. (2005b). Failure-envelope approach to modeling shock and vibration survivability of electronic and MEMs packaging. *Proceedings of the 55th Electronics Components and Technology Conference* (pp. 480-490). Orlando, Florida: IEEE.

Lall, P. P. (2006e). Models for reliability prediction of fine-pitch BGAs and CSPs in shock and drop-impact. *IEEE Transactions on Components and Packaging Technologies, 29*(3), 464-474.

Lall, P. P. (2008b). Failure-envelope approach to modeling shock and vibration survivability of electronic and MEMs packaging. *IEEE Transactions on Components and Packaging Technologies, 31*(1), 104-113.

Lall, P. S. (2008e). Principal component regression models for life prediction of plastic ball grid arrays on copper-core and no-core assemblies. *IEEE Intersociety conference on Thermal and Thermo-mechanical Phenomena in Electronic Systems* (pp. 770-785). Orlando, FL: IEEE.

Lall, P. S. (2012b). Leading Indicators for Prognostic Health Management of Electrical Connectors Subjected to Randaom Vibration. *IEEE Intersociety conference on Thermal and Thermo-mechanical Phenomena in Electronic Systems.* San Diego, CA: IEEE.

Lall, P. S. (2013a). Prognostics of damage accrual in SSL luminaires and drivers subjected to HTSL accelerated aging. *Proceedings of the ASME 2013 International Technical Conference and Exhibition on Packaging and Integration of Electronic and Photonic Microsystems.* Burlingame, CA: ASME. doi:10.1115/IPACK2013-73250

Lall, P. S. (2014). Reliability of solid-state lighting electrical drivers subjected to WHTOL accelerated aging. *14th IEEE Inter-Society Conference on Thermal and Thermomechanical Phenomena in Electonic Systms* (pp. 1164-1170). Lake Buena Vista, FL: IEEE.

Lall, P. W. (2012a). Comparison of Kalman-filter and extended Kalman-filter for the PHM of Electronics. *IEEE Intersociety conference on Thermal and Thermo-mechanical Phenomena in Electronic Systems.* San Diego: IEEE.

Lall, P. Z. (2013b). Assessment of Lumen Degradation and Remaining Life of LEDs using Particle Filter. *Proceedings of the ASME 2013 International Technical Conference and Exhibition on Packaging and Integration of Electronic and Photonic Microsystems.* Burlingame, CA: ASME.

Lin, Y. T. (2006). Materials challenges and solutions for the packaging of high power LEDs. *IEEE International Microsystems, Packaging, Assembly Conference* (pp. 1-4). Taipei, Taiwan: IEEE.

Lu, G. M. (2015). Color Shift Investigations for LED Secondary Optical Designs: Comparison between BPA-PC and PMMA. *Optical Materials, 45*, 37-41.

Lu, G. S. (2009). Analysis on failure modes and mechanisms of LED. *Reliability, maintainability and safety*, 1237-1241.

Lunia, A. K. (2014). Theoretical analysis of blue to white down conversion for light-emitting diode light with yttrium aluminum garnet phosphor. *Journal of Photonics for Energy, 4*, 043596-1- 043596-11.

Luo, X. W. (2010). Effects of moist environments on LED module reliability. *IEEE Transactions on device and materials reliability, 10*(2), 182-186.

McCluskey, M. D. (1998). Interdiffusion of In and Ga in InGaN quantum wells. *Applied physics letters*, 1281-1283.

McCluskey, P. M. (1999). Reliability of commercial plastic encapsulated microelectronics at temperatures from 125 C to 300 C. *n High Temperature Electronics, 1999. HITEN 99. The Third European Conference on (pp. 155-162). IEEE.*

McCluskey, P. M. (2000). Reliable use of commercial technology in high temperature environments. *Microelectronics Reliability, 40*, 1671-1678.

Mehr, M. Y. (2013b). Photodegradation of bisphenol A polycarbonate under blue light radiation and its effect on optical properties. *Optical Materials, 35*, 504-508.

Meneghini, M. D. (2012). Chip and package-related degradation of high power white LEDs. *Microelectronics Reliability*, 804-812.

Meneghini, M. P. (2006). High brightness GaN LEDs degradation during dc and pulsed stress. *Microelectronics Reliability*, 1720-1724.

Meneghini, M. T. (2006). High-temperature degradation of GaN LEDs related to passivation. *Electron Devices*, 2981-2987.

Meneghini, M. T. (2007). High temperature electro-optical degradation of InGaN/GaN HBLEDs. *Microelectronics Reliability,* 1625-1629.

Meneghini, M. T. (2007). High temperature electro-optical degradation of InGaN/GaN HBLEDs. *Microelectronics Reliability*, 1625-1629.

Meneghini, M. T. (2008, June). A review on the reliability of GaN-based LEDs. *IEEE Transactions on Device and Materials Reliability, 8*(2), 323-331.

Meneghini, M. T. (2008). A review on the reliability of GaN-based LEDsDevice and Materials Reliability. *Device and Materials Reliability*, 323-331.

Meneghini, M. T. (2010). A review on the physical mechanisms that limit the reliability of GaN-based LEDs. *Electron Devices,* 108-118.

Miller, N. K. (2014a). *LED Lighting in a Performing Arts Building at the University of Florida.* Gainsville, Florida: PNNL.

Miller, N. M. (2013). *Pedestrian Friendly Outdoor Lighting.* Richland, Washington: PNNL.

Mishra, S. P. (2002). In-situ sensors for product reliability monitoring. *Symposium on Design, Test, Integration, and Packaging of MEMS/MOEMS 2002* (pp. 10-19). International Society for Optics and Photonics.

Mishra, U. K. (2002). AlGaN/GaN HEMTs-an overview of device operation and applications. *PROCEEDINGS-IEEE* (pp. 1022-1031). IEEE.

Narendran, N. G. (2004). Solid-state lighting: failure analysis of white LEDs. *Journal of Crystal Growth, 268,* 449-456.

Narendran, N. G.-N. (2005). Extracting phosphor-scattered photons to improve white LED efficiency. *physica status solidi* , R60-R62.

Nelson, W. ,. (1990). *Accelerated Testing: Statistical Models, Test Plans, and Data Analysis.* New York: John Wiley & Sons.

Neudeck, G. W. (2002). *Introduction to Microelectronic Fabrication.* Modular Series on Solid State Devices, 5.

Nguyen, X. L. (2010). The fabrication of GaN-based light emitting diodes (LEDs). *Advances in Natural Science: Nanoscience and Nanotechnology, 1*, 1-5. doi:10.1088/2043-6254/1/2/025015

Ohno, Y. (2014). Practical Use and Calculation of CCT and Duv. *The Journal of the Illuminating Engineering Society of North America, 10*, 47-55.

Pecht, M. &. (2009). Physics-of-failure-based prognostics for electronic products. *ransactions of the Institute of Measurement and Control*, 309-322.

Philips Lumileds Lighting Company. (2006). *Luxeon Reliability.* Luxeon Reliability Datasheet RD25.

Pierret, R. F. (1987). *Advanced semiconductor fundamentals.* ,MA: Addison-Wesley, .

Pierret, R. F. (1996). *Semiconductor device fundamentals.* Pearson Education India.

Pierret, R. F. (2003). *Advanced semiconductor fundamentals (Vol. 6).* Reading, MA: Addison-Wesley.

Pust, P. W. (2014). narrow-band red-emitting Sr [LiAl3N4]: Eu2+ as a next-generation LED-phosphor material. *Nature materials*, 891-896.

Rohwer, L. S. (2003). Development of Phosphors for LEDS. Electrochem. *Electrochem. Soc. Interface*, (pp. 36-40).

Saha, B. &. (2009). Modeling Li-ion battery capacity depletion in a particle filtering framework. *Proceedings of the annual conference of the prognostics and health management society*, (pp. 2909-2924).

Saha, B. K. (2011). Model adaptation for prognostics in a particle filtering framework. *International Journal of Prognostics and Health Management*, 61.

Saxena, A. C. (2008). Metrics for Evaluating Performance of Prognostic Techniques. *International Conferance on Prognostics and Health Management.*

Saxena, A. C. (2009a). Evaluating Algorithm Performance Metrics Tailored for Prognostics. *IEEE Aerospace Conference.* IEEE.

Saxena, A. C. (2009b). On Applying the Prognostics Performance Metrics. *Annual Conference of the PHM Society.*

Schanda, J. (2007). *Colorimetry: Understanding the CIE System.* Hoboken: John Wiley & Sons Inc.

Schubert, E. F. (2006). *Light-Emitting Diodes.* Cambridge, UK: Cambridge University Press.

Smith, D. J. (2011). *Reliability, Maintainability and Risk 8e: Practical Methods for Engineers Including Reliability Centred Maintenance and Safety-Related Systems.* Elsevier.

Stanford Research Systems. (n.d.). *About Lock-In Amplifiers.* Stanford Research Systems Application Notes.

Su, Y. F. (2012). Light degradation test and design of thermal performance for high-power light-emitting diodes. *Microelectronics Reliability*, 794-803.

Suhir, E. (2002). Accelerated life testing (ALT) in microelectronics and photonics: its role, attributes, challenges, pitfalls, and interaction with qualification tests. *Journal of Electronic Packaging*, 281-291.

Sutharssan, T. B. (2011). Prognostics and Reliability Assessment of Light Emitting Diode Packaging. *IEEE International Conference on Electronic Packaging Technology & High Density Packaging.* IEEE.

Swanson, D. C. (2000). Prognostic modelling of crack growth in a tensioned steel band. *Mechanical systems and signal processing*, 789-803.

Swanson, D. C. (2001). A general prognostic tracking algorithm for predictive maintenance. *Aerospace Conference* (pp. 2971-2977). IEEE Proceedings.

Tampère, C. M. (2007). An extended Kalman filter application for traffic state estimation using CTM with implicit mode switching and dynamic parameters. *Intelligent Transportation Systems Conference* (pp. 209-216). IEEE.

Tan, C. M. ( 2008). Humidity effect on the degradation of packaged ultra-bright white LEDs. *Electronics Packaging Technology Conference*, (pp. 923-928).

Tarashioon, S. B. (2012). An approach to "Design for Reliability" in solid state lighting systems at high temperatures. *Microelectronics Reliability*, 783-793.

Tran, N. T. (2008). Studies of phosphor concentration and thickness for phosphor-based white light-emitting-diodes. *Lightwave Technology*, 3556-3559.

Tran, N. T. (2009). Effect of phosphor particle size on luminous efficacy of phosphor-converted white LED. *Lightwave Technology*, 5145-5150.

Trevisanello, L. M. (2008). Accelerated life test of high brightness light emitting diodes. Device and Materials Reliability. *Device and Materials Reliability*, 304-311.

Van Der Merwe, R. &. (2001). The square-root unscented Kalman filter for state and parameter-estimation. *coustics, Speech, and Signal Processing* (pp. 3461-3464). IEEE.

Van Der Merwe, R. (2004). Sigma-point Kalman filters for probabilistic inference in dynamic state-space models. *Doctoral dissertation*.

Vichare, N. M. (2006). Prognostics and health management of electronics. *Components and Packaging Technologies*, 222-229.

Wan, E. A. (2000). The unscented Kalman filter for nonlinear estimation. *Wan, E. A., & Van Der Merwe, R. (2000). The unscented Kalman filter for nonlinear estimation. In Adaptive Systems for Signal Processing, Communications, and Control Symposium* (pp. 153-158). IEEE.

Wang, J. J. (2006). A neural network and Kalman filter hybrid approach for GPS/INS integration. *2th IAIN Congress & 2006 Int. Symp. on GPS/GNSS,*.

Westland, S. a. (2004). *Computational Colour Science Using Matlab.* Hoboken, New Jersy: John Wiley & Sons, Inc.

Wikipedia. (2006, August 4 ). Retrieved from Wikipedia: https://en.wikipedia.org/wiki/File:Wiens_law.svg

Wyszecki, G. a. (1982). *Color Science: Concepts and Methods, Quantitative Data and Formulae* (2nd ed.). New York: John Wiley & Sons.

Xie, R. J. (2007). Silicon-based oxynitride and nitride phosphors for white LEDs - A review. *Science and Technology of Advanced Materials, 8*, 588-600.

Yang, S. C. (2010). Failure and degradation mechanisms of high-power white light emitting diodes. *Microelectronics Reliability*, 959-964.

Yang, Y. H. (2014). Acceleration factor analysis of aging test on gallium nitride (GaN)-based high power light-emitting diode (LED). *Thermal and Thermomechanical Phenomena in Electronic Systems (ITherm)* (pp. 178-181). IEEE.

Youn, C. J. (2003). nfluence of various activation temperatures on the optical degradation of Mg doped InGaN/GaN MQW blue LEDs. *Journal of Crystal Growth*, 331-338.

Zarchan, P. M. (2000). *Fundamentals of Kalman Filtering: A Practical Approach* (Vol. 190). Virginia: Progress in Astronautics and Aeronautics.

Zhang, R. &. (2012). Moldless encapsulation for LED wafer level packaging using integrated DRIE trenches. *Microelectronics Reliability*, 922-932.

Zhou, Y. L. (2012). A Remaining Useful Life Prediction Method Based on Condition Monitoring for LED Driver. *IEEE Prognostics & System Health Management Conference.* IEEE.

Zourides, V. G. (1989). Smart built-in-test (BIT): an overview. *The Systems Readiness Technology Conference* (pp. 67-74). IEEE Automatic Testing Conference.

Zukauskas, A. S. (2002). *Introduction into Solid-State Lighting.* New York: John Wiley & Sons Inc.